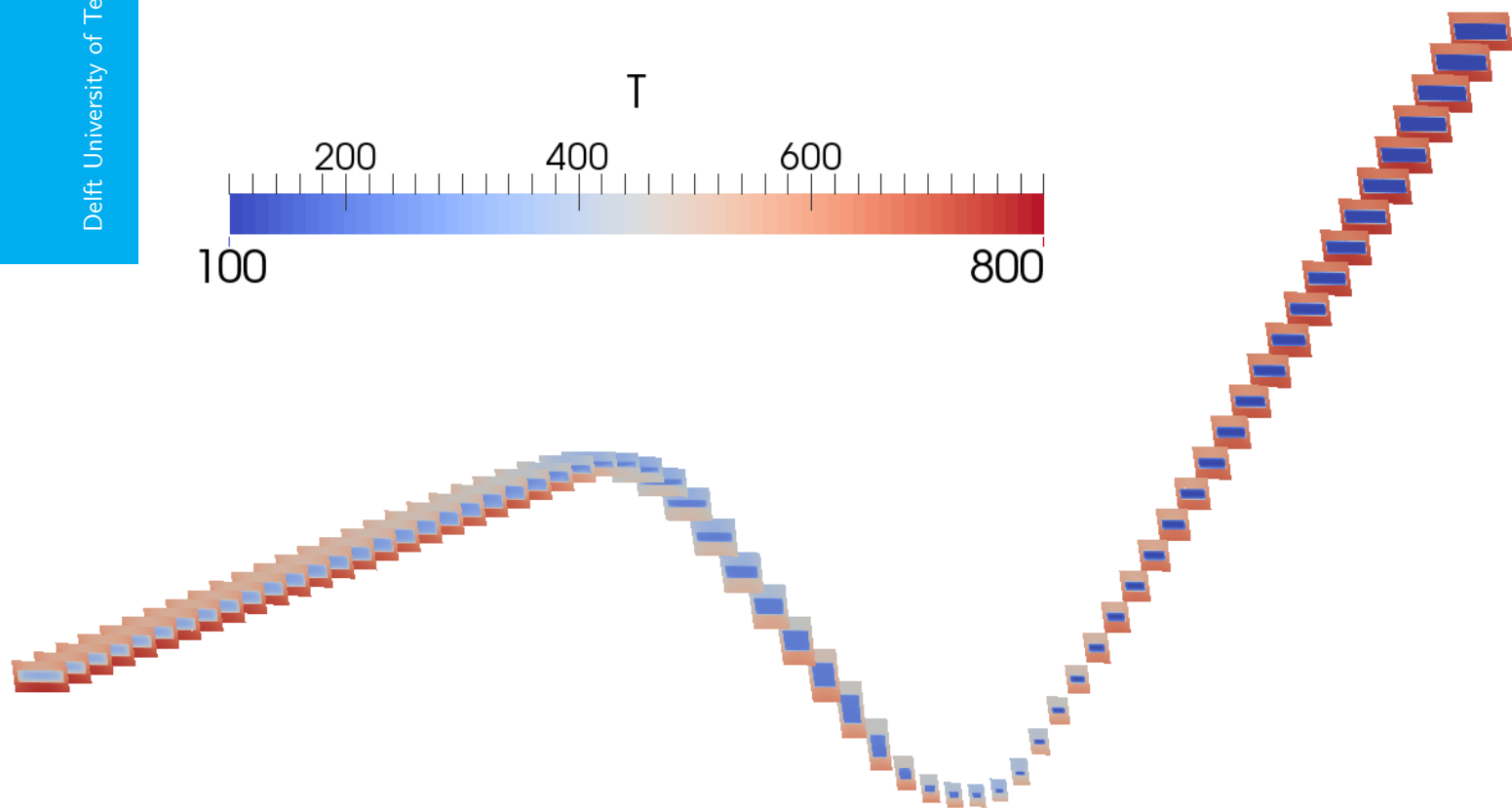
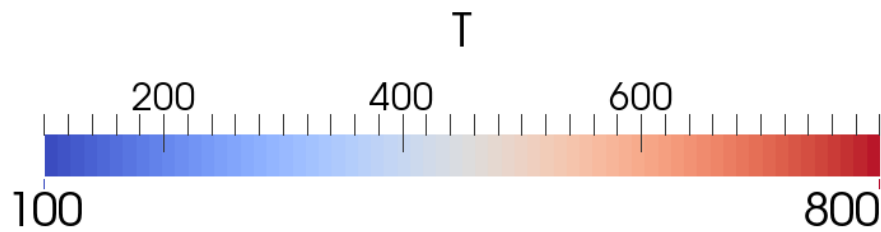


# Regenerative cooling analysis of oxygen/methane rocket engines

Luka Denies

Delft University of Technology





# REGENERATIVE COOLING ANALYSIS OF OXYGEN/METHANE ROCKET ENGINES

by

**Luka Denies**

in partial fulfillment of the requirements for the degree of

**Master of Science**

in Aerospace Engineering

at the Delft University of Technology,

to be defended publicly on Thursday December 10, 2015 at 15:30.

Student number:	4056256	
Supervisor:	Ir. B. T. C. Zandbergen	
Thesis committee:	Prof. dr. E. K. A. Gill,	TU Delft
	Dr. ir. F. F. J. Schrijer,	TU Delft
	Dr. R. Pecnik,	TU Delft

An electronic version of this thesis is available at <http://repository.tudelft.nl/>.



# REVISION HISTORY

<b>Revision</b>	<b>Date</b>	<b>Author(s)</b>	<b>Description</b>
1.0	2015-11-26	L. Denies	Initial version provided to graduation committee
1.1	2016-01-11	L. Denies	Updated captions of figures 5.26, 5.28 and 5.30-34 to clarify that the test article photo, experimental results and Fluent analysis are courtesy of CIRA



# ACKNOWLEDGEMENTS

This thesis is the final milestone of my degree in Aerospace Engineering, marking the end of my time as a student in Delft. As such, I would like to thank those who helped me bring this graduation project to fruition, but especially also the people who have made my life the past six years an unforgettable experience.

I owe gratitude to my supervisor, Barry Zandbergen, for his guidance, support and valuable feedback. Through discussions with him, I was forced to think deeply about the narrative of this thesis, bringing much needed focus. I thank Ferry Schrijer and René Pecnik for their interest in my project, their expertise and their much appreciated advice. Marco Pizzarelli provided helpful comments by e-mail.

I am deeply indebted to the people at CIRA in Italy for the access to their experimental data, but more importantly for their incredible hospitality. In particular, I want to thank Pasquale "il Festivo" Natale, Daniele Cardillo, Daniele Ricci, Marco Invigorito and Francesco Battista for their wonderful company, their help in rebuilding the test results, their expertise in CFD and for showing me their country. Grazie mille.

To my many *genootjes* (in Dutch: *afstudeerkamer-, beheers-, bestuurs-, commissie-, dispuuts-, huis-, ploeg-, senaats-, raads- en teamgenootjes*) and other friends in Delft, I am grateful for making my time in Delft truly the time of my life. Because of them, my student time was a valuable experience in itself, rather than the means to an end.

I want to thank my family for their unconditional support. Although I was rarely with them in Belgium, my mother, father and sister continued to support me in every possible way. Finally, my gratitude to Anouk, without whom it would all have been less meaningful.

Thank you all.

*Luka Denies  
Delft, November 2015*



# SUMMARY

Methane is a promising propellant for future liquid rocket engines. In the cooling channels of a regeneratively cooled engine, it would be close to the critical point. This results in drastic changes in the fluid properties, which makes cooling analysis a challenge.

This thesis describes a two-pronged approach to tackle this problem. Simple and fast engineering tools allow for the development of insight in the design space using rapid iterations and parametric analyses. However, they are often rather inaccurate. In contrast, detailed multi-dimensional tools for numerical analysis are more accurate, but they require more computation time. Both approaches are developed for the analysis of regenerative cooling channels of oxygen/methane engines. Each approach uses complex but accurate models for the thermodynamic and transport properties of methane.

OMECA (short for One-dimensional Methane Engine Cooling Analysis) is a one-dimensional tool that was developed in Python from scratch. This tool divides a nozzle into stations and analyses the one-dimensional thermal equilibrium at each station. It makes extensive use of semi-empirical equations to calculate the heat transfer at both the hot gas side and the coolant side. The tool is compared to a coupled multi-physics analysis tool, showing that the accuracy of the wall temperature is rather poor, with discrepancies of up to 150 K. Both at the hot gas and coolant side, large deviations are present. However, if the input heat flux is correct, OMECA predicts the coolant pressure drop and temperature rise with a 10% accuracy.

To obtain a higher accuracy at the coolant side, the open-source CFD package OpenFOAM is adapted for analysis of supercritical methane. Of particular note is the custom library that interpolates the fluid property tables at runtime. The selected solver is applicable to steady-state compressible flows. The software is then systematically validated using three validation cases. With experimental validation data obtained through cooperation with CIRA, an accuracy of 15 K for the wall temperature prediction is demonstrated. The pressure drop is predicted within 10%.

Traditionally, the launcher industry uses copper alloys as wall material in regeneratively cooled combustion chambers. They offer a high allowable temperature and high thermal conductivity, but are also heavy and expensive. Recently, several companies have demonstrated aluminium combustion chambers. Aluminium alloys have weight and cost advantages, but have lower allowable temperature and thermal conductivity.

The developed tools for cooling analysis are therefore employed to compare aluminium and copper for a generic 10 kN combustion chamber. It is discovered that a thermal barrier coating must be employed to protect the hot gas side of an aluminium combustion chamber, otherwise regenerative cooling is not feasible. Even with such a coating, the pressure drop required to cool the coated aluminium chamber is three times higher than the pressure drop required for a copper chamber.

A difference in pressure drop has effects on the vehicle level. A larger pressure drop in the cooling channel of a rocket engine necessitates a higher feed pressure. For a pressure fed engine, this means the tank must be stronger and heavier. It is found that even at modest fuel mass, the increase in tank mass is eight times as large as the decrease in engine mass offered by aluminium. This shows that using aluminium for the chamber wall is not advantageous with respect to copper for a pressure fed, regeneratively cooled, oxygen/methane rocket engine.



# CONTENTS

<b>1</b>	<b>Introduction</b>	<b>1</b>
1.1	Methane-fuelled rocket engines	1
1.2	Rocket engine cooling	2
1.3	Supercritical fluids	3
1.4	Cooling channel analysis	5
1.5	Combustion chamber materials	6
1.6	Research question	6
1.7	Research plan	6
1.8	Thesis structure	7
<b>2</b>	<b>Fluid and solid property models</b>	<b>9</b>
2.1	Methane properties	9
2.2	Chamber wall properties	15
<b>3</b>	<b>First order analysis</b>	<b>19</b>
3.1	Computational setup	19
3.2	Verification and validation	28
3.3	Parametric analysis	34
3.4	Exploring cooling channel design	43
3.5	Conclusion and recommendations	47
<b>4</b>	<b>Numerical method</b>	<b>49</b>
4.1	Governing equations	49
4.2	Pressure-velocity-density coupling	52
4.3	Turbulence modelling	53
4.4	Roughness modelling	57
4.5	Discretisation	59
4.6	Summary of numerical methods	62
<b>5</b>	<b>Validation</b>	<b>63</b>
5.1	Numerical analysis of heated methane	63
5.2	Numerical conjugate heat transfer analysis	75
5.3	Experimental data	84
5.4	Effect of uncertainty on design	92
5.5	Conclusions of validation campaign	93
<b>6</b>	<b>Results of CFD analysis</b>	<b>95</b>
6.1	Nozzle channel analysis	96
6.2	Nozzle channels with improved geometry	103
6.3	Mass calculation and comparison	108
6.4	Summary of results	109
<b>7</b>	<b>Conclusions and recommendations</b>	<b>111</b>
<b>A</b>	<b>OpenFOAM guidelines</b>	<b>113</b>
A.1	Convergence	113
A.2	Solvers	113
A.3	Wall functions	114



# LIST OF FIGURES

1.1	Illustration of a rocket engine with regenerative cooling . . . . .	3
1.2	Indication of thermodynamic state of various propellants in cooling channels [10] . . .	3
1.3	Mechanisms of heat transfer enhancement, impairment, deterioration and recovery. Figure from [27] . . . . .	4
2.1	Methane phase diagram showing variation of density with pressure and temperature as well as critical point [43] . . . . .	10
2.2	Variation of methane specific heat $c_p$ with temperature at various pressures. Curves for data from NIST [50], markers for model implemented in Python. . . . .	11
2.3	Comparison between fluid property models programmed in Python (markers) and NIST reference data [50] (curves) . . . . .	14
2.4	Discretisation error of density with bilinear interpolation . . . . .	15
2.5	Thermal conductivity variation of NARloy-Z with temperature [58] . . . . .	16
2.6	Ultimate and yield strength variation of NARloy-Z with temperature [58] . . . . .	16
2.7	Thermal conductivity variation of Glidcop Al-15 with temperature [59] . . . . .	17
3.1	Illustration of a thrust chamber cross-section with coolant channels . . . . .	20
3.2	Temperature fields in cross-section of cooling channel and wall. On the left a narrow part of the channel where temperature hardly varies in circumferential direction. On the right a wide part of the same channel with stronger circumferential temperature variations [63] . . . . .	20
3.3	Boundary layer temperature profile for various cases [66] . . . . .	22
3.4	Comparison of experimental heat flux with prediction from Bartz correlation for oxygen/methane engine [68] . . . . .	23
3.5	Flowchart of the One-dimensional Methane Engine Cooling Analysis (OMECA) program . . . . .	28
3.6	Cooling channel geometry of Hyprob rocket engine [63] . . . . .	29
3.7	Wall temperature and heat flux along Hyprob nozzle, OMECA and reference calculations [63] . . . . .	30
3.8	Bulk coolant pressure and temperature along Hyprob nozzle, OMECA and reference calculations [63] . . . . .	30
3.9	Convective, radiative and total heat flux for OMECA analysis of Hyprob nozzle . . . . .	31
3.10	Wall temperature and heat flux for Hyprob engine, calculated with OMECA (including heat flux modification) and reference calculations [63] . . . . .	32
3.11	Bulk coolant pressure and temperature for Hyprob engine, calculated with OMECA (including heat flux modification) and reference calculations [63] . . . . .	32
3.12	Hyprob engine wall temperatures for different Nusselt number correlations. Adiabatic wall temperature and hot gas convective coefficient are taken from reference analysis [63]. . . . .	33
3.13	Coolant state along cooling channel for Hyprob rocket engine. Adiabatic wall temperature and hot gas convective coefficient are taken from reference analysis [63]. OMECA and reference calculations [63] . . . . .	33
3.14	Contour of the generic rocket engine (contour created by Ralph Huijsman, DARE) . . . . .	35
3.15	Generic engine heat flux and wall temperature along nozzle . . . . .	35
3.16	Generic engine Reynolds number and Nusselt number in coolant channel along nozzle . . . . .	36
3.17	Total pressure and total temperature in coolant channel of generic engine . . . . .	36
3.18	Wall temperature along thrust chamber of generic engine with different Nusselt number correlations . . . . .	37
3.19	Variation of pressure drop and maximum wall temperature with thrust chamber thermal conductivity . . . . .	37

3.20	Variation of pressure drop and maximum wall temperature with number of cooling channels . . . . .	38
3.21	Variation of pressure drop and maximum wall temperature with number of cooling channels . . . . .	39
3.22	Variation of pressure drop and maximum wall temperature with roughness of cooling channels . . . . .	40
3.23	Variation of pressure drop and maximum wall temperature with coolant inlet pressure	40
3.24	Comparison of chamber wall wall temperature with coolant inlet pressure of 60 bar and 120 bar . . . . .	41
3.25	Variation of pressure drop and maximum wall temperature with physical size of the engine . . . . .	42
3.26	Variation of pressure drop and maximum wall temperature with chamber pressure . .	42
3.27	Variation of pressure drop and maximum wall temperature with chamber pressure, also changing fuel flow and channel height . . . . .	42
3.28	Copper nozzle wall temperature with preliminary channel geometry . . . . .	45
3.29	Coated aluminium nozzle wall temperature with preliminary channel geometry . . . .	47
4.1	Finite volume formulation in OpenFOAM [42] . . . . .	60
4.2	Sweby's region of TVD and second order flux limiters, with selected flux limiters . . . .	61
5.1	Pressure convergence on medium grid with different limiters . . . . .	64
5.2	Temperatures obtained on medium grid with different limiters . . . . .	64
5.3	Experimental data on temperature profile in boundary layer at $Pr = 0.7$ [103]. Note that $\theta^+$ is equivalent to $T^+$ . . . . .	66
5.4	Comparison of normalised heat flux for different boundary layer refinements . . . . .	67
5.5	Comparison of temperature contours at various cross-section along the channel . . . .	68
5.6	Comparison of density contours at various cross-section along the channel . . . . .	68
5.7	Comparison of streamwise velocity contours at various cross-section along the channel	68
5.8	Comparison of heat capacity contours at various cross-section along the channel . . . .	69
5.9	Comparison of wall heat flux at exit cross-section of channel with reference case [43] .	70
5.10	Comparison of bulk temperature along channel with reference case [43] . . . . .	70
5.11	Comparison of cooling efficiency along channel with reference case [43] . . . . .	71
5.12	Convergence of simulation on fine grid . . . . .	72
5.13	Discretisation error estimates . . . . .	73
5.14	Comparison of bulk temperature along channel for $k-\epsilon$ and Spalart-Allmaras turbulence model . . . . .	75
5.15	Conjugate heat transfer numerical validation case [104] . . . . .	76
5.16	Comparison of current and reference grids . . . . .	77
5.17	Comparison of inner wall temperature of solid along channel with reference case [104]	78
5.18	Heat transfer deterioration and recovery mechanisms [27] . . . . .	78
5.19	Specific heat contours along the channel at 60 mm, 120 mm, 180 mm, 240 mm and 300 mm . . . . .	79
5.20	Comparison of temperature contours of OpenFOAM and reference calculations . . . .	79
5.21	Comparison of methane bulk temperature and corresponding specific heat along channel with reference case [104] . . . . .	80
5.22	Comparison of inner wall temperature of solid along rough-walled channel with reference case [104] . . . . .	81
5.23	Temperature and specific heat profiles for rough wall on three grids . . . . .	81
5.24	Comparison of inner wall temperature for different roughness values . . . . .	83
5.25	Comparison of inner wall temperature for different turbulent Prandtl number values .	83
5.26	MTP experimental article [78]. Figure courtesy of CIRA ScpA. . . . .	85
5.27	Geometry and case setup of MTP in CFD [31] . . . . .	85
5.28	Cold flow pressure drop comparison. Experimental results and FLUENT analysis are courtesy of CIRA ScpA. . . . .	86
5.29	Mesh for experimental validation cases . . . . .	88

5.30	Pressure drop comparison for TC24. Experimental results and FLUENT analysis are courtesy of CIRA ScpA. . . . .	89
5.31	Comparison of temperature of embedded thermocouples at 4 mm with numerical results for TC24. Experimental results and FLUENT analysis are courtesy of CIRA ScpA. . . . .	89
5.32	Pressure drop comparison for TC26. Experimental results and FLUENT analysis are courtesy of CIRA ScpA. . . . .	90
5.33	Comparison of temperature of embedded thermocouples at 4 mm with numerical results for TC26. Experimental results and FLUENT analysis are courtesy of CIRA ScpA. . . . .	91
5.34	Comparison of different inlet conditions for turbulence with $k-\omega$ WF. Experimental results and FLUENT analysis are courtesy of CIRA ScpA. . . . .	91
5.35	Streamwise velocity profile on symmetry plane of channel at various cross-sections . . . . .	92
6.1	Varying cooling channel dimensions along nozzle axis for copper chamber . . . . .	96
6.2	Pressure distribution and in-plane velocities inside copper cooling channel . . . . .	96
6.3	Cross-sections of one of the meshes at (from left to right) $x=270$ mm (near inlet), $x=175.8$ mm (throat), $x=100$ mm and $x=0$ mm (near outlet). Solid domain is shown in red, fluid domain in gray. . . . .	97
6.4	Details of fluid mesh showing refinement along nozzle axis near throat and inlet . . . . .	97
6.5	Experimental validation with first order upwind discretisation compared to using a second order van Leer limiter . . . . .	99
6.6	Wall temperatures obtained for copper chamber with different meshes . . . . .	100
6.7	$y^+$ values obtained for copper chamber with different meshes. The red cells have a value of 30 or higher, satisfying the requirement. . . . .	100
6.8	Pressure distribution and Dean vortices due to curvature of cooling channel at throat section of copper nozzle . . . . .	101
6.9	Wall temperature of copper combustion chamber . . . . .	101
6.10	Total pressure and bulk temperature inside cooling channel of copper combustion chamber . . . . .	102
6.11	Wall temperature of uncoated aluminium combustion chamber . . . . .	103
6.12	Wall temperature of coated aluminium combustion chamber . . . . .	103
6.13	Cooling channel height in original and improved design . . . . .	104
6.14	Wall temperature of copper combustion chamber with improved cooling channel geometry . . . . .	104
6.15	Temperature of coolant and wall at four cross-sections of the channel at (from left to right) $x=260$ mm (near inlet), $x=175.8$ mm (throat), $x=100$ mm and $x=0$ mm (near outlet) . . . . .	105
6.16	Coolant total pressure drop and bulk temperature rise with improved cooling channel geometry for copper combustion chamber . . . . .	106
6.17	Wall temperature of uncoated aluminium combustion chamber with improved cooling channel geometry . . . . .	106
6.18	Wall temperature of coated aluminium combustion chamber with improved cooling channel geometry . . . . .	107
6.19	Improved cooling channel geometries for coated aluminium combustion chamber . . . . .	107
6.20	Coolant total pressure drop and bulk temperature rise with improved cooling channel geometry for coated aluminium combustion chamber . . . . .	108



# LIST OF TABLES

1.1	Summary of factors in rocket engine propellant selection (adapted from [15], isentropic expansion from combustion pressure 6.89 MPa; methane boiling temperature from [16])	2
2.1	Critical pressure and temperature for rocket propellants	9
2.2	Material properties for selected alloys	18
3.1	OMECA input parameters	27
3.2	Input parameters for analysis of Hyprob engine	29
3.3	Input parameters for analysis of generic engine	35
3.4	Summary of parametric analysis of generic engine	43
3.5	Combustion chamber requirements	44
3.6	Summary of results for three chamber designs analysed with OMECA	48
4.1	Modelling parameter values for $k-\epsilon$ turbulence model	54
4.2	Modelling parameter values for $k-\omega$ SST turbulence model	55
4.3	Modelling parameter values for Spalart-Allmaras turbulence model	56
5.1	Calculated values for $y^+$ for the different test grids	66
5.2	Calculation time for 3000 iterations	71
5.3	Estimate of simulation errors	75
5.4	Mesh parameters for coarse, medium and fine mesh for CHT validation case	76
5.5	Total pressure drop (in bar) obtained from OpenFOAM and by Pizzarelli et al.	82
5.6	Boundary conditions for experimental conditions replicated with OpenFOAM	87
5.7	Summary of validation results for tested turbulence and roughness models	92
6.1	Summary of results for copper and aluminium combustion chambers	109
A.1	Appropriate wall functions in OpenFOAM	114



# NOMENCLATURE

<b>A</b>	Area vector
<i>A</i>	Area
<i>a</i>	Coefficient of velocity equation
<i>a<sub>h</sub></i>	Reduced Helmholtz free energy
<b>b</b>	Body force vector
<i>c</i>	Coefficient
<i>c<sub>p</sub></i>	Specific heat at constant pressure
<i>C<sub>v1</sub></i>	Modelling coefficient of Spalart-Allmaras model
<i>c*</i>	Characteristic velocity
<i>C<sub>1</sub></i>	Modelling coefficient of <i>k-ε</i> turbulence model
<i>C<sub>2</sub></i>	Modelling coefficient of <i>k-ε</i> turbulence model
<i>C<sub>3</sub></i>	Modelling coefficient of <i>k-ε</i> turbulence model
<i>C<sub>b1</sub></i>	Modelling coefficient of Spalart-Allmaras model
<i>C<sub>b2</sub></i>	Modelling coefficient of Spalart-Allmaras model
<i>C<sub>kω</sub></i>	Cross-diffusion term for <i>k-ω</i> turbulence model
<i>C<sub>μ</sub></i>	Modelling coefficient of <i>k-ε</i> turbulence model
<i>c<sub>v</sub></i>	Specific heat at constant volume
<i>C<sub>w1</sub></i>	Modelling coefficient of Spalart-Allmaras model
<i>C<sub>w2</sub></i>	Modelling coefficient of Spalart-Allmaras model
<i>C<sub>w3</sub></i>	Modelling coefficient of Spalart-Allmaras model
<b>d</b>	Distance vector
<i>D</i>	(Hydraulic) diameter
<i>d</i>	Depth
<i>E</i>	Modulus of elasticity
<i>e</i>	Specific energy
err	Error
<i>F<sub>1</sub></i>	Blending function of <i>k-ω</i> SST turbulence model
<i>F<sub>2</sub></i>	Blending function for <i>k-ω</i> turbulence model
<i>f<sub>D</sub></i>	Darcy-Weisbach friction factor
<i>f<sub>v1</sub></i>	Damping function of Spalart-Allmaras model
<i>f<sub>w</sub></i>	Damping function of Spalart-Allmaras model
<i>g</i>	Function in Spalart-Allmaras model
<i>h</i>	Enthalpy
<i>h<sub>s</sub></i>	Roughness height
<b>H<sub>U</sub></b>	Term representing advection and diffusion terms of velocity equation
<b>I</b>	Identity matrix
<i>K</i>	Von Karman constant
<i>k</i>	Turbulent energy
<i>l</i>	Length
<i>ṁ</i>	Mass flow
<i>M</i>	Mach number
<i>n</i>	Normal to the surface

$Nu$	Nusselt number
$p$	Pressure
$\tilde{P}_k$	Production of turbulence
$Pr$	Prandtl number
$\mathbf{q}$	Heat flux vector
$q$	Heat flux
$R$	Radius
$r$	Recovery factor
$Re$	Reynolds number
$R_g$	Gas constant
$\mathbf{S}$	Surface vector
$\tilde{S}$	Intermediate variable for modulus of vorticity $S$
$S$	Modulus of vorticity
$s$	Correction factor in Bartz equation
$T$	Temperature
$t$	Thickness
$\mathbf{U}$	Velocity vector
$u$	Velocity
$u_\tau$	Friction velocity
$w$	Width
$w_s$	Geometric parameter
$x$	Coordinate in $x$ direction, generally streamwise
$y$	Coordinate in $y$ direction; distance to wall
$z$	Coordinate in $z$ direction
$\alpha$	Convective heat transfer coefficient
$\alpha_{\text{eff}}$	Effective thermal diffusivity
$\alpha_1$	Modelling coefficient of $k$ - $\omega$ SST turbulence model
$\alpha_2$	Modelling coefficient of $k$ - $\omega$ SST turbulence model
$\alpha_{\text{SST}}$	Modelling coefficient of $k$ - $\omega$ SST turbulence model
$\beta$	Flux limiter
$\beta_1$	Modelling coefficient of $k$ - $\omega$ SST turbulence model
$\beta_2$	Modelling coefficient of $k$ - $\omega$ SST turbulence model
$\beta^*$	Modelling coefficient of $k$ - $\omega$ SST turbulence model
$\beta_{\text{SST}}$	Modelling coefficient of $k$ - $\omega$ SST turbulence model
$\gamma$	Ratio of specific heats
$\epsilon$	Turbulent dissipation
$\eta$	Efficiency
$\kappa$	Thermal conductivity
$\nu_P$	Poisson's ratio
$\nu$	Kinematic viscosity
$\tilde{\nu}$	Intermediate variable for kinematic viscosity
$\xi$	Ratio of rough channel over smooth channel friction factor
$\rho$	Density
$\boldsymbol{\sigma}$	Stress tensor
$\sigma$	Stress
$\sigma_\epsilon$	Modelling coefficient of $k$ - $\epsilon$ turbulence model
$\sigma_k$	Modelling coefficient of $k$ - $\omega$ SST and $k$ - $\epsilon$ turbulence models

$\sigma_{vT}$	Modelling coefficient of Spalart-Allmaras model
$\sigma_{\omega}$	Modelling coefficient of $k$ - $\omega$ SST turbulence model
$\sigma_{\omega 2}$	Modelling coefficient of $k$ - $\omega$ SST turbulence model
$\boldsymbol{\tau}$	Viscous stress tensor
$\chi$	Ratio between kinematic viscosities in Spalart-Allmaras model
$\phi$	Generic variable
$\Psi$	Generic flux
$\Psi$	Correction factor
$\omega$	Specific turbulent dissipation

### Subscripts and superscripts

+	Dimensionless
0	Stagnation
allow	Allowable
att	Attractive
aw	Adiabatic wall
coat	Coating
cr	Critical
dil	Dilute gas
eff	Effective
exc	Excess
id	Ideal gas
ma	Mass averaged
rep	Repulsive
res	Residual
$b$	Bulk
$C$	Curvature
$c$	Coolant or coolant channel
$F$	Fin
$f$	Film
$h$	Hot gas
$i$	Inner chamber wall
$l$	Laminar
$N$	Neighbour point; off-diagonal entry of matrix
$n$	Nozzle
$o$	Outer chamber wall
$P$	Point; diagonal entry of matrix
$R$	Radiative
$r$	Rib
$s$	Surface $s$
$T$	Turbulent
$t$	Throat
$V$	Convective
$w$	Wall

### Acronyms

1D	One-dimensional
2D	Two-dimensional
3D	Three-dimensional

---

BL	Boundary layer
BLI	Boundary layer integration
CEA	Chemical Equilibrium and Applications
CFD	Computational fluid dynamics
CHT	Conjugate heat transfer
CIRA	Centro Italiano Ricerche Aerospaziale; Italian Aerospace Research Center
DARE	Delft Aerospace Rocket Engineering
D-B	Dittus-Boelter
DNS	Direct numerical simulation
GERG	Groupe Européen de Recherches Gazières; European Gas Research Group
LES	Large eddy simulation
LRE	Liquid(-propellant) rocket engine
MMH	Monomethylhydrazine
MTP	Methane Thermal Properties (experimental campaign conducted by CIRA)
NASA	National Aeronautics and Space Administration
NIST	National Institute of Standards and Technology
NTO	Nitrogen tetroxide
OF	OpenFOAM
RANS	Reynolds-averaged Navier Stokes
S-A	Spalart-Allmaras
SST	Shear Stress Transport
TC	Test condition
TVD	Total variation diminishing
ULA	United Launch Alliance
WF	Wall function

# 1

## INTRODUCTION

Liquid rocket engines are the workhorses of the launch vehicle industry. In 2013, 88% of all orbital launches were performed by a rocket with a liquid rocket engine on the first stage [1]. The total market size of the worldwide launch industry in that year was estimated to be 5.4 billion dollars, for only 69 rocket launches [2].

This shows two things. First: that there is substantial money going around in the launch business. Second, more importantly: that a single orbital launch is tremendously expensive. One of the longest standing challenges of rocket scientists and engineers alike is therefore to make access to space less expensive.

There are several conceivable strategies to achieve this. An old idea that was at the core of the Space Shuttle development is to design reusable launch vehicles instead of the current expendable ones. The idea has resurfaced in recent years. SpaceX is trying to recover the first stage of their vehicle by landing it vertically [3]. Both Airbus and United Launch Alliance (ULA) have announced plans to re-use the engines of the first stage by separating them from the first stage and recovering those [4, 5].

Other ideas are to reduce the operating costs (e.g. by abandoning the hard-to-handle hydrogen fuel in favour of methane) or to make use of less expensive materials or manufacturing techniques. For example, several groups are experimenting with additive manufacturing (commonly known as 3D printing) for rocket engine components [6, 7].

Here, we will focus on two possible solutions to reduce the cost of access to space. One is methane-fuelled rocket engines, which will be discussed in section 1.1. Another is using aluminium instead of copper alloys for the combustion chamber, decreasing cost and mass of the engine. This will be discussed in section 1.5.

When deciding on the chamber material, cooling is an important consideration. Most liquid rocket engines use regenerative cooling. To compare aluminium and copper, a regenerative cooling analysis of oxygen/methane rocket engines will be necessary. That is the topic of this thesis.

### 1.1. METHANE-FUELLED ROCKET ENGINES

An interesting propellant combination candidate for future space launch vehicles is oxygen/methane [8, 9]. Up to now, most liquid rocket engines that have flown burnt either a hypergolic propellant combination, oxygen/kerosene or oxygen/hydrogen [8]. In the past years, several groups have initiated development programs to demonstrate methane-fuelled engines [9–12]. In addition, both Blue Origin and SpaceX have announced they are developing large oxygen/methane first stage engines for orbital launch vehicles [13, 14].

Table 1.1 shows factors that play a role in the selection of the propellant combination for a launch vehicle powered by liquid rocket engines. Oxygen/hydrogen offers the highest specific impulse, but

Table 1.1: Summary of factors in rocket engine propellant selection (adapted from [15], isentropic expansion from combustion pressure 6.89 MPa; methane boiling temperature from [16])

Propellants	Oxygen/Kerosene	Oxygen/Methane	Oxygen/Hydrogen	NTO/MMH
Vacuum specific impulse [s]	358.2	371	455.3	341.5
Bulk density [kg/m <sup>3</sup> ]	1.03	0.89	0.32	1.20
Volume impulse [kg·s/m <sup>3</sup> ]	369	330	146	410
Oxidizer/Fuel boiling temperature	90 K / 445-537 K	90 K / 112 K	90 K / 20 K	294 K / 359 K
Handling issues	Oxygen cryogenic	Both oxygen and methane cryogenic	Hydrogen deep cryogenic and flammable	Very toxic and hazardous
Coking	Yes	Normally not	No	No
Additional advantages		In-situ resource utilization on Mars		Auto-ignition

low volume impulse, increasing the launch vehicle size and mass. In addition, hydrogen has a boiling temperature of 20 K, imposing severe handling constraints and increasing operating costs. The hypergolic combination of nitrogen tetroxide (NTO) and monomethylhydrazine (MMH) likewise offers the highest volume impulse and auto-ignition, but is extremely toxic. This necessitates extra protection, also increasing operating costs.

To avoid the high operating costs of these combinations, the traditional answer has been to use oxygen and kerosene. This propellant combination offers high volume impulse and relative ease of handling. This makes it an ideal combination for first stage engines. Drawbacks are the rather low specific impulse and the fact that kerosene may coke and form deposits in the engine and fuel channels [17].

Oxygen/methane also avoids the high operating costs of deep cryogenic or toxic propellants. It offers slightly higher specific impulse than oxygen/kerosene, at the cost of somewhat lower volume impulse [18]. This makes methane suitable for both first and second stages. Commonality of the propellants for all stages can also decrease operating costs [19]. Methane also does not coke like kerosene [20], which could reduce refurbishment costs for reusable rocket engines. An additional advantage for future Mars missions is that methane can easily be created on Mars.

The potential of methane-fuelled rocket engines was discussed in more depth in a literature study [1]. The conclusion was that using methane-fuelled rocket engines may reduce the cost of launch vehicles because the high operating costs of hydrogen and hydrazine are avoided. Using oxygen/methane engines for both stages of the vehicle can further reduce operating costs. Over kerosene, its benefits are a higher specific impulse and easier reusability due to the absence of coking. However, more research – or evidence from actual launch vehicles – is needed to definitively establish whether methane propellant could bring down the cost of access to space.

## 1.2. ROCKET ENGINE COOLING

The hot combustion gases inside liquid rocket engines can reach temperatures of up to 3600 K, causing heat fluxes of up to 160 MW/m<sup>2</sup> at the thrust chamber wall in case of the Space Shuttle Main Engine [21]. Modern liquid rocket engines need to be actively cooled to cope with this heat [8].

The most commonly used cooling method in large liquid rocket engines is regenerative cooling [8]. In regenerative cooling, one of the propellants used in the rocket engine (usually the fuel) is pumped through a jacket around the combustion chamber and/or nozzle (see fig. 1.1). As the fuel absorbs heat, its enthalpy increases, which improves the performance of the engine. The exhaust velocity increase is between 0.1 and 1.5% [8]. Because the heat transferred to the coolant is recovered, this technique is called regenerative cooling.

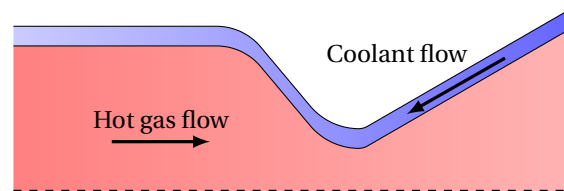


Figure 1.1: Illustration of a rocket engine with regenerative cooling

A disadvantage of regenerative cooling is that the feed pressure of the fuel must be equal to the sum of the chamber pressure, the injector pressure drop, the cooling channel pressure drop and any additional pressure losses present in the system [22]. It is therefore important to design the cooling channels and coolant tubing system such that the pressure losses are small.

Depending on the type and state of the coolant, different regimes may govern the behaviour of the coolant. If the coolant is liquid at all times and locations, heat transfer is governed by single-phase convection [22]. If the coolant temperature at the wall reaches the boiling temperature, it enters the nucleate boiling regime, in which much higher heat transfer rates can be attained [22].

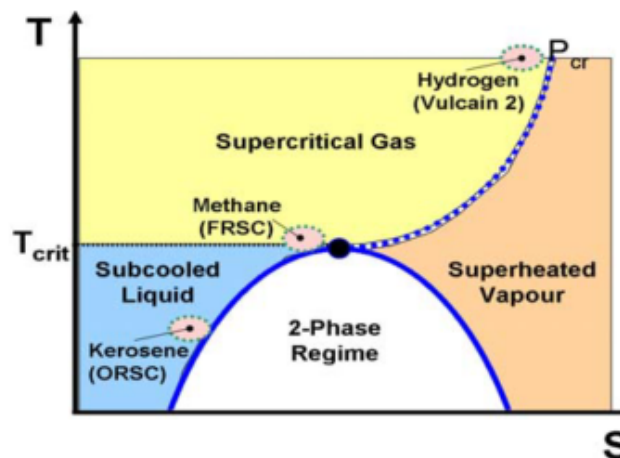


Figure 1.2: Indication of thermodynamic state of various propellants in cooling channels [10]

If the coolant is at supercritical pressure and the temperature is near the critical point, such as can be the case for methane, it will exhibit large variations in its thermodynamic variables [23]. Hydrogen, on the other hand, is often far above both critical pressure and temperature in a large part of the coolant ducts, in the regime of supercritical forced convection [24]. Figure 1.2 shows the relative situation for these three propellants.

### 1.3. SUPERCRITICAL FLUIDS

Fluids at supercritical pressure are characterised by the absence of a vapour curve; there no longer exists a phase change between liquid and gas. Instead, the fluid gradually changes from fluid-like at low temperatures to gas-like at high temperatures. This results in very high gradients of the fluid

properties near the critical point, necessitating the use of very detailed property models if one wants to analyse supercritical fluids [16].

The critical point of methane occurs at a temperature of 190.56 K and a pressure of 4.599 MPa [25]. In rocket engines with low to moderate combustion chamber pressure, the methane cooling would be close to the critical pressure, also crossing the critical temperature. This means that the fluid property variations are important to take into account.

Several interesting phenomena can occur when heat is transferred to fluids at supercritical pressure. These were already described in 1979 by Jackson and Hall [26] and are displayed in fig. 1.3.

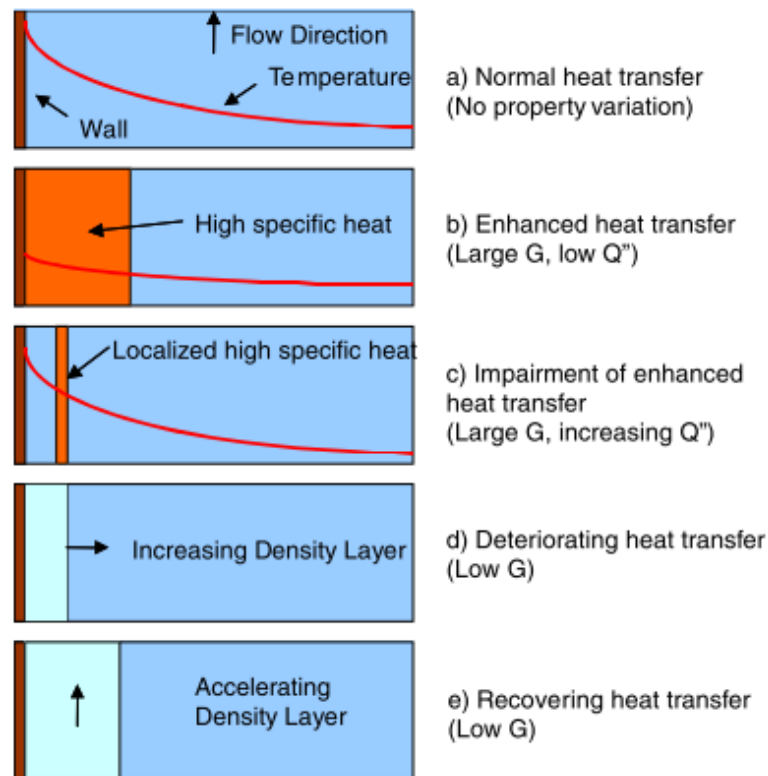


Figure 1.3: Mechanisms of heat transfer enhancement, impairment, deterioration and recovery. Figure from [27]

When a low heat flux is supplied to a fluid near the pseudo-critical temperature (where specific heat has its maximum value), a large region may develop with relatively uniform temperature and high specific heat. This high region of specific heat next to the wall causes an enhancement of heat transfer [27]. As the heat flux is increased, however, the temperature near the wall is not uniform anymore. Due to the large variation in specific heat, a smaller, local region of high specific heat is developed. Where this region is at a short distance from the wall, it can act as an insulating layer that impairs the heat transfer [27].

When the fluid temperature rises near the wall, a layer of low density, gas-like flow can be formed. This gas-like layer transfers heat worse than the liquid-like layer, because it has a far lower thermal capacity. This causes a deterioration of the heat transfer, especially when the gas-like layer is insulated by a high specific heat layer. This phenomenon is called heat transfer deterioration [27].

As the fluid is heated more along a channel, the low density layer will grow. This growing low density region will influence the bulk density of the flow, causing the fluid to accelerate. The increased velocity will increase convective heat transfer, leading to a recovering heat transfer [27].

## 1.4. COOLING CHANNEL ANALYSIS

Several approaches exist to analyse regenerative cooling of liquid rocket engines. The fastest and simplest are semi-empirical correlations to estimate the heat transfer coefficient. Such simple relations are needed in the preliminary design and system analysis phase of a liquid rocket engine [28]. One-dimensional relations can generally be programmed on a personal computer and have negligible computation time. These advantages make them ideally suited for preliminary design and system analysis [28].

One-dimensional relations by definition cannot resolve the thermal stratification (i.e. layers of different temperatures) that occurs in asymmetrically heated channels. Pizzarelli et al. have developed a quasi-two-dimensional model to account for this thermal stratification in methane cooling channels, while keeping the required computation time low [29]. The method solves the conservation equations of the fluid, complemented by equations for thermal balance of the solid parts of the domain for a single coolant channel [29]. Although the method has been extensively described in [29], its software implementation is not freely available.

The accuracy of one-dimensional and quasi-2D methods is limited. For this reason, multi-dimensional CFD methods have also been applied to methane cooling channels. Various multi-dimensional CFD methods have been developed to describe methane at supercritical pressure. The models are generally quite accurate with respect to pressure drop and flow properties, but show poorer accuracy for wall temperature prediction. Unfortunately, the latter is the most interesting variable when doing a cooling analysis. None of the methods examined are freely available.

Pizzarelli developed an in-house finite-volume 3D CFD solver at "La Sapienza" University of Rome that is capable of analyzing the flow of methane in cooling channels [16]. The turbulence model used is the Spalart-Allmaras one-equation model. The solver has been validated by comparison with an experiment with supercritical hydrogen, because of a lack of appropriate experimental data for methane [30]. Pizzarelli and his colleagues have published a wealth of papers on supercritical methane modelling using this solver. In a recent paper, they validated their method with experimental data on methane as well [31].

The group of Hua Meng at Zhejiang University has published several papers on CFD analysis of methane coolant channels [32–34]. Wang et al. demonstrate a simple axisymmetric two-dimensional CFD method in [32]. They complement the Navier-Stokes equation with a shear stress transport (SST)  $k-\omega$  turbulence model. Wang et al. mention that their model has been validated by comparison with supercritical carbon dioxide experiments [32].

Ruan et al. [33] and Wang et al. [34] from the same group report using the FLUENT program to perform CFD analysis on methane cooling channels. In both papers, the two-equation standard  $k-\epsilon$  turbulence model is implemented with enhanced wall modelling using the one-equation Wolfstein model to accurately model the strong temperature gradient near the wall [33, 34]. For this method, the authors refer back to the validation of Wang et al. in [32] and work on n-heptane previously carried out. Note that the FLUENT program is available at the Delft University of Technology, though not with the custom thermodynamic models.

Negishi et al. report the use of CRUNCH CFD software for analysis of methane coolant channels [35]. This is an unstructured, three-dimensional flow solver using a cell-vertex finite volume discretization. The high-Reynolds  $k-\epsilon$  turbulence model was used by Negishi et al, together with the Wolfstein near-wall treatment [35]. The results obtained from this simulation were validated with experimental results from two subscale methane/oxygen engine firings [35].

In summary, researchers have published about several CFD methods to model supercritical methane in rocket engine cooling channels. Both Pizzarelli et al. and Negishi et al. have validated their method with experimental data on methane. None of the published methods are freely available. Furthermore, it is noticeable that the researchers use different turbulence models. It would be interesting to investigate the effect of these turbulence models on the results of the CFD analysis.

## 1.5. COMBUSTION CHAMBER MATERIALS

The chamber walls for regeneratively cooled chambers are often made out of a copper alloy. Pure copper has a higher conductivity, but the alloying improves the strength of the material at high temperature [8]. High conductivity reduces the thermal stress in a thin-walled design [8]. The Vulcain engines 1 and 2 both use a CuAgZr alloy (with silver and zirconium) as material for the inner chamber wall [36, 37]. The Space Shuttle Main Engine uses NARloy-Z for the inner liner; this is also a CuAgZr alloy [21]. The LE-7 engine also uses a copper alloy [38]. However, these copper alloys are relatively heavy and very expensive.

Aluminium is also a candidate for thrust chamber construction. Historically, the only operational engine using an aluminium thrust chamber has been the Agena nozzle [39]. It had a relatively thick wall out of Al-6061 T6. Recently, interest in aluminium nozzles has resurfaced in the United States. Masten Space Systems has developed a small all-aluminium rocket engine, winning the NASA's Lunar Lander Challenge with it in 2009 [40]. XCOR and ULA announced in 2011 the successful demonstration of an aluminium alloy engine [41]. They state that their development could amount to substantial cost and mass savings for future upper stage engines [41].

## 1.6. RESEARCH QUESTION

Summarising the previous paragraphs, we can say that using methane as propellant could reduce the cost of access to space. One of the problems with methane is that it would likely be at supercritical pressure, relatively near its critical point inside regenerative cooling channels. Because fluid properties vary so drastically near the critical point, this complicates cooling analysis: accurate but complex models for fluid properties are required.

In addition to using methane propellants, the use of aluminium instead of copper alloys as chamber materials could also reduce cost of rocket engines. Aluminium has a lower melting temperature than copper, so it is mostly applicable to low heat flux engines with moderate chamber pressure. For this reason, the research will focus on a 10 kN thrust, 40 bar chamber pressure engine.

The research question of this thesis is:

**Is it advantageous to use aluminium instead of copper for the chamber wall of a small, regeneratively cooled oxygen/methane rocket engine?**

In order to investigate the feasibility, the performance of aluminium will be compared to a baseline copper alloy that has been used in rocket engines. For both materials, the following questions will be answered.

1. Is it possible to cool the thrust chamber wall to the allowable temperature or lower, using the fuel flow available?
2. How high is the pressure drop over the cooling channel?
3. By how much does the temperature of the coolant rise?
4. What is the estimated mass of the thrust chamber?
5. What is the system-level impact of the differences in pressure drop, temperature rise and chamber mass?

When these sub-questions have been answered, it will be possible to compare the performance of the copper and aluminium thrust chambers to each other. This in turn allows us to answer the central research question. Proving that aluminium is a feasible material for oxygen/methane engines would bring us one step closer to decreasing the cost of access to space.

## 1.7. RESEARCH PLAN

The objective of the thesis is to compare copper and aluminium alloys as material for oxygen/methane rocket engine thrust chambers. To do this, methods for analysis must be obtained or created.

A smart strategy is to first create a reasonably simple one-dimensional method based on semi-empirical

relations. This will allow us to probe the design space and understand how various parameters influence the performance of methane cooling channels. Since such a method is quite simple, it can be created from scratch with regular programming tools. Since the author is proficient in Python, this will be the language of choice.

However, to obtain more accurate predictions, it will likely be necessary to use detailed CFD methods. Several of these exist for supercritical methane, as shown in section 1.4. However, they are not freely available. OpenFOAM is a freely available, open-source CFD package with which the author has experience. Being open source, it is possible to write custom libraries and executables. It contains solvers for compressible flow as well as conjugate heat transfer methods that can couple fluid and solid domains [42].

Section 1.3 showed that one of the problems is that accurate property models are needed for supercritical methane. One of the first problems that must be tackled is therefore to make sure that detailed property models of methane can be used in OpenFOAM. An easy way to do this programmatically is to create tables of fluid properties and interpolate these tables at runtime. The expansion of OpenFOAM by adding the possibility to use tabulated equation of state (and other thermodynamic properties) will enable us to answer the research question. In addition, it will be a valuable addition to the open-source package in itself – extending beyond this field of research.

OpenFOAM in combination with the new property library must then be validated. This will be done in two steps: by comparing with numerical tools and by comparing with experimental data. In section 1.4, it was found that researchers use different turbulence models for supercritical methane. The experimental validation will make it possible to compare the different turbulence models.

When OpenFOAM has been validated, it can be used to perform a cooling analysis for copper and aluminium chambers and answer the research question.

The research plan can thus be divided into the following objectives:

1. Explore possible cooling designs for a small rocket engine with a one-dimensional model
2. Implement and verify a tabulated fluid property model in OpenFOAM
3. Validate the OpenFOAM tool with comparable numerical tools
4. Validate the OpenFOAM tool with experimental data and compare the performance of different turbulence models
5. Perform a cooling channel heat transfer analysis for a copper and aluminium chamber and compare the results

## 1.8. THESIS STRUCTURE

The next chapter of this thesis, chapter 2, focuses on the fluid property models required to accurately model near-critical methane. In addition, the properties of several potential chamber materials are discussed there.

Chapter 3 presents a first order analysis of the cooling system of a methane-fuelled rocket engine. This analysis is performed to achieve the first research goal: to explore design options for a small rocket engine.

The next three chapters focus on a detailed computation fluid dynamics (CFD) analysis of methane cooling channels. Chapter 4 describes the numerical method that was used in OpenFOAM, including several turbulence and roughness models. In this chapter, the second research goal is achieved.

Chapter 5 shows the extensive validation campaign that was performed to validate the software for analysis of heat transfer to supercritical methane in rocket engine cooling channels. The validation is performed in three stages. First a comparison to another numerical tool is performed, simulating the fluid only. Then this comparison is extended to a conjugate heat transfer model, also implementing a solid domain. The third validation case is a comparison with experimental data provided by the Italian Aerospace Research Centre CIRA. This chapter shows how research goals 3 and 4 were met.

The CFD software is then applied to simulate rocket engine cooling channels in chapter 6. This was

the fifth and final research goal. The cooling performance of copper and aluminium chambers is compared in order to answer the research question.

Finally, chapter 7 summarises the results of this thesis and reiterates the most important conclusions. Several recommendations are suggested to build on and improve the research presented here.

# 2

## FLUID AND SOLID PROPERTY MODELS

One of the objectives of the thesis is to perform a cooling analysis of rocket engine cooling channels filled with methane. A necessary first step is to have an accurate model of the relevant properties of methane. The research question is to compare copper and aluminium as wall material for methane-fuelled rocket engines. Here, it is important to know the properties of both these materials so they can be adequately compared.

This chapter is concerned with these fluid and solid property models. The properties of the methane coolant will be discussed in section 2.1. One of the goals of the research as defined in chapter 1 was to *"implement and verify a tabulated fluid property model in OpenFOAM"*. The implementation of this tabulated property model is also discussed in section 2.1. Section 2.2 describes the properties of selected copper and aluminium alloys.

### 2.1. METHANE PROPERTIES

Methane is the simplest hydrocarbon molecule with the chemical formula  $\text{CH}_4$ . It has a molecular weight of 16.04 g/mol and a boiling temperature of 111 K. This makes it denser and easier to liquefy (and handle) than deep-cryogenic hydrogen. On the other hand, as the lightest hydrocarbon it has a lower boiling temperature and density than kerosene. In that respect, it is situated between these two extremes as a propellant.

Figure 2.1 shows the phase diagram of methane, colored by density. On the bottom of the figure, one can distinguish the liquid and the gaseous phase from the density continuity. However, at pressures above the critical point, there no longer is a discontinuity between the liquid and the gaseous phase. Instead, there is a smooth but rapid change in density near the critical temperature. In general, the fluid properties will vary very rapidly near the critical pressure and temperature. The variations become smaller as the fluid gets farther away from the critical point.

It is worth noting that this behaviour occurs in all substances, albeit at different pressures and temperatures. Section 2.1 shows the critical pressures and temperatures for various rocket propellants. The table shows that the critical pressure of methane is relatively high. The critical temperature is much higher than for hydrogen and at the same time much lower than kerosene's critical temperature. Both of these factors cause methane to be much closer to its critical point inside rocket engine cooling channels.

Table 2.1: Critical pressure and temperature for rocket propellants

Propellant	$p_{\text{crit}}$ [MPa]	$T_{\text{crit}}$ [K]
Methane [44]	4.6	191
Kerosene [45]	2.4	640
Hydrogen [46]	1.3	33

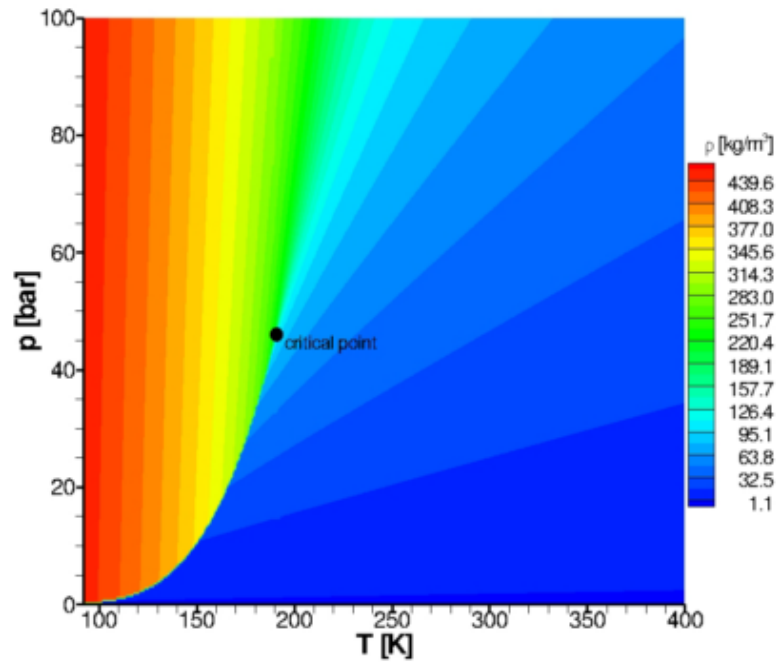


Figure 2.1: Methane phase diagram showing variation of density with pressure and temperature as well as critical point [43]

Because the coolant inside a regenerative cooling channel is afterwards fed to the injector, its pressure must necessarily be higher than the combustion pressure. Large engines such as the Vulcain and the Space Shuttle Main Engine have combustion pressures of approximately 10 and 20 MPa respectively [47, 48], and therefore even higher coolant pressures. In such engines, any of the propellants from section 2.1 would be so far from the critical pressure that the fluid property variations become very small.

In smaller engines (e.g. those used for the second stage of orbital launch vehicles) the combustion pressure is usually substantially lower. The LE-5B engine has a combustion pressure of 3.6 MPa [49], the RL10B-2 chamber pressure is 4.4 MPa. For such smaller engines, the coolant would be relatively close to the critical pressure. However, due to the expected pressure drop in the injector and cooling manifold, it is likely that the coolant would still be at supercritical pressure inside the cooling channel.

In addition, methane could cross the critical temperature inside a rocket engine cooling channel. When a fluid is near the critical pressure and goes from a subcritical temperature to a supercritical temperature, the flow is often called a transcritical flow. These flows, where large changes in the fluid properties are present, are expected in methane-fuelled rocket engines. As an example, the variation of the isobaric specific heat ( $c_p$ ) with temperature and pressure is shown in fig. 2.2.

Figure 2.2 clearly shows the rapid change in thermodynamic properties near the critical point. The specific heat increases by a factor 6 at 60 bar. The temperature at which this peak occurs increases with increasing pressure. This temperature of maximum  $c_p$  is called the pseudo-critical temperature; at this temperature the variation in fluid properties is the most severe. The dramatic variation in a thermodynamic property like  $c_p$  is important to take into account when performing a cooling analysis. Therefore, accurate models of the thermodynamic and transport properties of methane at supercritical pressure are necessary.

The absence of two-phase flow at supercritical pressure does have a substantial advantage in terms of modelling. No bubbles are formed, phenomena such as nucleate boiling do not occur. There is substantial difficulty in modelling two-phase flows and therefore this thesis focuses solely on methane at supercritical pressures. The fact that methane coolant is expected to be above the critical pressure even for relatively small engines justifies this focus.

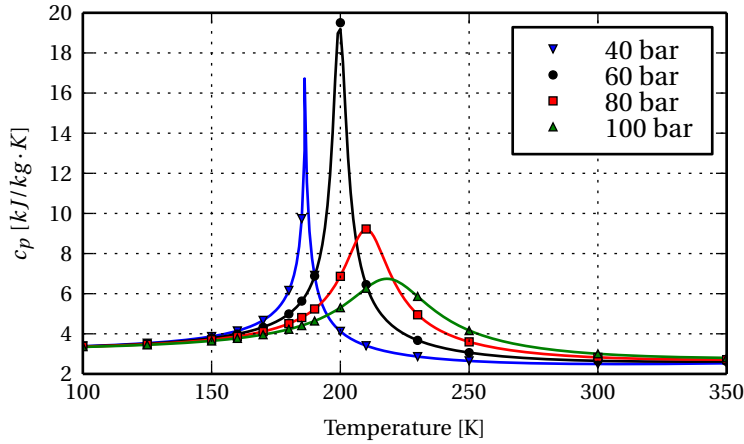


Figure 2.2: Variation of methane specific heat  $c_p$  with temperature at various pressures. Curves for data from NIST [50], markers for model implemented in Python.

### 2.1.1. THERMODYNAMIC PROPERTIES

The thermodynamic state of a fluid can be described by giving two of its state properties – e.g. pressure, temperature or density. These three properties can be related to each other through an equation of state. When the thermodynamic state is known, the values of the other thermodynamic properties (enthalpy, specific heat at constant pressure, etc.) are also fixed. The most well-known equation of state in aerospace engineering is the ideal gas equation of state. However, because we also want to describe methane at lower temperatures, where it behaves like a liquid, this equation of state does not suffice.

The following sections will detail the equation of state that was used to model methane throughout this thesis. The auxiliary relations that were used to derive the enthalpy and specific heat are also shown.

Several equations of state can be used to model supercritical methane. Pizzarelli as well as Wang et al. have used the modified Benedict-Webb-Rubin equation of state [16, 32]. This equation of state has a typical error in the density of 0.1-0.3%, deteriorating to 5% uncertainty near the critical point [44].

The NIST database [50] uses a relation by Setzmann and Wagner [51]. They claim an accuracy of 0.03% in the density. Kunz et al. have developed a new equation of state, called GERG-2004 [25]. This equation of state, though primarily aimed at mixtures of hydrocarbons, accurately reproduces experimental data for methane. It is as accurate as Setzmann and Wagner's equation of state for the density, but substantially more accurate for other thermodynamic properties [25]. Like Setzmann and Wagner's equation of state, the GERG-2004 represents the experimental data sets to within 0.02-0.03%. Nonetheless, the authors give a conservative uncertainty of 0.05% [25].

Because of the very high accuracy both in density and other, derived thermodynamic variables, the GERG-2004 equation of state was selected to model supercritical methane.

The GERG-2004 equation of state uses the reduced Helmholtz free energy to calculate various thermodynamic properties. The reduced Helmholtz free energy  $a_h$  for a pure fluid is given by eq. 2.1, where  $a_h^{\text{id}}$  is the part referring to an ideal gas and  $a_h^{\text{res}}$  is the residual term [25].

$$a_h = a_h^{\text{id}}(\rho, T) + a_h^{\text{res}}(\rho, T) \quad (2.1)$$

GERG-2004 provides analytical equations to calculate both terms. These equations contain empirical constants that were obtained by fitting experimental data to the relations. For methane, the ideal gas part  $a_h^{\text{id}}$  employs 11 empirical constants, while  $a_h^{\text{res}}$  requires 24 [25].

As eq. 2.1 shows, the reduced Helmholtz free energy obtained in this way depends on temperature and density. These are thermodynamic state variables, together fixing the state of the fluid. Other thermodynamic variables such as pressure, isobaric or isochoric heat capacity, enthalpy etc. are found by taking partial derivatives of eq. 2.1 at a specific  $(\rho, T)$  point.

For example, the pressure  $p$  is given by eq. 2.2, where the partial derivative of  $a^{\text{res}}$  with respect to the reduced density is included. For the other thermodynamic variables, similar relations including partial derivatives of  $a_h^{\text{id}}$  and  $a_h^{\text{res}}$  exist.

$$p = \rho R_g T \left( 1 + \frac{\rho}{\rho_{\text{cr}}} \frac{\partial a_h^{\text{res}}}{\partial \frac{\rho}{\rho_{\text{cr}}}} \right) \quad (2.2)$$

For a more thorough discussion, all the relevant equations as well as comparison of the equation of state with experimental data, the interested reader is referred to the work of Kunz et al. [25]. For now it will suffice to say that the relevant equations were programmed into a Python script such that  $p$ ,  $c_p$ ,  $c_v$  and  $h$  could be calculated for a  $(\rho, T)$  state. In addition, a function was written to reverse the equation of state; that is to find  $\rho$  for a specific  $(p, T)$ .

### 2.1.2. TRANSPORT PROPERTIES

In addition to the "pure" thermodynamic variables discussed above, transport properties also have to be modelled accurately to solve the heat transfer problem. The relevant transport properties in this case are viscosity and thermal conductivity.

#### VISCOSITY

The used viscosity model is the friction theory model proposed by Quiñones-Cisneros and Deiters [52]. For methane, it is valid in the region of 100-500 K with an average deviation of 0.83% and maximum deviation of 6.02% with respect to experimental data [52]. This friction model was also used by Urbano et al. to model methane in cooling channels [53].

The friction model is based on a separation of the pressure into three terms: the ideal pressure  $p_{\text{id}}$ , the residual repulsive pressure  $\Delta p_{\text{rep}}$  and the attractive pressure  $p_{\text{att}}$ . Equation 2.3 shows these terms.

$$p = p_{\text{id}} + \Delta p_{\text{rep}} + p_{\text{att}} \quad (2.3)$$

The ideal pressure is the pressure as expected from ideal gas theory; it is given by eq. 2.4.

$$p_{\text{id}} = \rho R_g T \quad (2.4)$$

The pressure is separated into a repulsive and an attractive part using van der Waals separation [52]. The attractive part of the pressure is also called internal pressure and is given by eq. 2.5, where the partial derivative is calculated using the GERG-2004 model described in section 2.1.1.

$$p_{\text{att}} = p - \left( \frac{\partial p}{\partial T} \right)_{\rho} T \quad (2.5)$$

The repulsive part of the pressure consists of the ideal pressure and a residual part, denoted by  $\Delta p_{\text{rep}}$ . If the pressure and the previous terms are known, it can be calculated with eq. 2.6.

$$\Delta p_{\text{rep}} = p - p_{\text{id}} - p_{\text{att}} \quad (2.6)$$

The viscosity is then given by adding several contributions that are related to these pressure terms, see eq. 2.7. For the term  $\mu_{\text{base}}$ , an empirical relation in  $T$  is used; the coefficients  $c$  are also calculated

based on empirical data.

$$\mu = \mu_{\text{base}} + c_{\text{id}} p_{\text{id}} + c_{\text{id},2} p_{\text{id}}^2 + c_{\text{rep}} \Delta p_{\text{rep}} + c_{\text{rep},2} \Delta p_{\text{rep}}^2 + c_{\text{att}} p_{\text{att}} + c_{\text{att},2} p_{\text{att}}^2 \quad (2.7)$$

For more information on the exact calculations and coefficients, the interested reader is referred to the paper by Quiñones-Cisneros and Deiters that describes the theory and equations in detail [52].

### THERMAL CONDUCTIVITY

The thermal conductivity of methane is calculated using two different models. The thermal conductivity is separated into three contributions: dilute gas  $\kappa_{\text{dil}}$ , excess  $\kappa_{\text{exc}}$  and critical thermal conductivity  $\kappa_{\text{cr}}$  (eq. 2.8).

$$\kappa = \kappa_{\text{dil}} + \kappa_{\text{exc}} + \kappa_{\text{cr}} \quad (2.8)$$

The dilute and excess thermal conductivity are calculated using relations given by Sanokidou et al. [54]. The critical thermal conductivity is calculated using equations from Olchoway and Sengers [55]. The former also contains equations for critical enhancement of the thermal conductivity, but the equations used are overly complex. Olchoway and Sengers propose a simpler model for the critical thermal conductivity.

The relevant equations to calculate the terms of eq. 2.8 nonetheless remain complicated and cumbersome, so they will not be reproduced here. It suffices to say that they all make extensive use of coefficients to match a theoretical model to the empirical data. More information can be found in the relevant papers [54, 55].

### 2.1.3. VERIFICATION

After implementing the equations for the thermodynamic and transport properties of methane, it was important to verify them. Although the equations themselves have been proven to represent methane's behaviour accurately, there could be implementation mistakes and errors in the Python code.

The density, specific heat, viscosity and thermal conductivity of methane were calculated for a variety of pressures and temperatures. The resulting values were compared to those in the NIST database [50]. Figure 2.3 shows the results of this comparison.

Figure 2.3 shows that the implemented equations indeed reproduce the NIST values very accurately. It is relevant to note that NIST uses a set of equations to obtain property tables that is different from the set of equations used in this work. This results in discrepancies, most notably in the thermal conductivity.

This is because the NIST database uses an older, less accurate model for thermal conductivity [56]. This model does not incorporate the critical enhancement of the thermal conductivity. Because of this reason, the calculated values of thermal conductivity are slightly higher than the NIST values in fig. 2.3, especially around the pseudo-critical temperature.

We can conclude that this verification shows favourable results: the equations are correctly implemented. The small discrepancy between the NIST values and the calculated values can be explained by the different models used and is unlikely to be the result of a programming error.

### 2.1.4. PROPERTY TABLES FOR OPENFOAM

The equations for methane's properties described above are very accurate, but highly complex and computationally intensive. This makes them unsuitable for direct use in CFD computations. An alternative solution is to generate property tables beforehand and interpolate these in the CFD program

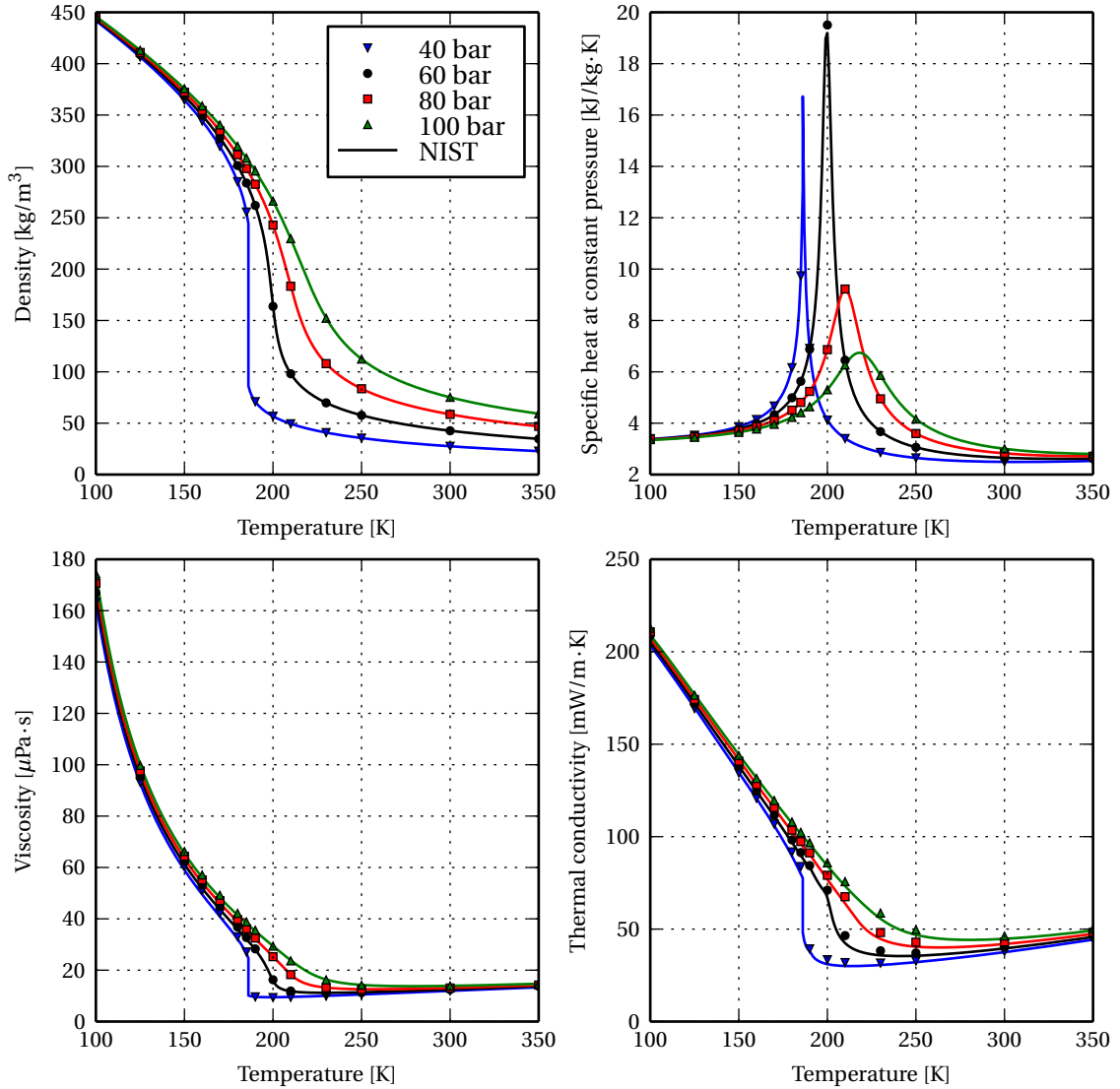


Figure 2.3: Comparison between fluid property models programmed in Python (markers) and NIST reference data [50] (curves)

at runtime [16]. In this way, the complex equations do not have to be evaluated at every time step for each cell, but rather only an inexpensive bilinear interpolation must be performed.

Two-dimensional tables of the properties were therefore generated, tabulated in pressure and temperature. Observation of fig. 2.3 shows there are regions of high gradients in the fluid properties, typical of a fluid near the critical point. However, there are also regions of fairly small change in fluid properties. This means that a regular grid of  $(p, T)$  points would be inadequate near the critical point, while being overly accurate far away from the critical point. A non-regular grid with more data points near the critical point provides high accuracy at relatively low computational cost.

Further observation shows that at locations of high gradients in density, there are also high gradients in other properties and vice versa. Because of this, all properties can be evaluated at the same  $(p, T)$  data points, simplifying the table generation program.

The tables were generated with the purpose of obtaining a nearly constant  $\Delta\rho$  between  $(p, T)$  data points. The target  $\Delta\rho$  was set at  $0.25 \text{ kg/m}^3$ , approximately 1.5% of the minimum density (the error is much smaller, as will be shown later). The properties were calculated and tabulated for pressures between 50 bar and 160 bar and at temperatures between 100 K and 1500 K.

When starting at the minimum pressure and temperature, the next temperature point was selected by calculating the expected temperature at which temperature would have fallen by  $0.25 \text{ kg/m}^3$ . Equation 2.9 shows the equation for this temperature. At a certain pressure, the properties were first calculated for all temperatures at this pressure. Note that these temperatures need not be the same for all pressures.

$$T_{\text{new}} = T_{\text{old}} + \frac{\partial T}{\partial \rho} 0.25 \quad (2.9)$$

To calculate the next pressure point, a similar equation was used. This equation was used at the critical temperature, because here the maximum variation in fluid properties is expected. The result is a non-regular set of  $(p, T)$  data points that have a nearly constant difference in density between them.

Because the gradient of the fluid properties is the largest near the critical point, the largest discretisation errors were expected in this region. To estimate the error, bilinear interpolation was performed for 5000  $(p, T)$  points. Temperatures of the test points ranged between 150 and 250 K (crossing the pseudo-critical temperature), while the pressure was the same for all points just above 50 bar. The pressure was in-between two pressure points of the look-up tables to test the accuracy of the bilinear interpolation.

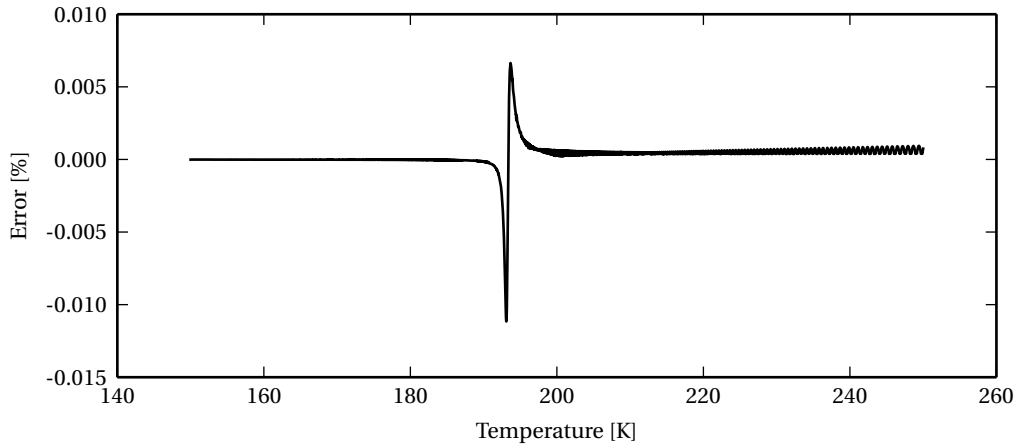


Figure 2.4: Discretisation error of density with bilinear interpolation

At all test points, the fluid properties were also calculated using the relations from section 2.1. The difference between both values is the discretisation error of the fluid properties. Figure 2.4 shows the discretisation error of the density. As expected, the error is largest near the pseudo-critical temperature. The error is below 0.015% for all data points, and substantially lower far away from the pseudo-critical temperature. The error of 0.015% is smaller than the experimental error of the GERG-2004 equation of state. The other fluid properties showed similar error percentages. This proves that discretisation errors of the fluid properties do not have a substantial effect on the error of the simulation.

Both the methane property models described earlier and the table generation script were programmed in Python. All of them are available to the community on Github [57].

## 2.2. CHAMBER WALL PROPERTIES

The final aim of this thesis is to compare copper and aluminium as materials for the combustion chamber wall. To be able to do this, it is important to know the properties of these materials. Because this work is not focused on materials science, two alloys – one copper and one aluminium alloy – were chosen as reference materials for the comparisons in this thesis.

### 2.2.1. COPPER

For copper, the chosen alloy was NARloy-Z, the chamber wall material of the Space Shuttle Main Engine. This is a high-strength, high-temperature copper alloy with 3% silver and 0.5% zirconium. The material properties of NARloy-Z were investigated in depth by Esposito and Zabora [58].

It has a high thermal conductivity (295 W/m·K at room temperature) typical for copper alloys, but is also heavy with a density of 9134 kg/m<sup>3</sup>. Figure 2.5 shows that the thermal conductivity is almost constant with temperature. For this reason, it was assumed constant at the room temperature values for all calculations.

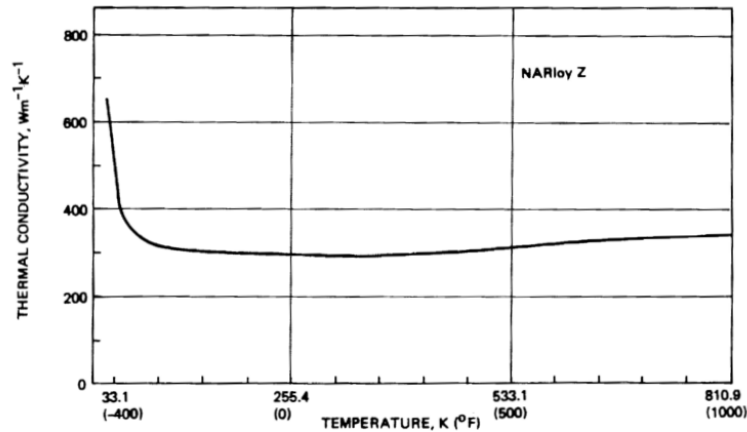


Figure 2.5: Thermal conductivity variation of NARloy-Z with temperature [58]

Both the yield and ultimate strength of NARloy-Z do deteriorate substantially when the temperature rises. Figure 2.6 shows the ultimate and yield stresses versus material temperature. According to Sutton, the allowable temperature of a rocket engine is usually chosen to be the temperature at which the strength has decreased to 60 - 75% of the room temperature strength [8]. This is temperature is often far below the melting temperature of the material.

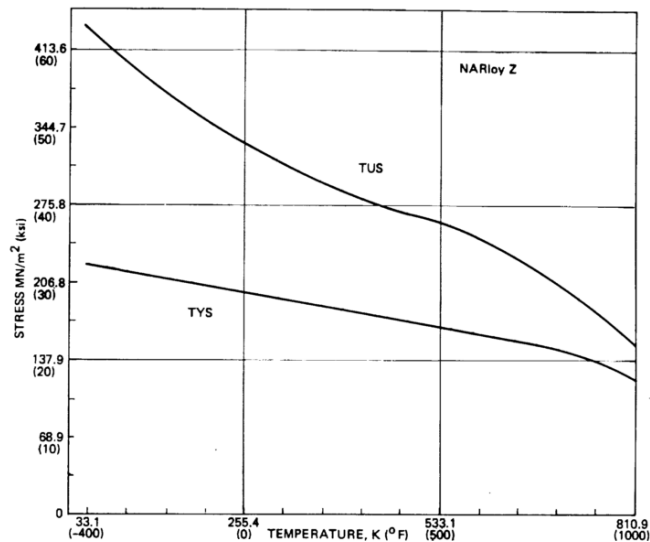


Figure 2.6: Ultimate and yield strength variation of NARloy-Z with temperature [58]

To find the allowable temperature of NARloy-Z, the curves of fig. 2.6 were digitised and interpolated. It turns out that at approximately 700 K, the yield strength has been reduced by 65%, while for the ultimate strength this point occurs at approximately 795 K. For simplicity, we can thus set the allowable temperature for NARloy-Z at 800 K. Since we are not trying to design an actual engine, but simply comparing two materials, using such a rough but representative value is justified.

In none of the simulations performed in this thesis, deformations or structural failure are modelled. In some simulations the wall temperatures found exceed the melting temperature of copper and aluminium alloys. Such a situation would lead to a failure of the engine in reality. However, as long as we are aware of this limitation, it is not problematic

The thermal expansion of the material and its effect on the dimensions are small: the linear expansion of Narloy-Z is less than 1% at 800 K [58]. The resulting thermal stresses are important for the structural design, but their impact on the cooling channel geometry is negligible. For this reason, they will be neglected in this thesis.

A copper alloy that was used in experiments by CIRA is Glidcop Al-15. In order to reproduce these experiments in chapter 5, the thermal conductivity of this material must be known. A fact sheet by SCM Metal Products shows the thermal conductivity of Glidcop Al-15 to be approximately linear with temperature, see fig. 2.7.

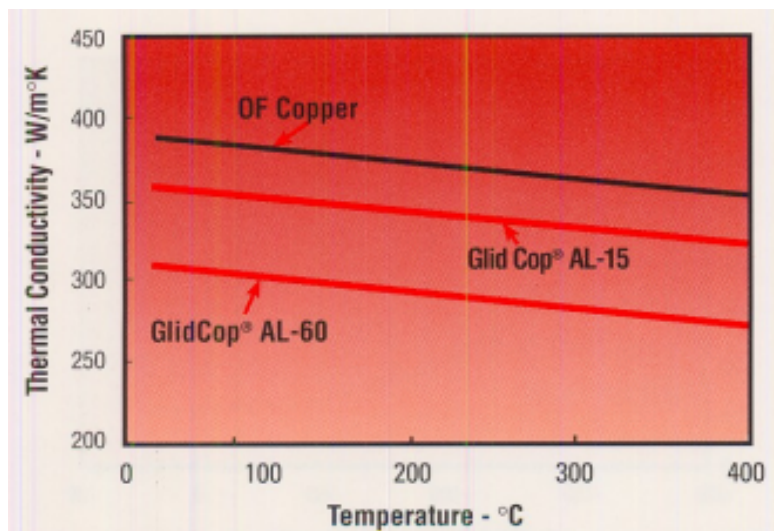


Figure 2.7: Thermal conductivity variation of Glidcop Al-15 with temperature [59]

It would be best to implement this variation of thermal conductivity in the simulation program. However, lacking sufficiently detailed data, it is also reasonable to use a constant thermal conductivity of for example 345 W/m · K, as was done by Pizzarelli et al. They showed that the chosen value for thermal conductivity only has a minor influence on the simulation results [31].

### 2.2.2. ALUMINIUM

For aluminium the Al-7075 T6 alloy was chosen as representative material. This is a high-strength material often used in the aerospace industry. Its main alloying elements are zinc, magnesium and copper. The room temperature thermal conductivity of Al-7075 T6 is 130 W/m · K according to a data sheet by CRP Meccanica [60].

The yield and ultimate strength of Al-7075 T6 at various temperature is listed in [61]. Interpolating this data, it is found that this alloy loses 65% of its yield strength at 437 K. At 513 K, it loses 65% of its ultimate strength. However, this is based on only 9 data points. Because of this inaccuracy, the allowable temperature is set to 500 K for aluminium.

The room temperature properties of NARloy-Z and Aluminium 7075 T6 are listed in table 2.2.

Table 2.2: Material properties for selected alloys

Property	NARloy-Z [58]	Al-7075 T6 [60]
Thermal conductivity [W/m·K]	295	130
Coefficient of thermal expansion [ $\mu\text{m}/\text{m}\cdot\text{K}$ ]	17.2	23.6
Density [ $\text{kg}/\text{m}^3$ ]	9134	2810
Specific heat capacity [J/kg·K]	373	960
Melting point [K]	Not given	750
Ultimate tensile strength [MPa]	314	572
Tensile yield strength [MPa]	192	503
Modulus of elasticity [GPa]	127	71.7
Poisson's ratio [-]	0.34	0.33

# 3

## FIRST ORDER ANALYSIS

First order methods based on semi-empirical relations are often used in rocket engine design. Such methods are fast and allow to evaluate a wide range of design options. Furthermore they can be used to find the influence of isolated design parameters in parametric studies. The main drawback of using semi-empirical relations is that their accuracy is often poor.

A program was written to perform a first order analysis of a methane-cooled liquid rocket engine. The program requires the input of an engine geometry including cooling channels, thrust chamber material conductivity, coolant inlet conditions and an output file from CEA (a NASA program to analyse rocket performance). Outputs include coolant conditions along the channel as well as chamber wall temperature.

The tool is called OMECA, short for One-dimensional Methane Engine Cooling Analysis. It was written in Python and has been made available online on Github [62]. It has been distributed to the Space Systems Engineering group at Delft University of Technology and the DARE (Delft Aerospace Rocket Engineering) student group.

Section 3.1 describes the computational setup of the program: the equations that are used as well as the underlying assumptions and limitations. The model is compared to a more complex analysis of a small oxygen/methane engine in section 3.2. Using this validation, the accuracy of OMECA can be established.

Section 3.3 shows the influence of various parameters on the heat transfer in the thrust chamber. Based on a generic 10 kN engine, the pressure drop and maximum wall temperature are predicted for varying inputs. Section 3.4 explores possible regenerative cooling channel designs for the same generic 10 kN engine. A preliminary comparison of copper and aluminium as chamber materials is performed. This was the first research goal of this thesis as defined in chapter 1: *"explore possible cooling designs for a small rocket engine with a one-dimensional model"*. Finally, section 3.5 shows the conclusions and recommendations of this chapter.

### 3.1. COMPUTATIONAL SETUP

Figure 3.1 shows part of a thrust chamber cross-section with rectangular coolant channels in the wall. The parameters describing the geometry are also defined in this figure.

The first order cooling analysis method evaluates the thermal equilibrium at multiple stations along the thrust chamber. The equilibrium model is one-dimensional (e.g. along the dashed line in fig. 3.1). It incorporates convection and radiation from the hot gas to the wall, conduction through the wall and convection from the wall to the coolant.

The assumption of one-dimensional (radial) heat transfer means that heat transfer in the longitudinal and circumferential direction is neglected. In reality, it is expected that peaks in heat transfer will

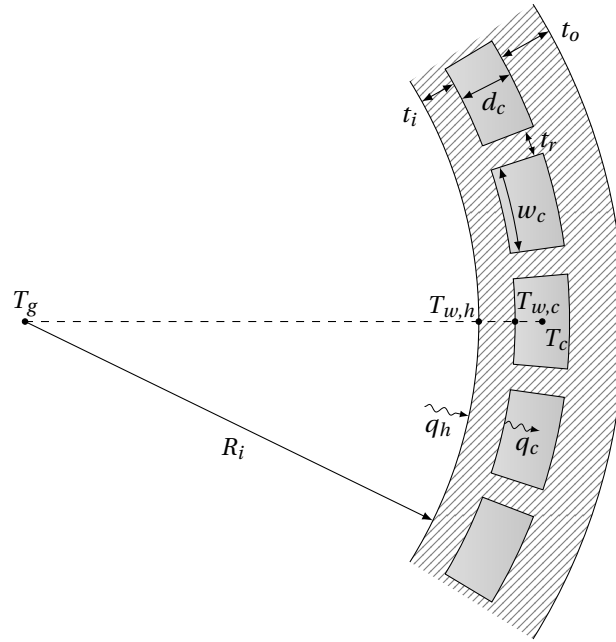


Figure 3.1: Illustration of a thrust chamber cross-section with coolant channels

be smoothed out along the longitudinal axis of the rocket through conduction in the chamber wall. On the other hand, the alteration of cooling channels and ribs in the circumferential direction will generate local maxima and minima in wall temperatures, see fig. 3.2. For narrow channels, Pizzarelli et al. found fairly uniform wall temperatures, but for wide channels the difference in local temperatures was in the order of 50 K [63].

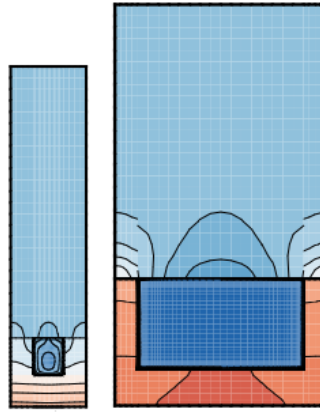


Figure 3.2: Temperature fields in cross-section of cooling channel and wall. On the left a narrow part of the channel where temperature hardly varies in circumferential direction. On the right a wide part of the same channel with stronger circumferential temperature variations [63]

$$q = \alpha_h (T_{aw} - T_{i,h}) + q_{R,h} = \frac{\kappa_i}{t_i} (T_{i,h} - T_{i,c}) = \alpha_{c,F} (T_{i,c} - T_{c,b}) \quad (3.1)$$

Equation 3.1 describes the three heat fluxes. Because we consider an equilibrium situation, the three fluxes  $q$  must be equal. In the equations,  $\alpha$  is the convective heat transfer coefficient, where the subscript  $h$  refers to convection from the hot gases, while  $c$  refers to the coolant.  $\kappa_i$  is the thermal conductivity of the inner wall and  $t_i$  is its thickness. The temperatures  $T_{aw}$ ,  $T_{i,h}$ ,  $T_{i,c}$  and  $T_{c,b}$  refer to the adiabatic wall temperature, hot gas side inner wall temperature, coolant side inner wall temperature and coolant bulk temperature respectively.

Equation 3.1 has been adapted from Huzel and Huang [15] in one aspect: the radiative flux  $q_{R,h}$  from the hot gas has been added. Huzel and Huang only considered convective heat transfer from the hot gases to the wall.

The wall temperatures  $T_{i,h}$  and  $T_{i,c}$  are not known. The thermal equilibrium of eq. 3.1 can be rewritten to calculate the heat flux through the chamber wall without knowing these temperatures. We then obtain eq. 3.2.

$$q = \frac{T_{aw} - T_{c,b} + \frac{q_{R,h}}{\alpha_h}}{\frac{1}{\alpha_h} + \frac{t_i}{\kappa_i} + \frac{1}{\alpha_c}} \quad (3.2)$$

Equation 3.2 allows the calculation of the heat flux and indirectly – through eq. 3.1 – the wall temperatures. The geometry of the thrust chamber defines the parameter  $t_i$ . Thermal conductivity  $\kappa_i$  is dependent on the chamber material used; a constant value was assumed for each calculation. Changes of the geometry due to thermal expansion or otherwise induced stresses of the material were neglected. Likewise, the thermal conductivity was assumed constant for each case, even though in reality it changes with temperature for rocket thrust chamber materials [58].

The hot gas parameters  $T_{aw}$ ,  $q_R$  and  $\alpha_g$  will be discussed in section 3.1.1. Section 3.1.2 will describe how the coolant temperature and heat transfer coefficient are obtained.

### 3.1.1. HOT GAS SIDE

The flow parameters of the hot combustion gases were calculated using NASA's CEA program [64]. For a given propellant and combustion chamber pressure CEA calculates the combustion products. Outputs include temperature, pressure, density, viscosity, specific heat, Prandtl number and Mach number at various area ratios. The gas composition is also given for each area ratio. The program was set to calculate chemical equilibrium conditions at all stations upstream of the throat and freeze the gas composition at the throat. CEA is a typical program for use in first order analysis, see for example [9, 65].

The convective heat flux from the hot gas is usually calculated using eq. 3.3. Note that in general, the convective heat flux  $q_{V,h}$  is dependent on the temperature difference between the hot gas and the wall and a coefficient  $\alpha_h$  that is supposedly independent of these temperatures [16].

$$q_{V,h} = \alpha_h (T_{aw} - T_{i,h}) \quad (3.3)$$

If an insulated wall is exposed to a high-speed flow, the flow temperature at the wall will be higher than the free-stream temperature. The flow is slowed down due to the wall and as a result it heats up. The temperature that an insulated (adiabatic) wall exposed to a flow would reach is called the adiabatic wall temperature  $T_{aw}$ .

If there is an outward heat flux at the wall, the wall temperature will be below  $T_{aw}$ . On the other hand, if there is a heat flux from the wall towards the flow, the wall temperature will be higher than  $T_{aw}$ . The boundary layer temperature profile for these cases is shown in fig. 3.3.

The adiabatic wall temperature is not necessarily a temperature of the actual hot gas flow because the wall is actively cooled and not adiabatic. Nonetheless it is used to calculate the heat flux because the heat transfer has little influence on the gas temperature [16] and it is easy to calculate.

In general, the stagnation temperature is not fully recovered at the wall. A recovery factor  $r$  is used to determine the adiabatic wall temperature, as eq. 3.4 shows. This factor depends on the Prandtl number  $Pr$ ; for turbulent flows it is be equal to  $Pr^{1/3}$  [16]. In eq. 3.4,  $\gamma$  is the ratio of specific heats and  $M$  is the Mach number.

$$T_{aw} = T_h \left( 1 + r \frac{\gamma - 1}{2} M^2 \right) \quad (3.4)$$

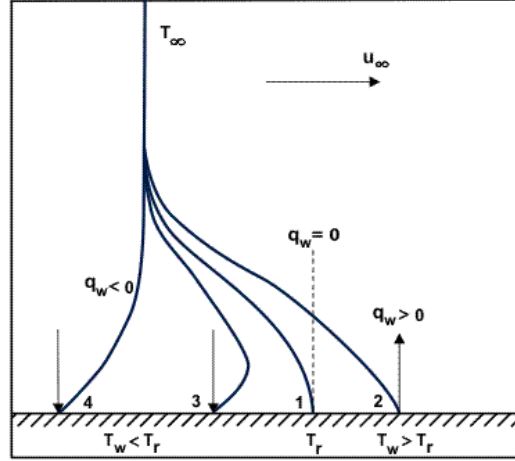


Figure 3.3: Boundary layer temperature profile for various cases [66]

To determine  $\alpha_h$ , semi-empirical relations are often used. The most well-known of these relations is the Bartz equation. Bartz started from the Dittus-Boelter relation for the Nusselt number (eq. 3.5). The Dittus-Boelter relation was originally developed for heat transfer in straight pipes. It is a relation for the Nusselt number  $Nu$  based on the Reynolds number  $Re$  and Prandtl number  $Pr$ .

Bartz rewrote it to eq. 3.6, where the fluid properties are evaluated at the film temperature (indicated with subscript  $f$ ). This film temperature is an intermediate temperature between the hot gas temperature and the wall temperature, to account for property variations in the boundary layer [67].  $D_t$  is the throat diameter,  $\mu$  is the viscosity,  $c_p$  is the specific heat at constant pressure,  $\rho$  is the gas density and  $u$  is the gas velocity.

$$Nu = 0.026 Re^{0.8} Pr^{0.4} \quad (3.5)$$

$$\alpha_h = \frac{0.026 \mu_f^{0.2} c_{p,f}}{D_t^{0.2} Pr_f^{0.6}} (\rho_f u)^{0.8} \quad (3.6)$$

Bartz then assumed that the specific heat  $c_p$  and Prandtl number  $Pr$  remain approximately constant with temperature. Flow momentum  $\rho_0 u$  is evaluated using ideal rocket theory from  $p_0, c^*$  and the area ratio. The density and viscosity are then corrected for the film temperature so we obtain  $\rho_f$  and  $\mu_f$ .

The final form of the convective coefficient correlation as proposed by Bartz is given by eq. 3.7, where  $s$  is the correction factor defined in eq. 3.8 [67]. The first term in eq. 3.8 is a temperature correction for density, while the second term is a correction for viscosity.

As discussed above, the thermal boundary layer is influenced by the temperature of the wall itself. This is reflected in Bartz equation by the appearance of the wall temperature  $T_{i,h}$  in eq. 3.8. The OMECA program uses an iteration loop to converge to a solution with consistent values for  $T_{i,h}$  and  $\alpha_h$ .

$$\alpha_h = \frac{0.026 \mu_0^{0.2} c_{p,0}}{D_t^{0.2} Pr_0^{0.6}} \left( \frac{p_0}{c^*} \right)^{0.8} \left( \frac{A_t}{A} \right)^{0.9} s \quad (3.7)$$

$$s = \left[ \frac{1}{2} \frac{T_{i,h}}{T_0} \left( 1 + \frac{\gamma-1}{2} M^2 \right) + \frac{1}{2} \right]^{-0.68} \left[ 1 + \frac{\gamma-1}{2} M^2 \right]^{-0.12} \quad (3.8)$$

The relation proposed by Bartz was not developed for methane-fuelled engines. Tamura et al. found that the Bartz equation overpredicted the heat flux for a 9.6 MPa chamber pressure oxygen/methane engine [68], as illustrated in fig. 3.4. The error in the maximum heat flux is about 25%.

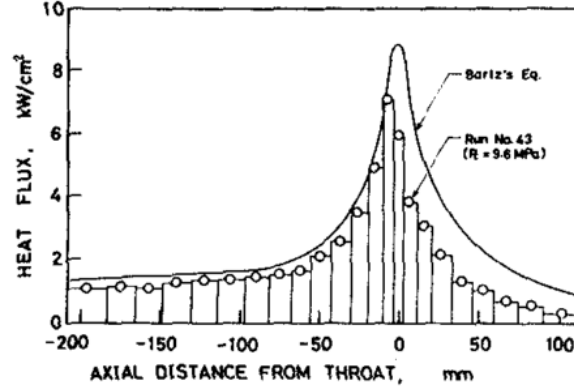


Figure 3.4: Comparison of experimental heat flux with prediction from Bartz correlation for oxygen/methane engine [68]

The above discussion was limited to convective heat transfer, which is the largest contribution to the heat flux from the hot gases [8]. Radiation, however, can also be a significant factor in the heat flux. Kirchberger analysed that in a small oxygen/hydrocarbon combustion chamber, radiation usually accounted for 3 to 8% of the heat transfer [69].

Symmetrical molecules usually do not have strong emission bands in the temperature ranges encountered in rocket engines, but unsymmetrical molecules do [8]. Kirchberger argues that in oxygen/methane rocket engines, radiation from water and carbon dioxide should be considered, while carbon monoxide radiation can be neglected [69]. The radiation from carbon monoxide molecules is estimated to be an order of magnitude smaller than that from carbon dioxide [69].

Empirical relations to calculate the heat flux due to radiation from the combustion gases have been taken from Kirchberger [69]. Equation 3.9 gives the radiative heat flux due to  $H_2O$ , while eq. 3.10 gives the heat flux due to  $CO_2$ . The partial pressures required in these equations were obtained from CEA. Equation 3.9 and eq. 3.10 are based on experiments with small oxygen/kerosene combustion chambers. In these experiments, the mixture ratio was varied between 1.4 and 3.4 at a nominal chamber pressure of 80 bar. Unfortunately the authors of the equations do not give an estimated accuracy [70].

$$q_{R,H_2O} = 5.74 \cdot \left( \frac{p_{H_2O}}{10^5} \cdot R_i \right)^{0.3} \left( \frac{T_h}{100} \right)^{3.5} \quad (3.9)$$

$$q_{R,CO_2} = 4 \cdot \left( \frac{p_{CO_2}}{10^5} \cdot R_i \right)^{0.3} \left( \frac{T_h}{100} \right)^{3.5} \quad (3.10)$$

### 3.1.2. COOLANT SIDE

For the coolant side calculations, the nozzle is also divided in a number of stations. It is assumed that for each station, the coolant properties are uniform and constant. Calculations of the coolant side start with the inlet properties of the methane coolant. Inlet total pressure and inlet temperature are boundary conditions provided by the user.

For each of the stations along the nozzle, the program carries out the same series of calculations. First the density  $\rho$  corresponding to the methane pressure and temperature is found iteratively using the GERG-2004 equation of state. This is necessary because the other fluid properties are calculated from density and temperature. With density and temperature known, specific heat  $c_p$ , viscosity  $\mu$  and thermal conductivity  $\kappa$  are now determined using the models shown in chapter 2.

Now the channel cross-sectional area and hydraulic diameter  $D$  are calculated for the current nozzle station. The program uses a constant rib thickness  $t_r$  because it is assumed that this thickness is limited by the manufacturing technique or the material strength. The channel width is then calculated from the number of channels. This leads to wide channels at large area ratios and narrow channels near the throat, increasing the heat transfer at this critical location. The channel height is taken for the complete rocket engine.

From the channel cross-sectional area, the velocity of the coolant is determined using a constant mass flow. The total pressure and total temperature are corrected for fluid velocity increases or decreases. This is done in order to avoid a rise in total pressure or temperature as the fluid accelerates and gains kinetic energy. Then the Reynolds number  $Re$  is calculated using eq. 3.11 and the Prandtl number  $Pr$  with eq. 3.12.

$$Re = \frac{\rho u D}{\mu} \quad (3.11)$$

$$Pr = \frac{c_p \mu}{\kappa} \quad (3.12)$$

The Reynolds number and Prandtl number are in turn inputs for the Nusselt number calculation. Three semi-empirical Nusselt number correlations have been programmed; the user can select which one should be used. The Dittus-Boelter equation (eq. 3.13) is a well-known and simple correlation to determine the Nusselt number in turbulent pipes. It was claimed by Urbano et al. to be very accurate (within 3%) for methane in round, symmetrically heated channels [53] when it is at supercritical pressure and supercritical temperature. It must be emphasised, however, that this high accuracy is only achieved for the last third of a 0.4 m long channel. Urbano et al. also found that the Taylor equation (eq. 3.14) was fairly accurate (with an error below 17% in most of the channel) for methane at supercritical pressure but subcritical temperature [53].

Ruan and Meng propose eq. 3.15 for supercritical methane, based on CFD analysis of asymmetrically heated, rectangular channels [33]. This yielded an error of 23% with respect to numerical simulations for methane at supercritical pressure and temperature crossing the critical point. Because this situation is more difficult to predict than the situation analysed by Urbano et al, the relation proposed by Ruan and Meng is quite promising.

$$Nu_b = 0.023 Re_b^{0.8} Pr_b^{0.4} \quad (3.13)$$

$$Nu_b = 0.023 Re_b^{0.8} Pr_b^{0.4} \left( \frac{T_b}{T_i} \right)^{\left( 0.57 - \frac{1.59D}{x} \right)} \quad (3.14)$$

$$Nu_b = 0.0069 Re_b^{0.9} (Pr_b)^{0.66} \left( \frac{\rho_i}{\rho_b} \right)^{0.43} \left( 1 + 2.4 \frac{D}{x} \right) \quad (3.15)$$

Note that both eq. 3.14 and eq. 3.15 require the determination of properties at the wall, either the temperature at the wall  $T_i$  or the density at this wall temperature,  $\rho_i$ . This is a similar problem as encountered with the determination of the hot gas convective coefficient and indeed the solution is the same. The determination of the  $T_i$  and  $\alpha_c$  is performed in an iterative manner, in order to come to a consistent solution.

The convective coefficient of the coolant for the current station is calculated from the Nusselt number using eq. 3.16. Any errors in the Nusselt number correlations result in large uncertainties in the

convective coefficient and therefore also in the wall temperatures. The reason why it is so difficult to obtain a proper Nusselt number correlation is the variation in fluid properties found in supercritical methane. This variation can generate local effects that are very hard to cover with a single semi-empirical equation.

In eq. 3.16,  $\Psi_C$  is a correction factor for the curvature of the channel.  $\Psi_\xi$  is a correction factor for channel roughness.

$$\alpha_c = \frac{\kappa (Nu \cdot \Psi_C \Psi_\xi)}{D} \quad (3.16)$$

In a curved channel, secondary vortices develop. These so-called Dean vortices alter the heat transfer coefficient. Several Nusselt number correlations for curvature exist [71, 72]. A choice was made to use the simplest one, given by eq. 3.17. For this relation it is only necessary to know local parameters, making it easy to implement.

$$\Psi_C = \left[ Re \left( \frac{D}{2R_C} \right)^2 \right]^{\pm 0.05} \quad (3.17)$$

The downside of this local approach is that it does not account for the development and dissipation of the vortices. For example, in reality Dean vortices will still be present in a straight part of the channel immediately downstream of a bend. Equation 3.17 does not correct for this.

The  $\pm$  sign in eq. 3.17 accounts for the difference between a concave and a convex bend. Because the heat transfer in rocket engine cooling channels is asymmetric, the orientation of a bend is critical. An increased heat transfer coefficient will occur in a concave bend (e.g. at the throat), so a positive exponent should be used. For convex bends, a negative exponent must be used.

CFD simulations on curved channels have shown that convex bends also increase the convective coefficient locally, but lead to a reduced coefficient in the region downstream of a convex bend [73, 74]. No Nusselt number correlations that can correct for this behaviour were found in literature.

Why then, one could ask, was eq. 3.17 implemented, despite the above shortcomings? The answer is that the heat transfer enhancement at the throat is modelled relatively well because it is in a concave bend. The throat is a critical region for heat transfer analysis because there the maximum wall temperature is expected. If the heat transfer is modelled correctly at the throat, at least a relatively accurate estimate of the maximum wall temperature can be obtained.

Another correction was implemented for the roughness of the channel. This correction is represented by  $\Psi_\xi$  and given by eq. 3.18; with  $\xi$  defined by eq. 3.19 [71].  $\xi$  is the ratio of the friction factor of a rough channel versus that of a smooth one. In eq. 3.19,  $f_D$  is the Darcy-Weisbach friction factor that will be defined in eq. 3.24.

$$\Psi_\xi = \frac{1 + 1.5Pr^{-1/6}Re^{-1/8}(Pr-1)}{1 + 1.5Pr^{-1/6}Re^{-1/8}(Pr\xi-1)} \xi \quad (3.18)$$

$$\xi = \frac{f_D(Re, h_s)}{f_D(Re, h_s = 0)} \quad (3.19)$$

We have found the convective coefficient  $\alpha_c$  for the coolant in contact with the hot chamber wall. However, the ribs also contribute to convective heat transfer towards the coolant. Popp and Schmidt reported an approach to also model this heat transfer [75]. Similar approaches based on classical fin theory have been reported by several researchers [9, 16, 69]. First a fin effectiveness is calculated to

determine how well the ribs transfer heat, using eq. 3.20.

$$\eta_F = \frac{\tanh\left(\sqrt{\frac{2\alpha_c t_r}{\kappa}} \frac{d_c}{t_r}\right)}{\sqrt{\frac{2\alpha_c t_r}{\kappa}} \frac{d_c}{t_r}} \quad (3.20)$$

The total convective coefficient  $\alpha_c$  is corrected for the presence of the ribs using eq. 3.21. This equation both corrects for the absence of convection at the hot wall where the ribs are located (the lost chamber wall area) and for the additional convection from the side walls of the coolant channel.

$$\alpha_{c,F} = \alpha_c \frac{w_c + 2\eta_F d_c}{w_c + t_r} \quad (3.21)$$

The fin treatment of the vertical walls is a source of error. The effect of using high aspect ratio cooling channels is widely documented [73, 76, 77], but no experimental validation data for eq. 3.20 could be found in literature.

With  $\alpha_{c,F}$  known, all parameters needed to solve the heat balance are available. We can use eq. 3.2 to find the heat flux and then calculate the wall temperatures with eq. 3.1.

Now the only thing left is to update the temperature and pressure of the coolant for the current station. It is assumed that the total heat transfer is fully absorbed by the coolant and the coolant is heated uniformly. The heat transferred is equal to the wall surface area of the current station multiplied by the heat flux. The temperature rise of the fluid is calculated with eq. 3.22.

$$\Delta T = \frac{q \cdot (2\pi R_i) l}{\dot{m}_c c_p} \quad (3.22)$$

The pressure drop over the current station is calculated with eq. 3.23, where  $l$  is the length of the station. The Darcy-Weisbach friction factor  $f_D$  is calculated by iteratively solving the Colebrook equation (eq. 3.24). Channel roughness height  $h_s$  is given by the user and constant for the complete channel.

$$\Delta p = f_D \frac{l}{D} \frac{1}{2} \rho u^2 \quad (3.23)$$

$$\frac{1}{\sqrt{f_D}} = -2 \log_{10} \left( \frac{h_s}{3.7D} + \frac{2.51}{Re \sqrt{f_D}} \right) \quad (3.24)$$

Then the program continues to the next station and performs the same calculations until the end of the coolant channel is reached.

### 3.1.3. OMECA PROGRAM SUMMARY

In the previous sections, the computational model and relevant equations for the first order analysis has been presented. We will now synthesises this information into a summary of the OMECA program.

Figure 3.5 shows a flowchart of the OMECA program, implementing the steps that were described in the previous sections. It is a simple Python script, such that the input parameters must be defined inside the script. The input parameters are given in table 3.1.

Only a steady-state analysis can be performed with the program. Many transient effects could be expected in real rocket engines: most prominently during startup and shutdown of the engine. But there could also be local, transient phenomena such as combustion instabilities leading to increased heat flux, temporary storing of thermal energy in the chamber material or transient vortices in the coolant channels. Such transient effects could affect critical parameters such as wall temperature and pressure drop, but they are not modelled in this analysis.

Table 3.1: OMECA input parameters

Input parameter	Unit	Information
Nozzle contour	m	Comma separated value file
Number of channels	-	
Rib thickness	m	Constant
Wall thickness	m	Inner chamber wall
Channel height	m	Constant or array
Fuel flow	kg/s	Only methane flow
Wall conductivity	W/m·K	Thermal conductivity of inner wall
Wall roughness height	m	
Coolant inlet pressure	Pa	
Coolant inlet temperature	K	
CEA file	-	Output file of CEA program
Modulus of elasticity	Pa	Wall material, Optional
Yield strength	Pa	Wall material, Optional
Poisson ratio	-	Wall material, Optional

However, it is expected that the worst case situation is at steady state; the combustion chamber is cooler than the design temperature at start of operations. As the engine is running, the wall temperature exponentially increases to the maximum temperature. This behaviour can be seen e.g. in the thermocouple data of the methane cooling experiments carried out by CIRA [78].

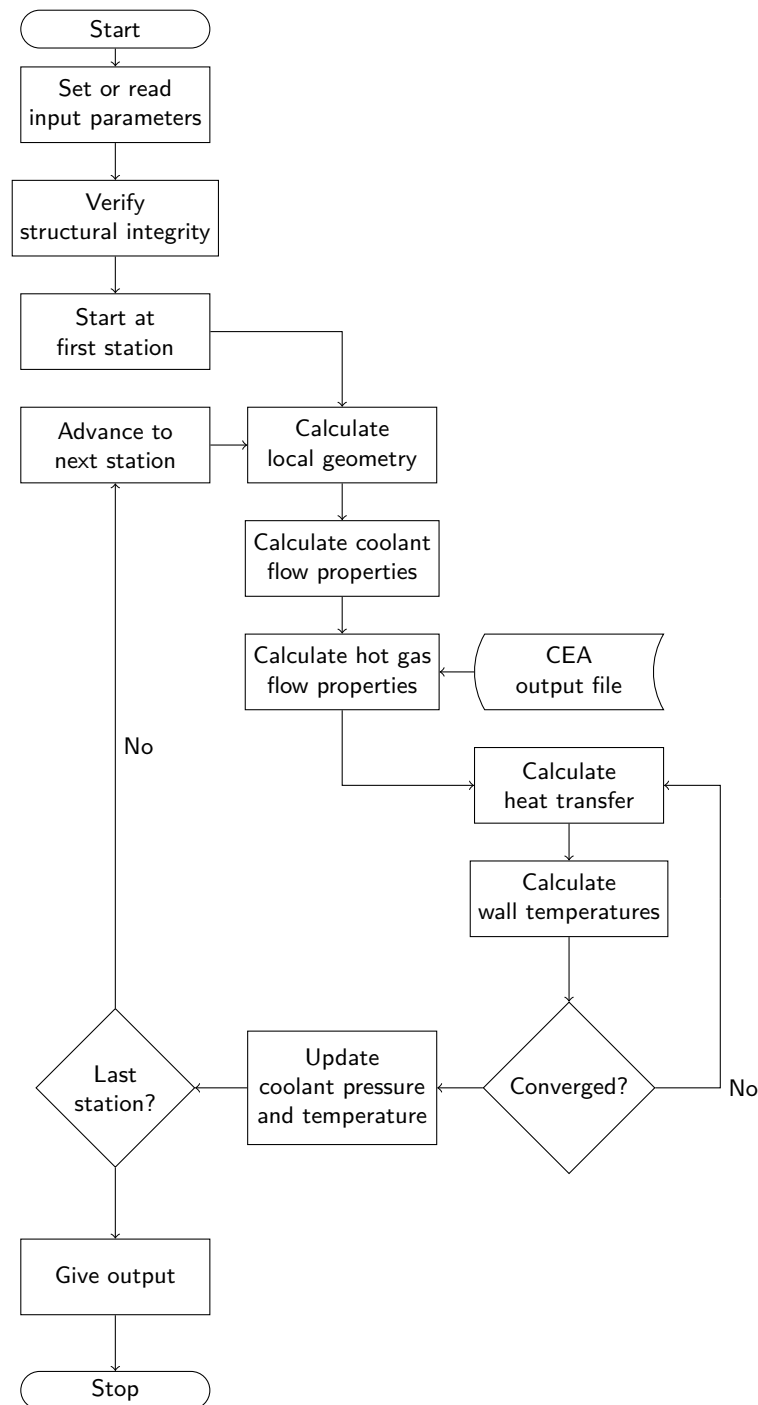


Figure 3.5: Flowchart of the One-dimensional Methane Engine Cooling Analysis (OMECA) program

### 3.2. VERIFICATION AND VALIDATION

After construction of the first order analysis program OMECA, verification and validation activities were carried out. First the implementation of all individual equations was verified. The verification of the coolant property model was already shown in chapter 2.

It is interesting to note that Pizzarelli et al. in 2011 reported a comparison of a 1D and a quasi-2D model to experimental values for the Vulcain engine. Their one-dimensional model is similar to the one reported in this chapter and leads to a maximum wall temperature of 1300 K for the Vulcain [29].

The real maximum wall temperature is somewhat below 800 K [29]. Thus, it would not be surprising if we find that the one-dimensional model implemented here also overestimates the wall temperature.

It would have been favourable to compare the results of the model to experimental data from an oxygen/methane rocket engine test campaign. Because no methane-fuelled rocket engine has been developed to fly on an orbital launcher yet, there is scant test data on such engines. On top of this, a test campaign is usually limited in the amount of variables that can be measured. A simulation can keep track of many variables, allowing to compare the newly developed model in more detail. Therefore, the model was compared to a more sophisticated analysis of an oxygen/methane rocket engine to validate it.

The analysis of an oxygen/methane demonstrator engine by Pizzarelli et al. was selected as validation case [63]. This demonstrator engine is developed by CIRA in the frame of the Hyprob program. The combustion chamber conditions are an engine pressure of 56 bar and mixture ratio of 3.35. The reference analysis was performed with a 3D conjugate heat transfer model for the chamber and cooling channel, coupled with a 3D CFD solver for the hot gases.

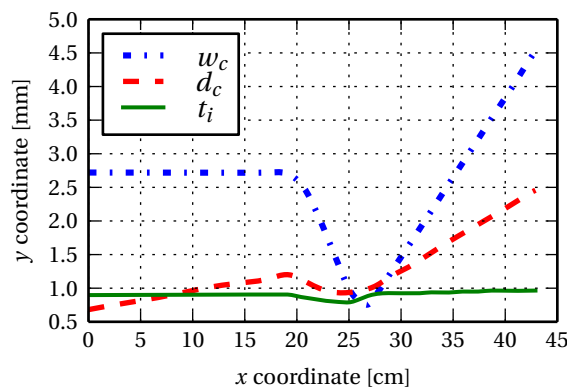


Figure 3.6: Cooling channel geometry of Hyprob rocket engine [63]

The nozzle and cooling channel geometry were determined from [63] using a curve digitizer program. Figure 3.6 shows the geometric parameters of the cooling channel obtained in this way. The nozzle contour was extracted in a similar matter from the figures in [63] as well as in [79]. The nozzle coordinates found were not accurate enough to determine the radius of curvature of the different parts of the nozzle, so the Nusselt number correction for curvature was disabled for all analyses of the Hyprob engine.

A flow of 20 g/s through each of the 96 cooling channels was prescribed, with an inlet pressure of 155 bar and inlet temperature of 110 K. Ruan's Bishop correlation was used to calculate the Nusselt number, because a large part of the flow was at supercritical temperatures. The input values are summarised in table 3.2.

Table 3.2: Input parameters for analysis of Hyprob engine

Input parameter	Value	Unit
Number of channels	96	-
Fuel flow	1.92	kg/s
Wall conductivity	365	W/m·K
Wall roughness height	0	μm
Coolant inlet pressure	150	bar
Coolant inlet temperature	110	K
Combustion pressure (CEA input)	56	bar
Mixture ratio (CEA input)	3.5	-

Figure 3.7 shows the wall temperature and heat flux that are obtained from the first order analysis, as well as the results of the reference analysis [63].

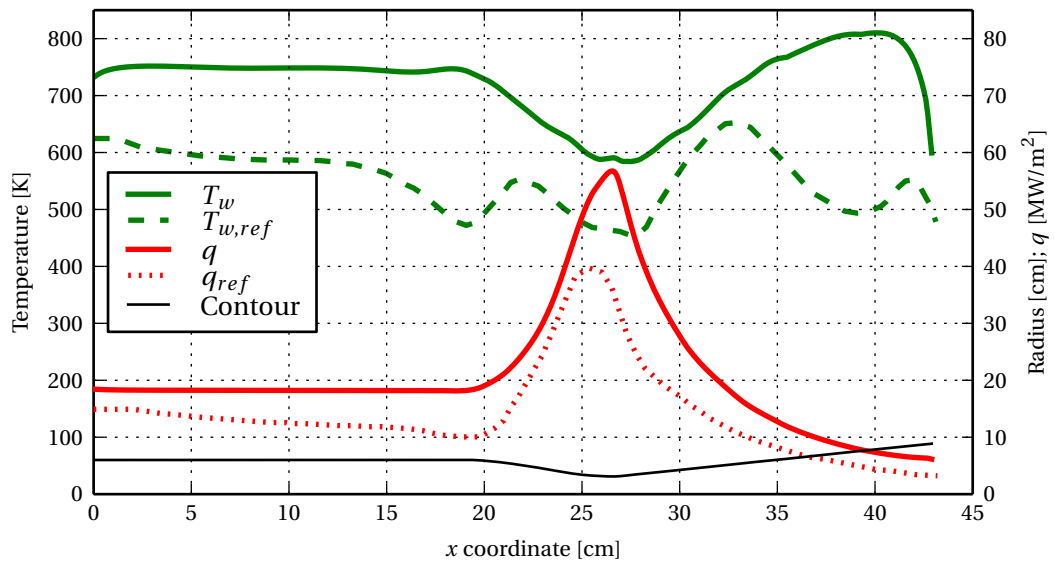


Figure 3.7: Wall temperature and heat flux along Hyprob nozzle, OMECA and reference calculations [63]

A comparison of both figures shows that the maximum heat flux is overestimated. The highest heat flux found from the 1D model is nearly  $57 \text{ MW/m}^2$ , while the 3D model predicts a heat flux around  $40 \text{ MW/m}^2$ . Both heat flux profiles look relatively similar, with an almost constant heat flux in the chamber, a peak at the throat and a decreasing flux along the nozzle.

The maximum wall temperature of 810 K, is substantially higher than the 650 K from the 3D analysis. On average, the wall temperature seems to be approximately 100 K higher. In addition, there are differences in the profile of the wall temperature along the nozzle. Both analyses show a distinct temperature minimum at the throat. The reference analysis also has two local minima on either side. Pizzarelli et al. attribute these peaks and valleys to the cooling channel geometry of this specific engine [63]. OMECA does not replicate the local minima and maxima. In the right part of fig. 3.7 there is a local maximum of the wall temperature predicted by the first order analysis, coinciding with a local minimum of the reference analysis.

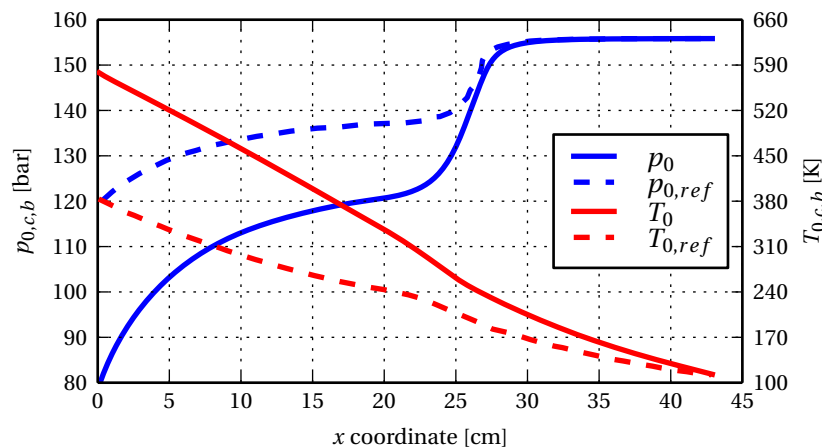


Figure 3.8: Bulk coolant pressure and temperature along Hyprob nozzle, OMECA and reference calculations [63]

Figure 3.8 shows the evaluation of the thermodynamic state of the coolant flowing through the channels. The coolant is flowing in a "counterflow" orientation, opposite of the direction of the combustion gases. It starts with a high pressure and low temperature at the end of the nozzle, heating up and losing pressure while moving towards the combustion chamber.

Figure 3.8 also displays the same variables as obtained by Pizzarelli et al. The trends of both figures are very similar. The total coolant pressure remains almost constant along the diverging part of the nozzle, because of the low coolant velocity (due to the high coolant density) and low heat flux. Then there is a sharp drop in total pressure associated with the maximum heat flux near the throat and the narrowing of the cooling channels. After this steep decrease, the pressure curve flattens out somewhat, but its slope gradually increases again towards the end of the channel. This increase corresponds to the narrowing of the cooling channel. Although the trend is very similar, the absolute value of the pressure drop is 76.4 bar, as opposed to 35.7 bar for the coupled 3D analysis.

When comparing the coolant temperature profiles, the trends are again relatively similar while the absolute values disagree. The temperature increases relatively constantly, with only a modest increase in steepness near location of maximum heat flux. The total temperature increase is 409 K, while the analysis of Pizzarelli et al. predicts only an increase of 271 K.

The main discrepancy of the OMECA results with respect to the 3D coupled analysis is the higher heat flux of the former. This high heat flux leads to an increased pressure drop and coolant temperature gain. Section 5.3.2 discussed the validity of the Bartz equation for heat transfer prediction of methane engines. It showed that for the demonstrator engine, the convective heat flux predicted by the Bartz equation alone was higher than the experimental heat flux. In the current model, not only was the Bartz equation used, a radiative heat flux was also implemented.

In other words, the heat flux is severely overpredicted. As the temperature increase is approximately two thirds higher than one predicted by Pizzarelli et al, this should also be about the magnitude of the heat flux overestimate (ignoring for a moment the variations in heat capacity of the coolant).

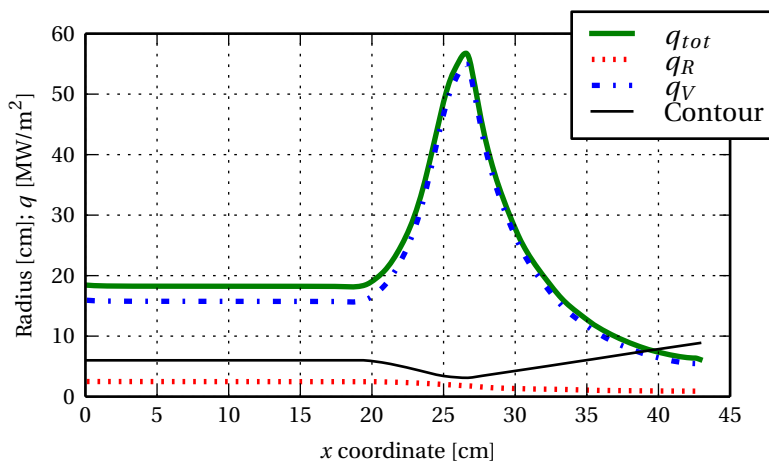


Figure 3.9: Convective, radiative and total heat flux for OMECA analysis of Hyprob nozzle

Figure 3.9 shows the predicted heat flux along the nozzle, divided into the convective and radiative heat fluxes. The integrated radiative heat flux is 0.3 MW, while the convective heat flux is 2.7 MW, summing to 3 MW for the complete engine. This means radiation accounts for approximately 10% of the heat flux, but fig. 3.9 illustrates that this percentage is not constant. At the throat, the radiative heat flux is only 3% of the full heat flux, while in the combustion chamber it accounts for 12%.

To remedy the large discrepancies in heat flux, the heat flux calculation was modified in the program. The Bartz equation overpredicted peak experimental heat flux measurements in an oxygen/methane engines by approximately 25% [68], see section 5.3.2. Therefore, the empirical coefficient in the Bartz equation was decreased by 25% from 0.026 to 0.0195. The original work of Bartz already noted that this coefficient was empirical, not theoretical [67].

Figure 3.10 shows the result of the first order analysis after this heat flux calibration. The maximum wall temperature is now 662 K, compared to 650 K for the coupled 3D simulation. The location of maximum wall temperature is completely different, however. The wall temperature profile is similar to the one obtained previously.

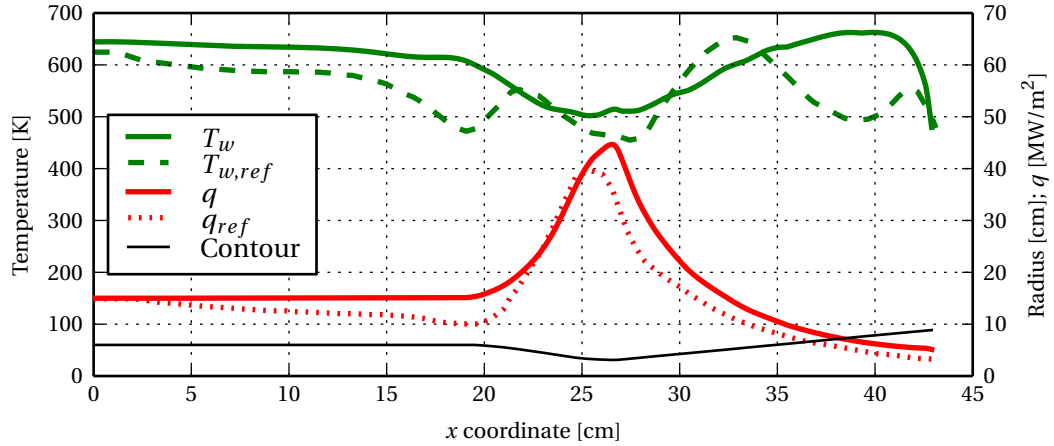


Figure 3.10: Wall temperature and heat flux for Hyprob engine, calculated with OMECA (including heat flux modification) and reference calculations [63]

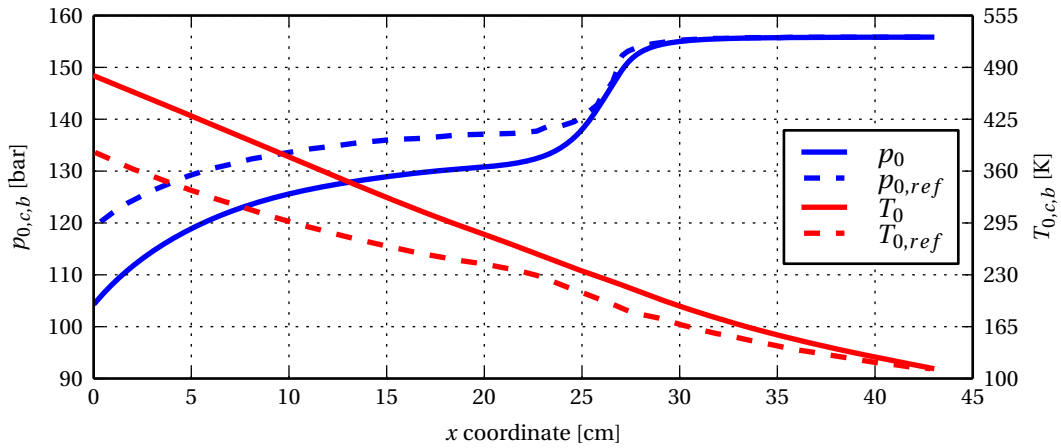


Figure 3.11: Bulk coolant pressure and temperature for Hyprob engine, calculated with OMECA (including heat flux modification) and reference calculations [63]

Figure 3.11 shows the coolant state along the channel. The pressure drop is 51 bar, as opposed to 35.7 in the reference analysis. The coolant temperature increased by 352 K along the channel, 81 K more than in the reference case. This difference indicates that the integrated heat flux from the model is still higher than the one predicted by the analysis of Pizzarelli et al. This seems reasonable, given that the area under the heat flux curve in fig. 3.10 is also larger than for the reference heat flux. Here it is important that Pizzarelli et al. neglected radiative heat transfer from the hot combustion gases to the wall.

It would be possible to further decrease the coefficient in the Bartz equation or to lower the heat flux otherwise. However, there is no experimental basis for this. Instead the coolant side will be investigated in isolation. This can be done by enforcing the hot gas side convective coefficient and adiabatic wall temperature that were found by Pizzarelli et al. The radiation module will be turned off. Doing so will result in obtaining almost the exact same heat flux. In this way, the discrepancies in the coolant channel can be examined in more detail.

The three different Nusselt number correlations were used to calculate the Nusselt number in the cooling channels. Figure 3.12 shows the resulting wall temperature profiles. It is clear that the heat flux is indeed very close to the reference heat flux. In general, the Taylor equation results in a wall temperature that is closest to the reference analysis, closely followed by Ruan's Bishop correlation. The two results are almost indistinguishable before the throat and then diverge somewhat. The Dittus-Boelter (D-B) correlation predicts a much lower wall temperature. For further calculations of the model in this

chapter, the Taylor equation will be used.

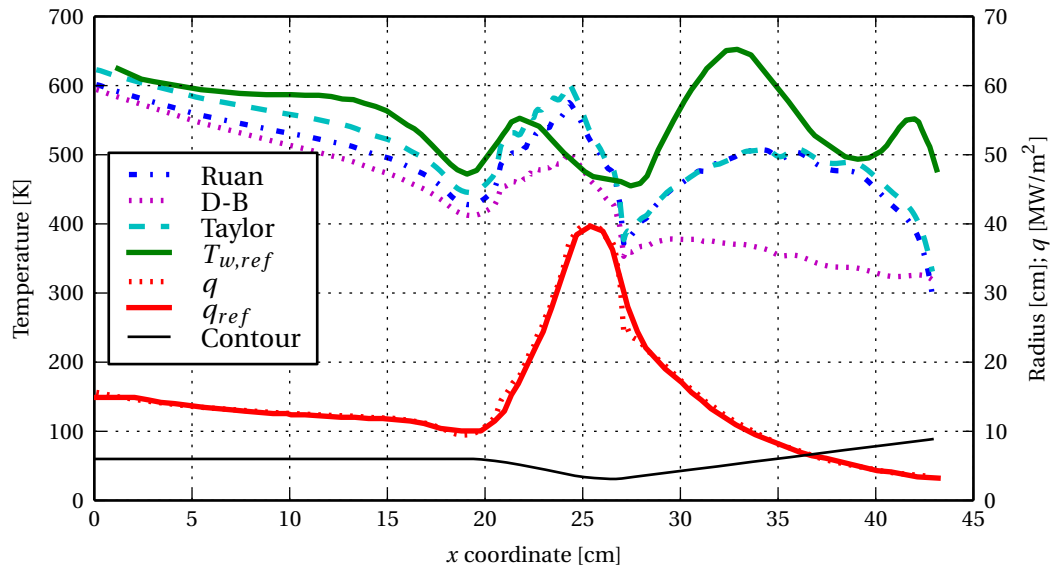


Figure 3.12: Hyprob engine wall temperatures for different Nusselt number correlations. Adiabatic wall temperature and hot gas convective coefficient are taken from reference analysis [63].

Even the Taylor equation overpredicts the wall temperature by 108 K just upstream of the throat, while underestimating the wall temperature by more than 170 K at one point along the diverging nozzle. An underestimate of such magnitude is unacceptable when designing a rocket engine. For example, at 500 K Al-7075 T6 retains 70% of its room temperature yield strength and 40% of its ultimate strength. At a temperature of 670 K, on the other hand, less than 30% of its yield and less than 18% of its ultimate strength would remain. Such a difference between expected and actual strength could easily lead to compromise of the rocket engine’s structural integrity.

The Nusselt number correlations cannot accurately predict the coolant-side heat transfer. Even when the same hot gas side parameters are enforced as in the reference analysis, errors of more than 150 K in the wall temperature are present. This confirms the need for a more accurate, higher-order analysis of the coolant channel to predict the convective coefficient.

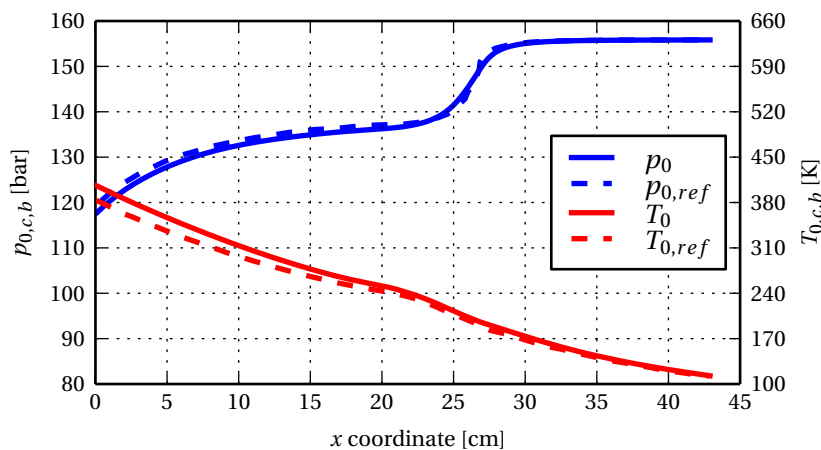


Figure 3.13: Coolant state along cooling channel for Hyprob rocket engine. Adiabatic wall temperature and hot gas convective coefficient are taken from reference analysis [63]. OMECA and reference calculations [63]

Figure 3.13 shows a comparison of the temperature rise and pressure drop along the channel for the Hyprob rocket engine with hot gas parameters taken from the reference analysis. It is clear that with

a correct heat flux, the pressure drop and temperature gain of the coolant are predicted accurately: the pressure drop is 37.9 bar, as opposed to 35.7 bar in the reference analysis. The temperature gain is calculated to be 284 K, only 13 K higher than predicted by Pizzarelli et al. This shows that pressure drop and temperature gain are calculated to an error smaller than 10%, provided that the incoming heat flux is correct.

In summary, we can conclude that OMECA overestimates the heat flux because the Bartz equation overestimates the heat flux for oxygen/methane engines. A calibration of Bartz by changing the coefficient to 0.0195 gives better results. More detailed methods (e.g. combustion CFD) for the analysis of the hot gas side heat transfer would be able to give more accurate heat fluxes.

When prescribing a heat flux equal to the reference, the performance of OMECA for cooling channel analysis can be analysed in isolation from the hot gas side. In this case, the wall temperature accuracy is approximately 150 K. This is insufficient for design purposes, for which OMECA is therefore unsuited. In section 5.4, this accuracy is compared to the accuracy of a detailed CFD tool and the effects of accuracy on design are investigated.

When the correct heat flux is prescribed, the total temperature gain of the coolant can be predicted accurately. The same holds for the pressure drop obtained with a certain cooling channel geometry. Both values can be predicted to within 10%.

These conclusions indicate that the first order tool OMECA is useful to perform parametric studies and investigate the sensitivity to different design parameters. In addition, the design space for a specific engine can be explored. For detailed design of regenerative cooling channels, however, more accurate tools will be required.

### 3.3. PARAMETRIC ANALYSIS

Despite the relative inaccuracy of the first order method presented in this chapter, it is very useful for a qualitative analysis. In the current section, a generic 10 kN oxygen/methane rocket engine will be analysed with OMECA. Then a parametric analysis will be performed to find out the effect of different design parameters on the cooling system. This will reveal what parameters are most important during the design of the cooling system.

#### 3.3.1. GENERIC 10 kN ENGINE

The generic engine contour and design parameters were created by the Delft Aerospace Rocket Engineering (DARE) student group and are not part of this thesis. The design was simply used as a generic engine to study in the parametric analysis.

The engine would generate a thrust of 10 kN at mixture ratio of 3.16, resulting in a specific impulse of 321 seconds and a mass flow of 3.176 kg/s. This in turn means that a methane mass flow of 0.76 kg/s is available to cool the engine.

Thrust chamber dimensions were generated for this baseline design by DARE students. Figure 3.14 shows these dimensions. They were computer-generated, so an accurate set of coordinates was available.

It was then attempted to create a baseline regenerative cooling channel layout using OMECA. 72 channels were chosen with rib thickness  $t_r$ , channel depth  $d_c$  and chamber thickness  $t_i$  all constant and equal to 1 mm. Channel roughness was set to  $6 \mu\text{m}$  and chamber conductivity to  $365 \text{ W/m}\cdot\text{K}$ , representative of copper. Coolant inlet pressure and temperature were set to 60 bar and 110 K. The inputs to OMECA are summarised in table 3.3.

Figure 3.15 displays the resultant heat flux and wall temperature along the thrust chamber. There are two main things to be noticed: the large decrease in wall temperature near the throat and the temperature increase at the converging part of the nozzle. The latter is due Nusselt number decrease associated with a concave bend in the cooling channel. The sharp temperature drop at the throat is due to a combination of two reasons. First the increased Reynolds number near the throat due to a

Table 3.3: Input parameters for analysis of generic engine

Input parameter	Value	Unit
Number of channels	72	-
Rib thickness	1	mm
Wall thickness	1	mm
Channel height	1	mm
Fuel flow	0.76	kg/s
Wall conductivity	365	W/m·K
Wall roughness height	6	μm
Coolant inlet pressure	60	bar
Coolant inlet temperature	110	K
Combustion pressure (CEA input)	40	bar
Mixture ratio (CEA input)	3.16	-

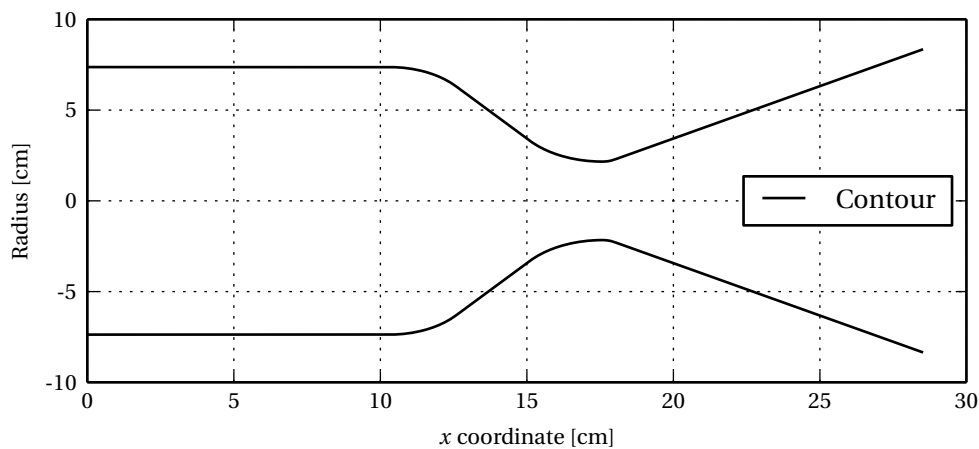


Figure 3.14: Contour of the generic rocket engine (contour created by Ralph Huijsman, DARE)

narrowing of the cooling channels. However, fig. 3.16 shows that the Nusselt number has a sharper spike than the Reynolds number. The reason for this is the increase in the Prandtl number near the pseudo-critical temperature. The local peak in specific heat near this temperature causes an increase in Prandtl number, affecting the Nusselt number as well.

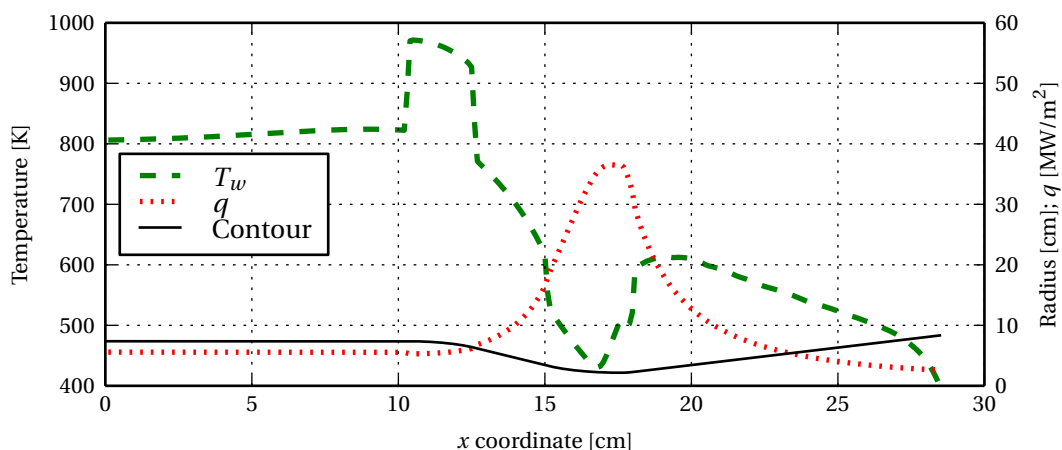


Figure 3.15: Generic engine heat flux and wall temperature along nozzle

From fig. 3.17, it is clear that the temperature of the coolant is indeed around the pseudo-critical temperature near the throat. The total temperature gain is 295 K, while the pressure drop is 5.9 bar. This

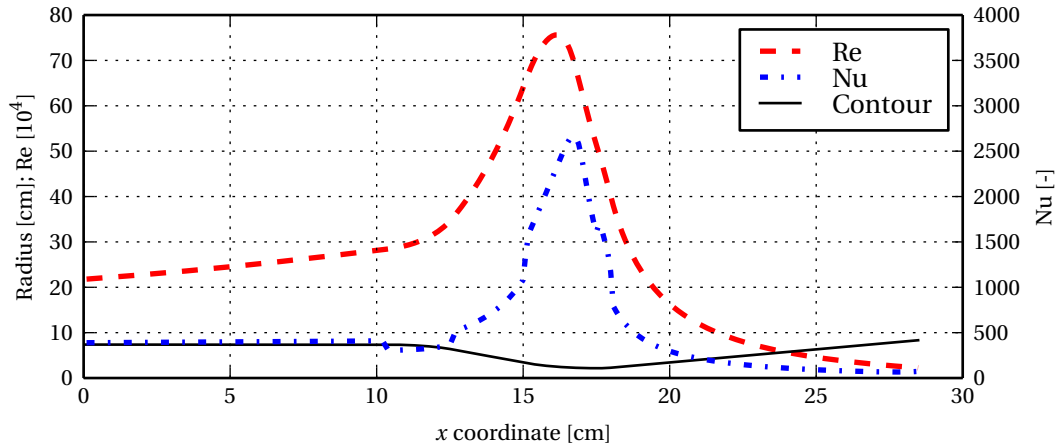


Figure 3.16: Generic engine Reynolds number and Nusselt number in coolant channel along nozzle

pressure drop is almost an order of magnitude smaller than the drop in the Hyprob coolant channel. The difference is caused by the difference in length of the channel, as well as the slightly wider channel of the generic engine.

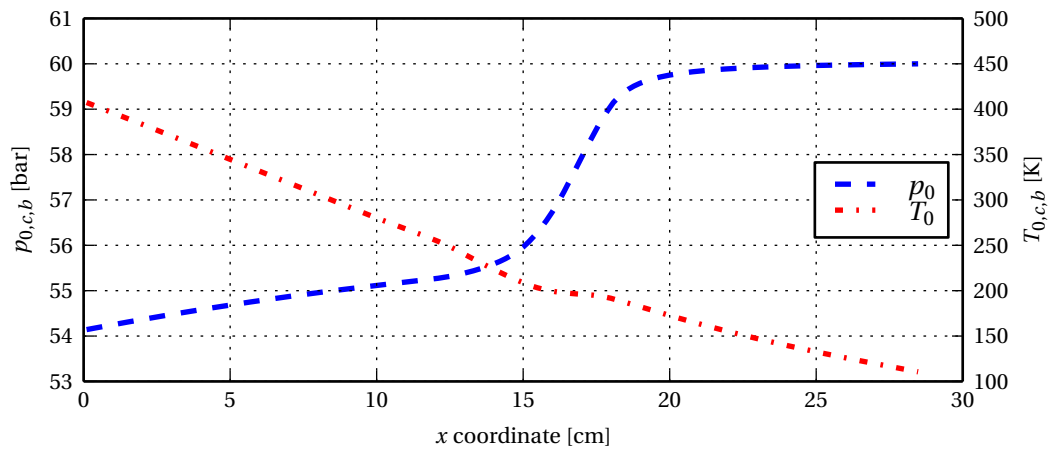


Figure 3.17: Total pressure and total temperature in coolant channel of generic engine

### 3.3.2. EFFECT OF NUMBER OF STATIONS

To study the influence of the nozzle discretization, an analysis was also carried out with only half the number of stations along the nozzle (one station every two mm instead of one per mm or 142 stations instead of 285). Halving the number of stations led to 0.03% decrease in maximum wall temperature, 0.25% decrease in coolant temperature rise and 0.32% increase in pressure drop. Clearly, the nominal number of stations is sufficient to obtain a result that is almost independent on the discretization. The discretization error is much smaller than the other errors in the model.

### 3.3.3. EFFECT OF NUSSOLT NUMBER CORRELATIONS

For the generic 10 kN engine, the effect of using different Nusselt number correlations was investigated again. The wall temperature resulting from the three correlations is shown in fig. 3.18. The differences are even larger than in the validation case. The maximum difference is in the diverging part of the nozzle, where Ruan's Bishop correlation leads to a wall temperature 415 K higher than the Dittus-Boelter correlation predicts. This finding drives home the point that more accurate analysis of the heat transfer to the coolant is necessary.

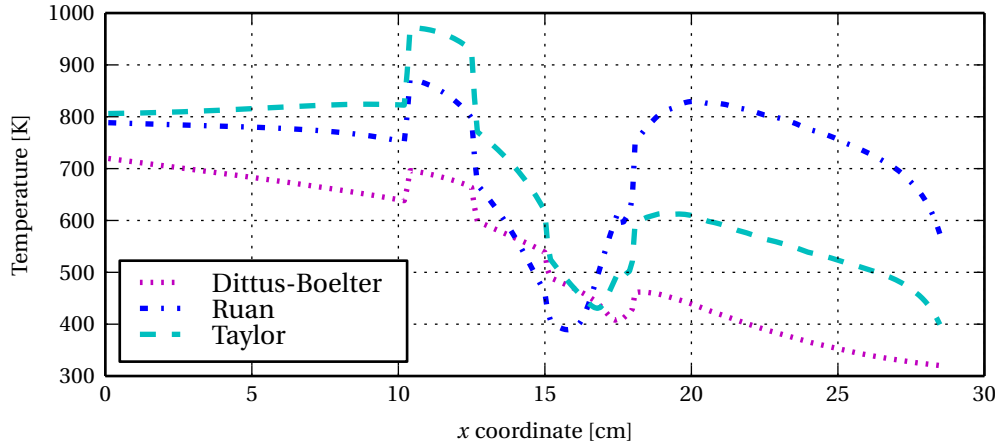


Figure 3.18: Wall temperature along thrust chamber of generic engine with different Nusselt number correlations

### 3.3.4. EFFECT OF THERMAL CONDUCTIVITY

One of the main purposes of this thesis was to investigate the viability of aluminium as a thrust chamber material. Aluminium has a lower thermal conductivity than the high temperature copper alloys commonly used. The analysis was carried out for the baseline engine, varying the thermal conductivity of the material for each calculation with increments of 10 W/m·K.

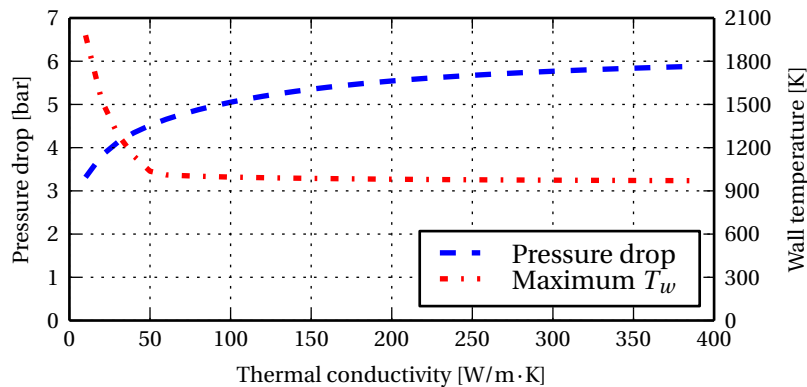


Figure 3.19: Variation of pressure drop and maximum wall temperature with thrust chamber thermal conductivity

Figure 3.19 shows the result of these calculations. The thermal conductivity has very little influence on the maximum wall temperature as long as it remains above 50 W/m·K. As it goes below that value, the wall temperature rises exponentially. We can explain this by interpreting the one-dimensional heat flow from eq. 3.2 (reprinted here for convenience) as a resistance equation. The three terms in the denominator are all thermal resistances – two for convective heating and one for conductive heating. As long as the thermal conductivity is higher than 50 W/m·K, the other terms dominate the heat flow. If the conductivity becomes lower than this threshold value, the thermal resistance of the chamber material is so high that the chamber starts functioning as an insulation. This leads to a sharp increase in hot gas side wall temperature.

$$q = \frac{T_{aw} - T_{c,b} + \frac{q_{R,h}}{\alpha_h}}{\frac{1}{\alpha_h} + \frac{t}{\kappa} + \frac{1}{\alpha_c}} \quad (3.2)$$

The pressure drop rises relatively smoothly with increasing thermal conductivity. This again can be explained with the use of eq. 3.2. As the thermal conductivity increases, the denominator becomes smaller, thereby increasing the heat flux from the hot gas to the coolant. This increased heat flux leads to higher temperatures of the coolant. The hot methane has a lower density and will flow faster,

leading to a net increase in pressure drop.

The reason why the wall temperature increases so sharply is that it only depends on the thermal equilibrium at a single location. If the thermal conductivity reaches a threshold value there, it will be the dominant factor that determines the wall temperature. The pressure drop, on the other hand, is a more global value that depends on the thermal equilibrium at all locations. Because the threshold value is not reached at all thrust chamber stations for the same thermal conductivity, the increase in pressure drop with thermal conductivity is more smooth.

The thermal conductivity of aluminium is around  $130 \text{ W/m}\cdot\text{K}$ . For high temperature copper alloys this value is higher with for example  $295 \text{ W/m}\cdot\text{K}$  for NARloy-Z. Figure 3.19 shows that the lower thermal conductivity of aluminium is not a cause for concern, if the wall thickness remains 1 mm. However, if thicker walls are used, the quotient of thickness and thermal conductivity may reach the threshold value. At 1 mm thickness, the threshold conductivity is around  $50 \text{ W/m}\cdot\text{K}$ , indicating a threshold quotient of  $2 \cdot 10^{-5} \text{ m}^2 \cdot \text{K/W}$ .

With this threshold quotient of thickness and thermal conductivity we can calculate corresponding maximum acceptable wall thicknesses for both materials. These are 5.9 mm for NARloy-Z and 2.6 mm for aluminium. We can conclude that for thin walls, the difference in thermal conductivity between aluminium and copper will not be important, but the maximum thickness is more restricted for a material with low thermal conductivity.

### 3.3.5. EFFECT OF NUMBER OF CHANNELS

The influence of the number of channels on the baseline engine was investigated. The rib thickness was kept constant, so if the number of channels is increased, the width of the channels decreased. For these calculations, the coolant input pressure was set to 100 bar instead of 60 bar, to avoid the coolant pressure dropping below the critical pressure for some calculations. Figure 3.20 shows the pressure drop and maximum wall temperature of the engine for a different number of channels.

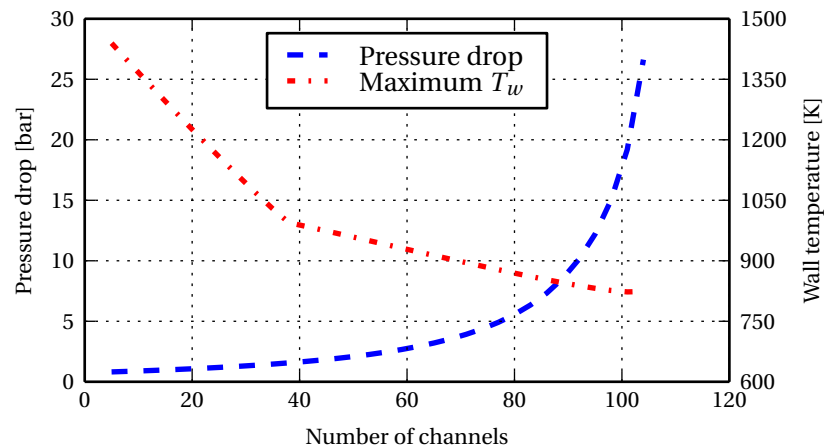


Figure 3.20: Variation of pressure drop and maximum wall temperature with number of cooling channels

As the number of channels increases, they become more narrow. This leads to higher flow rates, more convection and lower wall temperatures. However, high flow velocity and small hydraulic diameter also lead to a high pressure drop along the channel. The slope change in the temperature line around 40 channels is due to a shift in the location of maximum temperature. If the number of channels is small, this location is slightly downstream of the throat. If the number is larger than 40, the maximum wall temperature occurs at the converging part of the nozzle.

If the number of channels is above 80, the pressure drop rapidly increases with only a modest change in wall temperature. With 80 channels, the minimum channel width is approximately 0.7 mm for a depth of 1 mm. This means the channel has an aspect ratio of 1.43 at the throat. Increasing the number of channels to 100, the aspect ratio becomes 2.8 and the pressure drop along the channel

multiplies by four. This shows the strong dependence of pressure drop on cooling channel geometry. We will now examine the effect of channel depth, another geometric parameter.

### 3.3.6. EFFECT OF CHANNEL DEPTH

The channel depth affects the flow velocity of the methane in the channels. It was varied between 0.5 mm and 2 mm in increments of 0.1 mm. The coolant inlet pressure was set to 120 bar to avoid dropping below the critical pressure.

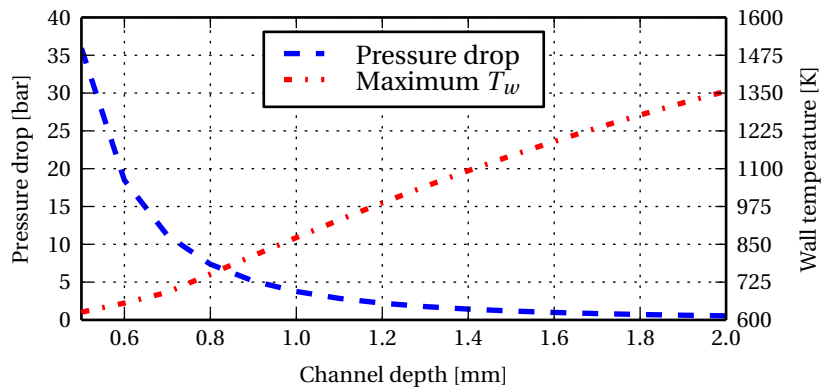


Figure 3.21: Variation of pressure drop and maximum wall temperature with number of cooling channels

Figure 3.21 shows again how strongly the cooling performance varies with the geometry of the cooling channels. Increasing the channel depth from 0.5 mm to 0.6 mm almost halves the pressure drop (from 35.9 bar to 18.5 bar). The temperature increases steadily when making the channels higher.

From fig. 3.21 and fig. 3.20, it is clear that making the channels smaller than strictly necessary carries a heavy penalty in terms of pressure drop. To minimize the pressure drop, one should strive for the maximum channel size that still maintains the wall temperature in the allowable temperature range.

Both the number of channels and the channel depth have an influence on the channel geometry. In the design of an engine, an optimum combination that minimizes the pressure drop should be chosen. Furthermore, the channel depth need not be constant. Once the number of channels is chosen, the depth can be varied along the nozzle. The depth should be chosen such that the wall temperature is close to the maximum allowable temperature (minus a design margin). In this way, the total pressure drop in the channel is minimal.

Furthermore, both fig. 3.20 and fig. 3.21 show that the cooling performance depends dramatically on channel geometry. A difference in only 0.1 mm can have a very large influence on the wall temperature. This means that tight tolerances will be required when producing a thrust chamber.

### 3.3.7. EFFECT OF CHANNEL ROUGHNESS

The channel roughness has an influence on the friction factor and thus on the pressure drop. Roughness also has an influence on the heat transfer through eq. 3.18. The pressure drop and maximum wall temperature were calculated for an engine with smooth channels and then with roughness increments of 1  $\mu\text{m}$ .

Figure 3.22 shows the expected trend of decreasing wall temperature with increasing roughness, as well as increasing pressure drop. Going from a smooth channel to a roughness of 6  $\mu\text{m}$  (the nominal value), the pressure drop increases by approximately 130%, while the maximum wall temperature drops by 300 K. These differences are of comparable magnitude to those found by Pizzarelli et al. when analysing the Hyprob engine [63].

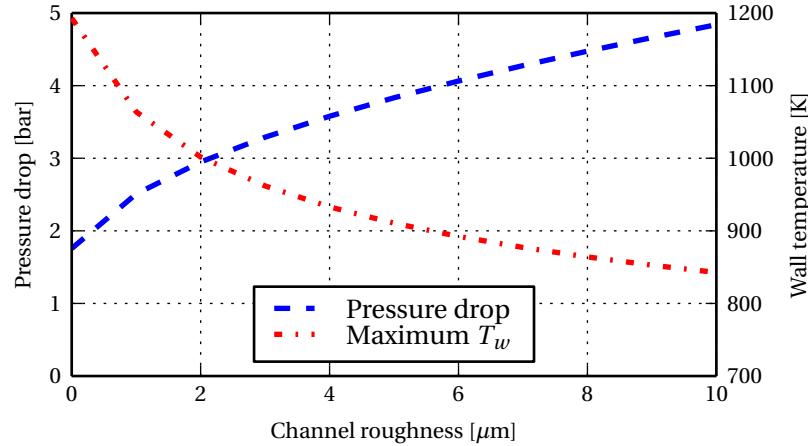


Figure 3.22: Variation of pressure drop and maximum wall temperature with roughness of cooling channels

### 3.3.8. EFFECT OF COOLANT INLET PRESSURE

The methane inlet pressure was varied from 55 bar to 123 bar to investigate its effect on the cooling qualities. Figure 3.23 shows that methane is a somewhat better coolant at elevated pressures, leading to a lower wall temperature and smaller pressure drop.

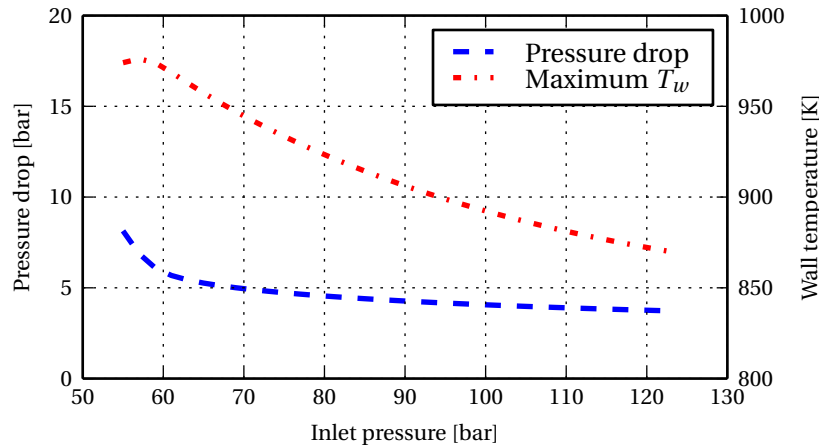


Figure 3.23: Variation of pressure drop and maximum wall temperature with coolant inlet pressure

Since the geometry is equal for all cases, the variation of the fluid properties of methane with pressure is the likely cause for the observed differences in pressure drop and wall temperature. To further investigate this effect, a comparison was made between two cases: coolant at 60 bar inlet pressure and at 120 bar inlet pressure. Figure 3.24 shows the resulting wall temperature profile.

There are clear temperature differences between the two cases, but they are not uniform. Near the throat, the lower pressure coolant leads to a lower wall temperature. In the converging section of the nozzle, the opposite happens: the lower pressure coolant leads to a higher wall temperature.

Equation 3.25 shows how the coolant convective coefficient depends on the fluid properties. It turns out that the temperature difference at the throat can be explained mostly by the higher  $c_p$  at low pressure. The low pressure coolant is closer to the critical point, leading to a sharp peak in  $c_p$  at the pseudo-critical temperature. At higher pressure, this  $c_p$  increase is much less pronounced, leading to a higher wall temperature near the throat.

$$\alpha_c \sim Nu \cdot \kappa \sim Re^{0.8} Pr^{0.4} \kappa \sim \mu^{-0.4} c_p^{0.4} \kappa^{0.6} \quad (3.25)$$

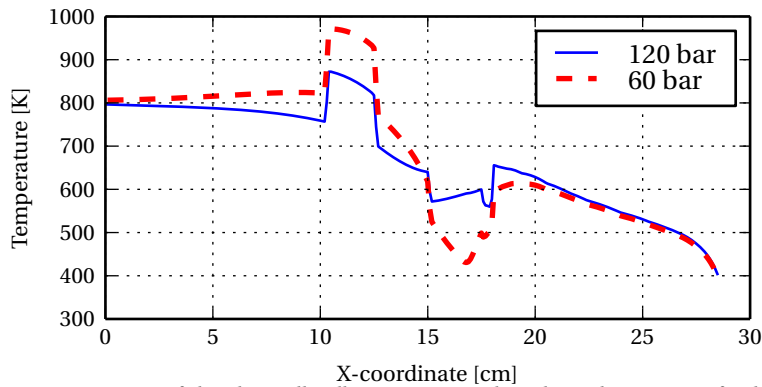


Figure 3.24: Comparison of chamber wall wall temperature with coolant inlet pressure of 60 bar and 120 bar

The difference in the converging section of the nozzle, between 10 and 12 cm from the inlet, is caused by a different phenomenon altogether. The high pressure coolant has a higher thermal conductivity, leading to enhanced convective cooling. Thus, the higher pressure coolant leads to a lower temperature wall at this location. As this is the location of maximum wall temperature, the effect shown in fig. 3.23 is due to this phenomenon.

The increased pressure drop at low pressure is mostly due to the higher convective coefficient at the throat. Because of the narrow channels at this location, an increase in heat flux rapidly leads to a higher pressure drop.

The differences observed due to a change in inlet pressure clearly demonstrate the importance of an accurate thermophysical model of methane. The changes in viscosity, thermal conductivity and specific heat have a strong impact on the cooling performance of methane. The intended chamber pressure of 40 bar for the generic 10 kN implies that the coolant pressure will be relatively close to the critical pressure. The strong changes in thermodynamic properties at this pressure must be accounted for in the cooling analysis.

### 3.3.9. EFFECT OF ENGINE SIZE

The effect of changing the physical size of the engine was also investigated. A linear scaling parameter was defined and applied to the nozzle contour. The number of channels was also multiplied by this parameter to retain the same channel width for each engine.

The amount of coolant also varied with engine size. The propellant mass flow in a rocket engine is proportional to the throat area, so the amount of coolant varied with the square of the linear scaling parameter. Lastly, the height of the cooling channels also varied with engine size. In an attempt to obtain similar maximum wall temperatures, the channel height was multiplied by the scaling parameter to the power of 1.25 (found by trial and error).

Figure 3.25 shows the maximum wall temperature and pressure drop for the resulting rocket engines. The maximum wall temperature is similar for all sizes. For very small engines, the amount of fuel is so small that very narrow channels are needed to cool the engine, leading to a larger pressure drop. However, it is interesting to see that the pressure drop is almost independent of the engine size, as soon as some minimum size is reached.

### 3.3.10. EFFECT OF CHAMBER PRESSURE

Lastly, the effect of changing chamber pressure was investigated. Different CEA analyses were executed to find the combustion gas parameters for these cases. The coolant inlet pressure was set to 60 bar for 10, 20 and 40 bar chamber pressure. For the other cases, the coolant inlet pressure was set to 20 bar above the chamber pressure. Figure 3.26 shows the results; as expected the increased heat flux with high chamber pressure leads to much higher wall temperatures and increased pressure drops.

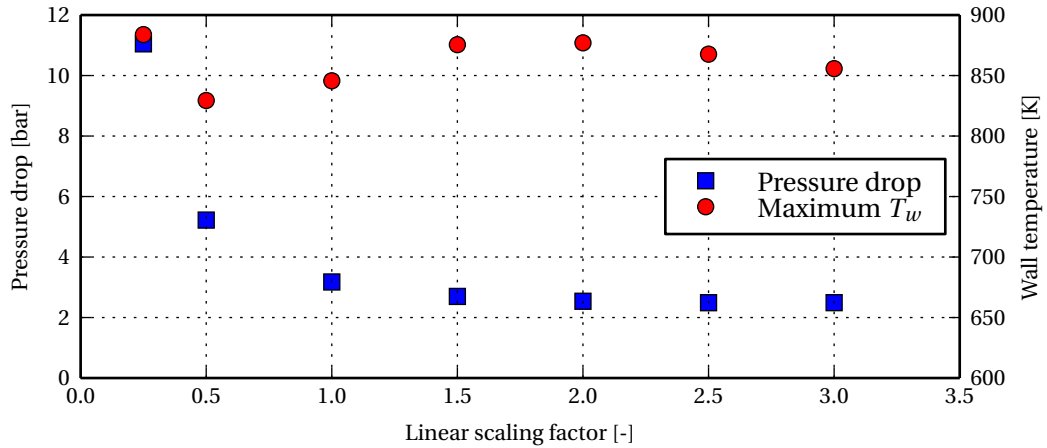


Figure 3.25: Variation of pressure drop and maximum wall temperature with physical size of the engine

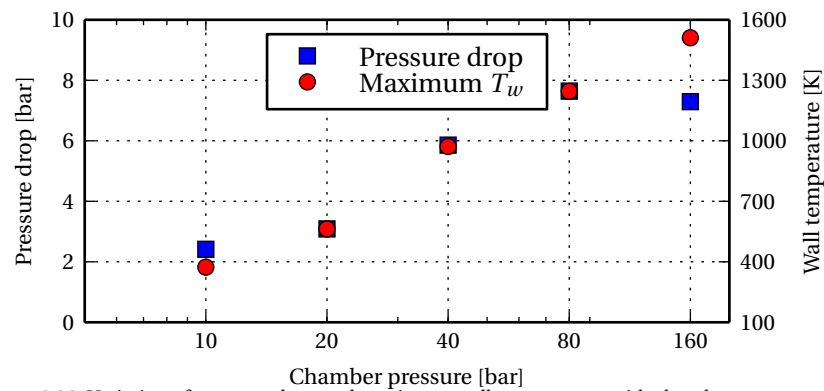


Figure 3.26: Variation of pressure drop and maximum wall temperature with chamber pressure

However, one should also take into account that the mass flow scales with chamber pressure. If the chamber pressure is higher, the engine can be made smaller or the propellant mass flow should be higher. In this case, the fuel flow was scaled with the chamber pressure. Simultaneously, the channel height was scaled with the square root of the chamber pressure; leading to a 0.5 mm height for 10 bar chamber pressure and 2 mm for a 160 bar chamber.

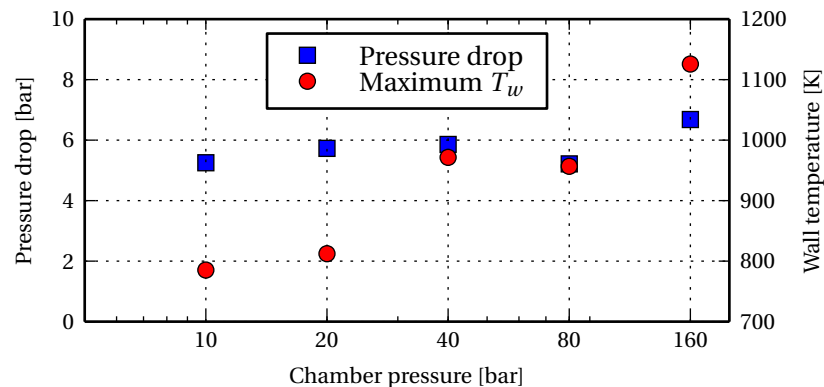


Figure 3.27: Variation of pressure drop and maximum wall temperature with chamber pressure, also changing fuel flow and channel height

In this case, fig. 3.27 shows that the differences in chamber pressure are substantially smaller. The increased heat flux due to higher chamber pressure is mitigated by the increased coolant flow rate, but it is not fully compensated.

This is an important result when considering testing of a rocket engine cooling system. One prefers to perform the initial tests at a condition where large margins are available. After verifying the successful operation at such conditions, one could proceed to testing at nominal conditions and even proceed to test the performance at extreme ones. In light of this, it is good to see that at low pressure, there will be a larger thermal margin even though the fuel flow is reduced. Thus, initial testing should be performed at low chamber pressure. Similarly, initial testing should be performed at low mixture ratio; this leads to lower flame temperatures and more fuel available as coolant.

### 3.3.11. SUMMARY OF PARAMETRIC ANALYSIS

In this section, a parametric analysis was carried out using the OMECA tool. A generic 10 kN engine was analysed with varying input parameters. Table 3.4 summarises the results. It shows the effect on pressure drop and maximum wall temperature of a 10% increase and decrease in one of the parameters.

Table 3.4: Summary of parametric analysis of generic engine

Change of Effect on	-10%		+10%	
	$\Delta p_0$	$T_w$	$\Delta p_0$	$T_w$
Wall conductivity	-0.79%	+0.14%	+0.66%	-0.12%
Number of channels	-21%	+2.3%	+31%	-2.3%
Channel depth	+37%	-6.9%	-24%	+6.7%
Wall roughness height	-3.3%	+1.2%	+3.2%	-1.1%
Coolant inlet pressure	+53%	+0.034%	-11%	-1.7%
Engine size	+2.7%	-1.2%	-5.2%	+1.2%

The effect of thermal conductivity is small compared to the other parameters as long as it remains above a threshold value. Increasing the number of channels has a similar effect on the pressure drop as decreasing the channel depth. However, the effect on wall temperature is approximately three times as large when changing the channel depth. This suggests that the latter is a good design variable.

The wall roughness height is even more advantageous in terms of trade-off between pressure drop and wall temperature. However, the effects do seem to level off according to fig. 3.22. Based on this first order analysis, it seems a good idea to have a high roughness height.

Lowering the coolant inlet pressure leads to a substantially higher pressure drop, while the wall temperature hardly changes. Apparently a coolant pressure close to the supercritical pressure is not advantageous. Combustion pressure has not been included in table 3.4 because its effects are clearly non-linear as evidenced in fig. 3.27.

With respect to engine size, the pressure drop goes down for a larger engine, while the maximum wall temperature rises. The ratio of pressure and temperature is similar to that of a roughness change. This suggests that it could be easier to cool a slightly smaller engine. However, fig. 3.25 also indicates that there is a limit to this down-scaling.

## 3.4. EXPLORING COOLING CHANNEL DESIGN

Armed with the knowledge gained in the past sections, an attempt will now be made to make a preliminary cooling system design for the generic 10 kN oxygen/methane engine. Two designs will be created: one using a traditional copper alloy and one using aluminium as chamber material.

The focus will be on creating a cooling channel geometry that is able to reduce the maximum wall temperature to the allowable temperature of the chamber material. A basic structural analysis will also be performed. Piping and manifold design, as well as detailed structural analysis are not included.

As mentioned earlier, the accuracy of OMECA does not allow to use it for proper design of the cooling channel geometry. Therefore, it can merely be used for an exploration of the design space and the creation of a first attempt at a design. The resulting cooling channel geometry can then be analysed

using a more sophisticated, accurate but also time-consuming method. This will be done in chapter 6.

### 3.4.1. REQUIREMENTS

Table 3.5 shows the combustion chamber requirements that are relevant to the cooling. In reality, there would also be requirements relating to the nozzle efficiency etc, but they are not relevant to the cooling design at this point.

Requirements CC-2 and CS-3 are related to the structural design of the engine; CC-1, CC-4 and CS-5 relate to the cooling channel design. Note that requirements CC-2 and CC-5 still contain TBC values because they must be verified at the end of the design cycle. CC-3 contains a TBD value, because the inlet coolant pressure is not known at this point.

The combustion chamber mass, pressure drop and cost are not indicated here because they relate to system-level decisions that have not been made yet. Obviously these parameters must be taken into account, but the current purpose is to explore the design space. That means we will try to find out what kind of pressure drops and chamber mass values are necessary to meet the requirements in table 3.5. In addition, we want to compare these results for two chamber materials; aluminium and copper.

Table 3.5: Combustion chamber requirements

Identifier	Requirement	Rationale
CC-1	The thrust chamber shall be regeneratively cooled	
CC-2	The thrust chamber shall be able to withstand chamber pressure of 60 bar (TBC).	Safety factor of 1.5
CC-3	The thrust chamber shall be able to withstand coolant pressure of TBD bar.	Hoop stress in tubes or external pressure on inner wall
CC-4	The hot gas side chamber wall temperature shall not exceed the chamber material's allowable temperature	
CC-5	Coolant channel exit pressure shall be at least 50 bar (TBC).	Chamber pressure plus injector pressure drop

Requirements such as CC-4 can be reformulated to include a temperature value only when the wall material is chosen. For different chamber materials, the allowable wall temperature will be different.

### 3.4.2. COPPER CHAMBER DESIGN

As reference material the NARloy-Z copper alloy was selected. This high temperature copper-silver-zirconium alloy was used as chamber material for the Space Shuttle Main Engine. Its maximum allowable wall temperature of NARloy-Z was defined as 800 K in section 2.2. The thermal conductivity of NARloy-Z is 295 W/m·K.

In the design of a regeneratively cooled rocket engine, one of the challenges is to connect the outer jacket to the inner liner of the chamber. An interesting solution to this problem is to produce a separate chamber and outer jacket that are not rigidly connected. Additional advantages are better fatigue behaviour because the thermal expansion of the inner liner is not constrained, as well as easy access to the coolant channels. Such a design must be slightly heavier because the inner liner must withstand the inward pressure of the coolant without support from the outer wall [80].

Because connecting the inner liner and outer jacket requires a difficult and expensive process, the copper chamber design uses separate parts for both. The chamber consists of a NARloy-Z nozzle with channels milled out. This chamber must be able to resist the inward pressure of the coolant without buckling or otherwise failing. The outer jacket is not subjected to high temperature, so it can be made

of aluminium or steel. In this phase, the focus will be on the inner chamber.

The high coolant pressure will cause compression of the chamber. To simplify the problem, the chamber will be modelled as a cylinder with the length of the engine and the maximum radius of the chamber. The compressive stress given by eq. 3.26 should not exceed the yield stress of the material. Equation 3.27 gives the critical pressure at which buckling occurs, taken from a NASA design criteria report [81].

$$\sigma = \frac{\Delta p}{R t_i} \quad (3.26)$$

$$p_{cr} = \frac{0.855}{(1 - \nu_p^2)^{3/4}} \frac{E}{\left(\frac{R}{t_i}\right)^{5/2} \left(\frac{L}{t_i}\right)} \quad (3.27)$$

At 800 K, the yield stress of NARloy-Z is approximately 120 MPa. Assuming the maximum coolant pressure is 60 bar, a thickness of 4.1 mm is required to withstand the hoop stress. Critical pressure for buckling is 133 bar at this thickness, so the hoop stress drives the thickness. A constant wall thickness along the nozzle was assumed in these calculations.

The rib thickness was also taken constant at 1 mm, while the channel height was varied piecewise linearly. Piecewise linear variation is simple to model and avoids steps inside the channel that induce pressure losses. The variation makes it possible to change the design to obtain a small pressure loss while still maintaining temperature below 800 K at all locations. Both the number of channels and the channel height were varied manually.

One of the possible design solutions is shown in fig. 3.28. The number of channels in this case was 64. The maximum channel width is 1.1 mm, while the minimum channel depth is 0.4 mm. This leads to a pressure drop of 9.8 bar and a temperature gain of 248 K in the coolant. The mass of the chamber (excl. the outer jacket) is approximately 4.7 kg.

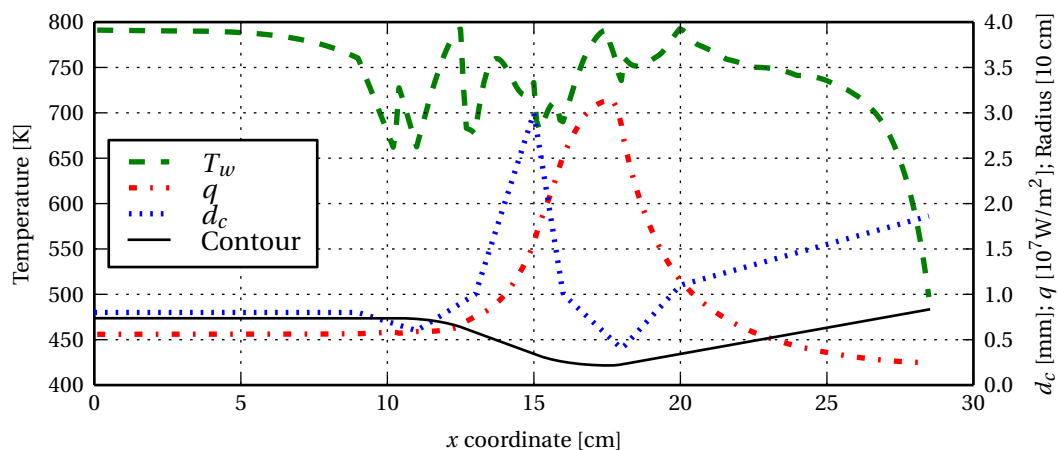


Figure 3.28: Copper nozzle wall temperature with preliminary channel geometry

The preliminary design of the copper nozzle shows that it is fairly easy to design a copper chamber that is able to withstand the heat load, while keeping the pressure loss reasonably low. A point of concern is that a thick wall is required to manage the stress from the high-pressure coolant. This in turn impacts the mass of the chamber. A design with separate chamber and jacket may not be optimal. Although

a rigidly connected outer jacket poses manufacturing issues and may increase production cost, the mass decrease and temperature decrease (which could be traded for a lower pressure drop) could be worth it.

At a wall thickness of 1 mm, the chamber mass (excluding the outer jacket) would go down to 1.3 kg. To accommodate a maximum wall temperature of 800 K, a pressure drop of only 2.5 bar is necessary. A design where both inner chamber and outer jacket are mechanically connected clearly offers substantial mass savings and lower pressure loss.

### 3.4.3. ALUMINIUM CHAMBER DESIGN

Aluminium 7075 T6 was taken as reference aluminium alloy. This is a typical aerospace alloy with good high temperature and fatigue properties. Its thermal conductivity is 130 W/m·K, with a maximum allowable temperature of 500 K (see section 2.2).

When performing the same analysis for aluminium, it immediately becomes clear that a similar design is impossible. Aluminium is weaker than copper, so a thicker inner chamber wall is needed to withstand the coolant pressure. In fact, a thickness of 8.8 mm is needed according to eq. 3.26. Because of this wall thickness, combined with its lower thermal conductivity, the aluminium wall now acts as an insulator and the wall temperature rises quickly. For the engine under consideration, an aluminium design with separate chamber and jacket is not feasible.

A design with a thin (1 mm) inner chamber wall is investigated. A pressure drop of several 100 bar is needed to cool the wall to 500 K. This clearly shows how large the difference is between an allowable temperature of 800 K and 500 K. In order to cope with this either the temperature of the hot gas must be brought down (e.g. by film cooling) or an insulation layer must be applied. Film cooling is inefficient for small engines (e.g. 30% of the methane flow is needed to cool a 19 kN engine according to [65]). In addition, the analysis of film cooling was outside the scope of this thesis. Protective coatings, however, can be analysed fairly easily.

An insulation layer has two purposes: to protect the aluminium underneath by creating a large temperature drop and to decrease the total heat flux. Adding such a layer will lower the maximum temperature of the chamber material underneath, but it will be subjected to a higher hot gas side temperature itself. In order to perform well as insulation material, it needs a low thermal conductivity and a high allowable temperature. For aluminium, two options exist: applying a thermal barrier coating or anodising the surface layer.

Thermal barrier coatings are usually ceramic materials (oxides) and are used in the aerospace industry for high temperature materials (e.g. turbine blades) [82]. Such coatings have been tested on tubes placed in oxygen/hydrogen rocket engines, showing a temperature benefit of 300 K for a coating of 100  $\mu\text{m}$  with respect to uncoated tubes [83, 84]. Thermal conductivity of these coatings was around 1 W/m·K. One of the drawbacks for the use of coatings in rocket engines is that there is a difference in thermal expansion between coating and base material. This may cause the coating to flake off [85].

Another option with similar result is to anodise the aluminium. Anodising is a process which creates an aluminium oxide layer on the surface. Because aluminium oxide has low thermal conductivity, this layer acts as insulation, similar to a thermal barrier coating. The thermal conductivity of the anodised layer is typically 1 W/m·K, while its thickness can be around 50  $\mu\text{m}$  [86].

An extra term has to be incorporated in the equation for the heat flux; it now becomes eq. 3.28. For the current analysis, the typical values of the anodized layer from [86] have been taken. However, it does not matter whether these values are realised with a thermal barrier coating or anodisation, as long as the quotient of thickness and thermal conductivity remains the same.

$$q = \frac{T_{aw} - T_{c,b} + \frac{q_{R,h}}{\alpha_h}}{\frac{1}{\alpha_h} + \frac{t_{\text{coat}}}{\kappa_{\text{coat}}} + \frac{t_i}{\kappa_i} + \frac{1}{\alpha_c}} \quad (3.28)$$

Now a preliminary design can be made for an aluminium chamber. After following the same design

process as with the copper chamber, a design with 80 coolant channels was made. The inlet pressure was set at 80 bar to compensate for the higher expected pressure drop. The channel height was again varied piecewise linearly.

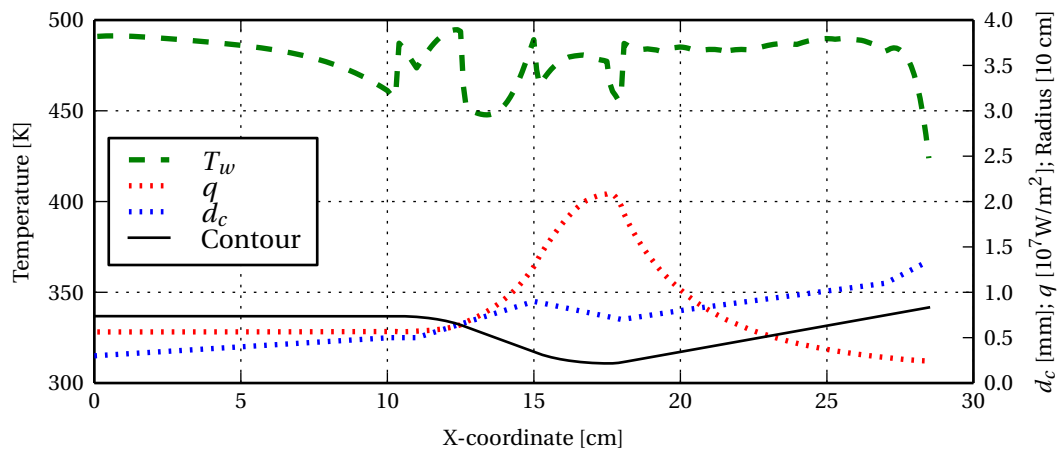


Figure 3.29: Coated aluminium nozzle wall temperature with preliminary channel geometry

The design and its wall temperature are shown in fig. 3.29. The maximum aluminium temperature is 495 K, with a pressure drop of 25.6 bar, substantially higher than both of the copper chamber designs. The maximum hot gas side wall temperature (at the anodised layer) is 1519 K, substantially lower than the melting point of aluminium oxide, which is 2323 K [82]. The temperature gain of the coolant is 234 K, somewhat lower than the copper engine. The mass of the inner chamber is only 0.4 kg.

We find that indeed, an aluminium chamber can be lighter than one made out of copper (0.4 kg versus 1.3 kg). However, this is excluding the weight of the outer jacket, piping, the injector etc. Moreover, the higher pressure drop necessitates a higher coolant inlet pressure, increasing the mass of the turbopump and/or propellant tanks. In addition, a thermal barrier coating or anodised layer is needed to maintain the low allowable wall temperature of aluminium. It was found that a relatively thin coating can sufficiently protect the aluminium such that regenerative cooling is possible. However, it is not without risk as the coating may crack or flake off, as noted earlier.

In general, the trade-off between a copper and aluminium engine should be performed on system level because there is a clear impact on the mass of the pressurization system. Furthermore, the costs of the required materials as well as manufacturing processes should be investigated and taken into account in such a trade-off.

### 3.5. CONCLUSION AND RECOMMENDATIONS

A one-dimensional model for heat transfer analysis of an oxygen/methane rocket engine has been constructed. The program, OMECA, has been validated against a coupled CFD/CHT model. Both at the hot gas side and at the coolant side, substantial deviations were found. On the hot gas side, it was found that the location of peak heat transfer is not accurately determined and the total heat transfer is overestimated. A calibration of the empirical constant in the Bartz equation was performed to bring the heat flux prediction more in line with experimental data. On the coolant side, none of the Nusselt number correlations could accurately predict the wall temperature. The Taylor equation proved to be closest to the reference analysis, but still shows a maximum deviation of more than 150 K. This confirms the need for CFD analysis of the coolant channels for detailed design.

Despite the shortcomings of the one-dimensional analysis in terms of absolute accuracy, it was used to perform a parametric analysis and generated results in line with expectations. Two major conclusions are drawn from the parametric analysis. First, that at a coolant inlet pressure of 60 bar, variations in the properties of methane have a strong influence on the cooling performance. Note that this result is dependent on the fact that only bulk variables of the flow are used in OMECA. Second, that the

cooling performance is very sensitive to the channel geometry. Tolerances of lower than 0.1 mm will be required in the construction of a thrust chamber. Optimization between the number of channels and the channel depth can be performed to find the minimum pressure drop at a certain allowable wall temperature.

OMECA was also used to perform a pre-design for a small oxygen/methane rocket engine. In this process, aluminium was compared to traditional copper alloy as a chamber material. It was found that only for copper, a design with a separate inner chamber and outer jacket is feasible. The required thickness for an aluminium wall to withstand the inwards pressure of the coolant, in combination with aluminium's lower thermal conductivity, inhibit the heat flow towards the coolant so much that the maximum wall temperature increases dramatically. A copper design with separate inner chamber and outer jacket would have a pressure drop of 9.8 bar. The inner chamber would weigh 4.7 kg.

If the inner chamber is joined rigidly to the outer jacket, it must not withstand the pressure alone and a lighter design can be made. In this case, a copper inner chamber would weigh 1.3 kg and have a pressure drop of 2.5 bar. For aluminium, the allowable temperature of 500 K would require massive pressure drop in the cooling channels. Therefore, the use of a ceramic insulation on the hot gas side is explored. Such an insulation, either a thermal barrier coating or a layer of anodised aluminium, is itself exposed to a high temperature. At the same time, it reduces the temperature of the aluminium beneath. With a typical layer of anodised aluminium, a pressure drop of 25.6 bar would be needed to keep the aluminium within the allowable temperature. This would lead to an inner chamber mass of 0.4 kg. However, because of differences in thermal expansion, between such ceramic layers and the base material, they are potentially troublesome. The practical issues associated with thermal barrier coatings or anodized layers should be investigated in more detail.

Table 3.6: Summary of results for three chamber designs analysed with OMECA

	Cu (1)	Cu (2)	Al (coated)
$T_{\text{allow}}$ [K]	800	800	500
Number of channels	64	64	80
$\kappa_j$ [W/m·K]	295	295	130
$t_i$ [mm]	4.1	1	1
$d_{\text{min}}$ [mm]	0.4	0.7	0.3
$\Delta p_{0,c}$ [bar]	9.8	2.5	25
$\Delta T_c$ [K]	248	273	234
Engine mass [kg]	4.7	1.3	0.38

The findings for both materials are summarised in table 3.6, where Cu (1) is the first copper design (with separate inner and outer wall), Cu (2) is the rigidly connected copper design and Al (coated) is the coated aluminium design.

When selecting the engine chamber material, the mass of the other components in the engine should also be taken into account. The trade-off should be made on a system level to account for changes in tank or pump mass because of coolant pressure drop. We will come back to this point in chapter 6 when results have been obtained with a more accurate method.

# 4

## NUMERICAL METHOD

The previous chapter discussed the use of a simple, one-dimensional method to analyse the heat transfer problem. It was demonstrated that this method is inaccurate. More detailed and computationally intensive methods are required to accurately predict the phenomena occurring in cooling channels filled with methane at supercritical pressure.

In the remainder of this thesis we will use a more detailed, multi-dimensional computational fluid dynamics (CFD) method in OpenFOAM. Several simulations even use conjugate heat transfer (CHT), modelling heat conduction in the surrounding solid as well. Modelling of the coolant fluid is much more challenging, so in this chapter the focus is on this aspect. The equations and models given here are software agnostic, but it is worth noting that appendix A contains some guidelines specifically with respect to using OpenFOAM for supercritical fluid modelling.

In CFD, the fluid is modelled as a continuum. Partial differential equations represent the behaviour of the fluid. These conservation equations result from the physical laws of conservation of mass, momentum and energy. The governing equations for this particular problem are described in section 4.1.

The equations for velocity and pressure must be coupled such that the solution of the simulation satisfies both equations. Because the fluid is compressible (the density changes are significant, although the flow velocity is rather low), pressure-velocity-density coupling is required. This is treated in section 4.2.

Two complicating factors must be taken into account when modelling the rocket engine cooling channels. Because of the high Reynolds number, turbulence must be taken into account. Section 4.3 shows how turbulence was modelled in this thesis. Section 4.4 on the other hand discusses the influence of wall roughness and how this was taken into account.

Section 4.5 discusses the discretisation methods that were used for this thesis, including the use of flux limiters. The tabulation of the fluid properties is also discussed. For this, a custom library was written that interpolates the fluid properties for each calculation cell during the simulation. Finally, section 4.6 gives a short summary of this chapter.

### 4.1. GOVERNING EQUATIONS

The governing equations are formulated in differential form in OpenFOAM, so this is the form that will be presented in this chapter. For the analysis of regenerative cooling, we are interested in the steady-state solution. The density of a supercritical fluid is far from constant, so the flow must be modelled as compressible – even though the Mach number is very low. The following paragraphs will therefore discuss the steady, compressible continuum equations in differential form. The discussion and equations presented here are largely based on the PhD thesis of Jasak [87], one of the original developers of OpenFOAM.

Conservation of mass in a steady flow means that for an arbitrary fluid volume, the divergence of the mass flux must be equal to zero. The mass flux is the fluid density  $\rho$  multiplied by the velocity vector  $\mathbf{U}$ . The equation for conservation of mass (also called continuity equation) is then given by eq. 4.1.

$$\nabla \cdot (\rho \mathbf{U}) = 0 \quad (4.1)$$

Any change in the momentum of a fluid volume should be balanced by a change in the forces acting on the fluid volume; i.e. a change in the stress tensor  $\boldsymbol{\sigma}$  or a change in the body forces  $\mathbf{b}$ . Body forces are generally negligible in the application of rocket engine channels due to the high Reynolds number and the low Grashof number [30]. Because of this, they will not be incorporated in the solver.

$$\nabla \cdot (\rho \mathbf{U} \mathbf{U}) = \nabla \cdot \boldsymbol{\sigma} + \rho \mathbf{b} \quad (4.2)$$

The stress tensor  $\boldsymbol{\sigma}$  can be split into a pressure and a shear stress part, as eq. 4.3 shows. Here we assume the pressure is the average normal stress in the fluid. The viscous stress tensor  $\boldsymbol{\tau}$  for a Newtonian fluid is also worked out in eq. 4.3. It is the deviatoric part of the stress tensor. This viscous stress tensor can again be decomposed into a part due to deformation or shear strain (the term including the gradient of  $\mathbf{U}$ ) and a part due to volumetric strain (the last term).

$$\boldsymbol{\sigma} = -p\mathbf{I} + \boldsymbol{\tau} = -p\mathbf{I} + \mu [\nabla \mathbf{U} + (\nabla \mathbf{U})^T] - \left(\frac{2}{3}\mu \nabla \cdot \mathbf{U}\right) \mathbf{I} \quad (4.3)$$

With the stress tensor split into a pressure and a shear stress term, the momentum equation becomes eq. 4.4. The form of this equation closely resembles the way the equations are implemented in OpenFOAM code. An example of this is given below. (There is a sign difference because the term `turb.divDevRhoReff(U)` is negative in OpenFOAM.)

$$\begin{aligned} \nabla \cdot (\rho \mathbf{U} \mathbf{U}) &= -\nabla p + \nabla \cdot \boldsymbol{\tau} & (4.4) \\ & \text{fvm}::\text{div}(\text{phi}, \mathbf{U}) \\ & == \\ & - \text{fvc}::\text{grad}(p) \\ & - \text{turb}.\text{divDevRhoReff}(\mathbf{U}) \end{aligned}$$

The third equation is for conservation of energy. If the body or stress forces perform work, this causes a change in the specific energy  $e$  of the fluid. A change in energy can also be caused by the heat flux  $\mathbf{q}$ . Energy sources and sinks are disregarded in this equation.

$$\nabla \cdot (\rho e \mathbf{U}) = \rho \mathbf{b} \cdot \mathbf{U} + \nabla \cdot (\boldsymbol{\sigma} \cdot \mathbf{U}) - \nabla \cdot \mathbf{q} \quad (4.5)$$

The above equation is written in terms of the specific energy  $e$ , but the OpenFOAM solver instead uses the enthalpy  $h$ . Therefore, eq. 4.5 must be rewritten in terms of  $h$ . Enthalpy equals the specific energy plus a pressure-related term minus the kinetic energy (eq. 4.6).

In order to obtain the enthalpy equation, we first split the stress term from eq. 4.5 into a pressure term and a shear stress term in eq. 4.7. If this equation is now rewritten in terms of  $h$ , the pressure term we just obtained disappears as it is incorporated by the divergence of enthalpy. A new term appears in order to account for the kinetic energy. The resulting enthalpy equation is eq. 4.8.

$$h = e + \frac{p}{\rho} - \frac{|\mathbf{U}|^2}{2} \quad (4.6)$$

$$\nabla \cdot (\rho e \mathbf{U}) + \nabla \cdot (p \mathbf{U}) = \rho \mathbf{b} \cdot \mathbf{U} + \nabla \cdot (\boldsymbol{\tau} \cdot \mathbf{U}) - \nabla \cdot \mathbf{q} \quad (4.7)$$

$$\nabla \cdot (\rho h \mathbf{U}) + \nabla \cdot \left( \rho \frac{|\mathbf{U}|^2}{2} \mathbf{U} \right) = \rho \mathbf{b} \cdot \mathbf{U} + \nabla \cdot (\boldsymbol{\tau} \cdot \mathbf{U}) - \nabla \cdot \mathbf{q} \quad (4.8)$$

The heat flux  $\mathbf{q}$  is easily written in terms of the temperature gradient using Fourier's heat conduction theorem. The thermal conductivity  $\kappa_{\text{eff}}$  now appears in the equation, where the subscript eff refers to effective. This effective thermal conductivity is the sum of the fluid's intrinsic thermal conductivity and an additional contribution generated by turbulence.

The existing OpenFOAM solver uses a linearisation of enthalpy with respect to temperature to write the heat flux as a function of temperature. It uses a different variable  $\alpha_{\text{eff}}$  (effective thermal diffusivity). This variable is defined as  $\kappa_{\text{eff}}$  divided by  $c_p$ . (Note that a common definition of thermal diffusivity also includes  $\rho$  in the denominator; this is not the case here.)

$$\mathbf{q} = -\kappa_{\text{eff}} \nabla T = -\alpha_{\text{eff}} c_p \nabla T \approx -\alpha_{\text{eff}} c_p \frac{dh}{dT} \nabla h \approx -\alpha_{\text{eff}} c_p \frac{1}{c_p} \nabla h = -\alpha_{\text{eff}} \nabla h \quad (4.9)$$

The above definition of the heat flux as function of enthalpy is very useful because it is a diffusive term for the unknown in the equation. This diffusive term stabilises the system of linear equations. In addition, if the fluid's specific heat capacity is close to constant, this definition is quite accurate.

However, in the case of supercritical fluids, the specific heat capacity can vary by a factor of 10. In this case, the assumption that temperature is linear with enthalpy is invalid and the above definition fails. However, if we do not include the diffusive term in the enthalpy equation, the matrix equation solver will fail to converge.

The solution is to use a clever trick: we first subtract the term  $\alpha_{\text{eff}} \nabla h$  at the left hand side, but also subtract it at the right hand side of the matrix equation. Afterwards the correct heat flux ( $\kappa_{\text{eff}} \nabla T$ ) is subtracted from the right hand side. The result is that the enthalpy-based heat flux is present in the matrix equation and helps stabilise the implicit calculation. However, it is cancelled out explicitly and the net result is the correct, temperature-based heat flux.

In the OpenFOAM solver code that was developed, this trick is represented by the following code, where `fvm` represents implicit, left-hand side terms and `fvc` represents explicit, right-hand side terms:

```
- fvm::laplacian ( turbulence->alphaEff () , he)
+ fvc::laplacian ( turbulence->alphaEff () , he)
- fvc::laplacian ( turbulence->kappaEff () , T)
```

Because the two  $\alpha_{\text{eff}} \nabla h$  terms cancel, the final enthalpy equation then becomes eq. 4.10, where body forces have once again been neglected.

$$\nabla \cdot (\rho h \mathbf{U}) + \nabla \cdot \left( \rho \frac{|\mathbf{U}|^2}{2} \mathbf{U} \right) = \nabla \cdot \boldsymbol{\tau} \cdot \mathbf{U} + \nabla \cdot \kappa_{\text{eff}} \nabla T \quad (4.10)$$

In the standard OpenFOAM solvers, the influence of the shear stress terms on the energy equation was disregarded. This is probably because these terms are often very small; viscous heating only becomes appreciable at high velocities [88, 89]. For completeness, the shear stress terms were added to the energy equation of the custom solver.

The set of the three conservation equations is printed again below. Equations 4.1, 4.4 and 4.10 are the governing equations for conservation of mass, momentum and energy respectively.

$$\nabla \cdot (\rho \mathbf{U}) = 0 \quad (4.1)$$

$$\nabla \cdot (\rho \mathbf{U} \mathbf{U}) = -\nabla p + \nabla \cdot \boldsymbol{\tau} \quad (4.4)$$

$$\nabla \cdot (\rho h \mathbf{U}) + \nabla \cdot \left( \rho \frac{|\mathbf{U}|^2}{2} \mathbf{U} \right) = \nabla \cdot \boldsymbol{\tau} \cdot \mathbf{U} + \nabla \cdot \kappa_{\text{eff}} \nabla T \quad (4.10)$$

When performing a conjugate heat transfer (CHT) analysis, the solid domain is also modelled. In comparison with the CFD method for the fluid, solving for the solid domain is fairly trivial. The governing equation for heat transfer in the solid is derived from Fourier's law of heat conduction and given by eq. 4.11.

$$0 = \nabla \cdot \left( \frac{\kappa}{c_p} \nabla c_p T \right) \quad (4.11)$$

## 4.2. PRESSURE-VELOCITY-DENSITY COUPLING

A typical approach to solving the Navier-Stokes equations in low-velocity flows is to combine the momentum equation and continuity equation to obtain an equation for the pressure [88]. The pressure field can be constructed such that it guarantees continuity, after which the velocity field can be calculated from the pressure. In this subsection, the derivation of this pressure equation is discussed.

The starting point is the momentum equation eq. 4.12, reordered such that terms which contain  $\mathbf{U}$  appear at the left-hand side.

$$\nabla \cdot (\rho \mathbf{U} \mathbf{U}) - \nabla \cdot \boldsymbol{\tau} = -\nabla p \quad (4.12)$$

When the momentum equation is discretised to form an implicit equation for the velocity, it can be written as eq. 4.13. Here,  $a$  are the coefficients for the velocity equation in matrix form. The subscript  $P$  refers to the diagonal entries of the coefficient matrix; while the subscript  $N$  represents any off-diagonal terms. In the discretisation scheme for an arbitrary cell, this means that  $N$  relates to the neighbour cells that are present in the discretisation scheme, while  $P$  indicates the cell itself [88].

$$a_P \mathbf{U}_P + \sum_N a_N \mathbf{U}_N = -\nabla p \quad (4.13)$$

Now a simplifying term is introduced in eq. 4.14. The off-diagonal parts of the coefficient matrix (which represent advection and diffusion terms) are lumped together in the new variable  $\mathbf{H}_\mathbf{U}$ .

$$\mathbf{H}_\mathbf{U} = -\sum_N a_N \mathbf{U}_N \quad (4.14)$$

If this substitution is carried out and the velocity is isolated from eq. 4.13, it can be rewritten as eq. 4.15.

$$\mathbf{U}_P = \frac{1}{a_P} \mathbf{H}_\mathbf{U} - \frac{1}{a_P} \nabla p \quad (4.15)$$

Recall that we want to use the continuity equation, which states that the divergence of the mass flow is zero. We are dealing with compressible flows, so in order to use this equation, all terms are now multiplied by the density  $\rho$ . The discretised momentum equation multiplied by  $\rho$  is given by eq. 4.16 [90].

$$\rho \mathbf{U}_P = \frac{\rho}{a_P} \mathbf{H}_\mathbf{U} - \frac{\rho}{a_P} \nabla p \quad (4.16)$$

$\nabla \cdot \rho \mathbf{U} = 0$ , so if the divergence of all terms is taken the left-hand side disappears. The pressure equation can then be written as eq. 4.17. This is the form that is implemented in the pressure-based Open-

FOAM solvers.

$$\nabla \cdot \left( \frac{\rho}{a_p} \nabla p \right) = \nabla \cdot \left( \rho \frac{\mathbf{H}\mathbf{U}}{a_p} \right) \quad (4.17)$$

When the pressure field has been found iteratively, the velocity is reconstructed using eq. 4.15.

### 4.3. TURBULENCE MODELLING

Although it is believed that the Navier-Stokes equations themselves accurately model turbulence, the required temporal and spatial resolutions to do so necessitate vast computational resources. Thus, the cost of Direct Numerical Simulation (DNS) of turbulence is prohibitive for all but the simplest low Reynolds number applications [88].

Another option is to use Large Eddy Simulation (LES), in which only the largest turbulent scales are computed directly, and smaller scales are modelled. Though this can be done for more complex geometries and higher Reynolds number than DNS can handle, it still requires substantial computation power [88]. LES simulations of supercritical fluid in rocket engine cooling channels have recently been reported by Ribert et al. [91].

The most popular engineering approach is to use Reynolds-averaged Navier-Stokes (RANS) equations. In this approach, none of the turbulent scales are directly computed. Instead, only the average effect of turbulence on the flow is modelled. This results in the addition of one or more equations to the governing equations of the flow. RANS modelling is the approach that was followed in this thesis. Several turbulence models of this family are discussed below.

#### 4.3.1. $k$ - $\epsilon$ MODEL

In OpenFOAM, turbulence is implemented as a direct correction of the momentum and energy equations. The corrected momentum equation is given in eq. 4.18, where the effective shear tensor  $\boldsymbol{\tau}_{\text{eff}}$  is given by eq. 4.19.

$$\nabla \cdot (\rho \mathbf{U}\mathbf{U}) = -\nabla p + \nabla \cdot \boldsymbol{\tau}_{\text{eff}} \quad (4.18)$$

$$\boldsymbol{\tau}_{\text{eff}} = \mu_{\text{eff}} [\nabla \mathbf{U} + (\nabla \mathbf{U})^T] - \left( \frac{2}{3} \mu_{\text{eff}} \nabla \cdot \mathbf{U} \right) \mathbf{I} \quad (4.19)$$

The only difference between  $\boldsymbol{\tau}$  and its effective variant  $\boldsymbol{\tau}_{\text{eff}}$  is the appearance of the effective viscosity  $\mu_{\text{eff}}$ . The effective viscosity is defined as the sum of the laminar or molecular viscosity  $\mu_l$  and the turbulent viscosity  $\mu_T$ , see eq. 4.20. Notice that the subscript  $T$  indicates "turbulent", while the superscript  $T$  in eq. 4.19 refers to the transpose of a matrix as usual.

$$\mu_{\text{eff}} = \mu_l + \mu_T \quad (4.20)$$

Similarly, the influence of turbulence on the energy equation is implemented directly with the use of the parameter  $\alpha_{\text{eff}}$ . This is the sum of the laminar diffusivity and the turbulent diffusivity. The effective thermal conductivity  $\kappa_{\text{eff}}$  can be obtained by multiplying  $\alpha_{\text{eff}}$  by  $c_p$ .

The turbulent thermal diffusivity depends on the turbulent viscosity and the turbulent Prandtl number. The turbulent Prandtl number is given by the user. It was set to 0.9 in this thesis; the same value was used by two independent research groups for rocket engine cooling channels [16, 92].

$$\alpha_{\text{eff}} = \frac{\kappa_l}{c_p} + \frac{\mu_T}{Pr_T} \quad (4.21)$$

The momentum and energy equations are both influenced by turbulence through the turbulent vis-

cosity  $\mu_T$ . In the  $k$ - $\epsilon$  model, this parameter is calculated with eq. 4.22. It depends on the turbulent energy  $k$  and the turbulent dissipation  $\epsilon$ , which is why the model is called the  $k$ - $\epsilon$  turbulence model.

$$\mu_T = \rho C_\mu \frac{k^2}{\epsilon} \quad (4.22)$$

The compressible  $k$ - $\epsilon$  model implemented in OpenFOAM is based on work by El Tahry [93]. The equations for  $k$  and  $\epsilon$  are given by eq. 4.23 and eq. 4.24. These are solved by OpenFOAM in addition to the conservation equations to yield the turbulent viscosity such that its influence on the momentum and energy equations can be modelled. In essence, they are convection-diffusion equations for the transport of turbulent energy and turbulent dissipation. However, contrary to the conservation equations they also contain production and destruction terms. Note that the operator  $:$  represents the double dot product of two second order tensors; this yields the sum of the element-by-element multiplication of the terms of both tensors.

$$\nabla \cdot (\rho \mathbf{U} k) = \nabla \cdot \left( \frac{\mu_T}{\sigma_k} \nabla \cdot k \right) + \mu_T \left( \nabla \mathbf{U} : \left[ \nabla \mathbf{U} + (\nabla \mathbf{U}^T) - \frac{2}{3} \nabla \cdot \mathbf{U} \cdot \mathbf{I} \right] \right) - \frac{2}{3} \rho k \nabla \cdot \mathbf{U} - \rho \epsilon \quad (4.23)$$

$$\nabla \cdot (\rho \mathbf{U} \epsilon) = \nabla \cdot \left( \frac{\mu_T}{\sigma_\epsilon} \nabla \cdot \epsilon \right) + C_1 \frac{\epsilon}{k} \mu_T \left( \nabla \mathbf{U} : \left[ \nabla \mathbf{U} + (\nabla \mathbf{U}^T) - \frac{2}{3} \nabla \cdot \mathbf{U} \cdot \mathbf{I} \right] \right) - \left( \frac{2}{3} C_1 + C_3 \right) \rho \epsilon \nabla \cdot \mathbf{U} - C_2 \frac{\rho \epsilon^2}{k} \quad (4.24)$$

In these equations, the parameter  $C_\mu$  is an empirical constant, while the parameters  $C_1, C_2, C_3, \sigma_k$  and  $\sigma_\epsilon$  are modelling parameters. Their values – as reported by El Tahry – are given in table 4.1 [93].

Table 4.1: Modelling parameter values for  $k$ - $\epsilon$  turbulence model

$C_\mu$	0.09
$C_1$	1.44
$C_2$	1.92
$C_3$	-0.33
$\sigma_k$	1
$\sigma_\epsilon$	1.3

#### 4.3.2. $k$ - $\omega$ SST MODEL

Another popular two-equation model is the  $k$ - $\omega$  Shear Stress Transport (SST) model by Menter [94]. In OpenFOAM, the 1993 model is implemented, albeit with coefficients from a 2003 update paper authored by Menter [95].

The shear stress transport model is in fact a blend between the  $k$ - $\omega$  model and the  $k$ - $\epsilon$  model discussed earlier.  $\omega$  is the specific dissipation of turbulence, while  $k$  is again the turbulent intensity. The equations for  $k$  and  $\omega$  are given by eq. 4.25 and eq. 4.26, respectively.

$$\nabla \cdot (\rho \mathbf{U} k) = \bar{P}_k - \beta^* \rho k \omega + \nabla \cdot (\mu + \sigma_k \mu_T \nabla \cdot k) \quad (4.25)$$

In eq. 4.25,  $\bar{P}_k$  is the production of turbulence, which is given by eq. 4.27. It is similar to the production term in the  $k$ - $\epsilon$  model, but incorporates a limiter to prevent build-up of turbulence in stagnation regions [95].  $\mu_T$  once again is the turbulent viscosity, while  $\beta^*$  and  $\sigma_k$  are modelling coefficients.

$$\nabla \cdot (\rho \mathbf{U} \omega) = \alpha_{\text{SST}} \rho S^2 - \beta_{\text{SST}} \rho \omega^2 + \nabla \cdot (\mu + \sigma_\omega \mu_T \nabla \cdot \omega) + 2(1 - F_1) \rho \sigma_\omega \frac{1}{\omega} (\nabla k) (\nabla \omega) \quad (4.26)$$

$$\bar{P}_k = \min \left\{ \mu_T \left( \nabla \mathbf{U} : \left[ \nabla \mathbf{U} + (\nabla \mathbf{U}^T) - \frac{2}{3} \nabla \cdot \mathbf{U} \cdot \mathbf{I} \right] \right), 10 \cdot \beta^* \rho k \omega \right\} \quad (4.27)$$

In the equation for  $\omega$ , eq. 4.26,  $F_1$  is the blending function given in eq. 4.28. This function blends the model from  $k$ - $\omega$  behaviour near the wall to  $k$ - $\epsilon$  away from the wall [94].  $\alpha_{\text{SST}}$  and  $\beta_{\text{SST}}$  are blended variables, given by eq. 4.29 and eq. 4.29. They blend between the modelling coefficients  $\alpha_1$  and  $\alpha_2$  as well as between  $\beta_1$  and  $\beta_2$ .

$$F_1 = \tanh \left( \left\{ \min \left[ \max \left( \frac{\sqrt{k}}{\beta^* \omega y}, \frac{500\mu}{y^2 \omega \rho} \right), \frac{4\rho\sigma_{\omega 2} k}{C_{k\omega} y^2} \right] \right\}^4 \right) \quad (4.28)$$

$$\alpha_{\text{SST}} = \alpha_1 F_1 + \alpha_2 (1 - F_1) \quad (4.29)$$

$$\beta_{\text{SST}} = \beta_1 F_1 + \beta_2 (1 - F_1) \quad (4.30)$$

In the blending function  $F_1$  (eq. 4.28),  $y$  is the wall distance and  $\sigma_{\omega 2}$  another modelling constant.  $C_{k\omega}$  is the cross-diffusion term of eq. 4.26 [94]. Equation 4.31 gives this term.

$$C_{k\omega} = \max \left( 2\rho\sigma_{\omega 2} \frac{1}{\omega} (\nabla k) (\nabla \omega), 10^{-10} \right) \quad (4.31)$$

The turbulent viscosity is determined from  $k$  and  $\omega$  using eq. 4.32. Another blending function,  $F_2$  is given by eq. 4.33.  $S$  is the modulus of vorticity [94]. In the later version of the SST model, it has been replaced by the rate of strain [95], but OpenFOAM uses the vorticity.

$$\mu_T = \frac{a_1 \rho k}{\max(a_1 \omega, S F_2)} \quad (4.32)$$

$$F_2 = \tanh \left\{ \left[ \max \left( \frac{\sqrt{k}}{\beta^* \omega y}, \frac{500\mu}{y^2 \omega \rho} \right) \right]^2 \right\} \quad (4.33)$$

The modelling coefficients of the  $k$ - $\omega$  shear stress transport model are given in table 4.2.

Table 4.2: Modelling parameter values for  $k$ - $\omega$  SST turbulence model

$\alpha_1$	$\frac{5}{9}$
$\alpha_2$	0.44
$\beta_1$	$\frac{3}{40}$
$\beta_2$	0.0828
$\beta^*$	0.09
$\sigma_k$	0.85
$\sigma_{\omega 1}$	0.5
$\sigma_{\omega 2}$	0.856
$a_1$	0.31

### 4.3.3. SPALART-ALLMARAS MODEL

A simpler turbulence model is the Spalart-Allmaras model. This one-equation model was devised by Spalart and Allmaras [96]. Equation 4.34 shows that the turbulent viscosity  $\mu_T$  is modelled through the eddy viscosity  $\nu_T$ , which in turn depends on the  $\tilde{\nu}$  – the variable that is solved by the model – and a damping function  $f_{\nu 1}$ .

$$\mu_T = \rho \nu_T = \rho \tilde{\nu} f_{\nu 1}(\chi) \quad (4.34)$$

The damping function  $f_{v1}$  depends on the ratio between the eddy viscosities,  $\chi = \tilde{\nu}/\nu$ . It is given by eq. 4.35.

$$f_{v1}(\chi) = \frac{\chi^3}{\chi^3 + C_{v1}^3} \quad (4.35)$$

The convection, diffusion, production and destruction of  $\tilde{\nu}$  is governed by eq. 4.36. The term on the left hand side is the convection term, while the first two terms on the right hand side govern diffusion of  $\tilde{\nu}$ . The penultimate term of the right-hand side is the production term and the last one the destruction term.

$$\nabla \cdot (\rho \mathbf{U} \tilde{\nu}) = \nabla \cdot \left( \frac{\rho \tilde{\nu} + \mu}{\sigma_{vT}} \nabla \cdot \tilde{\nu} \right) + \frac{C_{b2}}{\sigma_{vT}} \rho |\nabla \tilde{\nu}|^2 + C_{b1} \rho \tilde{S} \tilde{\nu} - C_{w1} f_w \rho \frac{\tilde{\nu}^2}{y^2} \quad (4.36)$$

The production term contains the variable  $\tilde{S}$ , which is defined in eq. 4.37. In this equation,  $S$  is the modulus of vorticity,  $y$  is the distance to the nearest wall and  $K$  is the Von Karman constant (often denoted as  $\kappa$  in other texts). The function  $f_{v2}$  is another damping function defined by eq. 4.38.

$$\tilde{S} = S + \frac{\tilde{\nu}}{K^2 y^2} f_{v2}(\chi) \quad (4.37)$$

$$f_{v2}(\chi) = 1 - \frac{\chi}{1 + \chi f_{v1}(\chi)} \quad (4.38)$$

The destruction term of eq. 4.36 contains the function  $f_w$ , given by eq. 4.39. It is related to a characteristic length  $l$  defined by eq. 4.40. The function  $g$  is defined by eq. 4.41.

$$f_w = g(l) \left[ \frac{1 + C_{w3}^6}{g^6(l) + C_{w3}^6} \right]^{\frac{1}{6}} \quad (4.39)$$

$$l = \frac{\tilde{\nu}}{\tilde{S} K^2 y^2} \quad (4.40)$$

$$g(l) = l + C_{w2} (l^6 - l) \quad (4.41)$$

It is clear from these equations that both the production and destruction of the eddy viscosity are related to the distance from the nearest wall. At the wall itself, the proper boundary condition for the eddy viscosity is to set it to zero.

The modelling coefficients used in the Spalart-Allmaras model are given in table 4.3. Recall that the turbulent Prandtl number  $Pr_T$  is 0.9.

Table 4.3: Modelling parameter values for Spalart-Allmaras turbulence model

$K$	0.41
$C_{b1}$	0.1355
$C_{b2}$	0.622
$C_{v1}$	7.1
$C_{w1}$	$\frac{C_{b1}}{K^2} + \frac{1+C_{b2}}{\sigma_{vT}}$
$C_{w2}$	0.3
$C_{w3}$	2
$\sigma_{vT}$	0.66666

## 4.4. ROUGHNESS MODELLING

The roughness of a wall can influence the fluid flowing past it. In rocket engine cooling channels, roughness increases both heat transfer and pressure loss. Several approaches exist to take this influence into account in CFD codes.

### 4.4.1. BOUNDARY LAYER INTEGRATION

One option is to fully integrate the boundary layer. Aupoix has proposed several approaches to account for wall roughness, while still having computational nodes down to the viscous sub-layer [97–99]. These approaches rely on a shift in the wall distance, to obtain a non-zero velocity at the wall. The resulting non-zero turbulence mimics the flow behaviour near a rough wall.

#### SPALART-ALLMARAS

For the Spalart-Allmaras model, a straightforward adaptation has been proposed by Aupoix and Spalart [97]. This approach, which in their paper is called the *Boeing extension*, modifies the conventional Spalart-Allmaras model in the following manner.

The wall distance  $y$  is modified using eq. 4.42, where  $h_s$  is the roughness height. Inside the turbulence model, the wall is moved to a virtual point inside the flow, so the turbulence parameters are non-zero at the wall. The distance the wall is moved depends on the roughness height, so a rougher wall leads to higher turbulence at the wall. In addition, the equation for  $\chi$  is modified to eq. 4.43 to achieve good predictions at small roughness heights [97].

$$y = y_{\text{true}} + 0.03 \cdot h_s \quad (4.42)$$

$$\chi = \frac{\tilde{v}}{v} + 0.5 \frac{h_s}{y} \quad (4.43)$$

Finally, the boundary condition for  $\tilde{v}$  is modified to allow for non-zero turbulence at the wall. Equation 4.44 shows the new boundary condition, where  $\tilde{v}_1$  is the value of  $\tilde{v}$  at the first point from the wall.

$$\tilde{v}_w = \tilde{v}_1 \frac{0.03 h_s}{y} \quad (4.44)$$

Aupoix and Spalart compared their roughness modification of the Spalart-Allmaras model to experimental data from several different sources. They conclude that it produces reasonable results, but report two important drawbacks. First, that the roughness height  $h_s$  "is not simply proportional to the physical size of the roughness" [97].

The second drawback is that the effects of roughness on heat transfer and skin friction are not characterised by the same value of the roughness height. That is, if the roughness height is tuned for skin friction (e.g. pressure drop in a channel), it will not correctly predict heat transfer effects of roughness.

This difference is because these roughness effects are linked to different physical mechanisms. The increased skin friction is mainly due to pressure drag on the roughness elements present in the flow. The increased heat transfer, however, is related to the increased wetted surface of the rough wall [97]. This means the Reynolds analogy no longer holds for rough surfaces, which according to Aupoix and Spalart is consistent with the experimental results of Dipprey and Sabersky [100]. It will be demonstrated later in this thesis that indeed, the Spalart-Allmaras roughness correction does not accurately predict both heat transfer and pressure drop at the same time.

The above adaptation for the Spalart-Allmaras turbulence model was programmed in OpenFOAM. It was manually verified that the implementation was correct; further verification results from the model

are shown in chapter 5.

### *k*- $\omega$ SST

Aupoix recently published a comparison of various similar adaptations for the *k*- $\omega$  SST model [98]. In this paper, he demonstrates that the so-called Nikuradse adaptation matches experimental results reasonably. This model was implemented in OpenFOAM for this thesis.

The model is based on a similar idea as the roughness adaptation for the Spalart-Allmaras model: obtain a non-zero turbulence at the wall by shifting the wall. However, in this case no changes to the turbulence model itself are needed, only the boundary conditions on *k* and  $\omega$  are altered.

First, the roughness height is made dimensionless using eq. 4.45. The friction velocity  $u_\tau$  is defined as eq. 4.46.

$$h_s^+ = \frac{h_s u_\tau}{\nu} \quad (4.45)$$

$$u_\tau = \sqrt{\frac{\mu_w \frac{\partial u}{\partial y}}{\rho_w}} \quad (4.46)$$

Similarly, the turbulence variables *k* and  $\omega$  are made dimensionless with eq. 4.47 and eq. 4.48.

$$k^+ = \frac{k}{u_\tau^2} \quad (4.47)$$

$$\omega^+ = \frac{\omega \nu}{u_\tau^2} \quad (4.48)$$

The turbulent kinetic energy at the wall is defined by eq. 4.49. It is based on an empirical relation for data obtained by Nikuradse [98].

$$k_w^+ = \max \left\{ 0, \frac{1}{\sqrt{\beta^*}} \tanh \left[ \left( \frac{\ln \frac{h_s^+}{30}}{\ln 8} + 0.5 \left[ 1 - \tanh \frac{h_s^+}{100} \right] \right) \tanh \left( \frac{h_s^+}{75} \right) \right] \right\} \quad (4.49)$$

The specific dissipation at the wall is defined by eq. 4.50.

$$\omega_w^+ = \frac{400000}{k_s^{+4}} \left( \tanh \frac{10000}{3k_s^{+3}} \right)^{-1} + \frac{70}{k_s^+} \left[ 1 - \exp \left( -\frac{h_s^+}{300} \right) \right] \quad (4.50)$$

#### 4.4.2. WALL FUNCTIONS

In order to model the behaviour inside the boundary layer, one can also use suitable wall functions for the turbulent viscosity and turbulent thermal conductivity. These allow for the use of relatively coarser grids, because the first grid point near the wall can be further away than without wall functions. In OpenFOAM, wall functions are implemented for *k*,  $\epsilon$ ,  $\omega$ ,  $\mu_T$  and  $\kappa_T$ .

The wall function for *k* is straightforward, it is simply a boundary condition that enforces a zero gradient of the turbulent intensity at the wall.

The wall function for  $\epsilon$  is given by eq. 4.51, where *k* should be evaluated at the centre of the first cell. *y* is the wall distance and the other variables are modelling coefficients of the *k*- $\epsilon$  model.

$$\epsilon_w = \frac{C_\mu^{\frac{3}{4}} k^{\frac{3}{2}}}{K y} \quad (4.51)$$

For  $\omega$ , the wall function calculates the harmonic mean between a viscous term (the first one) and a logarithmic term (the second one), see eq. 4.52. Once again,  $k$  should be evaluated at the centre of the first cell, while the parameters with subscript  $w$  are evaluated at the wall.

$$\omega_w = \sqrt{\left(\frac{6\mu_w}{\rho_w \beta_1 y^2}\right)^2 + \left(\sqrt{\frac{k}{C_\mu^{1/4} K y}}\right)^2} \quad (4.52)$$

The turbulent viscosity  $\mu_T$  is evaluated from the molecular viscosity, the nondimensional wall distance  $y^+$  and the local Reynolds number  $Re$  (eq. 4.53). The latter is defined in eq. 4.54. The  $y^+$  value is modified by the roughness height  $h_s$  in a complicated manner, such that the value of  $\mu_T$  increases as the roughness height increases.

$$\mu_T = \mu_w \left(\frac{y^+}{Re} - 1\right)^2 \quad (4.53)$$

$$Re = \frac{\rho_w |\mathbf{U}| y}{\mu_w} \quad (4.54)$$

It is interesting to note that the wall function for  $\mu_T$  described here (referred to in OpenFOAM as `mutURoughWallFunction`), performed well in the tests that were run. Another wall function for  $\mu_T$ , called `mutKRoughWallFunction`, led to nonsense results for supercritical heat transfer analysis.

Finally, the wall function for  $\kappa_T$  (in OpenFOAM actually the one for thermal diffusivity) simply makes use of the calculated value for  $\mu_T$  and the turbulent Prandtl number  $Pr_T$ , see eq. 4.55.

$$\kappa_T = \frac{\mu_T c_p}{Pr_T} \quad (4.55)$$

## 4.5. DISCRETISATION

OpenFOAM is a colocated finite-volume CFD package. The domain is divided into a number of volumes, where all fluid properties are known only at the center of each volume or cell. The governing equations are then applied to these finite volumes.

However, the governing equations do not only contain the values at the cell centres. They contain vector operators such as the gradient, divergence and Laplacian. How these terms are discretised is an important aspect of computation fluid dynamics that can severely influence the results [88].

A central discretisation scheme was chosen for all these terms. This scheme is of second order, making it accurate with modest computational requirements [88]. It was found, however, that central discretisation of the convective terms induces non-physical oscillations in the solution. Figure 5.2 later in this chapter shows an example of such an oscillatory solution.

Several simulations were ran to pinpoint the cause of these oscillations. Moving from variable fluid properties and real gas behaviour to a constant property, perfect gas model did nothing to remove them. The strongly changing density, viscosity and specific heat were not the culprit. A common solution to spurious oscillations obtained with central discretisation is to refine the grid, but at 320 cells in horizontal direction, the wiggles remained present in the converged solution.

In the end, it was realized the oscillations were caused by the strong gradients that are inherently present in supercritical flows [91]. Peeters et al. used a very similar OpenFOAM solver to model heat transfer to supercritical carbon dioxide [101]. They employed upwind schemes for the convective terms. It was found that also in the current case, using upwind discretisation of the convective terms removed the oscillations altogether. This a classic result in CFD. However, upwind schemes are only first order. Even worse, they introduce substantial numerical diffusion. In general, their use is not

counselled due to the poor resulting accuracy [88].

A common solution to prevent oscillations while retaining accuracy is to use flux limiters. These switch between upwind discretisation in regions of steep gradients and central discretization in regions of smooth changes. Flux limiters are the subject of the next section.

#### 4.5.1. FLUX LIMITERS

A flux limiter is a tool used in CFD to switch between upwind and central discretisation. Upwind schemes are dissipative and therefore inaccurate, but they are very stable. Central schemes, on the other hand, are accurate but can induce oscillations – especially in regions where steep gradients of the fluid properties are present. Limiters use upwind discretisation near steep gradients and central discretisation in other regions; the result is a stable scheme that is still accurate [88].

Before we can start to understand how limiters function in OpenFOAM, it is important to show the finite volume formulation used by OpenFOAM. It is depicted by Figure 4.1. The flow variables are known and stored in each cell centroid (in this case the points  $P$  and  $N$ ). However, fluxes are integrated over faces such as  $\mathbf{S}_s$  (a vector with direction normal to the surface and surface area magnitude).

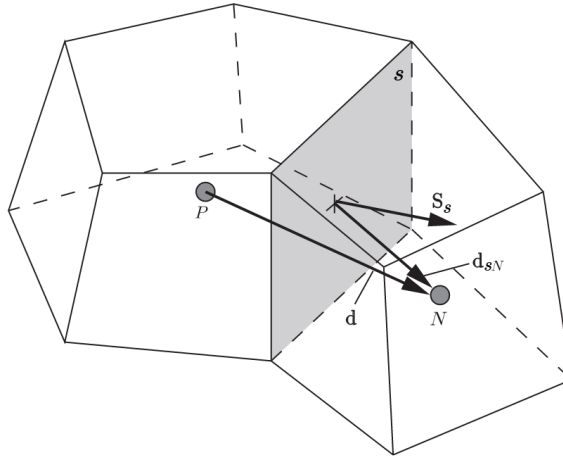


Figure 4.1: Finite volume formulation in OpenFOAM [42]

We will use the situation in fig. 4.1 to illustrate the how the flux limiter functions in OpenFOAM. The value of a generic flux  $\Psi$  is known at the points  $P$  and  $N$  as  $\Psi_P$  and  $\Psi_N$  respectively. Now we want to use these values to calculate  $\Psi_s$ , the value at the face.

A central discretisation scheme for  $\Psi_s$  would use linear interpolation, as shown in eq. 4.56.  $w_s$  is a purely geometrical parameter based on relative position and angle of the face with respect to the interpolation points, as shown in eq. 4.57.

$$\Psi_s = w_s \Psi_P + [1 - w_s] \Psi_N \quad (4.56)$$

$$w_s = \frac{|\mathbf{S}_s \cdot \mathbf{d}_{sN}|}{|\mathbf{S}_s \cdot \mathbf{d}|} \quad (4.57)$$

The linear interpolation as shown in eq. 4.56 is of second order accuracy. Using such an interpolation scheme may cause oscillations in the presence of strong gradients. As mentioned earlier, one possible solution is to use an upwind scheme, but this is only first order accurate.

To tackle this problem, we make use of a limiter. It switches between first order upwind and second order central schemes, depending on the presence of gradients. The presence of successive gradients is defined by eq. 4.58, where  $(\nabla \Psi)_P$  is the full gradient over cell  $P$ , calculated with linear interpola-

tion.

$$r = 2 \frac{\mathbf{d} \cdot (\nabla \Psi)_P}{\Psi_N - \Psi_P} \quad (4.58)$$

In case of a very smooth solution,  $r$  will approximate 1. When sharp gradients are involved,  $r$  will be close to zero. The variable  $r$  is used by all limiters as a measure for the steepness of the flux gradient. A limiter is a function  $\beta(r)$  that is used in the calculation of the flux at the cell face in eq. 4.59.

$$\Psi_s = (1 - \beta[1 - w_s]) \Psi_P + \beta[1 - w_s] \Psi_N \quad (4.59)$$

We can see that as  $\beta$  becomes smaller, the value of  $\Psi_s$  is biased to point P (upwind). If  $\beta = 0$ , the scheme is fully upwind. If  $\beta = 1$ , the scheme is central.

Flux limiters can be constructed such that they are total variation diminishing (TVD) which means that they do not induce oscillations. It is possible that they satisfy at the same time the criterion of second order accuracy [102]. In this work, we will investigate three flux limiters: the Superbee limiter, the van Leer limiter and the minmod limiter. Their definitions are given by eq. 4.60, eq. 4.61 and eq. 4.62 respectively.

$$\beta(r) = \max[0, \min(2r, 1), \min(r, 2)] \quad (4.60)$$

$$\beta(r) = \frac{r + |r|}{1 + r} \quad (4.61)$$

$$\beta(r) = \max[0, \min(1, r)] \quad (4.62)$$

The requirements for TVD flux limiters that also offer second order accuracy can easily be visualised, as was already shown by Sweby [102]. In fig. 4.2, the shaded region is Sweby's region of TVD and second order limiters. The behaviour of the three selected limiters in terms of mapping  $r$  to  $\beta(r)$  is also shown and confirms that they satisfy the requirements.

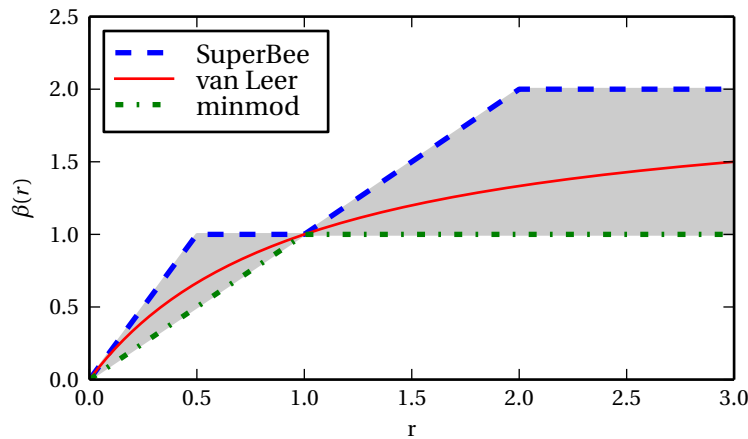


Figure 4.2: Sweby's region of TVD and second order flux limiters, with selected flux limiters

The performance of the various limiters will be evaluated using the first validation case in chapter 5. There it will be shown that the flux limiters indeed suppress unphysical oscillations in the solution.

Because the limiters are second order accurate, the method is formally of second order. This means that when decreasing the grid spacing by an order of two, the error should also be reduced by an order of two. Discretisation errors will also be discussed in chapter 5

### 4.5.2. FLUID PROPERTIES

The fluid properties are also discretised. Because the equation of state and the other equations defining fluid properties are so complex (see section 2.1), it would be too time-consuming to calculate them for each cell at run-time. To circumvent this problem, the fluid properties required by the CFD solver are tabulated as functions of pressure and temperature. From the resulting look-up tables, the fluid properties for each cell are calculated with bilinear interpolation.

The generation of the fluid property lookup tables was performed with a  $\Delta\rho$  of  $0.25 \text{ kg/m}^3$ . For this reason, there are more data points at pressures and temperatures close to the (pseudo-)critical point. After calculation of all fluid properties at one  $(p, T)$  data point, partial derivatives were used to guess the next  $(p, T)$  data point, with a difference in density of  $0.25 \text{ kg/m}^3$ . The error in the fluid properties obtained with this approach was discussed in section 2.1.3.

A module was written in C++ to use the tabulated properties within the OpenFOAM package. This module reads the look-up tables supplied by the user and interpolates the required fluid properties for each volume of the grid. Verification activities confirmed the correct functioning of the module. The module has been made available for the OpenFOAM user community [57] and has generated some interest among its members.

## 4.6. SUMMARY OF NUMERICAL METHODS

In this chapter, the numerical methods used to perform CFD and CHT simulations were discussed. Section 4.1 showed the governing equations for conservation of mass, momentum and energy. It also discussed how these are implemented in OpenFOAM. The energy conservation equation for the solid domain was given as well.

Section 4.2 discussed how the governing equations for the fluid were coupled and solved. In particular, it discussed pressure-velocity-density coupling. In this method, the equations for conservation of mass and momentum are combined to create a pressure equation.

Section 4.3 showed the RANS turbulence models that are used in this thesis: the standard  $k-\epsilon$  model, the  $k-\omega$  SST model and the Spalart-Allmaras model. Section 4.4 discussed two approaches for wall roughness modelling. One was the full integration of the boundary layer, using adapted boundary conditions. The other was to use wall functions that take roughness into account.

Section 4.5 then showed the discretisation schemes used. For the divergence terms in the governing equations, flux limiters can be needed to suppress oscillations in the solution. The fluid properties were tabulated for a set of pressure and temperature data points. Tables were created with a density difference of approximately  $0.25 \text{ kg/m}^3$  between two neighbouring data points. A custom library was written and implemented in OpenFOAM to interpolate these fluid properties.

# 5

## VALIDATION

This chapter shows the validation of the numerical method that was laid out in the previous chapter. First, the CFD method will be compared to another CFD method in an isolated manner (without coupling to a solid domain). The flow of supercritical methane in a straight, asymmetrically heated channel is analysed and compared in section 5.1. Then a coupled conjugate heat transfer analysis with both a fluid and a solid domain is compared to a similar numerical analysis in section 5.2. Finally, the results of the solver are compared to experimental data in section 5.3 to complete the validation of the developed method.

### 5.1. NUMERICAL ANALYSIS OF HEATED METHANE

The first validation case is the numerical analysis of supercritical methane in a straight channel carried out by Pizzarelli et al. [43]. In this case, the flow of methane through a straight channel with rectangular cross-section is considered. The channel is 0.1 mm wide, 0.8 mm high and 30 mm long. These dimensions are intentionally smaller than the expected geometry of a rocket engine cooling channel in order to decrease the required computational resources [43]. Methane is at supercritical pressure in the complete channel. It enters at subcritical temperature and is heated to the pseudo-critical temperature in the channel.

Methane enters the channel at a temperature of 130 K and a total pressure of 90 bar. The static pressure at the exit plane is 70 bar. The top wall is cold with its temperature is set to 130 K, while the bottom wall has a temperature of 600 K. The side wall goes linearly from 600 K to 130 K along its 0.8 mm height. The Spalart-Allmaras turbulence model was used by Pizzarelli et al, so it was also adopted here.

Calculations were carried out for three grids, with one grid representing half of the channel due to symmetry along the vertical axis. The three grids were a coarse grid with  $8 \times 5 \times 15$  cells (in directions length  $\times$  half-width  $\times$  height), a medium grid with  $16 \times 10 \times 30$  cells and a fine grid with  $32 \times 20 \times 60$  cells. The number of cells in each direction is doubled when increasing the fineness of the grid. The reason for this is twofold. First, it facilitates mapping of the solution from a coarser grid to a finer grid (to reduce computation time). Secondly, it makes it possible to carry out a grid independence study, as will be discussed later.

#### 5.1.1. EFFECT OF FLUX LIMITER

In section 4.5, the use of flux limiters was discussed. This is a suitable location to discuss the performance of the different flux limiters and select one of them. The medium grid was used to evaluate the performance of the various flux limiters. This grid was chosen as a compromise between accuracy and computation time. For comparison, the performance without flux limiters, i.e. with a central discretisation scheme was also measured.

Figure 5.1 shows the residuals of the pressure equation as a measure of convergence. In most cases

this equation was the dominant one for convergence of the solution, having the highest residuals and needing the most inner iterations. The first 1000 iterations are shown. Although the simulations were performed for longer, the residuals did not become smaller for any of the cases.

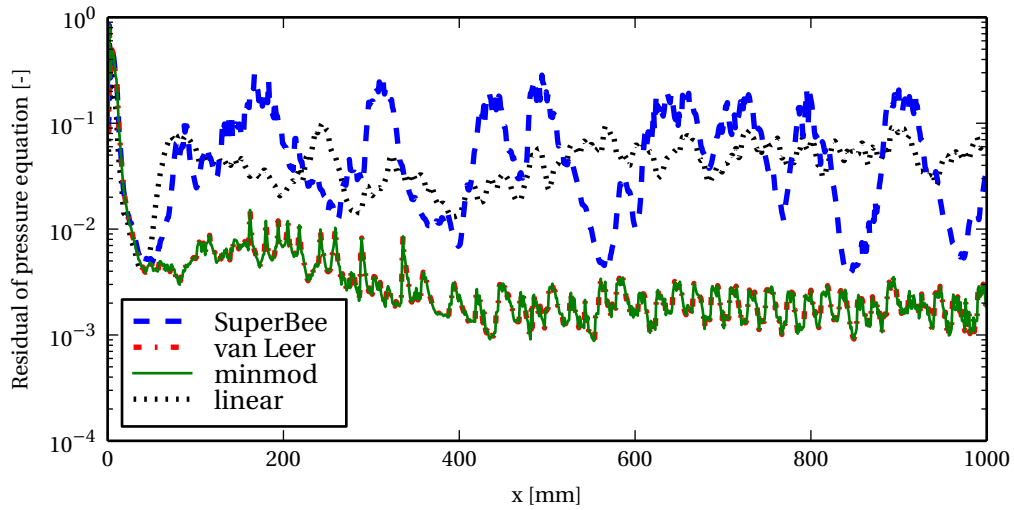


Figure 5.1: Pressure convergence on medium grid with different limiters

The minmod and van Leer limiters yielded exactly the same results in this case. The residuals are therefore also the same, with a reduction of approximately  $10^{-3}$ . The SuperBee limiter has the highest iteration error, at a similar level as the linear differencing scheme without flux limiter. Clearly van Leer and minmod are superior choices with regards to convergence.

This trend is to be expected, the SuperBee limiter is less dissipative than the van Leer and minmod limiters. It is however peculiar that van Leer and minmod offer exactly the same results, because the implementation of the flux limiters is different, see section 4.5.

All limiters are successful in suppressing the oscillations caused by the linear interpolation at high gradients. Figure 5.2 shows the bulk temperature along the channel after the last outer iteration for all four cases. While the linear interpolation causes an oscillatory solution of the temperature, the other three lines almost coincide.

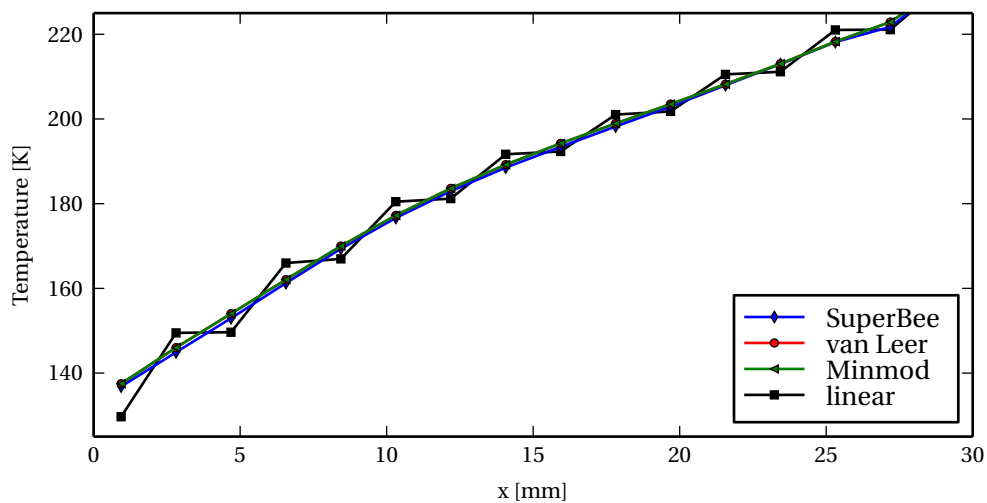


Figure 5.2: Temperatures obtained on medium grid with different limiters

The differences between the limiters are very small in this case. In other test cases, Sweby found that

the minmod limiter was more diffusive than the van Leer limiter [102]. Sweby has recommended the van Leer limiter as both reliable and accurate. This, combined with the relatively good convergence shown above, led to the selection of the van Leer limiter for the work in this thesis.

### 5.1.2. EFFECT OF BOUNDARY CELL SIZE

During the course of the validation activities, it was realised that there is a variable with an enormous effect on the results, one that may not be immediately obvious.

The flow behaviour of supercritical methane through the channel is dominated by the heat transfer into the fluid. This is not only the main parameter of interest, it also influences all other flow properties. If the temperature changes, this affects the density and velocity as well as the thermodynamic properties such as thermal conductivity and heat capacity. Because of the simple geometry and pressure boundary conditions, the flow is almost completely dependent on the heat transfer.

The heat flux into the fluid is calculated from the turbulent thermal conductivity and the temperature gradient between the hot wall and the first fluid volume. This is a problem because there is only a linear relation between wall distance and temperature very close to the wall. The accuracy of the heat transfer (and thus of the complete flow description) is highly dependent on the distance between the wall and the first fluid element.

Consider a generic boundary layer of a flow in  $x$ -direction, with a wall located at  $y = 0$ . The velocity in  $x$ -direction is given by  $u$ . The distance  $y$  to the wall can be made into the dimensionless parameter  $y^+$  with the use of eq. 5.1 [89].

$$y^+ = y \sqrt{\frac{\rho}{\mu} \frac{\partial u}{\partial y}} \quad (5.1)$$

The velocity can also be made dimensionless with equation eq. 5.2. In the viscous sublayer ( $y^+ \leq 5$ ), the relation between the dimensionless wall distance and the dimensionless velocity can be approximated as a linear function, such that  $u^+ \approx y^+$  [89]. Thus, for good approximation of the boundary layer, one computation node should be located at  $y^+ \leq 5$ . Often, having a node at  $y^+ \approx 1$  is advised for optimal accuracy [88].

$$u^+ = u \sqrt{\frac{\rho}{\mu} \frac{\partial u}{\partial y}} \quad (5.2)$$

For the temperature, a similar relation can be derived.  $T^+$  is the dimensionless temperature, defined by eq. 5.3. Close to the wall, there is again an approximately linear relation: eq. 5.4. The region of validity for this relation depends on the Prandtl number  $Pr$ .

$$T^+ = \frac{T_w - T}{q_w} c_p \sqrt{\rho \mu \frac{\partial u}{\partial y}} \quad (5.3)$$

$$y^+ \approx Pr T^+ \quad (5.4)$$

At high temperatures, supercritical methane exhibits gas-like behaviour, with a Prandtl number of approximately 0.7. Kader collected experimental data for the variation of the dimensionless temperature with dimensionless wall distance. Figure 5.3 shows this variation for a gas with  $Pr = 0.7$ .

Kader also gave a relation to calculate the extent of the linear region for dimensionless temperature. Using this relation, we find that this region extends up to  $y^+ \approx 3.7$  for  $Pr = 0.7$ . At lower fluid temperatures, the Prandtl number is higher and the region of validity of eq. 5.4 is larger.

Thus, we have found a constraint on the cell size for accurate heat transfer modelling. The dimensionless wall distance  $y^+$  should be at most 3.7. The value of  $y^+$  can easily be calculated from the flow field using eq. 5.1. For more details on the derivation of the equations presented above, the reader is referred to White [89].

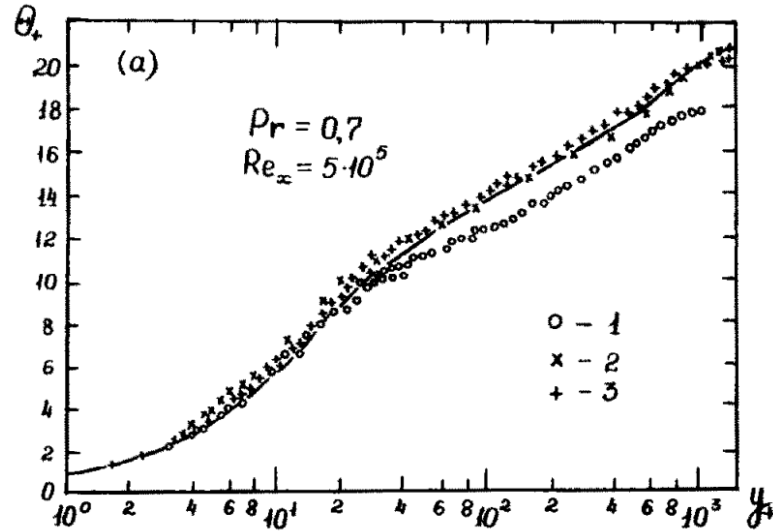


Figure 5.3: Experimental data on temperature profile in boundary layer at  $Pr = 0.7$  [103]. Note that  $\theta^+$  is equivalent to  $T^+$

Now we will see in practice how the heat transfer varies when the grid is refined near the boundary layer. Five test grids were defined, each with  $15 \times 15 \times 30$  cells. Even though the number of cells was equal for each grid, the refinement of the cells towards the walls differed. After performing the CFD simulations, the maximum and average  $y^+$  on the relevant walls was calculated for each grid. These values are shown in table 5.1.

Table 5.1: Calculated values for  $y^+$  for the different test grids

Grid	Bottom wall			Side wall		
	$y$ [ $\mu\text{m}$ ]	Max $y^+$	Mean $y^+$	$y$ [ $\mu\text{m}$ ]	Max $y^+$	Mean $y^+$
Very coarse in BL	1.7	16.4	9.8	0.52	18.2	6.7
Coarse in BL	0.99	11.3	5.7	0.31	12.6	3.7
Medium in BL	0.56	7.1	3.0	0.18	7.9	1.9
Fine in BL	0.32	4.0	1.5	0.10	4.6	1.0
Very fine in BL	0.17	2.1	0.8	0.056	2.5	0.5

The two grids that were coarsest in the boundary layer (BL) have almost no points in the region where eq. 5.4 is valid. Therefore, it is expected that these grids will generate an erroneous solutions. The other three grids all have most of their points within the region of validity (the average  $y^+$  is below 3.7). Therefore, it is expected that the results of these grids will be close. Still, some differences could be expected as the maximum  $y^+$  for the medium grid is still outside the linear region.

Figure 5.4 shows that the reasoning above was correct. The grids without a cell in the linear region have a substantial error in the heat flux. The maximum difference with respect to the very fine grid is 23.8% for the very coarse grid and 13.5% for the coarse grid. The grid with medium refinement in the boundary layer has a much lower maximum discrepancy of 2.0%, while that of the fine grid is 1.9%. The differences are largest near the exit of the channel. At this location, the highest temperatures are encountered. This results in an increased viscosity and higher  $y^+$  value for the same refinement. Simultaneously, the Prandtl number decreases and the region of validity shrinks. For these reasons, it is to be expected that the channel exit is the critical region for boundary layer grid refinement.

It should be cautioned that refining the grid near the walls inevitably sacrifices accuracy in the center of the domain. In light of this, a  $y^+$  near those obtained with the medium or fine grid (i.e. maximum  $y^+$  near 3.7, at the edge of the validity region) is probably optimal for global accuracy of the solution if the number of cells is restricted.

Note that fig. 5.4 shows the average normalized heat flux along the channel for each test grid. The heat transfer is divided only by the bottom area of the channel (not including the side wall area) to be

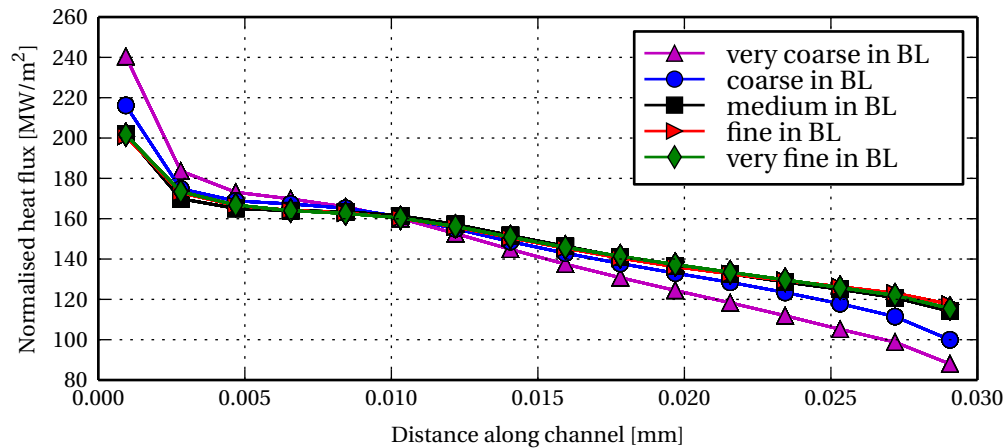


Figure 5.4: Comparison of normalised heat flux for different boundary layer refinements

consistent with the evaluation of heat flux in a rocket engine. In a rocket engine, the heat flux at the combustion chamber is calculated based on the surface area of the combustion chamber. This surface area is again in contact with the cooling channels. Therefore we only use the area of the channel that would be in contact with the combustion chamber to normalize the heat flux.

### 5.1.3. COMPARISON WITH REFERENCE DATA

The performance of limiters and the effect of refining the grid in the boundary layer have been examined. Using the conclusions from these investigations, solutions are now calculated and compared to the results found by Pizzarelli et al. [43]. Their results were obtained on a mesh with  $30 \times 20 \times 60$  cells, very similar to the current  $32 \times 20 \times 60$  OpenFOAM mesh.

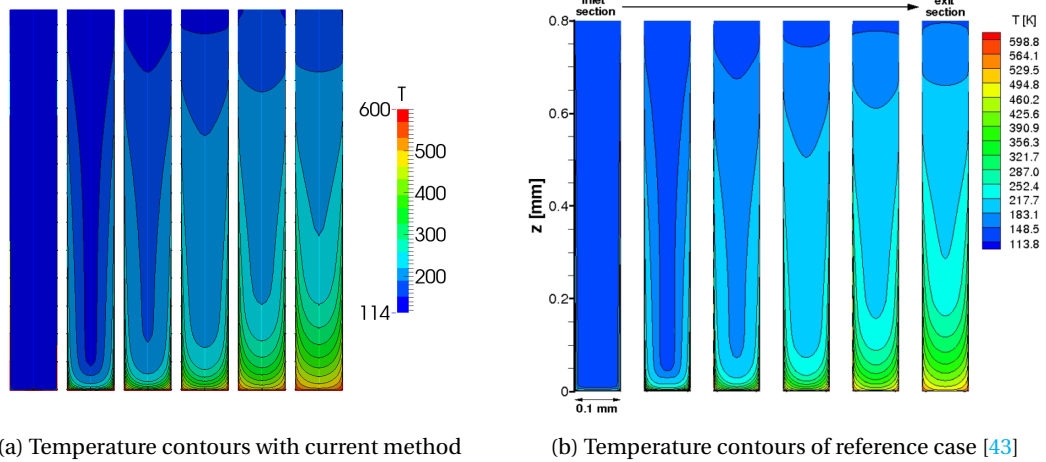
This section starts with a qualitative, global comparison of both solutions. The value of several fluid properties will be shown along cross-sections of the channel. The results from the current analysis are shown on the left and can be compared to the results from Pizzarelli et al. on the right. Cross-sectional slices were taken at the inlet, at consecutive intervals of 6 mm and at the exit. Although the colour scales do not agree perfectly, the contour lines are for the same values in both the reference data and the current data.

The first variable to be compared is the most obvious one to check in a heat transfer problem: temperature. Figure 5.5 shows coloured contour plots of the temperature on six cross-sections of the channel. Both solutions are very similar. The temperature starts at a uniformly low value and develops a stratified profile with hotter layers near the bottom and cooler layers near the top. The contour shapes and positions of both solutions match very well.

The density is a function of temperature and pressure. In this straight channel, the pressure variations along a cross-section are negligible. Therefore, the density profile in a single section is a direct consequence of the temperature profile. The comparison of current and reference data for density is shown in fig. 5.6. High density flow is found at the channel inlet and near the cold top; as the methane heats up its density drops. Because the flow is supercritical there is no abrupt phase change from liquid to gaseous. Nonetheless, the hot fluid behaves gas-like while the cold fluid behaves more like a liquid.

The differences between the density at the symmetry axis and the wall are well reproduced. For example, in the fourth section of fig. 5.6a, the horizontal density gradient at the top is small, then becomes large in the middle of the channel and decreases again towards the bottom. The same trend is seen in fig. 5.6b.

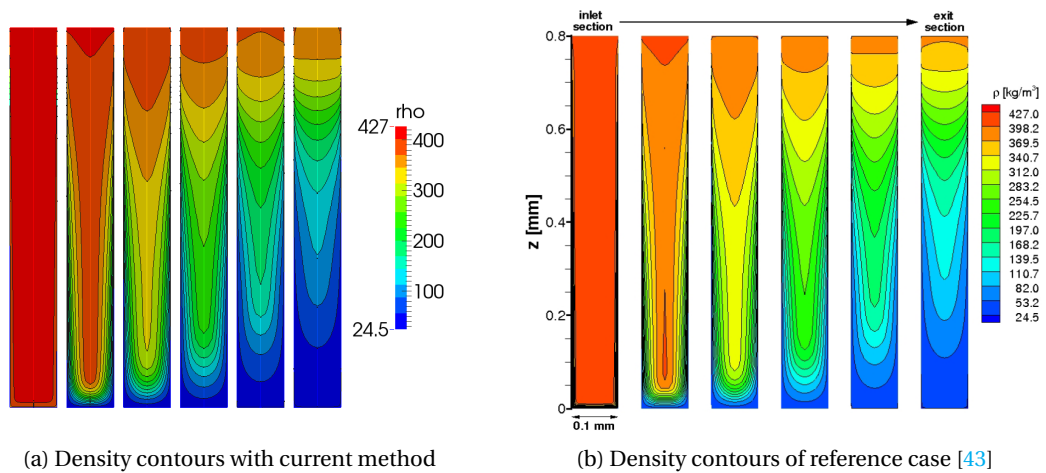
Figure 5.7 shows the streamwise velocity of the coolant. In both cases, the low density fluid near the bottom is accelerated to a much higher velocity than the liquid-like methane near the top. Near the end of the channel, this difference becomes especially large. As a result, the flow at the exit is highly



(a) Temperature contours with current method

(b) Temperature contours of reference case [43]

Figure 5.5: Comparison of temperature contours at various cross-section along the channel

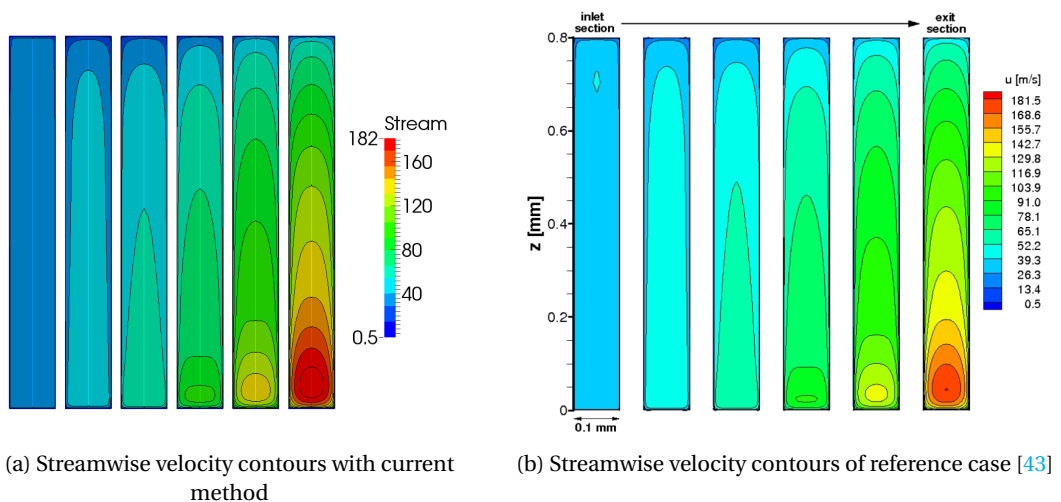


(a) Density contours with current method

(b) Density contours of reference case [43]

Figure 5.6: Comparison of density contours at various cross-section along the channel

stratified in terms of velocity. However, the velocity contours at the bottom of the channel are not at the same locations. It seems a higher velocity is reached in the OpenFOAM simulation.



(a) Streamwise velocity contours with current method

(b) Streamwise velocity contours of reference case [43]

Figure 5.7: Comparison of streamwise velocity contours at various cross-section along the channel

It has repeatedly been emphasised that the variation of fluid properties in a transcritical fluid is important to take into account. At this point, it is therefore interesting to consider one of these properties. In fig. 5.8, the specific heat at constant pressure is visible.

Clearly, there is a large variation in  $c_p$  along the channel and within a single cross-section. Unlike the density and temperature, the specific heat does not change monotonously from the hot bottom to the cold top. Instead, there is a zone of high  $c_p$  somewhere in the centre of the channel. Simultaneously, there is a zone of low thermal conductivity at this region. These are caused by the local extrema in these properties at the pseudo-critical temperature. The peaks become more pronounced near the end of the channel as the pressure drops closer to the critical pressure. This is the reason for the maximum  $c_p$  value in the ultimate cross-section.

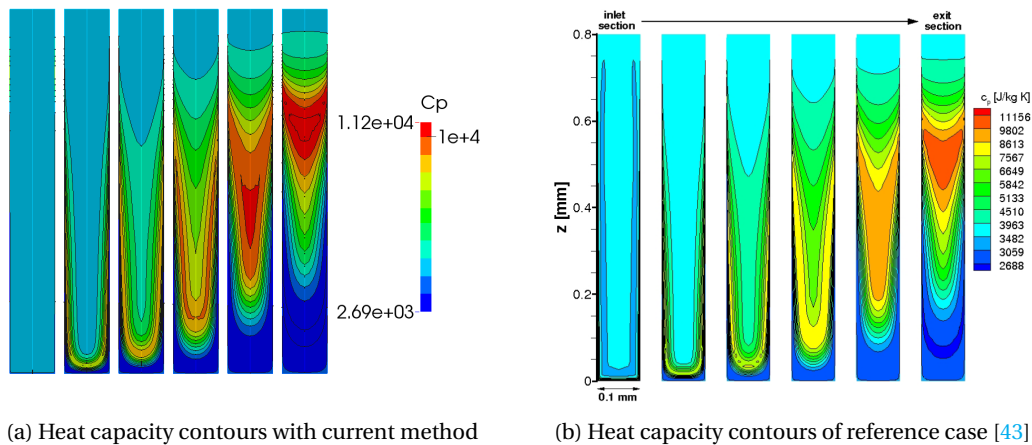


Figure 5.8: Comparison of heat capacity contours at various cross-section along the channel

Because the specific heat varies so drastically with temperature, these figures also show the biggest differences. For instance, in the penultimate slice of the OpenFOAM simulation there is an extra contour visible that is not present in the reference simulation. Nonetheless, the overall agreement remains excellent.

We can conclude from this first comparison that qualitatively, the results match the validation case very well. Now it is time to compare the two methods quantitatively and in more detail. To do this, we first compare the heat flux along the bottom and side wall at the channel exit.

The heat flux along the bottom wall is shown on the left side of fig. 5.9. The heat flux along the side wall is shown on the right side of the same figure. At the bottom wall, the maximum heat flux is 1.1% higher than in the reference analysis. At the side wall, the differences are larger. Near 0.6 mm from the bottom, there is a maximum positive difference of 2.7% because the kink in the heat flux is more pronounced. Near the top side, there is a negative heat flux with a minimum of  $-2.9 \text{ MW/m}^2$ , while the reference analysis found a heat flux of approximately  $-1.9 \text{ MW/m}^2$ .

This negative heat flux is caused by the boundary condition on temperature along the side wall. The temperature varies linearly from 600 K at the bottom to 130 K at the top. The fluid has been heated along the channel and due to mixing the fluid at the top is now warmer than 130 K. This results in the small region of negative heat flux. In reality, such a situation would not occur because conduction in the solid wall would prevent it from arising.

Figure 5.9 also shows the heat flux obtained with an enthalpy-based heat flux formulation, as opposed to a temperature-based formulation. In chapter 4, it was argued that this enthalpy-based formulation (used by e.g. Peeters et al. [101]) is incorrect for supercritical fluids because of the non-linearity between temperature and enthalpy. Figure 5.9 shows that the resulting difference is rather minor; only at the kink a very small deviation is visible.

The mass-averaged temperature (eq. 5.5) found along the channel also corresponds very well with the reference data. This is illustrated by fig. 5.10. The mass-averaged temperature from the analysis of the

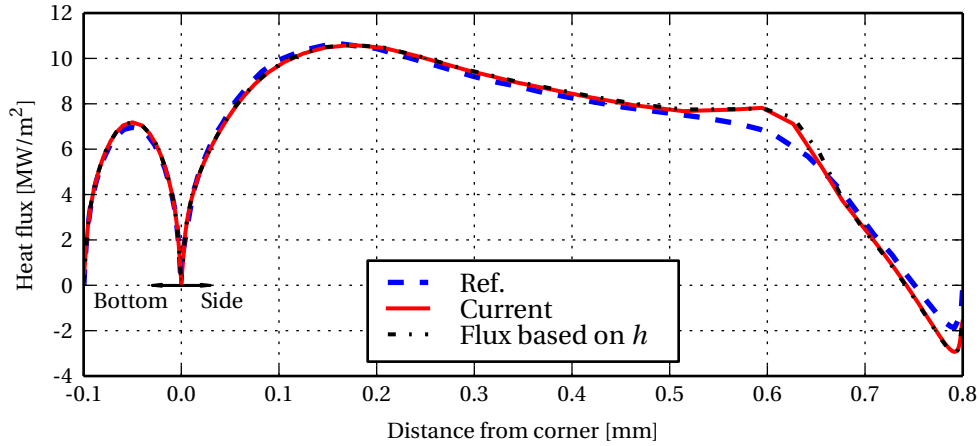


Figure 5.9: Comparison of wall heat flux at exit cross-section of channel with reference case [43]

fine grid agrees diverges slightly from the reference value up to a maximum difference of 5.7 K.

$$T_{\text{ma}} = \frac{1}{\dot{m}} \int \rho \mathbf{U} \cdot d\mathbf{A} \quad (5.5)$$

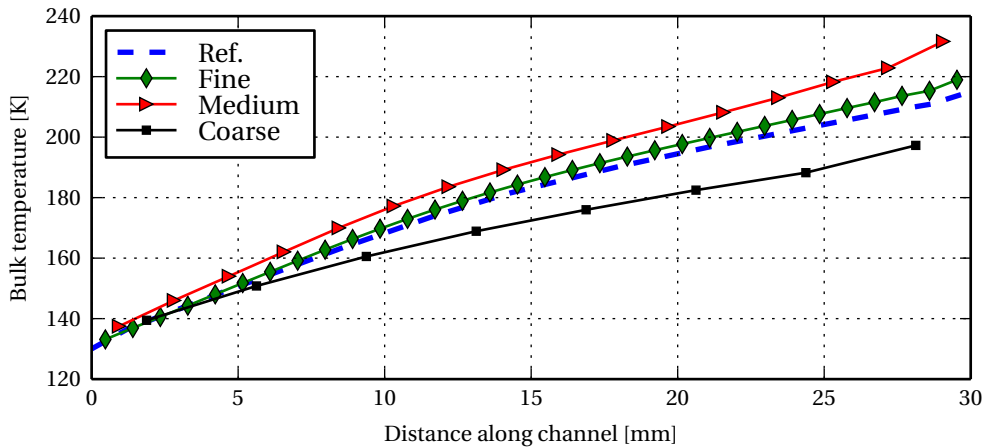


Figure 5.10: Comparison of bulk temperature along channel with reference case [43]

To gauge the performance of a cooling channel, an interesting measure is the cooling efficiency given by eq. 5.6. This is the heat exchanged per length of channel per mass flow. Figure 5.11 shows the cooling efficiency in the reference as well as the current analysis.

$$\eta_c = \frac{1}{\dot{m}} \frac{d\dot{q}}{dx} \quad (5.6)$$

From fig. 5.11 it is clear that in the largest part of the channel, both analyses predict a very similar cooling efficiency. The largest difference is at the inlet, where OpenFOAM predicts a substantially higher efficiency. The reason for this overprediction of efficiency is the relative lack of cells in streamwise direction at the inlet. The fluid cell directly adjacent to the wall has a temperature of 130 K, leading to a high heat flux. In reality, a boundary layer would start to form.

Figure 5.10 also shows the mass-averaged temperature profiles obtained with the medium and coarse grid. As discussed earlier, the flow behaviour is dominated by the heat flux. For this reason, mass-averaged temperature is a sensible parameter to use when comparing the performance of the grids.

The most surprising result from fig. 5.10 is that the solution does not approach the grid-independent

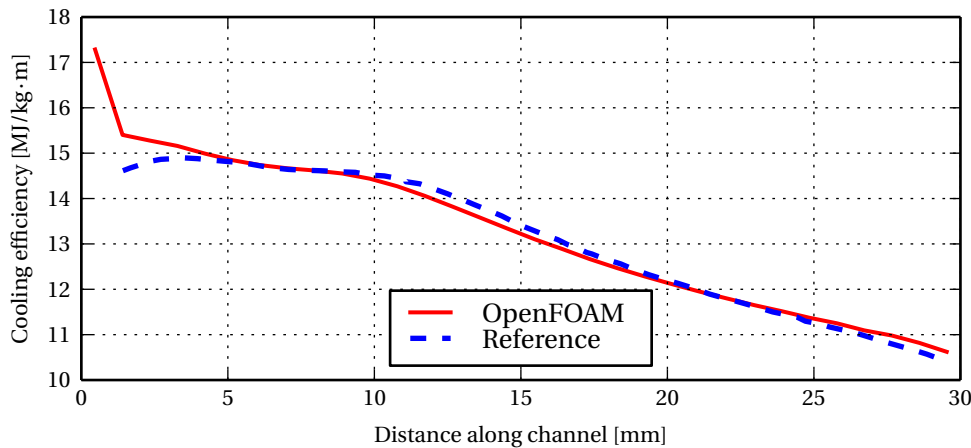


Figure 5.11: Comparison of cooling efficiency along channel with reference case [43]

solution monotonously, as could be expected from CFD theory [88]. The coarse grid underpredicts the mass-averaged temperature, while the medium grid overpredicts it. The coarse grid has maximum  $y^+$  values in the order of 20 and average values of around 11, which is clearly outside the linear region of the temperature profile as discussed in section 5.1.2.

Whatever the cause, the fact that the error does not decrease monotonously thwarts any attempt to estimate the true order of the scheme. Usually, this order can be estimated by comparing the solution on three grids. Richardson extrapolation can then be used to estimate the grid-independent solution (a solution that is free of discretisation errors) [88]. This problem will be addressed in the next section.

Now it is also interesting to investigate the calculation time of the solution on the different grids. All calculations were performed in parallel on 4 Intel Xeon CPU E5-2670v2 processors with 2.5 Ghz clock speed. (Of course this was overkill for the coarse grid, but it was done for the sake of comparison.) Table 5.2 shows the calculation time for 3000 iterations on each grid. Convergence was reached in each case after these iterations. Note that the values in table 5.2 do not denote the aggregated calculation time; when running on a single processor, the calculation would take approximately four times longer.

Table 5.2: Calculation time for 3000 iterations

Grid	Total time [s]	Time per iteration [s]	Time per iteration per cell [ $\mu$ s]
Coarse	95	0.032	53
Medium	852	0.284	59.2
Fine	5623	1.87	48.8

Table 5.2 shows that the calculation time increases with the number of cells, as expected. The time per iteration per cell, however, does not increase with the amount of cells. The fine grid is faster per iteration per cell than the coarse and medium grids. This is likely because running the code in parallel is inefficient for grids with a small number of cells.

In a 2011 study, Pizzarelli et al. note that a CFD computation with their method takes 70 hours or for a mesh with 36000 cells [29]. Let us assume that the 70 hours refers to the calculation time for a single processor (or the aggregated calculation time of parallel run). Then we must compare the 70 hours to 6.2 hours for the calculation on the fine mesh of 38400 cells in OpenFOAM, meaning their method is 11 times slower. This is a difference in computation time of an order of magnitude! Even when we account for differences in the processors (the Intel Xeon CPU E5-2670v2 was not even available in 2011), the current OpenFOAM method is several times faster than the in-house solver of "La Sapienza" University of Rome.

The most likely reason for the difference in computation time is that theirs is an unsteady solver, while

the one shown in this thesis is steady-state. Because we are primarily interested in the steady-state behaviour, this is not a problem. The possibility to analyse transient behaviour is sacrificed for a tenfold decrease in computation time.

#### 5.1.4. ERROR ESTIMATION

Throughout the previous sections, the accuracy of the CFD simulation has been mentioned in some relevant areas. Now an attempt will be made to estimate the errors in the solution on the fine grid in a systematic way. The approach of Ferziger and Perić [88] will be followed.

The errors in a CFD solution can be divided into three types. They will be discussed in the following order:

1. Iteration errors
2. Discretisation errors
3. Modelling errors

##### ITERATION ERRORS

Iteration or convergence errors are the errors made in calculating the solution to the linear matrix equations. That is, the iteration error is the difference between the calculated and the exact solution of the linearised equations.

There are two common ways to see if a simulation has converged. One is to see if the residuals of the simulation have been decreased by several orders of magnitude. The other is to use a monitoring variable that indicates the state of the system (e.g. a force). Both methods were used in this case, as monitoring variable the mass-averaged temperature at the channel exit was chosen. This variable represents the integrated heat flux; if it no longer changes this indicates that the system has probably achieved steady state.

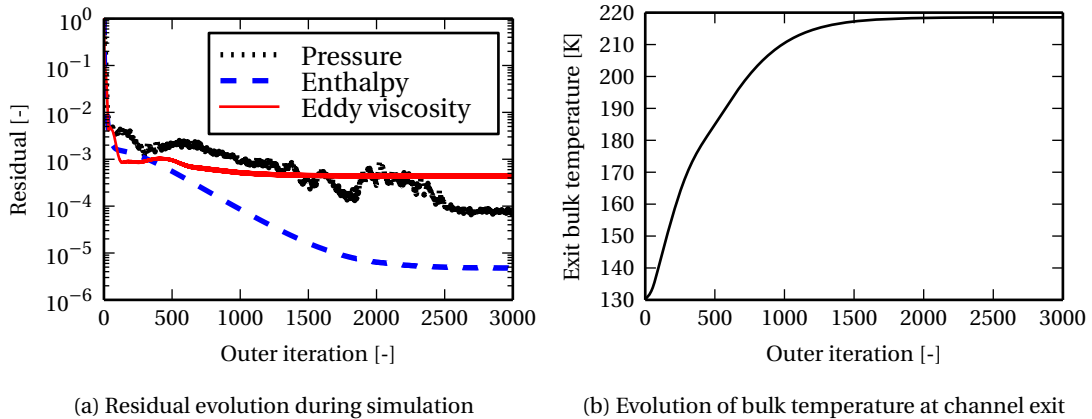


Figure 5.12: Convergence of simulation on fine grid

Figure 5.12 shows these indicators of convergence. Figure 5.12a demonstrates that the residuals have fallen by several orders of magnitude by the end of the simulation. The residual of the pressure (i.e. the momentum equation) has fallen by 4 orders of magnitude, the residual of the enthalpy (energy equation) by 5 and the residual of  $\tilde{\nu}$  (turbulence equation) by 3 orders. According to Ferziger and Perić, if the residuals have fallen by 3 to 4 orders of magnitude, the solution is accurate within 0.01-0.1% [88]. Keep in mind that this accuracy only addresses the iteration error, i.e. how closely the solution matches the exact solution of the linearised system of equations.

It is interesting to note that both the enthalpy and the  $\tilde{\nu}$  residuals start oscillating as they decrease. This is probably caused by the variable fluid properties. When running a similar simulation with constant fluid properties, the residuals decreased faster and without oscillation.

Figure 5.12b confirms that the simulation has converged; the bulk temperature at the outlet no longer

changes. In fact, the maximum change in the last 100 iterations is 0.002 K.

### DISCRETISATION ERRORS

Discretisation error is the error caused by the division of the domain into finite volumes. A common way to evaluate the discretisation error is by Richardson extrapolation [88]. The same calculation is carried out on three grids; from the results the order of convergence can be calculated. In addition, the error as well as the grid-independent solution can be estimated.

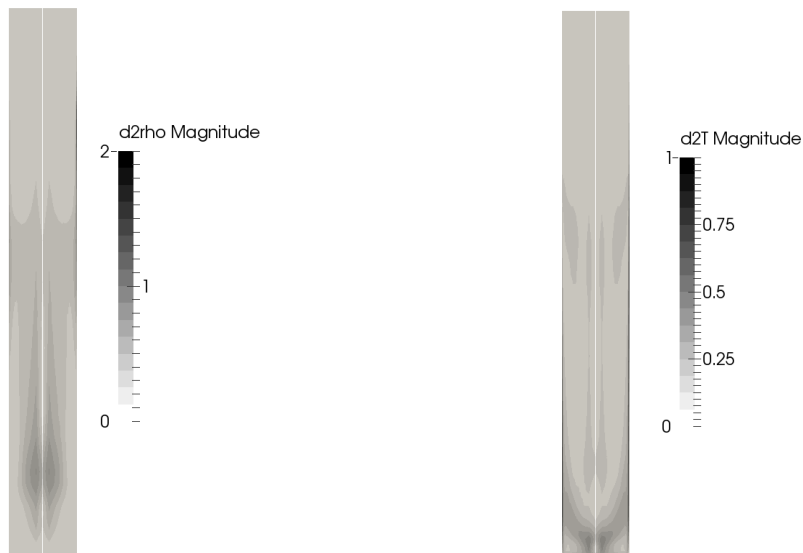
A problem is that this method only functions if all three grids are fine enough that the error is decreasing monotonously. Figure 5.10 demonstrated that this requirement was not fulfilled for all three grids.

Generating solutions on ever finer grids is not always possible, as it could require too much computational resources. In addition, it is useful to know where the discretisation errors are largest so the grid can be refined accordingly. Another method to estimate the discretisation error should then be used, one that only requires the calculation result on a single grids.

A method based on Taylor expansion can be used to calculate the leading truncation error term. Because the CFD method used here is second order, it estimates the solution as linear between two cell centres. The largest error therefore occurs at regions where the second derivative of the solution is large [88]. If the grid is orthogonal, the error (err) of a generic variable  $\phi$  can be numerically estimated with eq. 5.7 [87].

$$\text{err}(\phi) \approx \frac{1}{24} \left| \Delta x^2 \frac{\partial^2 \phi}{\partial x^2} + \Delta y^2 \frac{\partial^2 \phi}{\partial y^2} + \Delta z^2 \frac{\partial^2 \phi}{\partial z^2} \right| \quad (5.7)$$

Figure 5.13 shows the discretisation errors estimated with eq. 5.7 for a slice at the middle of the channel. The maximum errors in the density are around 0.5% (absolute error of  $1.41 \text{ kg/m}^3$ ) and located near the side and bottom walls (hard to see on the figure). This is in line with the expectations, there are strong temperature and density gradients inside the thermal boundary layer. The error terms in  $y$  and  $z$  direction, are an order of magnitude higher than in the  $x$  direction. This indicates that grid refinement along these directions would be more beneficial than refinement along the length of the channel.



(a) Error in density according to eq. 5.7

(b) Error in temperature according to eq. 5.7

Figure 5.13: Discretisation error estimates

The temperature error shows behaviour similar to the density error. The maximum error on the slice

is approximately 0.35% (0.91 K). The highest error in  $y$  direction is located at the side wall, while the maximum error in  $z$  direction is at the bottom wall, as expected. The error in the rest of the domain is much smaller.

On the complete domain, the largest discretisation errors are found at the inlet. Here, the discretisation error in  $x$  direction is the largest contributor. The maximum error in temperature is 29.2 K, while the maximum density error is  $23.5 \text{ kg/m}^3$ . These large errors are due to the development of the thermal boundary layer. At the inlet, the temperature is still at a uniform 130 K. A thin layer of hot methane is established in the next cells, creating large gradients. The maximum error decreases to about 1% after five cells.

We can conclude that the average discretisation error is approximately 1%. This is the approximate error at the wall in most of the domain, which defines the heat transfer rate. From the location of maximum errors, two conclusions can be drawn. In general, refinement of the cells along the cross-section ( $y$  and  $z$  direction) of the channel will benefit the accuracy the most. However, near the inlet a grid that is refined in the  $x$ -direction is more important.

Another part of discretisation error is due to the use of look-up tables for the fluid properties instead of calculating them using the actual equations. In chapter 2, it was shown that this error is below 0.015%. The discretisation errors of the fluid properties do not have a substantial effect on the error of the simulation.

### MODELLING ERRORS

The modelling errors are probably the largest errors present in the simulation. The Navier-Stokes equations are thought to accurately model continuum fluids. RANS turbulence models on the other hand, are engineering models that are used to estimate the average effect of turbulence on the flow behaviour.

To make matters worse, the solution to this heat transfer problem is highly dependent on the turbulence model. Turbulent heat transfer depends on the values of  $\kappa_T$  (turbulent thermal conductivity) and  $\mu_T$  (turbulent viscosity). Those values are calculated by the turbulence model and in this way directly affect the solution of the simulation. As will be shown later in this thesis, the choice of turbulence model has a substantial effect on the main parameters of interest (e.g. fluid bulk temperature and heat flux).

To quantify the modelling errors, comparison with experimental data is necessary. This will be done in section 5.3. However, as a first demonstration for the importance of modelling errors, a comparison will be made between the Spalart-Allmaras turbulence model and the  $k-\epsilon$  turbulence model. Both analyses were performed with the same boundary conditions, on the same grid.

Figure 5.14 shows the bulk temperature obtained with the two different turbulence models. Although the general trend is the same, the temperature difference is enormous. The exit mass-averaged temperature found with the  $k-\epsilon$  model is 274 K, 55 K higher than with the Spalart-Allmaras model. The total heat transferred to the fluid with the  $k-\epsilon$  model is more than 60% higher than the Spalart-Allmaras heat transfer!

At least one of the turbulence models results in a very large modelling error. The 60% difference between the models is substantially larger than both the iteration error and the discretisation errors.

The equations that were used to calculate the fluid properties of methane also contain model errors. As shown in section 2.1, the errors in the density is below 0.05%. The maximum errors in thermodynamic ( $h$ ,  $c_p$ ) and transport properties ( $\mu$ ,  $\kappa$ ) are in the order of several percent in the critical region; usually they are much smaller.

The modelling error caused by the turbulence model is the dominating factor for the error of the simulation as a whole. For this reason, comparison with experimental data is vital. Experimental validation will allow for the selection of a suitable turbulence model with a minimal modelling error.

In summary, the errors of the simulation that was performed are given in table 5.3. The iteration errors

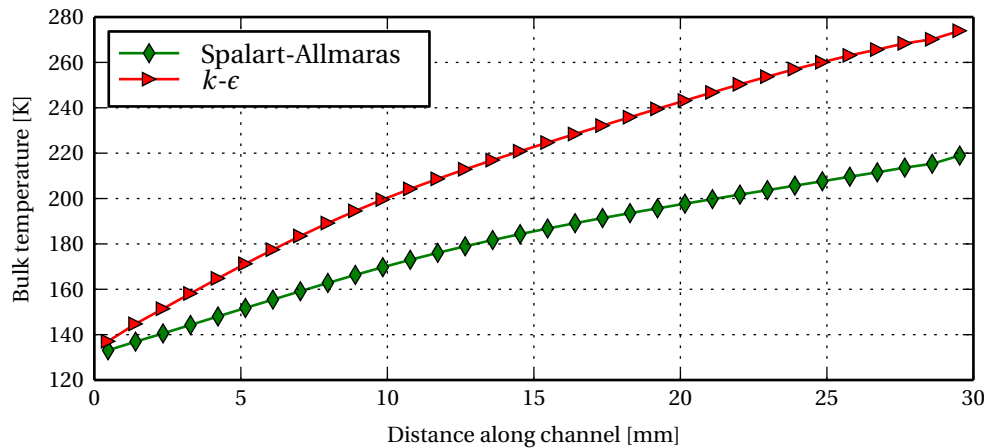


Figure 5.14: Comparison of bulk temperature along channel for  $k-\epsilon$  and Spalart-Allmaras turbulence model

are the smallest, in the order of 0.1 to 0.01%. The discretisation errors are for the largest part of the domain around 1%. The modelling error may be as high as 60%, as two different turbulence models result in radically different results.

Table 5.3: Estimate of simulation errors

Iteration error	$\approx 0.1-0.01\%$
Discretisation error	$\approx 1\%$
Modelling error	$\approx 60\%$

### 5.1.5. CONCLUSION

The aim of the first validation case was mainly to verify whether the equations were implemented correctly in OpenFOAM and whether the typical features of supercritical flow could be reproduced. From the figures presented at the start of this section, it was clear that these features could be reproduced. A good example was the local peak in  $c_p$ , inhibiting heat transfer from the bottom layer to the top layer.

Furthermore, the comparison of both local heat fluxes and global cooling efficiency showed excellent agreement with the reference analysis. This demonstrates that the model as currently implemented in OpenFOAM produces results comparable to the state of the art in supercritical fluid modelling. The first validation case can thus be considered successful.

## 5.2. NUMERICAL CONJUGATE HEAT TRANSFER ANALYSIS

The second validation case is a numerical conjugate heat transfer case. In addition to CFD calculations of the fluid, thermal transport in the surrounding solid is also modelled. This coupled fluid-solid analysis is called conjugate heat transfer (CHT) analysis. Using such a coupled method is required to predict the wall temperature of a regeneratively cooled rocket engine.

Before comparing the conjugate heat transfer model with experimental data in section 5.3, it is first compared to an existing numerical CHT model. In this way, numerical errors can be estimated. The validation case is the analysis presented in [104] by Pizzarelli et al.

The case consists of the analysis of a straight, constant rectangular cross-section channel filled with methane. The temperature and mass flow at the inlet are prescribed; the same holds for the exit pressure. The channel is 1 mm wide and 3 mm high. It is surrounded by a copper alloy that is 1 mm thick below the channel and next to the channel. This copper block is heated from below with a uniform, prescribed heat flux. The top and sides of this block are modelled as adiabatic. Figure 5.15 summarises

the geometry and boundary conditions of this simulation case. The point of this case is to analyse and quantify the cooling effect of the methane flowing through the channel on the copper wall.

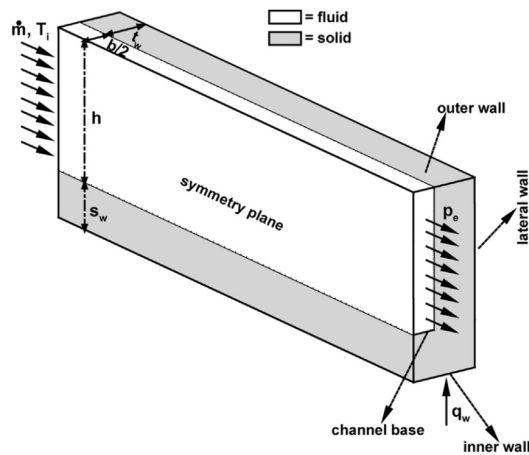


Figure 5.15: Conjugate heat transfer numerical validation case [104]

Pizzarelli et al. have analysed this case using three different meshes: a coarse, medium and fine mesh. These have the following number of cells in the fluid domain:  $16 \times 16 \times 64$ ,  $32 \times 32 \times 128$  and  $64 \times 64 \times 256$ . These cell numbers are in the directions length  $\times$  half-base  $\times$  height. The meshes are more refined in the direction of the boundary layer. The flow symmetry is exploited by simulating only half the domain.

Before performing this validation, it was hypothesised by the author that refinement of the mesh in streamwise direction was more important. This hypothesis was partly the result of conversations with CIRA engineers with experience in supercritical flow modelling. To test this hypothesis, the grids used for this validation case were more refined in  $x$  direction than the grids by Pizzarelli et al. To reduce computation time, there were less cells in  $y$  and  $z$  direction.

Three grids were created, all of which had a similar height of the first cell at the wall. Therefore, the  $y^+$  values for all meshes are also similar. As was shown in section 5.1, the  $y^+$  value is of enormous importance for the wall heat transfer. By keeping this value the same, this influence can be eliminated and the focus of the grid refinement study is on the effect of the number of cells.

The coarse mesh has  $50 \times 10 \times 25$  cells, the medium mesh  $100 \times 20 \times 50$  and the fine mesh  $200 \times 40 \times 100$ . All meshes have a slight refinement in  $x$ -direction at the inlet and outlet. Because the  $y^+$  value at the walls is similar, the main difference between the meshes is in the growth factor, i.e. how fast the cells become bigger away from the wall. Table 5.4 summarises the mesh refinement parameters of the three meshes. The average  $y^+$  value for the walls in contact with the solid was approximately 0.65 for all meshes.

Table 5.4: Mesh parameters for coarse, medium and fine mesh for CHT validation case

Grid	Bottom wall		Side wall	
	$y$ [ $\mu\text{m}$ ]	Growth ratio	$y$ [ $\mu\text{m}$ ]	Growth ratio
Coarse	0.27	1.92	0.27	1.97
Medium	0.27	1.31	0.28	1.33
Fine	0.25	1.13	0.28	1.13

The medium and fine grids that were adopted for OpenFOAM calculations are shown in fig. 5.16a.

The meshes by Pizzarelli et al. and the OpenFOAM meshes do not have the same amount of cells in each direction. Though the cell sizes used by Pizzarelli et al. is not known, casual observation of fig. 5.16 shows that their grids and the ones presented here are dissimilar in terms of refinement of the fluid domain. The meshes for the solid domain are extremely similar, though these are

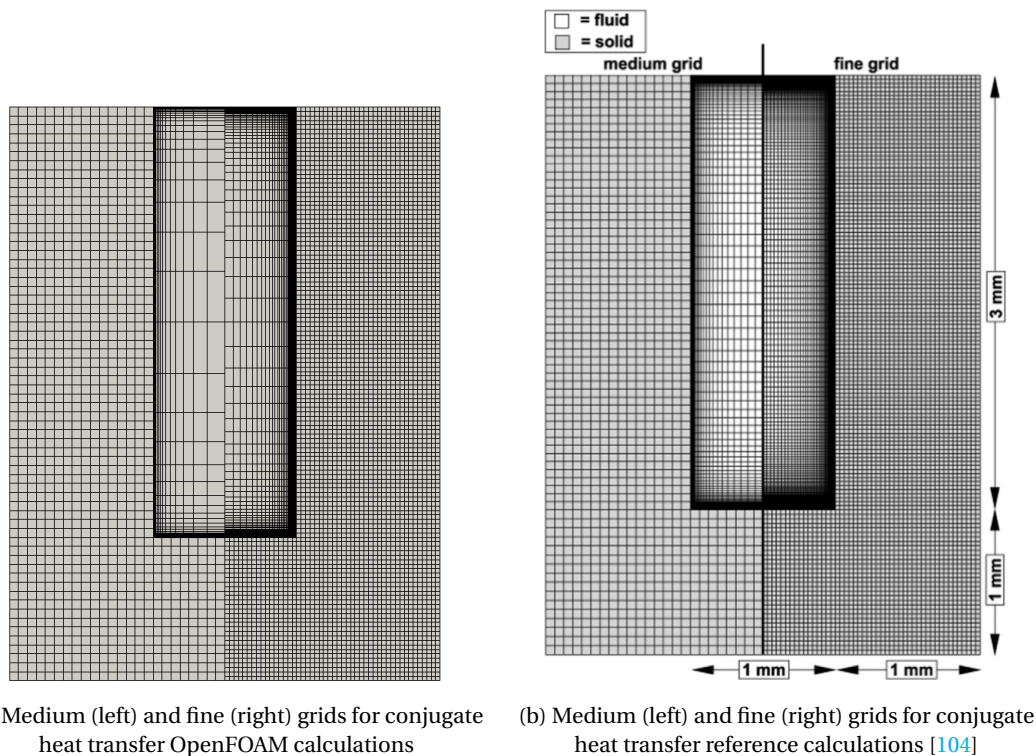


Figure 5.16: Comparison of current and reference grids

not expected to affect the solution much because the heat transfer equation is such a simple linear equation.

We will now compare the results from CHT simulations in OpenFOAM to the results published by Pizzarelli et al. All simulations are performed with a fluid inlet temperature of 120 K and mass flow of 20 g/s. The prescribed outlet pressure is 53.4 bar, while the heat flux at the bottom wall is 11.1 MW/m<sup>2</sup>. The thermal conductivity of the solid material is fixed at 387.6 W/m·K. First, a channel with smooth walls will be analysed. Then the effects of wall roughness will be investigated. Finally, the influence of the turbulent Prandtl number on the results will be examined.

### 5.2.1. SMOOTH WALLS

In terms of numerical modelling, performing calculations on smooth walls is easier than on rough walls. CFD calculations do not require additional modelling for smooth walls, like they do for including roughness effects. It will later be shown that roughness effects play a substantial role in rocket engine cooling channels. Their inclusion will be necessary to accurately predict realistic heat transfer rates, but when comparing numerical models it is possible to disregard them at first.

Recall that the purpose of the conjugate heat transfer model is to analyse the cooling effect of methane on the surrounding solid. In addition, CHT provides the possibility to calculate the wall temperature. The wall temperature depends on the cooling effect and is an important measure in rocket engine cooling design. Because it is such an important metric, we will use it to compare the results of the OpenFOAM calculations to the reference calculations.

Figure 5.17 shows the wall temperature along the channel obtained with the three meshes and compares them to the reference results. These wall temperatures were obtained at the bottom of the solid domain along the centerline and represent the maximum temperature in the solid.

All wall temperature profiles in fig. 5.17 show a clear peak, indicating that heat transfer deterioration is taking place. In a regular, non-supercritical single-phase fluid, we would not expect such a peak. Instead a minimal wall temperature would be found at the inlet, increasing monotonically towards

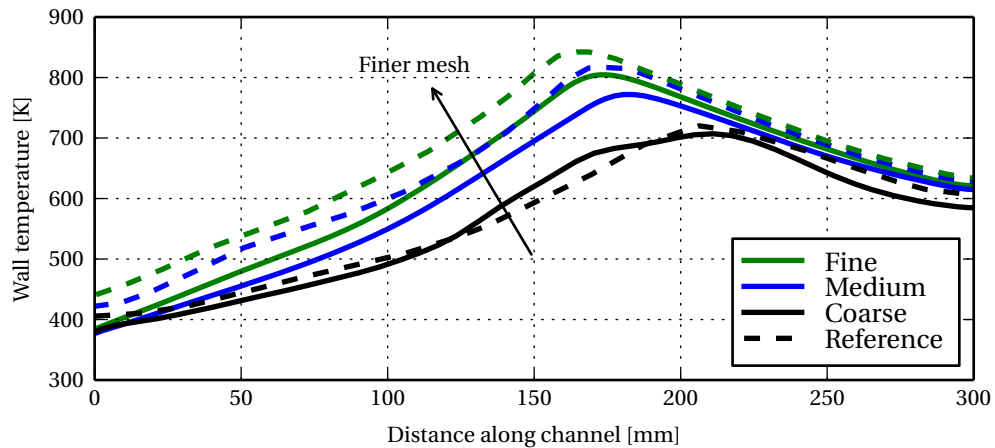


Figure 5.17: Comparison of inner wall temperature of solid along channel with reference case [104]

the outlet as the thermal boundary layer grows and the bulk temperature of the fluid increases.

Because the methane in this case is at supercritical pressure, different phenomena occur. Pizzarelli et al. explain the heat transfer deterioration by the origination of a near-gaseous layer near the hot wall [104]. This high temperature layer has a low density and low thermal capacity, insulating the wall and increasing its temperature. Further along the channel, the low-density region is larger, increasing the fluid velocity. This in turn increases the heat transfer rate and leads to heat transfer recovery [104]. These mechanisms are illustrated in fig. 5.18 and were already described in 1979 by Jackson and Hall [26].

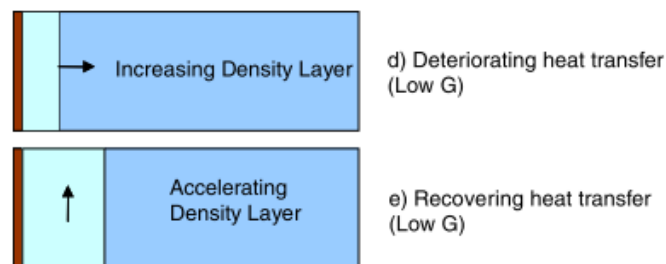


Figure 5.18: Heat transfer deterioration and recovery mechanisms [27]

A contributing factor is that there exists a region of both high specific heat and low thermal conductivity. Figure 5.19 shows isobaric specific heat ( $c_p$ ) contours at five cross-sections along the channel. Near the pseudo-critical temperature, the fluid has a local maximum specific heat and minimum thermal conductivity. This means the gas-like layer near the wall is insulated from the liquid-like core of the fluid. This phenomenon has also been described by Jackson and Hall [26]. As expected, the maximum  $c_p$  value along the channel is reached at the outlet, where the static pressure is lowest and therefore closest to the critical point.

The result of this heat transfer deterioration is a maximum wall temperature around 180 mm from the channel inlet. The temperature of the solid and fluid are shown at this location in fig. 5.20, both for OpenFOAM and the reference solution. The results are similar but the solid temperature contours are not located at the same height. OpenFOAM predicts a lower wall temperature at this location, which was already visible in fig. 5.17. The fluid temperature contours are close to the wall; the core fluid remains at fairly low temperature with respect to the methane near the wall.

Returning to fig. 5.17, it is clear that both the current and reference results are converging with an increasingly fine mesh. However, the OpenFOAM results are not converging as rapidly as the reference results. The OpenFOAM results of the fine mesh almost coincide with the reference results on the medium mesh of Pizzarelli et al. This shows the fallacy of the hypothesis stated earlier: clearly

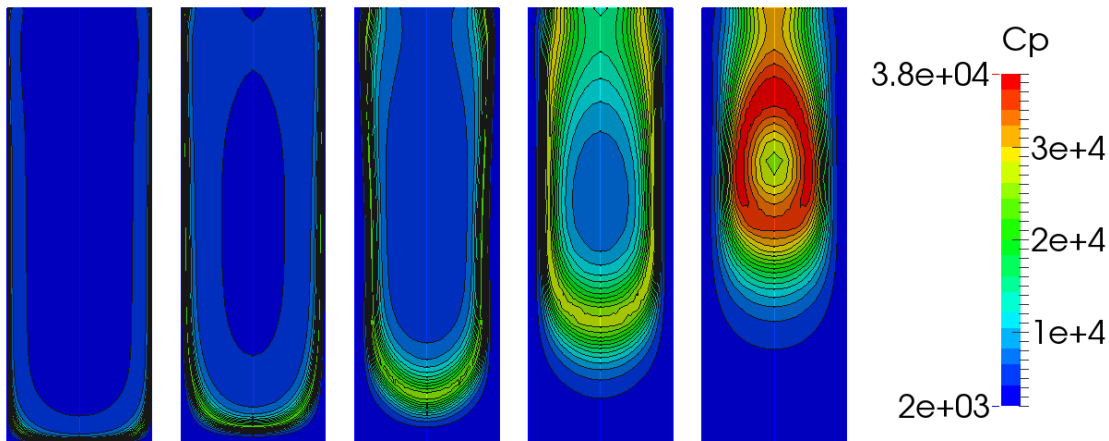
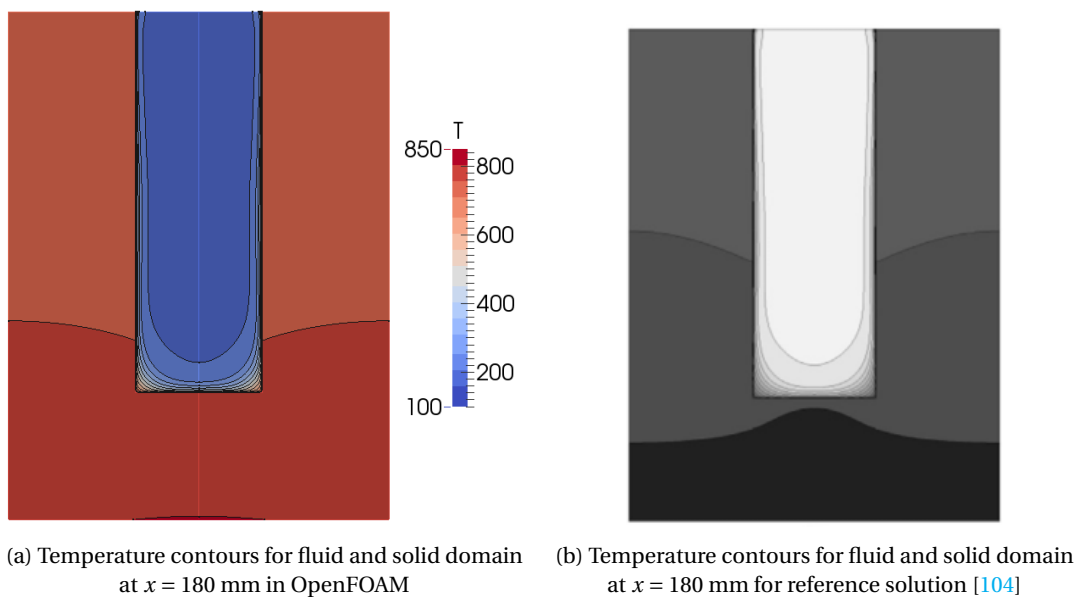


Figure 5.19: Specific heat contours along the channel at 60 mm, 120 mm, 180 mm, 240 mm and 300 mm



(a) Temperature contours for fluid and solid domain at  $x = 180$  mm in OpenFOAM (b) Temperature contours for fluid and solid domain at  $x = 180$  mm for reference solution [104]

Figure 5.20: Comparison of temperature contours of OpenFOAM and reference calculations

the number of cells in  $y$  and  $z$  direction (i.e. perpendicular to the streamwise direction) is most important to obtain grid-independent results, more important than the number of cells in streamwise direction.

The maximum wall temperature increases from 707 K on the coarse mesh to 772 K on the medium mesh to 805 K on the fine mesh. According to Richardson extrapolation, a further increase of approximately 33 K could be expected for a fully grid-independent solution. This is relatively consistent with the results obtained by Pizzarelli et al. The peak wall temperature value found by Pizzarelli et al. is 842 K, 37 K higher than the maximum value predicted by OpenFOAM.

The pressure drop along the channel is not nearly as sensitive to the adopted mesh. For the coarse mesh, a total pressure drop of 3.14 bar was found. This drop decreases to 3.05 bar for the medium mesh and 3.02 bar for the fine mesh. Pizzarelli et al. reported a total pressure drop of 2.8 bar for the case with smooth walls.

To further investigate the results, it is instructive to look at the bulk temperature along the channel. At this moment, it is important to note that the bulk temperature is not equal to the mass flow-averaged temperature found with eq. 5.5. Instead, the bulk temperature is the temperature at which the fluid would be if it remained at the same pressure, but all thermal energy would be equally dis-

tributed.

Since temperature and enthalpy are not linearly related in supercritical flows, the bulk temperature is not necessarily the same as the mass flow-averaged temperature. To find the bulk temperature, one must take the mass flow-averaged enthalpy of the fluid and find the corresponding temperature using the thermodynamic models of chapter 2.

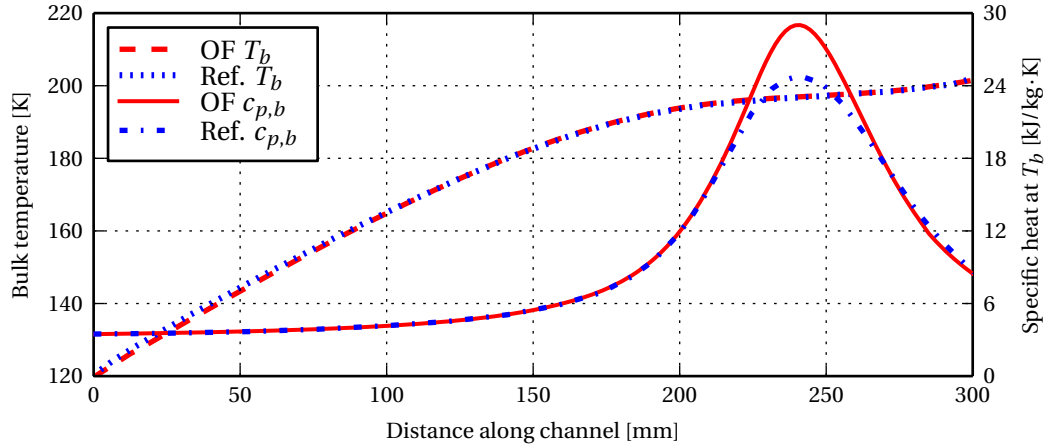


Figure 5.21: Comparison of methane bulk temperature and corresponding specific heat along channel with reference case [104]

Figure 5.21 shows the bulk temperature found in this manner for both the OpenFOAM and the reference analysis. In addition, it shows the specific heat at this bulk temperature. The bulk temperature agrees marvellously with the reference results; the curves are close to identical.

The specific heat values deviate around the pseudo-critical temperature. This is because Pizzarelli et al. use a different model for the thermodynamic properties, giving different results around this pseudo-critical temperature. Here it should be emphasized that fig. 5.21 does not show the bulk specific heat, but rather the specific heat corresponding to the bulk temperature. The deviation in specific heat only influences those few cells that are around the pseudo-critical temperature and not the majority of cells that are relatively far away from this temperature.

It was further checked if the total enthalpy exchanged was consistent for the complete simulation. The total heat impressed at the hot part of the solid domain is 4995 W. At convergence, the heat flux from the solid domain into the fluid domain was 4994.8 W, while the reverse heat flux was 4994.99 W. These values show that the heat exchanged is consistent, although small errors are present. The difference between enthalpy inflow and enthalpy outflow is 4971.52 W. The remainder of the energy is converted to kinetic energy; the fluid is moving at higher velocities at the outlet than at the inlet.

In conclusion, we can say that the software performs well for this conjugate heat transfer problem. The bulk temperature predicted by OpenFOAM is almost exactly the same as that predicted by Pizzarelli et al. Checks on the conservation of energy show that all heat is transferred towards the fluid, as expected in a steady state analysis. Unfortunately, a poor choice of grid resulted in poor grid convergence. A grid-independent solution has not been found, but Richardson extrapolation of the current solutions predict a maximum wall temperature in line with that predicted by Pizzarelli et al.

### 5.2.2. INFLUENCE OF ROUGHNESS

As discussed in chapter 4, the wall roughness of the channel influences both skin friction and heat transfer at the wall. This in turn affects the wall temperature and pressure drop, two important design parameters for the cooling system. Therefore, the influence of wall roughness is now investigated. The implemented roughness model is one proposed by Aupoix and Spalart [97] and referred to as the "*Boeing extension*" in their paper. Pizzarelli in personal communication affirmed that they also used this model for the roughness modelling with Spalart-Allmaras.

First, the same case is run again, but now with a wall roughness height of  $4.5\ \mu\text{m}$ . Figure 5.22 shows the wall temperatures obtained with the three meshes as compared to those published by Pizzarelli et al. Unlike in the smooth wall case, OpenFOAM now overpredicts the wall temperature. The solutions found by OpenFOAM seem to converge on an even higher maximum wall temperature.

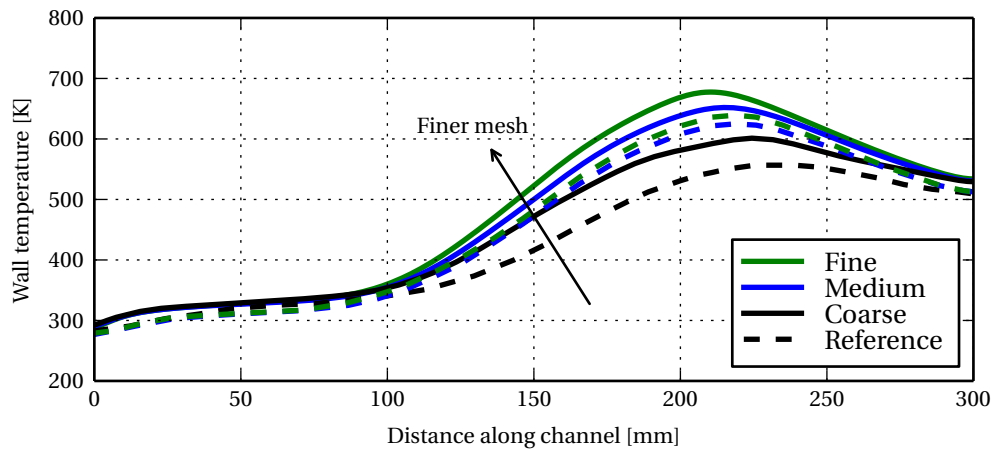


Figure 5.22: Comparison of inner wall temperature of solid along rough-walled channel with reference case [104]

To discover what is happening, it is interesting to look at the variation of fluid properties along the centreline of the channel at 150 mm in fig. 5.23. Figure 5.23a shows the temperature profile close to the bottom wall (the first 0.1 mm). It is clear that for all grids displayed, there are sufficient grid points to have a proper solution. The fine grid has several grid points inside the viscous sublayer with linear temperature distribution, assuring a correct heat flux is calculated. In addition, the grid points are concentrated in the region of the highest gradient: near the wall.

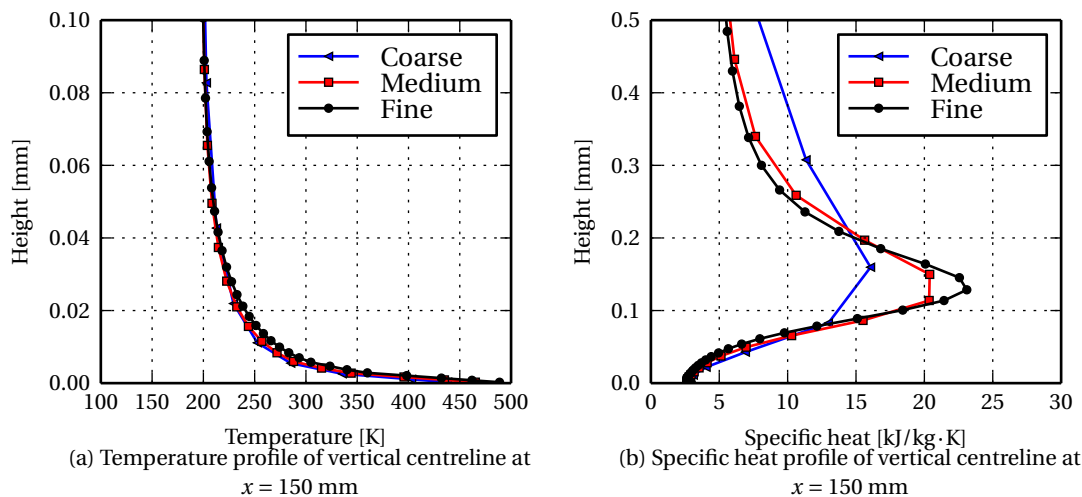


Figure 5.23: Temperature and specific heat profiles for rough wall on three grids

Figure 5.23b shows the variation of  $c_p$  along the same centerline, from the bottom to a height of 0.5 mm. Here we have a different situation: though the grid points are still concentrated near the wall, the highest gradients are found roughly at a distance between 0.1 and 0.2 mm from the wall. It should be emphasized that this distance is not fixed; the  $c_p$  profile will look different depending on the location along the channel because the maximum  $c_p$  depends on the temperature. The coarse and medium grids do not have enough data points to represent the solution of the fine grid. Even on the fine mesh, more grid points in this region will likely change the solution for specific heat.

As discussed earlier, the high specific heat layer forms an insulating layer between the low density

flow at the wall and the high density core. It plays an important role in the heat transfer deterioration phenomenon. To predict this phenomenon accurately, therefore, it is required to have sufficient cells in the region of high  $c_p$ . This can be obtained by having a low growth ratio in the mesh, i.e. the ratio between the sizes of two subsequent cells.

In other words, we have found another constraint on the mesh. In the previous validation case, it was shown that the  $y^+$  value should be below 3.7 to obtain correct results. We have now shown through fig. 5.23b that the growth ratio of the cells in the boundary layer should also be sufficiently small to capture the peak in  $c_p$ . Unfortunately, a general rule on the required growth ratio cannot be given since the location of the  $c_p$  peak varies.

Another possible reason for the discrepancy between the OpenFOAM solution and the one performed by Pizzarelli et al. is the fluid property model. The GERG-2004 model used in this thesis results in markedly higher  $c_p$  values around the pseudo-critical point, as evidenced by fig. 2.3 and fig. 5.21. This increased value of specific heat would result in a stronger insulating effect and therefore more severe heat transfer deterioration. This would explain the higher wall temperatures found in fig. 5.22.

Kunz et al. claim their GERG-2004 model predicts thermodynamic variables like  $c_p$  with increased accuracy with respect to older models [25] like the one used by Pizzarelli et al. This would mean results obtained on a sufficiently fine mesh with the current fluid property model, are more accurate than the ones obtained by Pizzarelli et al. In any case, this demonstrates again the need for extremely accurate property models if heat transfer in supercritical fluids is to be analysed.

We can say that the difference in thermodynamic models would increase the effect of heat transfer deterioration because of the higher peak in  $c_p$ . A coarse mesh, on the other hand, would decrease the effect of heat transfer deterioration, because there would be a lower peak in  $c_p$ , see fig. 5.23b. It is therefore likely that the higher wall temperatures found in fig. 5.22 can be attributed to the difference in thermodynamic property model. The lower wall temperatures on smooth walls (see fig. 5.17) are on the other hand likely the product of insufficient mesh resolution.

The pressure drop values found with OpenFOAM are listed in table 5.5. The pressure drop is not very sensitive to the mesh, decreasing only very modestly as the mesh is refined. The pressure drop is close to the one found by Pizzarelli et al, but not identical. The effect of roughness is clear: the pressure drop increases by 0.54 bar going from a smooth wall to one with 4.5  $\mu\text{m}$  roughness height.

Table 5.5: Total pressure drop (in bar) obtained from OpenFOAM and by Pizzarelli et al.

Grid	Smooth wall		Rough wall	
	OF	Ref. [104]	OF	Ref. [104]
Coarse	3.14	-	3.62	-
Medium	3.05	-	3.59	3.5
Fine	3.02	2.8	3.56	-

To further investigate the influence of roughness, another simulation was performed with a roughness height of 10  $\mu\text{m}$ . Figure 5.24 shows the wall temperature found on the fine mesh for all three roughness values.

Increased wall roughness leads to reduced wall temperatures as the heat transfer is increased. The increased turbulence at the wall leads directly to a higher heat transfer. This keeps the wall cooler than in the smooth case. In addition, the increased turbulent mixing makes it easier to overcome the insulating layer of low thermal conductivity and high specific heat.

Even at the moderate roughness height of 10  $\mu\text{m}$ , the heat transfer deterioration phenomenon almost disappears completely; the wall temperature increases nearly monotonously. Although the maximum temperature is reduced from 805 K to 412 K, the pressure drop increases only by 2.23 bar to 5.25 bar. A doubling of the pressure drop is a very reasonable price to pay for bringing the temperature down by almost 400 K. This suggests that having a rocket engine cooling channel with sufficient wall roughness will be able to prevent heat transfer deterioration as well.

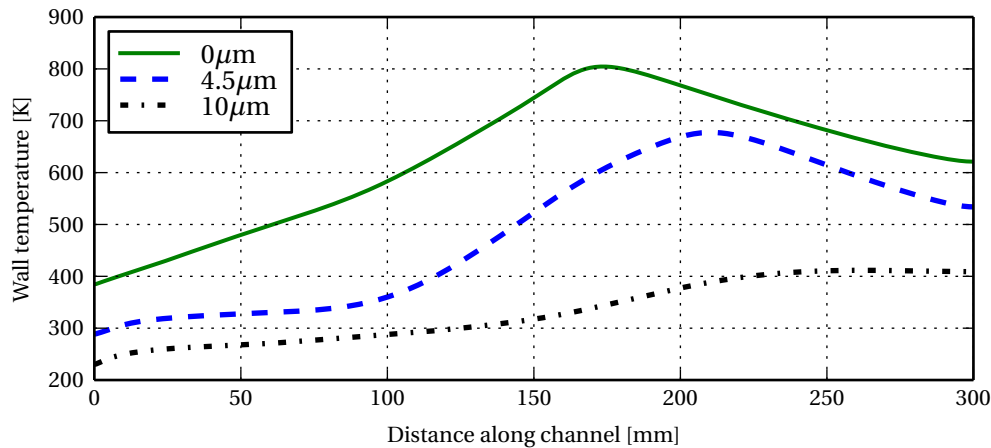


Figure 5.24: Comparison of inner wall temperature for different roughness values

### 5.2.3. INFLUENCE OF TURBULENT PRANDTL NUMBER

Another variable in the CFD code that has a substantial influence on the results is the turbulent Prandtl number. As stated in chapter 4, the turbulent Prandtl number was set to 0.9 in the simulations in this thesis, a decision based on literature.

By changing the turbulent Prandtl number, the relative influence of turbulence on momentum diffusion (through  $\mu_T$ ) and on thermal diffusion (through  $\kappa_T$ ) can be set. Thus, if both the wall roughness and Prandtl number are tuned, it will almost always be possible to match a simulation to experimental results. Although this tuning approach will not be followed in this thesis, it is instructive to show the influence of a change in the turbulent Prandtl number.

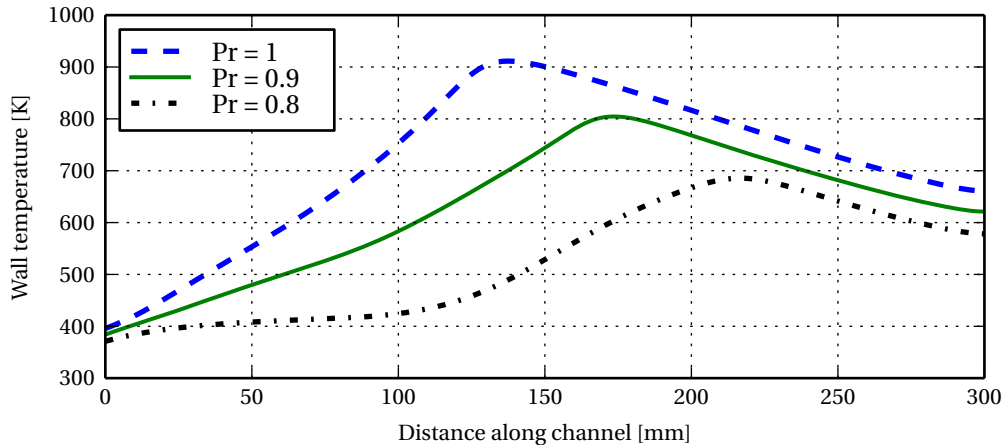


Figure 5.25: Comparison of inner wall temperature for different turbulent Prandtl number values

Figure 5.25 shows the wall temperature profile for three analyses with Prandtl number 0.8, 0.9 and 1.0. As expected, if the Prandtl number is increased, the wall temperature increases as well. A higher Prandtl number means a lower  $\kappa_T$  and therefore lower heat transfer rates. This increases the wall temperature.

The influence is rather substantial. The maximum wall temperature for a turbulent Prandtl number of 1 equals 911 K, decreasing to 805 K if  $Pr_T$  is 0.9 and to 686 K for a turbulent Prandtl number of 0.8. In fact, the influence on wall temperature seems similar to the influence of roughness shown in fig. 5.24.

As discussed earlier, however, the influence is mostly limited to the heat transfer. The impact on pressure drop is much smaller: 2.96 bar for  $Pr_T = 1.0$ , 3.02 for a turbulent Prandtl number of 0.9 and

2.89 bar for  $Pr_T$  equal to 0.8. Remarkably the largest pressure drop is found for  $Pr_T$  of 0.9.

#### 5.2.4. CONCLUSIONS OF NUMERICAL CHT VALIDATION

The OpenFOAM method was extended to conjugate heat transfer problems. This second validation case was intended to show that the CHT method can indeed be used to successfully predict conditions in the solid domain surrounding the methane coolant. Most importantly, conjugate heat transfer allows the prediction of wall temperatures.

In general, we can say that this goal has been achieved. OpenFOAM predicts similar wall temperatures to the reference analysis and shows the same trends. Thermal energy is correctly transferred across the boundary between the fluid and solid domain. This results in a bulk temperature that is equal to the one found by Pizzarelli et al.

However, the wall temperatures solutions were not exactly the same as the reference solutions. Two reasons can be given for this discrepancy. First, the mesh was not identical. It was hypothesised that refinement in streamwise direction was more important than refinement of the cross-section. This hypothesis turned out to be wrong; grid convergence was not accelerated with more cells in  $x$  direction. In addition, it was shown that refinement of the mesh at the location of maximum  $c_p$  is important to correctly predict heat transfer deterioration. This requires a low growth ratio of the cells near the wall – which combined with the required  $y^+$  at the wall means a high number of cells is required.

The second reason the results did not match perfectly with the reference analysis was that different thermodynamic models were used. In particular, the predicted specific heat values near the pseudo-critical temperature in the GERG-2004 model are markedly higher than the ones given by Pizzarelli et al. This results in a stronger heat transfer deterioration effect for the case of the rough wall.

The effect of roughness on skin friction and heat transfer is strong. For a roughness height of 10  $\mu\text{m}$ , the heat deterioration phenomenon all but disappears. Through the increased turbulence, the heat transfer inside the fluid is able to overcome the insulating layer of low thermal conductivity and high specific heat. This suggests that heat transfer deterioration will not occur inside rocket engines with realistic roughness values. The increased heat transfer due to roughness is paid for with an increase in the pressure drop; with a roughness height of 10  $\mu\text{m}$  it is 74% higher than for a smooth wall.

The turbulent Prandtl number is a modelling constant that influences the heat transfer in CFD simulations. Literature showed that several researchers use a value of 0.9 for methane, but this value is not written in stone. The effect of increasing turbulent Prandtl number is an increase in the wall temperature. The pressure drop almost does not change with varying turbulent Prandtl number.

### 5.3. EXPERIMENTAL DATA

In the last validation case, we finally check whether the developed model agrees with reality. The previous validation cases only compared two numerical models. Now, the results from OpenFOAM simulations will be compared to test data from an experiment on supercritical methane cooling [78]. This experiment was performed by the Italian Aerospace Research Center CIRA at Purdue University in the United States.

The Methane Thermal Properties (MTP) experiment consisted of a Glidcop (copper alloy) test article with a 1 mm  $\times$  3 mm channel through which methane was pumped, see fig. 5.26. This test article was designed by CIRA specifically for this experiment. The bottom of the article was heated to simulate an asymmetrically heated rocket engine cooling channel. A detailed description of the experimental test campaign is given in [78].

In the experiments, methane was pumped through the channel at a fixed mass flow that was measured with a flow meter. Electrical resistance heaters in the bottom of the test article could be switched on to provide a heat source. The heating power was measured from the electrical power provided to the heaters. At the inlet and outlet, static pressure and temperature of the fluid were measured. Furthermore, thermocouples were located on the top of and embedded inside the copper alloy at



Figure 5.26: MTP experimental article [78]. Figure courtesy of CIRA ScpA.

various locations along the channel to measure the temperature of the solid.

The interfaces at the inlet and outlet of the fluid channel are quite complex; they connect round pipes to the rectangular channels (see fig. 5.26) and have additional geometric details inside. Because of time and compatibility constraints, these were not modelled in this work. Instead, only the straight channel was modelled in OpenFOAM. This is comparatively a much simpler geometry. The resulting case geometry is similar to fig. 5.27 – the figure is taken from Pizzarelli et al, who have also attempted to validate their CFD method using the MTP data [31]. Glidcop was modelled with a constant thermal conductivity of  $345 \text{ W/m}\cdot\text{K}$ , as discussed in section 2.2.

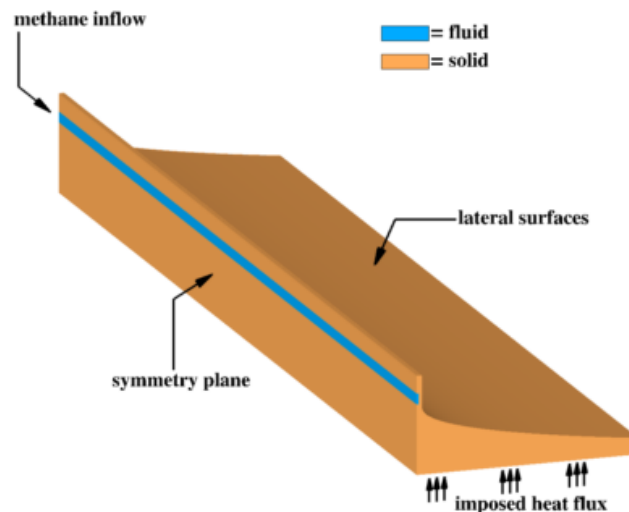


Figure 5.27: Geometry and case setup of MTP in CFD [31]

For the previous, numerical validation cases, the Spalart-Allmaras turbulence model has been used extensively. To model roughness, a boundary layer integration (BLI) approach developed by Aupoix has been used. This was because the reference results were generated with the same Spalart-Allmaras model.

However, in section 5.1, it was also demonstrated that the turbulence model choice can have an important influence on the results of a heat transfer analysis. This is corroborated by several studies in the field of nuclear engineering: especially for supercritical fluids large differences between turbulence models should be expected [105–108].

This experimental validation will therefore also be used to compare different turbulence models to each other and to the experimental data. The  $k-\omega$  SST and standard  $k-\epsilon$  models will be used in addition to the Spalart-Allmaras model.

Furthermore, instead of fully integrating the boundary layer, the wall function approach will also be tested. Wall functions have the potential to vastly reduce the necessary computation time because the requirement for wall refinement of the mesh is so relaxed.

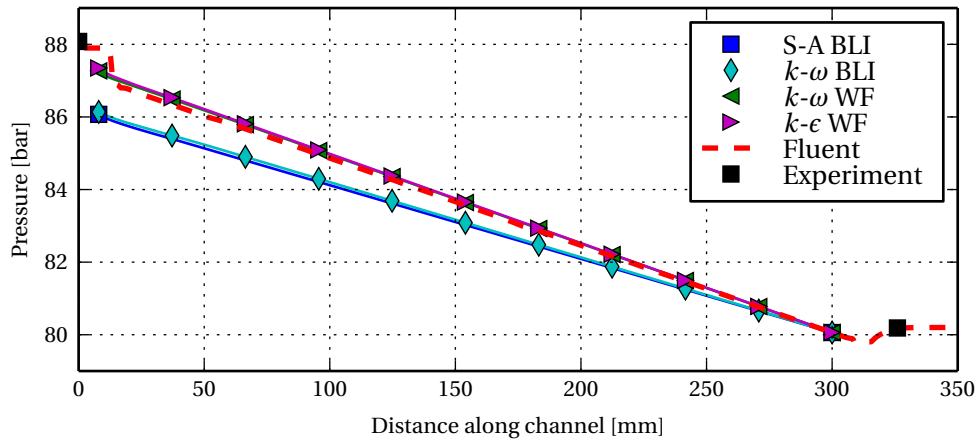


Figure 5.28: Cold flow pressure drop comparison. Experimental results and FLUENT analysis are courtesy of CIRA ScpA.

The four approaches to deal with turbulence and roughness that will be tested are:

- Spalart-Allmaras with boundary layer integration (S-A BLI)
- $k-\omega$  Shear Stress Transport with boundary layer integration ( $k-\omega$  BLI)
- $k-\omega$  Shear Stress Transport with wall functions ( $k-\omega$  WF)
- Standard  $k-\epsilon$  with wall functions ( $k-\epsilon$  WF)

The relevant equations for all of these approaches are described in chapter 4.

In cooperation with CIRA, several MTP test conditions were simulated in OpenFOAM. Section 5.3.1 shows a cold flow test that was rebuilt. After this, section 5.3.2 shows the validation of the developed model using two hot flow test conditions. Finally, in section 5.3.3 the effect of inlet turbulence on the results is discussed.

### 5.3.1. COLD FLOW TEST

The cold flow test (designated by CIRA as test condition 43 or TC43) consisted of an experimental run with the heaters switched off. As such, the cold methane flows through the channel at nearly constant temperature. This test is important to characterise the pressure drop through the channel. The pressure drop depends on the wall roughness. By varying the roughness height of the wall until the correct pressure drop is found, the empirical roughness height is found.

Earlier, it was shown that the wall roughness height also has a substantial effect on the heat transfer rate to the fluid. By determining the roughness height of the wall from the cold flow test pressure drop, the chosen value is no longer derived from heat transfer. The cold flow pressure drop is very predictable as many phenomena found in the heated supercritical flow are eliminated. For this reason, it is suitable to determine the correct value of the roughness height.

This approach eliminates the wall roughness as a "calibration factor" for the heat transfer rate, an approach that was chosen by Pizzarelli et al. [31]. Tuning the wall roughness to the heat transfer rate without considering pressure drop is problematic. It is possible that the wall roughness is used simply as a calibration factor to compensate for various modelling errors. This is likely to result in erroneous pressure drop predictions.

CIRA determined from Fluent CFD analyses of the cold flow tests that the wall roughness was 14.5  $\mu\text{m}$ . Figure 5.28 shows the experimental pressure values as well as the results obtained by CIRA with Fluent for the cold flow case (TC43). This analysis also considers the inlet and outlet interfaces. The pressure is well predicted; a pressure drop of 7.70 bar for Fluent versus 7.89 bar measured or a difference of 2.5%.

Lacking the inlet and outlet interfaces, the OpenFOAM simulations are difficult to relate to the experimental pressure values. Since the Fluent analysis corresponds so well to the experimental data, it can

be used as a benchmark for the pressure drop inside the channel. The pressure value at the end of the straight part obtained in Fluent is applied as a boundary condition in OpenFOAM. The pressure at the inlet of the straight channel can then be compared. Note that the solid domain was not simulated for these cases; the fluid domain was simulated with adiabatic temperature conditions.

Figure 5.28 shows excellent agreement between the pressure drop inside the straight channel for the models with wall functions (WF). The  $k-\epsilon$  model predicts the highest pressure drop, 0.18 bar higher than Fluent. Notice that this difference makes the pressure of  $k-\epsilon$  closer to the experimental value. The  $k-\omega$  model with wall functions yields a pressure drop of 0.13 bar higher than Fluent.

The models that fully integrate the boundary layer predict a lower pressure drop inside the channel. The  $k-\omega$  model with full boundary layer integration (BLI) yields a pressure drop of 0.94 bar smaller than Fluent. The difference between the reference and Spalart-Allmaras is 1.03 bar. Clearly, the pressure drop is not well predicted by these models for the wall roughness height of 14.5  $\mu\text{m}$ . In fact, a 1 bar difference means there is a discrepancy in pressure drop of almost 14%.

One could try to change the wall roughness height for these models in order to obtain a better match to the experimental pressure drop. Nonetheless, the current value does yield good results for heat transfer, as will be shown later. Moreover, previous researchers have already pointed out that these models fail to predict the influence of roughness on heat transfer and skin friction simultaneously, see section 4.4.

### 5.3.2. HOT FLOW TESTS

Having proven that the cold flow tests can be reasonably replicated with the current roughness height, at least for the wall function approaches, we can continue with hot flow tests. Two experimental conditions were replicated. More would have been favourable to prove the validity of the software for different conditions. Due to the limited time spent by the author at CIRA, only these two cases were selected, however.

In addition, it would be better if the experiments were performed at pressures closer to the critical pressure, where the fluid property variations are larger. It is expected that at such conditions, the deviations between the CFD model and experimental data would be larger. Heat transfer deterioration may be present at such pressures, an important phenomenon to study. However, no such experiments have been performed for methane to date.

Again the inlet and outlet interfaces were not simulated so the boundary condition on outlet pressure was taken from the value in Fluent. The inlet temperature, mass flow and input power boundary conditions were all taken directly from the experimentally measured values. The boundary conditions for test conditions 24 and 26 are given in table 5.6. The major difference between the two is the outlet pressure. The remaining boundary conditions were equal for both cases: adiabatic outer walls for the solid domain and 2% turbulence at the inlet of the fluid domain.

Table 5.6: Boundary conditions for experimental conditions replicated with OpenFOAM

Test	$p_{\text{outlet}}$ [bar]	$T_{\text{inlet}}$ [K]	$\dot{m}$ [g/s]	Power [W]
TC24	102.40	137.1	20.87	10749
TC26	119.84	140.8	20.57	11058

The symmetry of the problem was exploited by simulating only half of the channel in each case. Two different meshes were used for the fluid domain; one for the wall function approach and one for the boundary layer integration approach. When using wall functions, the  $y^+$  value should be around 30.

A mesh of  $350 \times 10 \times 30$  cells in length  $\times$  half-base  $\times$  height was chosen for the wall function approach. The first cell from the wall is at a distance of approximately  $5 \cdot 10^{-5}$  m for all walls.

For the boundary layer integration approach, a substantially denser and more refined mesh is needed in the boundary layer. The increased computational resources needed for this lead to a compromise in the number of cells in the streamwise direction. A fluid mesh of  $200 \times 40 \times 100$  cells was finally

designed. This mesh has a first cell at approximately  $5 \cdot 10^{-7}$  m with a growth factor of 1.12 in both  $y$  and  $z$  directions.

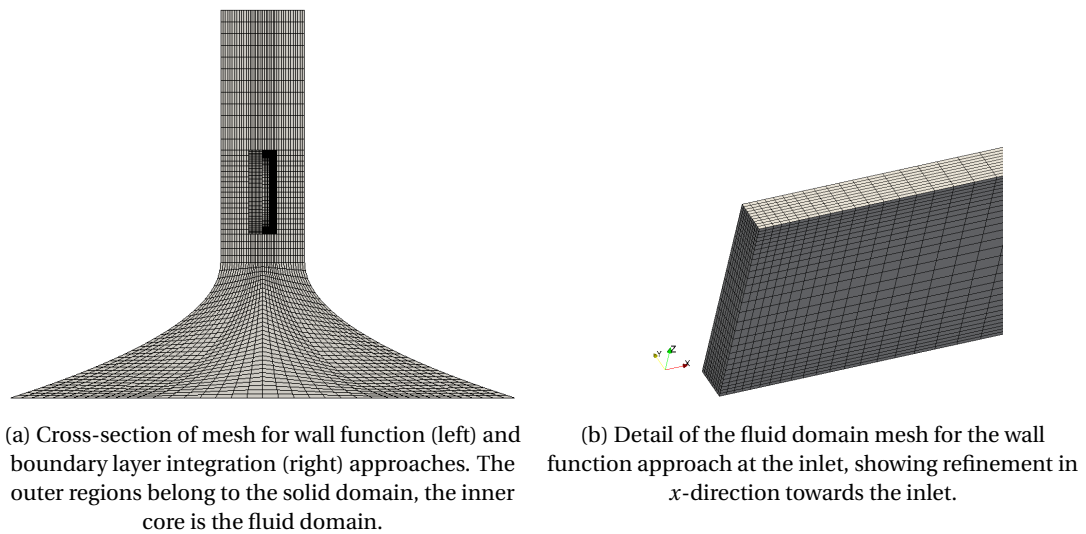


Figure 5.29: Mesh for experimental validation cases

The solid domain is very similar for both meshes. The distribution of cells in a cross-section is exactly the same, with 1152 cells each. The number of cells in  $x$  direction equal for the fluid and solid domain. The curved edge of the domain was obtained from CIRA and conforms to shape of the test article that was used in the experiments. It is cut off at a distance of approximately 6 mm below the channel, because this was the limit of the shape obtained from CIRA. Figure 5.29a shows a cross-section of the resulting meshes.

In the streamwise direction, both meshes are refined near the inlet and outlet. This is to avoid high discretisation errors in this zone. Such errors were encountered in section 5.1 and can be avoided using this refinement. Figure 5.29b shows a detail of the mesh that displays this refinement.

#### TEST CONDITION 24

Figure 5.30 shows the experimentally measured pressure values, the Fluent result obtained by CIRA and the pressure curves for all four OpenFOAM approaches. Instead of the straight line obtained earlier, this figure shows that the pressure drop increases towards the outlet of the channel. This can be explained by the effect of heating: as the fluid density drops, the velocity increases. Since pressure drop is proportional to the square of velocity, it will increase if the density drops.

The  $k-\omega$  wall function approach conforms best to the Fluent analysis and the experimental pressure. The results from Spalart-Allmaras and  $k-\epsilon$  are almost identical with a pressure loss that is 0.28 bar or 3.2% smaller. The  $k-\omega$  approach with boundary layer integration once again performs worst in terms of pressure drop, with a discrepancy of 20% with respect to the reference analysis. The actual pressure loss measured in the test is 0.47 bar higher than the one found with Fluent. All methods including the reference analysis therefore underestimate the pressure drop.

The comparison of the temperature found with the conjugate heat transfer analysis to the embedded thermocouple data is shown in fig. 5.31. An uncertainty of 10 K for the thermocouple data is assumed, as was done by Pizzarelli et al. in their validation [31]. The most important uncertainties are due to the uncertainty of the thermocouple itself, errors induced by the data acquisition system and the uncertainty in the location of the thermocouple.

A fourth thermocouple was present in the experiment at approximately 240 mm from the inlet [78]. However, CIRA considered the data from this thermocouple inaccurate and unreliable. Its output has been discarded by Pizzarelli et al. as well [31]. For these reasons, the data from this thermocouple has been omitted here as well.

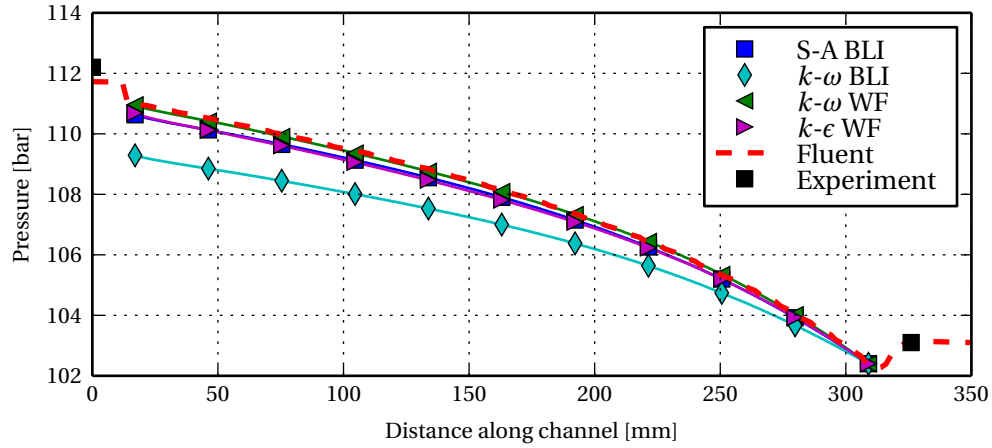


Figure 5.30: Pressure drop comparison for TC24. Experimental results and FLUENT analysis are courtesy of CIRA ScpA.

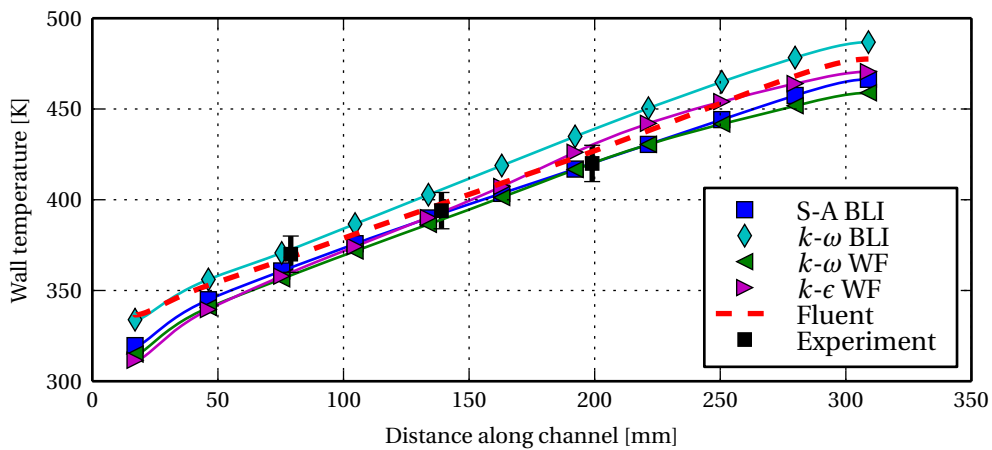


Figure 5.31: Comparison of temperature of embedded thermocouples at 4 mm with numerical results for TC24. Experimental results and FLUENT analysis are courtesy of CIRA ScpA.

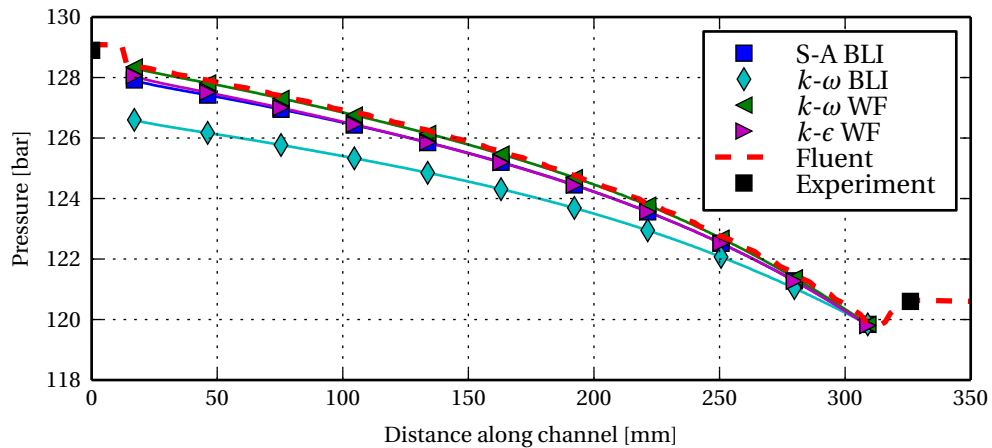


Figure 5.32: Pressure drop comparison for TC26. Experimental results and FLUENT analysis are courtesy of CIRA ScpA.

Figure 5.31 shows that with all turbulence models, reasonable wall temperature values are obtained. The maximum temperature difference between the models is 28 K and occurs at the outlet. The Spalart-Allmaras turbulence model seems to provide the best agreement with thermocouple data, resulting in temperatures within the uncertainty at all three locations. It is closely followed by the  $k-\omega$  wall function model and the  $k-\epsilon$  model. It is notable that at the first thermocouple, these models all predict a temperature that is lower than the reading. The thermal conductivity is assumed constant, as mentioned earlier. In section 2.2, it was discussed that in fact the thermal conductivity of Glid-cop varies with temperature. It is possible that implementing a variable thermal conductivity could improve the results further, but this was not done in this study due to schedule constraints.

The  $k-\omega$  boundary layer integration method results in an overprediction of the wall temperature, especially at the third thermocouple. Increasing the wall roughness height for this model would increase the pressure losses and increase the heat transfer. It is probable that this would improve the agreement of the model with experimental data. However, this was not very enticing for this study as the other three models provided quite good agreement already.

#### TEST CONDITION 26

For test condition 26, the results are extremely similar to the results from test condition 24. Figure 5.32 shows the pressure comparison for this test condition. Again, all models produce reasonable pressure curves with the  $k-\omega$  BLI model giving the largest discrepancy. The main difference with TC24 is that this time, the experimentally measured inlet pressure is below the value found with Fluent. Note that Votta et al. do not mention the type or accuracy of the pressure sensors used, so it is impossible to verify if this falls within the experimental error for the pressure.

Figure 5.33 shows that the wall temperature results are also very similar to test condition 24. All turbulence and roughness approaches give values to within 20 K of the thermocouple readings. The maximum deviation between the models is again 28 K. The second test condition confirms the validity of the model.

#### 5.3.3. INFLUENCE OF INLET TURBULENCE

Earlier, it was shown that a relatively low temperature was predicted at the first thermocouple with three different methods. One of the hypotheses that could explain this discrepancy was a too high level of turbulence at the inlet. Furthermore, the turbulence boundary condition at the inlet is one that is difficult to justify as there is no experimental data.

For these reasons, it was interesting to investigate the influence of inlet turbulence on the pressure drop and wall temperature. TC24 was simulated with different turbulence levels at the inlet. The  $k-\omega$  WF model was selected, as it provided good results earlier and comes at reduced computation cost

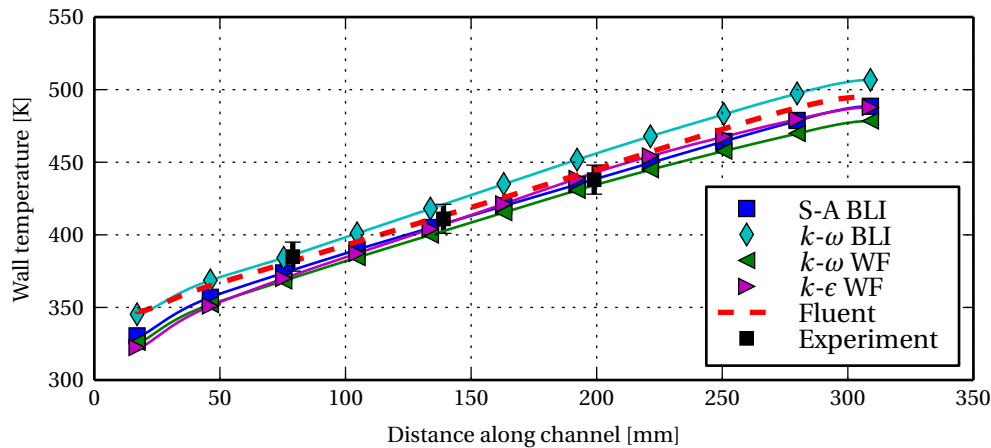


Figure 5.33: Comparison of temperature of embedded thermocouples at 4 mm with numerical results for TC26. Experimental results and FLUENT analysis are courtesy of CIRA ScpA.

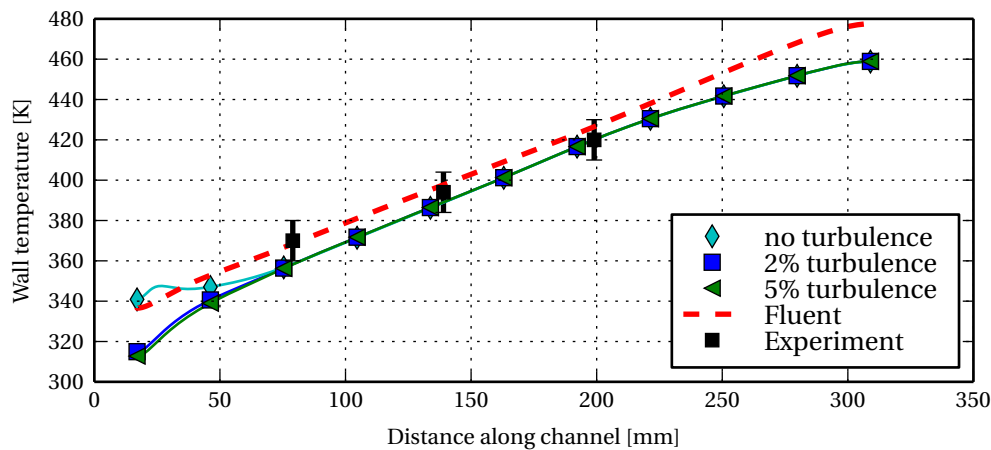


Figure 5.34: Comparison of different inlet conditions for turbulence with  $k-\omega$  WF. Experimental results and FLUENT analysis are courtesy of CIRA ScpA.

with respect to BLI models.

Figure 5.34 shows that the influence of the inlet turbulence is limited to the first 50 mm of the channel. After this point, the turbulence generated by the channel is so high that the inlet value no longer matters. At 50 mm, the length-to-diameter ratio is approximately 33.

As expected, having zero turbulence at the inlet results locally in higher wall temperatures because heat transfer is less efficient. The influence of an increase in inlet turbulence from 2% to 5%, however, is almost negligible. The pressure curves are almost identical; the difference in pressure drop between zero turbulence and 5% turbulence is 1.5%.

Figure 5.35 shows what the flow development looks like in terms of velocity profile. Starting from a uniform velocity, the walls slow down the fluid. In Figure 5.34 the flow cannot be distinguished from a developed flow anymore at  $x = 97$  mm. The asymmetrical flow profile is due to the asymmetrical heating of a supercritical fluid. The lower density of the fluid at the bottom results in a higher flow velocity.

#### 5.3.4. EXPERIMENTAL VALIDATION CONCLUSIONS

The results of the experimental validation are satisfying on several levels. Three of the tested modelling approaches predict the pressure drop in the channel within 10% of the experimental value. They si-

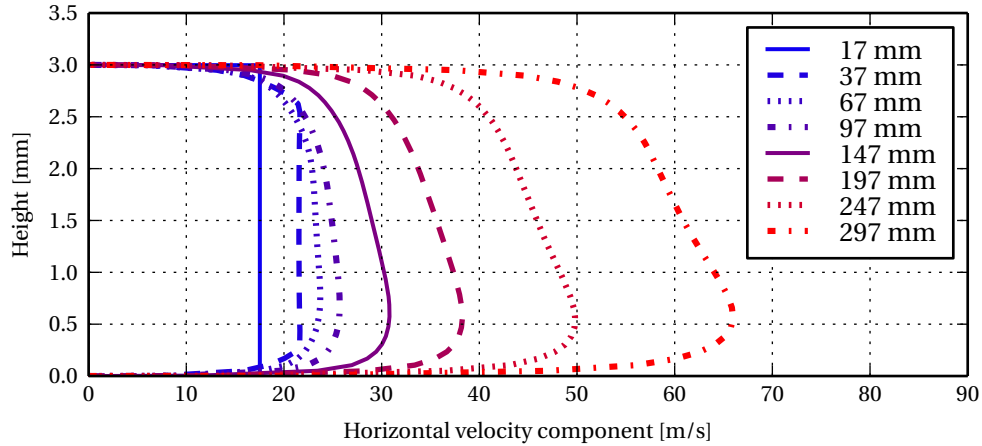


Figure 5.35: Streamwise velocity profile on symmetry plane of channel at various cross-sections

multaneously predict the wall temperature within 15 K at the three measured locations. Furthermore, two of these successful models use wall functions instead of boundary layer integration which significantly reduces the required computation time.

Table 5.7 shows a summary of the results obtained with the different turbulence models. The Spalart-Allmaras model gives the best agreement with thermocouple data, while the  $k-\omega$  model gives the best comparison with pressure data when corrected for pressure drop at the interfaces. The calculation time for the boundary layer integration methods is almost 20 times as high as for the wall function methods. Taking all these considerations into account, the  $k-\omega$  SST model with wall function approach is recommended for further use.

Table 5.7: Summary of validation results for tested turbulence and roughness models

Model	Time	$\Delta p$ [bar]	$\Delta T$ [K]
S-A BLI	18 h	0.3 to 0.9 bar	$\pm 10$
$k-\omega$ BLI	18 h	1.6 to 2.2 bar	$\pm 20$
$k-\omega$ WF	1 h	-0.1 to 0.6 bar	$\pm 15$
$k-\epsilon$ WF	1 h	0.2 to 0.8 bar	$\pm 15$

An important side note is that the wall roughness has a substantial effect on both wall temperature and pressure drop. The excellent agreement with experimental values was only possible because the roughness height was characterised with the cold flow test.

Absent an experimentally determined value for wall roughness, the determination of the roughness height becomes guesswork. Different manufacturing techniques will result in a different surface finish and thus a different roughness height. Since the hydrodynamic roughness height is not directly correlated to the physical height of the roughness elements [97], cold flow experiments will remain necessary to determine it. Such experiments are therefore of crucial importance to correctly predict the heat transfer and pressure drop.

#### 5.4. EFFECT OF UNCERTAINTY ON DESIGN

The errors in wall temperature estimate and coolant pressure drop have been quantified in section 5.3. It is clear that the CFD and CHT simulations are substantially more accurate than the first order analysis performed in chapter 3.

The accuracy of the one-dimensional method was estimated to be 150 K for the wall temperature. When designing, this accuracy is the minimum margin of error one could take. In other words, if the tool were meant for design, this means that the cooling channels would have to be designed for a maximum wall temperature of  $T_{\text{allow}} - 150$  at the highest.

The error in wall temperature of the CHT simulations, however, was only about 15 K. This means one could design the copper chamber for a wall temperature of 785 K. However, in reality the error will probably be larger. The dynamic range of temperatures found in a rocket engine is much larger than the one present in the experiment. The effects of curvature and of changing cross-sections were not included in the validation. There may be stronger fluctuations in the mass flow or inlet pressure in an actual engine than in controlled experiments. For these reasons, it seems prudent to take a margin of error that is larger than 15 K. A reasonable value seems 50 K, taking into account that the actual wall temperature range is almost 3 times as large as the experimental temperature range.

It is interesting to evaluate what the impact of accuracy and margin of error is on the design of a rocket engine and/or associated launch vehicle. Below, a short and rather simplified analysis is shown. This allows us to make an approximate quantification of the effects of uncertainties on design.

As an example, let us consider the throat region of the generic 10 kN engine discussed in chapter 3. According to the first order analysis, the throat heat flux is approximately  $31.6 \text{ MW/m}^2$ . Let us assume the coolant temperature at the throat is 200 K. We can now calculate the required convective cooling coefficient  $\alpha_c$  to achieve a certain wall temperature.

For a maximum wall temperature of 800 K, the required value of  $\alpha_c$  is  $52.7 \text{ kW/m}^2 \cdot \text{K}$ . When the maximum wall temperature is set to 785 K (the proven accuracy of the CHT method in OpenFOAM without extra margins),  $\alpha_c$  is required to be  $54.0 \text{ kW/m}^2 \cdot \text{K}$ .

With the more reasonable margin of 50 K, the design wall temperature becomes 750 K and  $\alpha_c$  rises to  $57.5 \text{ kW/m}^2 \cdot \text{K}$ . This is approximately a 5% increase from the value required to keep the temperature at 800 K. If the design wall temperature is reduced to 650 K, was required for the first order method, the required  $\alpha_c$  is  $70.2 \text{ kW/m}^2 \cdot \text{K}$ , a third more than for 800 K.

Since  $\alpha_c$  is proportional to  $u^{0.8}$ , the more stringent cooling requirement will mean a substantially higher flow velocity  $u$ . This in turn will drastically increase the pressure drop. Because pressure drop is proportional to the square of the velocity, it is approximately proportional to  $\alpha_c$  to the power 2.5 (eq. 5.8).

$$p \sim u^2 \sim (\alpha_c^{1.25})^2 \sim \alpha_c^{2.5} \quad (5.8)$$

The 5% increase in  $\alpha_c$  at a design margin of 50 K would thus mean a pressure drop increase of 13%. The 33%  $\alpha_c$  increase in the case of the first order method with an error of 150 K would mean a pressure drop that is 105% higher than the one required in reality.

An increased pressure drop in the engine results in heavier tanks and/or turbopumps. Assuming a pressure-fed engine, the tank mass scales directly with pressure, see eq. 5.9.

$$t = \frac{R\Delta p}{2\sigma_{\text{allow}}} = \frac{R(p_{\text{injector}} + p_{\text{drop}})}{2\sigma_{\text{allow}}} \quad (5.9)$$

Let us simplify and assume that the tank pressure is equal to the pressure drop plus the pressure at the injector (around 50 bar). The pressure drop in the channels is around 10 bar for a wall temperature of 800 K (chapter 3). The 50 K margin would then lead to a tank mass increase of 2.1%. The 150 K margin would instead lead to a tank mass increase of 18%.

It is clear that the discussion above is a gross oversimplification of reality. However, this superficial calculation shows that the high accuracy demonstrated in this chapter can have real results. A better accuracy leads to smaller margins and can therefore result in a substantially lighter vehicle.

## 5.5. CONCLUSIONS OF VALIDATION CAMPAIGN

Validation of the tool that was developed in the OpenFOAM framework was an important task of this thesis. Three of the research objectives were associated with this task (although number two was partly demonstrated in chapter 2):

2. Implement and verify a tabulated fluid property model in OpenFOAM
3. Validate the OpenFOAM tool with comparable numerical tools
4. Validate the OpenFOAM tool with experimental data and compare the performance of different turbulence models

The results obtained in this chapter clearly showed that the typical phenomena linked to supercritical flows were reproduced by the tool. These include strong fluid property variations, heat transfer deterioration and asymmetric velocity profiles. This proves that the tabulated fluid property model (objective 2) was correctly implemented.

The wall temperature and heat flux profiles obtained with OpenFOAM matched the ones obtained with comparable numerical tools very well. If there were discrepancies, sufficient explanations for them could be offered. In section 5.1, the agreement with the reference heat flux profile was especially impressive and encouraging. Objective 3 can also be considered fulfilled.

The effects of roughness and turbulent Prandtl number on the simulation results were investigated. A high roughness increases both heat transfer and skin friction, while an increased turbulent Prandtl number decreases heat transfer and leads to higher wall temperatures. The turbulent Prandtl number has little influence on pressure drop. At realistic roughness values, the heat transfer deterioration phenomenon disappears due to the increased turbulence. This suggests that heat transfer deterioration will not be problematic in rocket engines.

The presence of these tuning variables is both a blessing and a curse. They can be used to make the simulation results adhere to the experimental values. This is beneficial, but it can also mask important other errors. It was therefore decided to stick with a turbulent Prandtl number of 0.9 for the simulations in this thesis, using cold flow tests to match roughness height to the pressure drop.

The experimental validation was very successful. All turbulence models were able to match the experimental wall temperature to within 20 K. Three of the approaches yielded a pressure drop with an error smaller than 1 bar. The differences between the different turbulence models were small, especially when compared to the differences found in literature or the ones found in section 5.1. Research objective 4 has been met.

The OpenFOAM tool was shown to have an accuracy that is much better than the one from the one-dimensional analysis in chapter 3. Accounting for error sources not present in the experiment as well as the elevated temperature inside rocket engines, the required error margin for design is estimated to be 50 K. This improved accuracy allows for smaller design margins and e.g. lower tank mass.

It is important to note that the excellent agreement between experimental and numerical results was only possible because the roughness height could be determined from the cold flow tests. If the roughness height were not known, the uncertainty in the wall temperature and pressure drop would be much larger. Thus, experiments to characterise the wall roughness obtained with a certain manufacturing process are a requirement to obtain accurate predictions from the method.

Finally, the method developed in OpenFOAM was shown to be fast. When analysing a similar number of cells, it was 11 times faster than the in-house solver of La Sapienza University of Rome. In addition, it was shown that wall functions are also able to model the heat transfer, which reduced the computational resources by a factor of 18. Together, that means the new OpenFOAM method is 200 times faster than the academic standard. If we take into account a factor 2 for the differences in computational architecture (the reference computations were published in 2011), the new method is still able to reduce the required computation time by two orders of magnitude.

# 6

## RESULTS OF CFD ANALYSIS

In chapter 1, the research question of this thesis was stated as follows:

**Is it advantageous to use aluminium instead of copper for the chamber wall of a small, regeneratively cooled oxygen/methane rocket engine?**

With an accurate, validated tool for methane cooling channel analysis available, we can now proceed to try and answer this research question. Instead of the straight channels with constant cross-section that were analysed in chapter 5, this chapter will deal with cooling channels inside the wall of a rocket engine. These channels are curving and their width and height may vary rapidly, making both mesh generation and CFD analysis more challenging.

The subquestions that we set out to answer at the start of this thesis are listed below. We will attempt to answer these questions in this chapter. They will aid us in answering the main research question given above. Subquestions 1 to 4 must be answered for the different chamber materials (copper and aluminium), while subquestion 5 synthesises the answers of the previous subquestions.

- Is it possible to cool the thrust chamber wall to the allowable temperature or lower, using the fuel flow available?
- How high is the pressure drop over the cooling channel?
- By how much does the temperature of the coolant rise?
- What is the estimated mass of the thrust chamber?
- What is the system-level impact of the differences in pressure drop, temperature rise and chamber mass?

In all the designs of chapter 3, it was assumed that the rib thickness between the channels was fixed at 1 mm. We will continue to work under this assumption, which means that the width of the channels is fully defined when the number of channels is selected. In addition, the number of channels will be kept equal.

This chapter is divided into four parts. First, section 6.1 shows the regenerative cooling analysis of the cooling channel geometries generated in chapter 3. Based on the detailed CHT results, these geometries are improved in section 6.2. The OpenFOAM method developed in chapter 4 chapter 5 allows us to answer subquestions 1 to 3 for both copper and aluminium chambers.

In section 6.3, the mass of the two chambers is calculated and compared to answer subquestion 4. In addition, the system-level impact of chamber wall material choice is investigated. In particular, the influence of the pressure drop on the tank mass of a pressure-fed system is analysed. This analysis provides an answer to subquestion 5. The results are summarised in section 6.4

## 6.1. NOZZLE CHANNEL ANALYSIS

In chapter 3, a one-dimensional analysis tool was used to generate cooling channel geometries. A copper and aluminium chamber were analysed. The channel geometries were adapted such that the wall temperature was close to the allowable temperature of the material. This minimises the pressure drop over the cooling channel.

Chapter 3 also showed that the one-dimensional tool was one of low fidelity: the wall temperature can locally deviate by more than 150 K from a CFD solution. In this section, the same cooling channels geometries will therefore be used for a conjugate heat transfer analysis in OpenFOAM. In this way, it is possible to verify whether the geometries indeed keep the wall temperature below the allowable temperature.

### 6.1.1. COOLING CHANNEL GEOMETRY AND MESHING

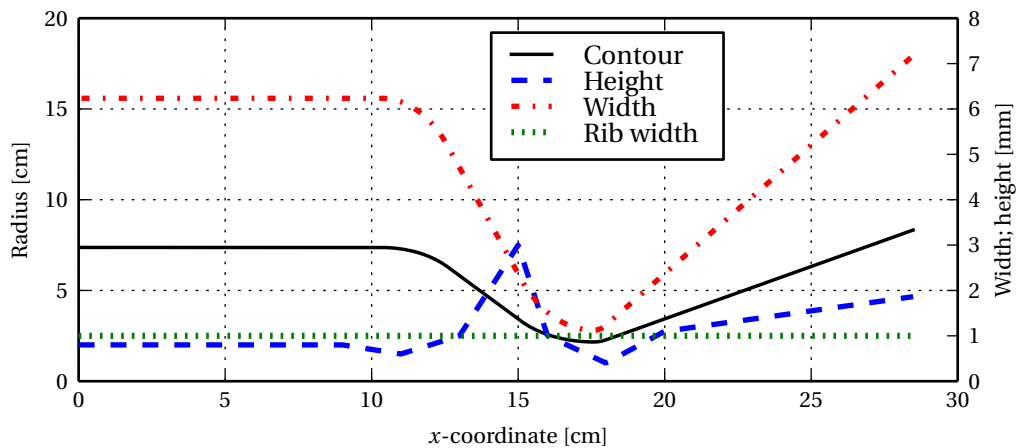


Figure 6.1: Varying cooling channel dimensions along nozzle axis for copper chamber

Figure 6.1 shows the cooling channel geometry that was obtained for the copper combustion chamber in chapter 3. It is obvious that the variations in channel height and width are significant and must be taken into account for the CFD analysis. The cooling channel width is dictated by the nozzle contour; the rib thickness does not vary so the channel width must vary to compensate for the changing nozzle diameter. The cooling channel height was a design variable that was varied intentionally to obtain an allowable wall temperature at all locations along the nozzle.

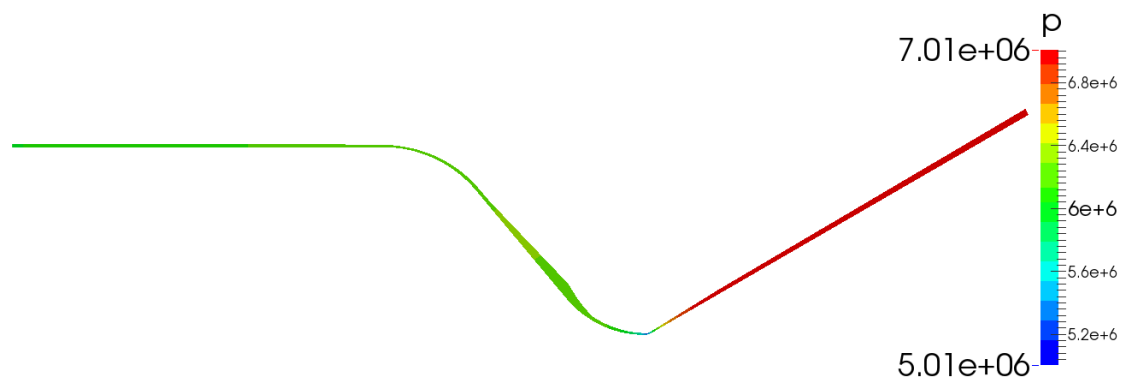


Figure 6.2: Pressure distribution and in-plane velocities inside copper cooling channel

A Python script was written in order to translate the geometry shown in fig. 6.1 into a three-dimensional mesh definition. This mesh definition was a `blockMeshDict` file, a typical mesh definition for OpenFOAM. Figure 6.2 displays the resulting geometry (including pressure distribution).

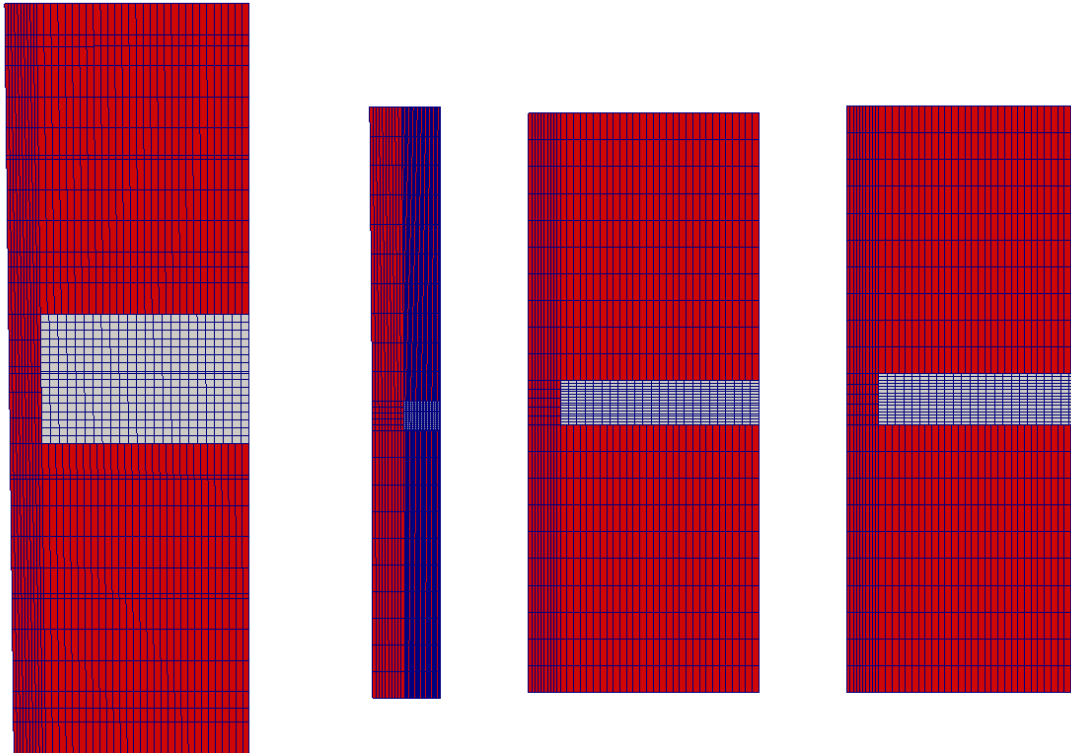
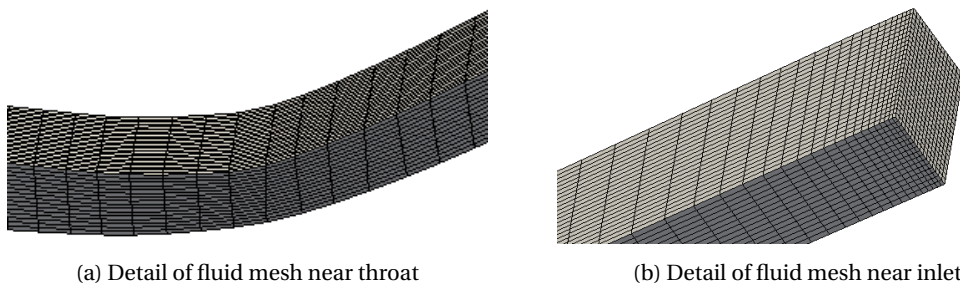


Figure 6.3: Cross-sections of one of the meshes at (from left to right)  $x=270$  mm (near inlet),  $x=175.8$  mm (throat),  $x=100$  mm and  $x=0$  mm (near outlet). Solid domain is shown in red, fluid domain in gray.

Because the chamber is more or less radially symmetric and the channels themselves are symmetric along the vertical axis, only half a channel must be simulated. The circumferential curvature of the channel was neglected. The channel half-base is less than one percent of the nozzle diameter, justifying this simplification. In addition, the channel height is small with respect to the nozzle radius, so the difference in width between the inner and outer wall is also small.

Some cross-sections of the half-channel mesh are shown in fig. 6.3. Because of the varying dimensions, it is impossible to create a mesh with the same cell size at all locations along the nozzle axis. Figure 6.3 shows for example that at the throat, the fluid mesh is much more fine than at the inlet of the channel. For the wall function approach that will be used, the  $y^+$  value should not be lower than around 30. Therefore, only  $24 \times 16$  cells are used along the half-base and height of the channel, otherwise the mesh would become too fine at the wall.



(a) Detail of fluid mesh near throat

(b) Detail of fluid mesh near inlet

Figure 6.4: Details of fluid mesh showing refinement along nozzle axis near throat and inlet

The refinement in streamwise direction is much more important to obtain accurate results. Especially in regions of strong curvature like the throat, a large number of cells is needed to obtain a good solution. Also, as we saw earlier, it is good practice to do a local refinement in the streamwise direction at the inlet, to allow for boundary layer development. Figure 6.4 shows the refinement of the fluid mesh

at these two locations. The total number of cells in  $x$  direction was 500.

### 6.1.2. SOLVER AND BOUNDARY CONDITION SETUP

Based on the results of the experimental validation section 5.3, the  $k-\omega$  SST model was selected, using wall functions to take into account the wall roughness. Because a generic rocket engine is being simulated, there is no experimental data to characterise the wall roughness height. Because of this, the roughness of the experimental validation case (14.5  $\mu\text{m}$ ) was adopted here as a reasonable estimate.

The inlet boundary condition on the fluid domain was a prescribed mass flow equal to the total methane fuel flow in the engine divided by the number of channels (64 for the copper nozzle, 80 for the aluminium nozzle). The inlet temperature was 110 K. The outlet pressure was fixed to 60 bar. This was done because the fluid properties were tabulated for pressures higher than 50 bar. Because the static pressure drops by several bar at the throat (see fig. 6.2), the outlet pressure was set to 10 bar above this minimum pressure.

The most important aim of the simulation is to obtain a wall temperature estimate. The wall temperature influences the heat flux, so we cannot directly prescribe either the temperature or the heat flux. To obtain the correct heat flux at the hot wall, we impose a custom Neumann boundary condition on the temperature, given by eq. 6.1. The derivation of this boundary condition from the equations for convection and conduction (eq. 3.1) is straightforward.

$$\frac{dT}{dn} = \frac{\alpha_h}{\kappa} (T_{\text{aw}} - T_w) \quad (6.1)$$

The values for  $\kappa$  and  $T_w$  are defined inside the CHT simulation. The adiabatic wall temperature  $T_{\text{aw}}$  and the convective heat transfer coefficient  $\alpha_h$  are due to convection from the hot combustion gases to the wall. These parameters are external to the CHT simulation and must be supplied as inputs.

This was done by tabulating the values obtained from the first order analysis as a function of  $x$  coordinate. That is, they are the results of the CEA analysis and Bartz' equation (corrected with a coefficient of 0.0195 instead of 0.026), see section 3.2). These tables were supplied as text files to OpenFOAM.

If radiative heat transfer is to be taken into account, eq. 6.1 becomes slightly more complicated, resulting in eq. 6.2. It now incorporates  $q_R$ , the radiative flux.

$$\frac{dT}{dn} = \frac{\alpha_h (T_{\text{aw}} - T_w) + q_R}{\kappa} \quad (6.2)$$

If in addition to radiative heat transfer, there is also a coating present on the wall surface, the boundary condition becomes even more complicated. Equation 6.3 shows this boundary condition, where the thickness and thermal conductivity of the coating now also influence the heat transfer. Note that this equation is not restricted to coatings per se, it can also be any other type of layer with a small thickness and different thermal conductivity. The CHT analysis will yield the wall temperature of the material below this layer, it does not predict the temperature of the insulating layer itself.

$$\frac{dT}{dn} = \frac{1}{\frac{1}{\alpha_h} + \frac{t_{\text{coat}}}{\kappa_{\text{coat}}}} \frac{(T_{\text{aw}} - T_w) + \frac{q_R}{\alpha_h}}{\kappa} \quad (6.3)$$

These custom Neumann boundary conditions using tabulated values were implemented in OpenFOAM. Use was made of the versatile swak4foam library to avoid C++ coding for this task.

### 6.1.3. RESULT VERIFICATION

Unfortunately, the more complicated geometry also deteriorated the convergence behaviour of the solver. Even with settings that worked well for the validation cases described in chapter 5, the residuals (indicative of iteration errors) would not decrease more than an order of magnitude. In other words, the simulations did not result in a converged solution.

In the end, the van Leer limiter and associated second order accuracy were abandoned. Instead, the more dissipative and less accurate upwind scheme was used for discretisation of divergence terms. This scheme has been used in the past for supercritical fluids, for example by Peeters et al.[101]. In personal communication, the lead author of this study agreed that it is difficult to obtain convergence for supercritical fluid simulations, making it necessary to resort to upwinding.

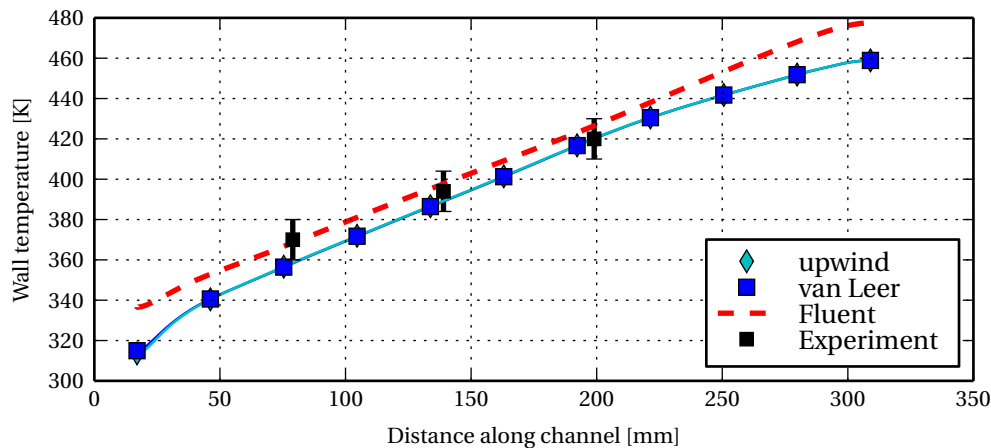


Figure 6.5: Experimental validation with first order upwind discretisation compared to using a second order van Leer limiter

To investigate whether this change has a large influence on the results, the experimental validation case TC24 was analysed again, now with upwind discretisation. Figure 6.5 shows the results as compared to the second order van Leer limiter. The lines are identical, save for a very small deviation at the inlet. This demonstrates that we can use upwind discretisation for rocket engine cooling channels without worrying about its effect on accuracy.

Figure 6.6 shows the wall temperature profile obtained from 3 different meshes with this upwind discretisation. Clearly, the simulations converge towards a grid-independent solution. A fourth simulation with 1000 cells in the streamwise direction did not reach convergence for the pressure equation. However, the solution results did not change substantially from the results of the fine solution shown in fig. 6.6. This indicates that the fine mesh is sufficient to obtain proper results. The simulation method seems to be conservative: using a coarser grid leads to a higher predicted wall temperature than using a finer grid.

At the inlet and near the throat, the largest differences between the simulations are found. This is because the temperatures there are closest to the pseudo-critical temperature, so there are relatively large variations in the fluid properties. Closer to the exit, the temperatures are so high that methane essentially behaves like a gas, making the number of cells less important. In addition, there is a strong curvature near the throat. This strong curvature requires a high number of cells in the streamwise direction. It should be noted that the results of fig. 6.6 were obtained with convective heating only, radiation was not included.

As mentioned earlier, it is important to check the  $y^+$  values that are obtained with the mesh. Wall functions yield good results when the first cell point is inside the logarithmic layer, so  $y^+$  should be above 30 and below around 300. When below 30, a  $y^+$  closer to zero means larger expected errors generated by the wall function. When inspecting the final solution, it turns out that the average  $y^+$  of the fine solution is 36. Most cells indeed have a  $y^+$  value that adheres to the requirements.

Figure 6.7 shows the  $y^+$  values that were obtained. Near the inlet of the channel, the  $y^+$  values are

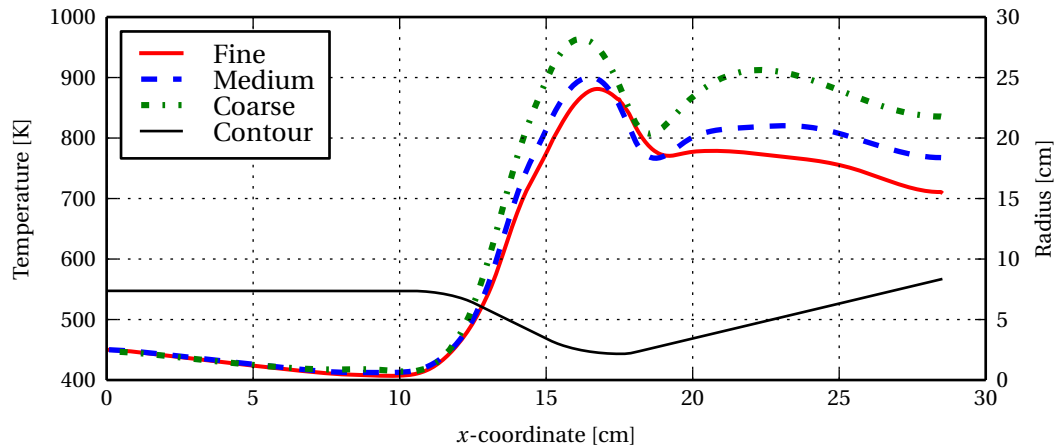


Figure 6.6: Wall temperatures obtained for copper chamber with different meshes

very low on all walls. Between the curved section there are also regions of low  $y^+$  values, but in more irregular patterns and not on all walls. It was found that all regions of low  $y^+$  corresponded to regions with low flow velocities at the first wall and therefore low shear stresses. This is in accordance with eq. 5.1.

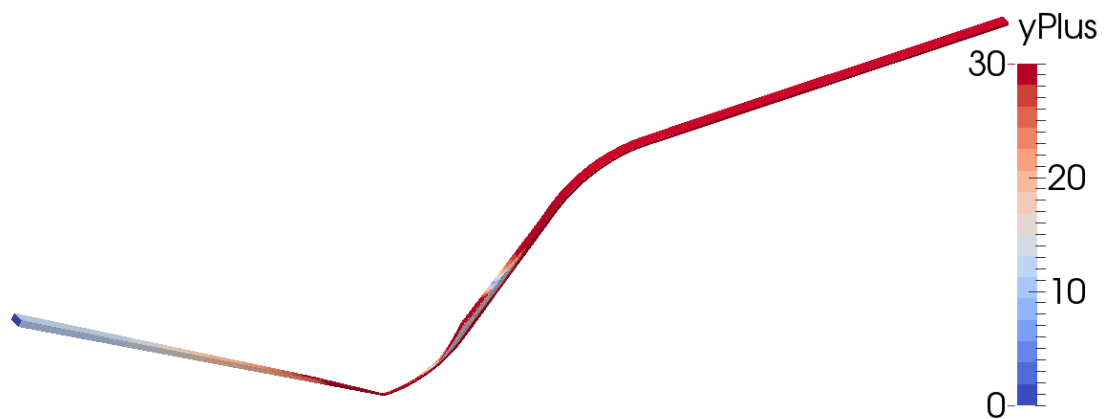


Figure 6.7:  $y^+$  values obtained for copper chamber with different meshes. The red cells have a value of 30 or higher, satisfying the requirement.

These regions are naturally also regions of low heat flux. Because of this, they are not very important for the determination of the total heat flux and the wall temperature. Only near the inlet of the channel, where a low  $y^+$  value is uniformly present at all walls, it is possible that the accuracy of the wall function approach is compromised. Luckily, this is not a very critical region because the local heat flux is very low. The total pressure drop incurred in this section of the channel is also small.

In summary, the  $y^+$  values are inside the region of validity for most cells. There are regions where  $y^+$  is too low, but they are either not critical to the local heat flux or not critical to the cooling of the chamber. Since some of the variations are so local, it would be hard to design a mesh that conforms to the requirement at all locations. We can conclude that the proposed mesh is suitable to obtain accurate results with the wall function approach.

The channel curvature induces a pressure difference inside the cross-section: the fluid at the outer side of the bend is at a higher pressure than at the inner side. This in turn results in a secondary flow, the so-called Dean vortices. This is a well known phenomenon in rocket engine cooling channels, studied numerically in many studies [29, 109, 110]. The Dean vortices improve the heat transfer in curved channels at the expense of increased pressure drop.

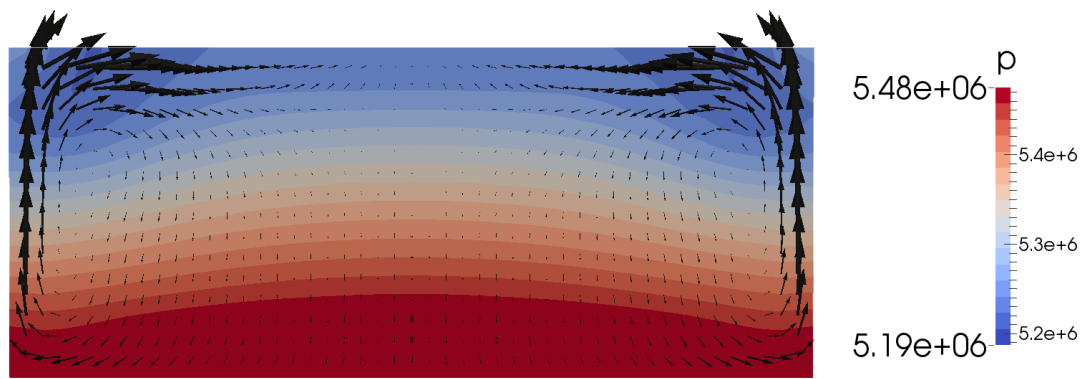


Figure 6.8: Pressure distribution and Dean vortices due to curvature of cooling channel at throat section of copper nozzle

Figure 6.8 shows the non-uniform pressure distribution and the secondary vortices at the throat as a result of the strong curvature there. This confirms that this important phenomenon is indeed modelled in the current software. Because curvature was not present in the validation cases of chapter 5, it was important to verify that the expected behaviour occurred in the simulations.

As a last step, it was verified that the Mach number of the flow was far below the critical Mach number. Because the cooling channel is severely constricted near the throat, the channel could act as a supersonic nozzle. However, it was found that the maximum Mach number remained below 0.5 for all simulations, even at the location of the highest fluid velocity.

#### 6.1.4. SIMULATION RESULTS

Having verified that the simulation is converged, the  $y^+$  values are suitable for wall functions and the effect of curvature is correctly predicted, we can now study the results in more detail and compare them to the one-dimensional analysis performed in chapter 3.

Figure 6.9 shows the wall temperature of the copper chamber (with dimensions from fig. 6.1) versus the one obtained from a one-dimensional analysis – including radiative heat transfer to the chamber wall. Note that this temperature profile looks different from the one in chapter 3 because both the outlet pressure and the assumed roughness are different from the values that were assumed in that chapter.

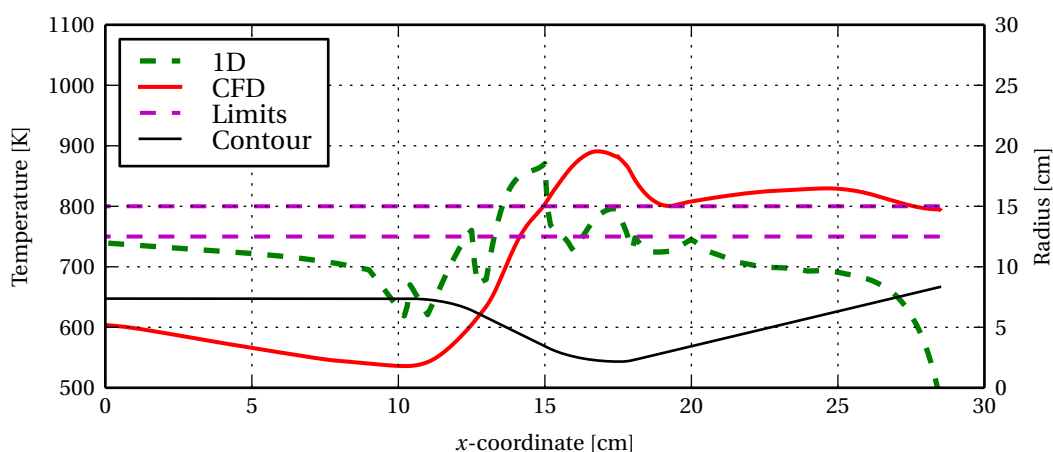


Figure 6.9: Wall temperature of copper combustion chamber

The differences between the two simulations are substantial: approximately 150 K near the outlet and inlet of the channel. This error is consistent with one found in the validation of the first-order tool carried out in chapter 3. The wall temperature at the throat exceeds the allowable temperature of

800 K by almost 100 K. This means the current design of the cooling channels does not satisfy the requirements.

The total pressure as well as the bulk temperature inside the channel are displayed in fig. 6.10. As was found in chapter 3, these variables are in much better agreement with the first order method than the wall temperature. The total pressure drop predicted by the CFD simulation is 11.84 bar, while the first order method predicts 12.96 bar, a 9% difference. The discrepancies are largest in the throat region, where the heat flux and flow velocity are highest. At this location, the total pressure curve from OpenFOAM shows erratic behaviour (a local increase of total pressure along the channel). There are two reasons for this. The calculation of total pressure is performed with an incompressible formula because the Mach number was not available. Second, the total pressure is calculated for slices perpendicular to the  $x$  axis, which are not necessarily perpendicular to the flow direction. Because of this, there are small errors, especially in regions of high velocity and strong curvature like the throat.

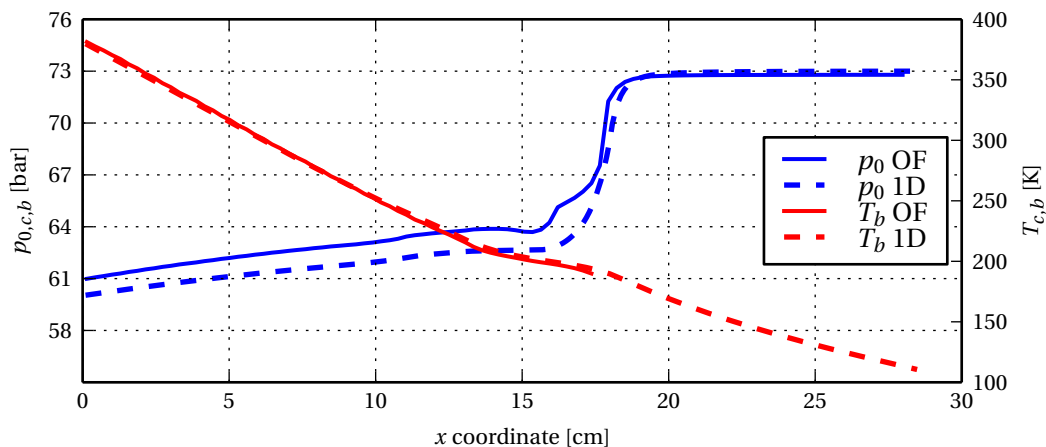


Figure 6.10: Total pressure and bulk temperature inside cooling channel of copper combustion chamber

The bulk temperature is almost exactly the same, because it is a direct consequence of the incoming heat flux. The wall temperatures of the first order method and the CHT method are so close that the heat flux is nearly identical for the two cases. In the first order method, the total heat exchanged per half-channel is 6412 W. In OpenFOAM, the heat exchanged is 6396 W. The difference is only 0.2%. This agreement also confirms that neglecting the circumferential curvature of the inner wall is an allowable assumption.

Figure 6.11 shows the wall temperature for the aluminium chamber design from chapter 3, but without a thermal barrier coating. Again, there are clear discrepancies between the first order method and the CFD results, but now the first order method underpredicts the wall temperature near the channel outlet. This is opposite from the behaviour seen in fig. 6.9 for the copper chamber.

As expected, without a thermal barrier coating the temperature becomes much higher than the allowable wall temperature of 500 K for aluminium. The peak temperature occurs near the throat and is approximately 775 K.

Figure 6.12 shows the wall temperature obtained with the same cooling channel geometry when a thermal barrier coating of 50  $\mu\text{m}$  thickness and 1  $\text{W/m}\cdot\text{K}$  thermal conductivity is present. Now, the wall temperature is below the allowable temperature of 500 K for the largest part of the nozzle, except at around  $x = 18$  cm where it exhibits a peak of around 590 K.

Figures 6.9, 6.11 and 6.12 showed the wall temperature obtained with the current cooling channel design. In all cases, the allowable temperature of the chamber wall material was exceeded. An improved design of the cooling channels is necessary to meet the requirements.

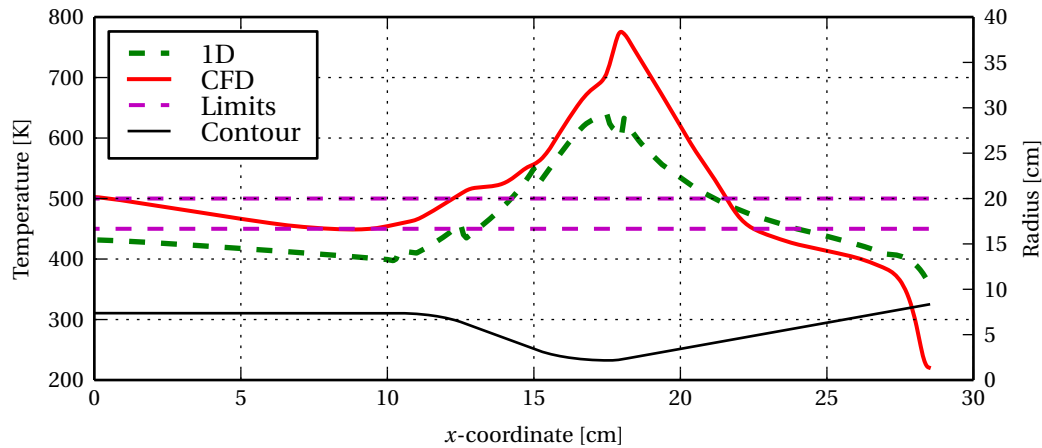


Figure 6.11: Wall temperature of uncoated aluminium combustion chamber

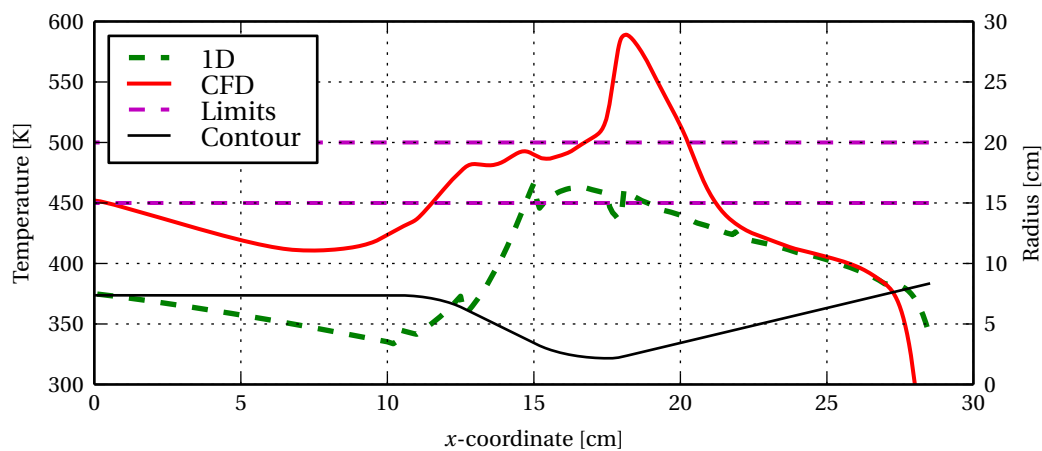


Figure 6.12: Wall temperature of coated aluminium combustion chamber

## 6.2. NOZZLE CHANNELS WITH IMPROVED GEOMETRY

The number of channels and rib thickness was kept constant, as mentioned in the introduction of this chapter. We will therefore consider only the height of the channel as a design variable. By varying the height, the velocity of the coolant can be adjusted. This in turn influences the cooling effect as well as the pressure drop.

We want to change the height of the cooling channels such that the wall temperature is close to the allowable wall temperature. Accounting for a margin of error of 50 K, this temperature is 750 K for copper and 450 K for aluminium.

From the simulations shown in section 6.1, the convective heat transfer coefficient of the coolant can be calculated. The convective heat transfer coefficient scales with  $u^{0.8}$ , where  $u$  is the (bulk) coolant velocity [111]. Assuming constant mass flow, the effect of channel height on the convective coefficient can be calculated.

In fact, if we assume that there are no other changes to the convective coefficient than the one caused by height changes, the required channel height at each location can be calculated directly. This assumption seems reasonable because the coefficient is mainly dependent on curvature and fluid temperature, density, viscosity and thermal conductivity. These are expected to stay roughly equal at a given location.

The required channel height can then be estimated using eq. 6.4, which has been derived using the equations for mass flow and heat flux. As a simplifying assumption, the temperature drop due to

conduction in the chamber wall has been neglected.

$$d_{\text{new}} = d_{\text{old}} \left[ \frac{q}{(T_{\text{allow}} - T_c) \alpha_{c,\text{old}}} \right]^{-1.25} \quad (6.4)$$

For the copper chamber, we set the allowable temperature  $T_{\text{allow}}$  to 750 K, based on the error margin of 50 K (see section 5.4). This results in the channel height shown in fig. 6.13.

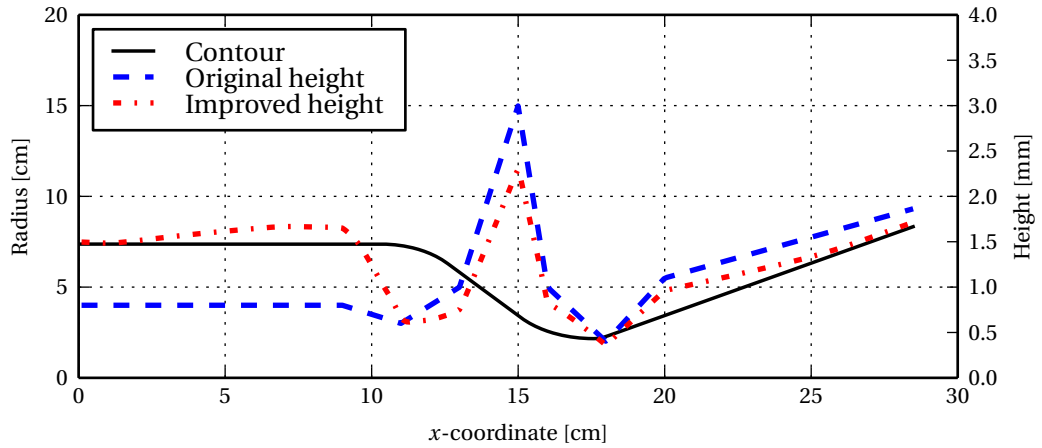


Figure 6.13: Cooling channel height in original and improved design

Figure 6.14 shows the resulting wall temperature in green. The temperature profile is far from the flat profile that was intended. The improvement brings the wall temperature closer to the design temperature near the channel inlet and outlet, but not near the throat. In other words, at the high heat flux locations, the wall temperature is still relatively far from the design temperature.

In order to calculate the required channel height, conduction through the wall was neglected. It seems now that this assumption is justified at low heat flux locations, but not at locations of high heat flux. This can be explained using eq. 3.2. If the convective heating coefficients at the coolant and hot gas sides are large, the thermal conduction through the wall becomes more important. The 4 mm thick wall (required for an inner chamber wall that can sustain the pressure forces without support from the outer wall) inhibits the heat flux at the throat so much that the temperature there hardly changes.

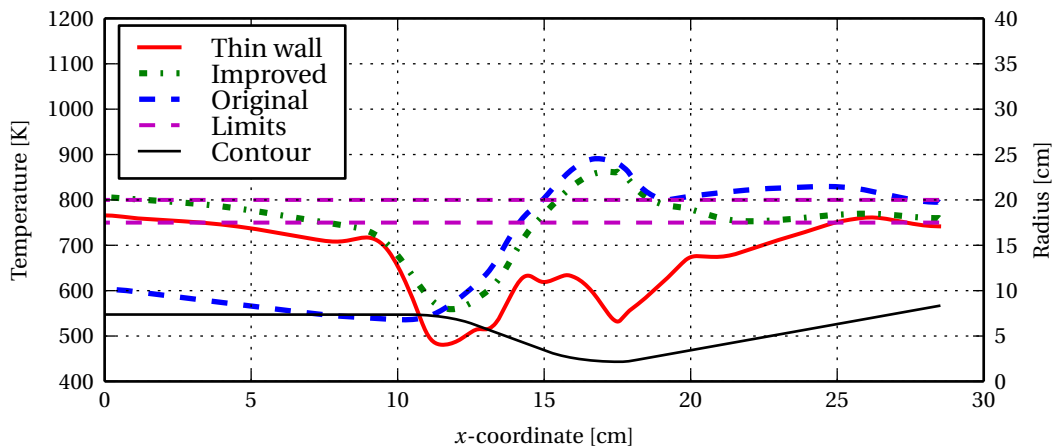


Figure 6.14: Wall temperature of copper combustion chamber with improved cooling channel geometry

We can confirm this by using the same cooling channel geometry, but now with a thin-walled chamber (with 1 mm wall thickness). This results in the red temperature curve in fig. 6.14. Indeed, we observe

large differences between the thick and thin-walled chambers, especially at the throat. The temperature difference there is 330 K! This shows that at the critical locations, a high thermal conductivity and small chamber wall thickness will be advantageous for cooling performance. Fortunately, the required thickness from a structural point of view is dependent on the nozzle radius, which is minimum at the throat. Therefore, a smaller thickness at this location may be tolerated.

In order to bring the thick-walled design (the green curve in fig. 6.14) to a temperature below 750 K at the throat, an increase in pressure drop is probably needed. At the throat, a decrease in channel height directly causes a large pressure drop because the coolant velocity is already high there. Let us therefore focus now on the thin-walled chamber. Its wall temperature is below the allowable temperature of 800 K at all locations along the nozzle and below the design temperature almost everywhere. In addition, the aluminium chambers will also be thin-walled, allowing for a direct comparison of both wall materials.

Figure 6.15 shows the temperature of coolant and wall at four sections along the channel of the thin-walled copper chamber. In all sections, the maximum wall temperature is found along the symmetry axis at the hot gas interface. This justifies that the values for wall temperature (e.g. in fig. 6.14) are taken at those locations.

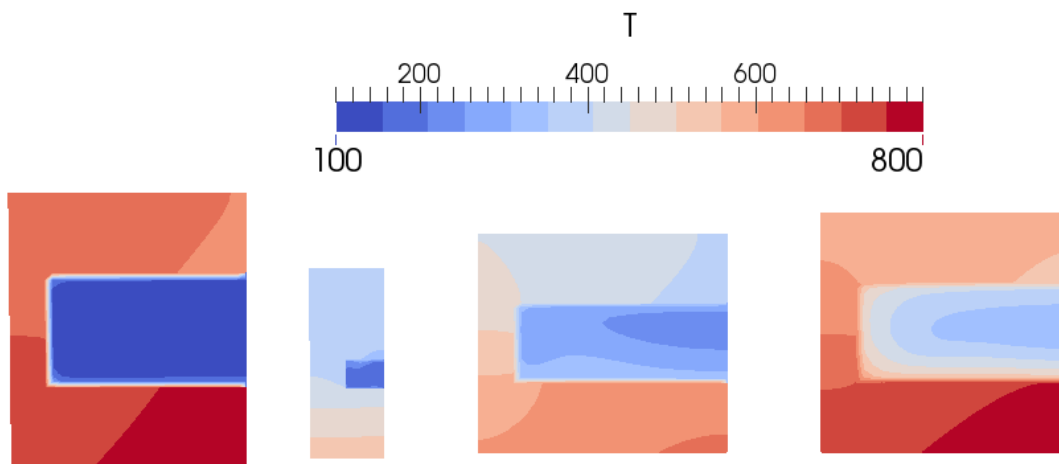


Figure 6.15: Temperature of coolant and wall at four cross-sections of the channel at (from left to right)  $x=260$  mm (near inlet),  $x=175.8$  mm (throat),  $x=100$  mm and  $x=0$  mm (near outlet)

From fig. 6.15, one notices that the temperature contours at the throat are almost horizontal, meaning that there is little temperature variation in the circumferential direction. At locations where the channels are wider, there is a clear difference in temperature between the symmetry plane and the rib plane. This is in line with findings by Pizzarelli et al [63], see e.g. fig. 3.2.

The temperature difference between the inner and outer wall grows from around 100 K at the channel inlet to around 200 K at the channel outlet. Parts of the outer wall are at temperatures of around 650 K. This should be taken into account in the engine design; the material of the outer jacket must be able to deal with this high temperature.

Figure 6.16 shows the pressure drop and bulk temperature inside the cooling channel. The bulk temperature rise is almost linear. This is because the bulk temperature is near the pseudo-critical temperature at the throat where the heat flux is maximum. In other words, the peak in heat capacity coincides with the peak in heat flux, smoothing the bulk temperature rise. The pressure drop, on the other hand, is clearly concentrated near the throat. In this region, the high heat flux must be matched by a correspondingly high convective heat coefficient. This is obtained by narrowing the channel and increasing the flow velocity, leading to a high pressure drop.

The total pressure drop over the channel is 14.4 bar. It is clear that further optimisation of the cooling channel geometry is possible to increase the wall temperature between 10 and 20 cm to a value that is closer to the allowable temperature. This will decrease the pressure drop in this region.

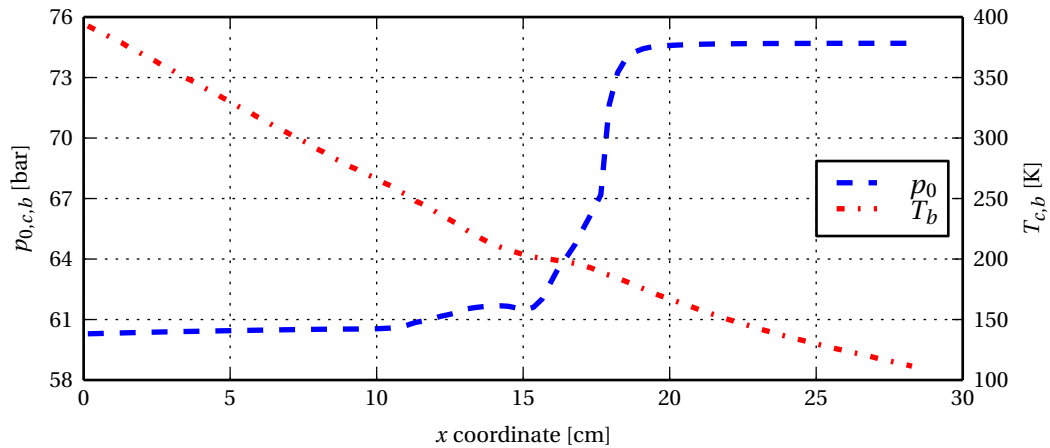


Figure 6.16: Coolant total pressure drop and bulk temperature rise with improved cooling channel geometry for copper combustion chamber

An important note is that the static pressure drops to 50 bar locally near the throat. The simulation artificially kept the pressure at 50 bar minimum because this was the minimum pressure at which methane properties were tabulated. There is therefore a tiny region in which the pressure is constrained and a small error is present. Because the region is so small, the real pressure will be only slightly below 50 bar, so the induced error on the simulation is very small. More importantly, this means the static pressure drop at the throat can be substantial: more than 10 bar in this case.

A large local static pressure drop is important to take into account when analysing a fluid near its critical pressure. It could mean that the pressure locally drops below the critical pressure. That would mean that the physics change completely: two-phase phenomena such as bubble formation start to occur. Two-phase flow cannot be modelled with the current method, so one should be careful to keep the static pressure above the critical pressure when using it.

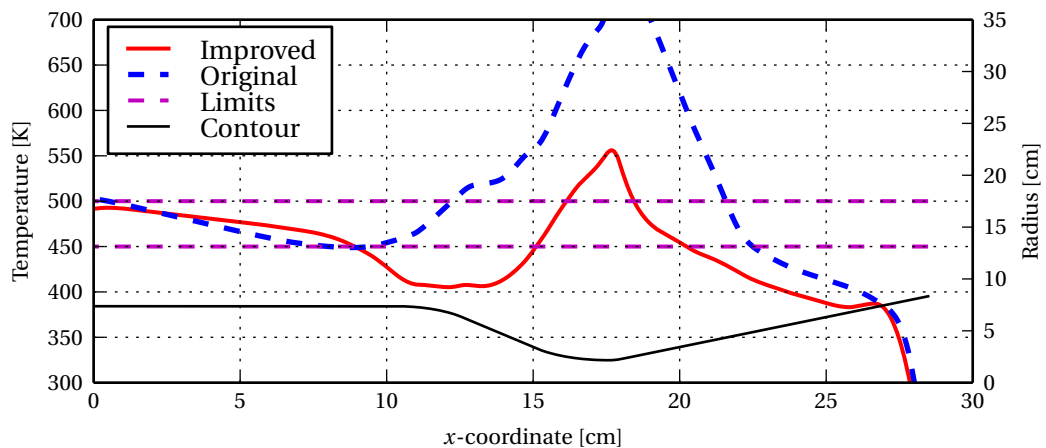


Figure 6.17: Wall temperature of uncoated aluminium combustion chamber with improved cooling channel geometry

It was also attempted to create a design for an uncoated aluminium chamber. The procedure was the same as for the copper chamber. Figure 6.17 shows that the wall temperature of this improved design still exceeds both the design and allowable temperature near the throat. This is despite a pressure drop of 173 bar! Clearly, this pressure drop is not feasible for a small rocket engine, especially if the pressure drop in the copper chamber is more than an order of magnitude smaller. This confirms the results from chapter 3.

The results with an improved cooling channel geometry for the aluminium chamber with a thermal barrier coating are presented in fig. 6.18. After the first improvement, the results were promising but

not entirely satisfactory. Between the combustion chamber and the throat the temperature remains below the design temperature. Between the throat and the diverging section, however, the temperature is much too high.

A second, manual change of the geometry was performed to obtain lower wall temperatures in this region. Figure 6.18 also shows the wall temperature resulting from this second improvement. Now the maximum wall temperature is below the allowable temperature, but above the design temperature.

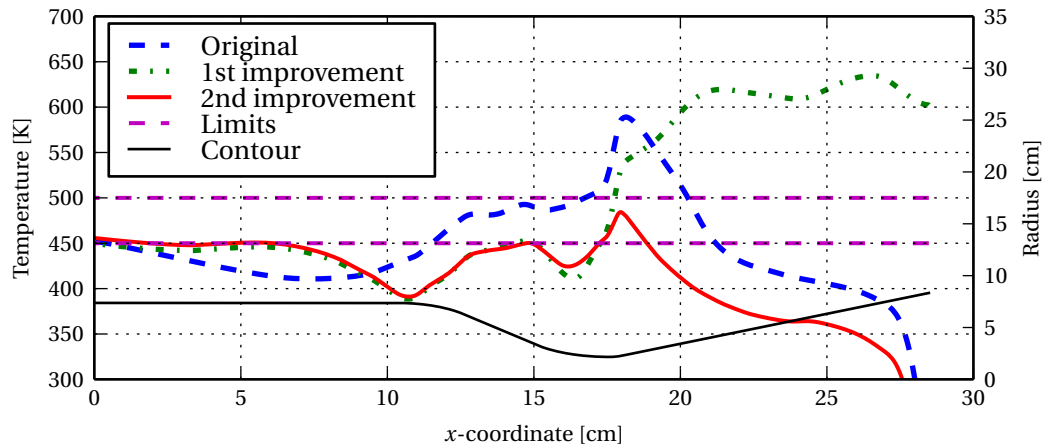


Figure 6.18: Wall temperature of coated aluminium combustion chamber with improved cooling channel geometry

Figure 6.19 shows the three cooling channel height profiles that were used to obtain these results. Again, it is clear that small changes in the channel height have substantial influence on the wall temperature. Furthermore, we can clearly see that the cooling effects are not local. Relatively small changes in the geometry in one location may introduce a large temperature difference elsewhere in the channel. For example, consider that around  $x = 20$  mm, the cooling channel dimensions of the original and first improvement cases are equal. The wall temperatures at this location are drastically different, however.

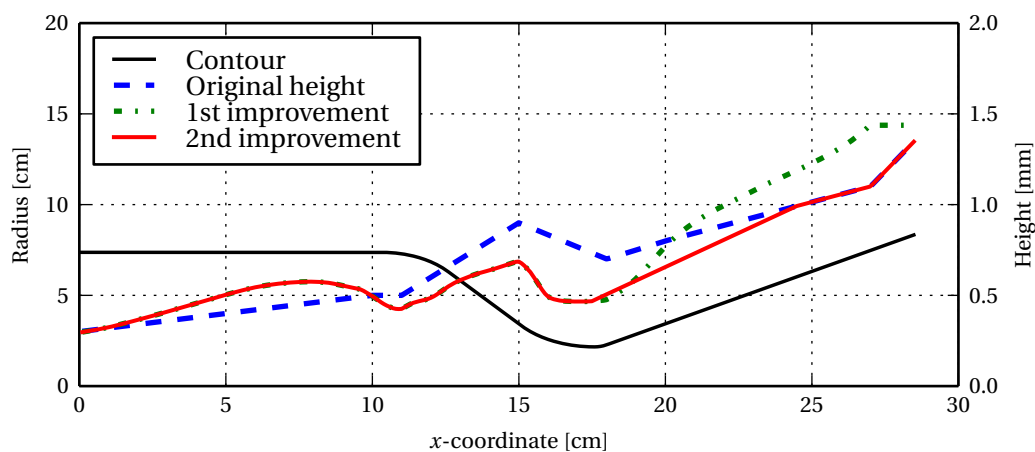


Figure 6.19: Improved cooling channel geometries for coated aluminium combustion chamber

Figure 6.20 shows the evolution of total coolant pressure and bulk temperature inside the cooling channels for the second improvement. The exit bulk temperature is somewhat lower than for the copper combustion chamber (355 K versus 393 K), because of the insulating effect of the thermal barrier coating.

The total pressure differences between the aluminium chamber and the copper chamber are large. Next to the large pressure drop in the throat, there is now also a large drop near the channel outlet.

To obtain enough cooling from the already hot, gas-like methane, a high flow velocity is required in this region. Recall that the targeted wall temperature is 450 K, while the coolant bulk temperature increases towards 350 K at the outlet. This results in a substantial pressure drop between  $x = 0$  cm and  $x = 10$  cm. The total pressure drop with this design is 44.2 bar, about three times the pressure drop of the copper combustion chamber.

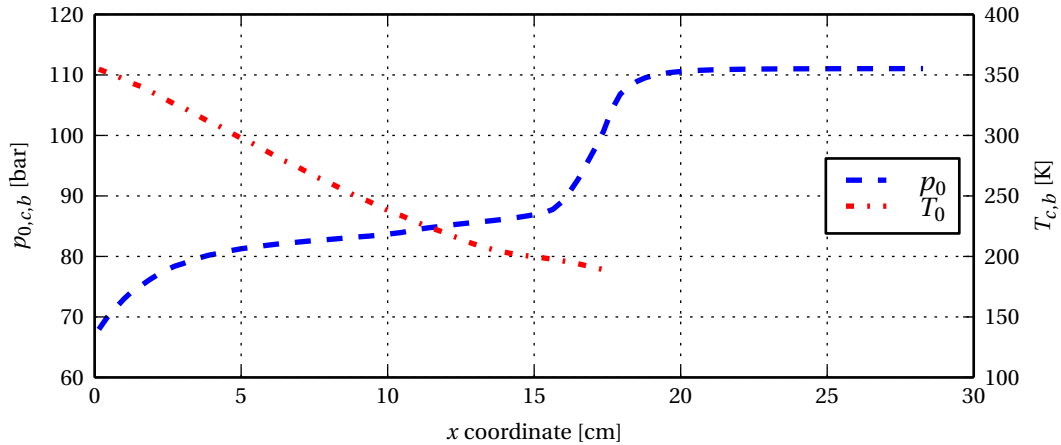


Figure 6.20: Coolant total pressure drop and bulk temperature rise with improved cooling channel geometry for coated aluminium combustion chamber

Further optimisation of the cooling channel geometry is needed to achieve the design goals, i.e. to keep the wall temperature below the design temperature. Nonetheless, there is only a small region of the combustion chamber wall that is above this temperature. It can therefore be expected that the pressure drop will not change much for an optimised design. We can answer the research questions based on the results from the second improved design for a coated aluminium chamber.

The improved designs are still not optimal; they do not offer the minimum pressure drop for a set allowable temperature. A thorough optimisation study would be required to find the best cooling channel geometry for a specific chamber wall material. In such a study, the following parameters could be taken into account and varied:

- Channel height
- Number of channels
- Rib width
- Turning angle of the channels with respect to nozzle axis

The differences between the copper and aluminium chamber results shown here are stark. This is largely due to the big differences in allowable wall temperature between copper and aluminium. Here, it is useful to note that the results could change if different alloys were chosen. However, the results are mainly driven by the fact that the allowable temperature differs by approximately 300 K. This difference will not decrease substantially when considering other copper and aluminium alloys.

The large difference in pressure drop is especially noteworthy. Even with a thermal barrier coating, the pressure drop required to cool an aluminium chamber will be above 40 bar. For a copper chamber, the pressure drop will be between 12 and 14 bar. Although the designs are not optimal, the estimates that were obtained are useful to assess the system-level impact of the chamber wall material selection, as outlined in the research subquestions. This is done in the next section.

### 6.3. MASS CALCULATION AND COMPARISON

To assess whether the chamber mass decrease offered by aluminium is relevant, it is useful to calculate the approximate mass of both copper and aluminium rocket engines. This was done by dividing the engine in segments of 1 mm and adding the contributions from the inner and outer chamber walls as well as the ribs. We consider both a copper and an aluminium chamber with wall thickness of 1 mm.

For a copper wall, the chamber mass is 1.30 kg. For aluminium, the engine mass would be reduced to 0.37 kg.

In the previous section, it was shown that the pressure drop required in the cooling channels of an aluminium chamber is substantially higher. This means that either the tank mass will increase (in a pressure fed design) or the turbopump mass will increase (in a pump fed design). Since the engine under consideration is rather small, it would likely be pressure fed. In addition, the mass of a tank is more easily estimated than turbopump mass. Let us therefore estimate the required tank mass for a pressure fed engine, using some rough assumptions and "ballpark" figures.

We assume a spherical tank containing 100 kg of methane, a rather modest amount of fuel. It is at a pressure of 50 bar (the approximate pressure before the injector if the chamber pressure is 40 bar) plus the coolant pressure drop. The temperature is assumed to be 110 K. The maximum allowable stress of the tank material is assumed to be 400 MPa, a reasonable value for an aluminium tank. This allows the calculation of the required wall thickness using eq. 5.9.

For a copper chamber with pressure drop of 14 bar, the tank radius is 0.38 m. At a pressure of 64 bar, the required wall thickness is 3 mm, resulting in a tank mass of 16 kg. For the aluminium chamber with a pressure drop of 44 bar, the tank pressure is 94 bar. Although the radius remains the same, the required wall thickness becomes 4.5 mm. This increases the tank mass to 24 kg.

The increased pressure drop has a large effect on the tank mass. In case of pump fed engines, an increase of turbopump mass and size can be expected, though the magnitude will be smaller (this is in fact the reason why turbopumps are used in rocket engines [8]). For the modest fuel mass of 100 kg, the tank mass increase of 8 kg is much larger than the rocket engine mass decrease. This shows that aluminium chambers with thermal barrier coatings would not have mass advantages over copper chambers on the vehicle level, especially if they are pressure fed.

## 6.4. SUMMARY OF RESULTS

Table 6.1 summarises the results of this chapter. Recall that the designs have not been optimised: some locations are above the design temperature, other are far below it. Nonetheless, the differences between both materials are large enough allow us to draw conclusions and answer the research questions, as explained in section 6.2.

Table 6.1: Summary of results for copper and aluminium combustion chambers

	Copper	Aluminium
$T_{\text{design}}$ [K]	750	450
$d_{\text{min}}$ [mm]	0.3	0.3
$\Delta p_{0,c}$ [bar]	14	44
$\Delta T_c$ [K]	283	245
Engine mass [kg]	1.3	0.37
Tank mass [kg]	16	24

Both materials are considered in a design with wall thickness of 1 mm. This means they are rigidly connected. There is no separate inner and outer chamber. Such a design would only be possible for copper. For aluminium, the required thickness combined with its lower thermal conductivity makes a design with separate inner and outer chamber impossible. For aluminium, it is assumed there is a thermal barrier coating on the hot gas side wall. The presence of a thermal barrier coating insulates the aluminium and reduces the wall temperature. For more information, see chapter 3.

Let us now answer the subquestions one by one.

1. *Is it possible to cool the thrust chamber wall to the allowable temperature or lower, using the fuel flow available?*

Yes, both for aluminium and copper this is possible. However, for an aluminium chamber, it is only possible to cool the chamber to the allowable temperature if a thermal barrier coating is applied. The required channel depth is small, approximately 0.3 mm for both the copper

chamber and the coated aluminium chamber.

2. *How high is the pressure drop over the cooling channel?*

The pressure drop over a coated aluminium chamber will be higher than 44 bar, while the pressure drop for a copper chamber is around 14 bar.

3. *By how much does the temperature of the coolant rise?*

The temperature rise is only influenced by the heat flux, because steady-state is assumed. It is 283 K for the copper chamber and 245 K for the aluminium chamber.

4. *What is the estimated mass of the thrust chamber?*

For a similar design, the copper chamber is 1.3 kg while the aluminium chamber weighs only 0.38 kg.

5. *What is the system-level impact of the differences in pressure drop, temperature rise and chamber mass?*

The higher pressure drop required for a coated aluminium chamber more than offsets the difference in chamber mass for a pressure fed engine, even at modest fuel mass, making a vehicle with a pressure fed aluminium engine heavier than one with a pressure fed copper engine. The system level impact of the temperature rise is negligible. Any change in coolant temperature rise is offset by a corresponding difference in heat loss inside the engine.

In the next chapter, the final conclusions and recommendations of this thesis are given, based on the results obtained here.

# 7

## CONCLUSIONS AND RECOMMENDATIONS

The research question of this thesis was

**Is it advantageous to use aluminium instead of copper for the chamber wall of a small, regeneratively cooled oxygen/methane rocket engine?**

The answer to this question – the first conclusion of this thesis – is:

1. The higher allowable temperature of copper (around 800 K) with respect to aluminium (around 500 K) is a substantial advantage for a regeneratively cooled combustion chamber. For an aluminium chamber, a thermal barrier coating is required to make regenerative cooling feasible. Even so, the pressure drop for a coated aluminium chamber was 44 bar, as opposed to 14 bar for an uncoated copper chamber. If the engine is pressure fed, the mass savings in the combustion chamber (1 kg) are more than offset by the increase in tank mass (8 kg) when using aluminium, even at the modest fuel mass of 100 kg. We can conclude that on the system level, it is not advantageous to use aluminium instead of copper for the chamber wall of a small, pressure fed, regeneratively cooled oxygen/methane rocket engine.

Several additional conclusions can be drawn from the research presented in this thesis.

2. Very small channel dimensions and very fine tolerances are required to cool the chambers to their allowable temperatures. For a small engine like the 10 kN generic engine that was investigated, there is so little fuel available for cooling that the channels must be very narrow. This is a complicating factor in the manufacturing process of a rocket engine.

Several additions were made to OpenFOAM in order to analyse rocket engine cooling channels filled with methane at supercritical pressure. The most prominent addition is a library to interpolate fluid property tables at runtime. Others are a change in the enthalpy equation of the solver, roughness boundary conditions for the Spalart-Allmaras and  $k-\omega$  turbulence models and new boundary conditions to model the heat transfer from the hot combustion gases. In the spirit of open-source software, these additions have been made available for the public [57]. This means that there is now a freely available tool that can be used for CFD and CHT analysis of methane rocket engine cooling channels.

3. The OpenFOAM tool has been successfully adapted for analysis of supercritical methane. It has been validated by comparison with numerical and experimental results on straight, constant cross-section channels. It demonstrated an accuracy of 15 K for wall temperature when using the  $k-\omega$  SST turbulence model with wall functions. The pressure drop was predicted to within 0.6 bar.
4. The influence of the turbulence and roughness model is small for the investigated case. All models predicted a wall temperature within 20 K from the experimental data. Three of the investigated approaches yield a pressure drop error smaller than 10%. Approaches using wall functions instead of full boundary layer integration were successful.

5. However, the wall roughness influence the results of the analysis substantially. The roughness height requires experimental determination: using a cold flow test the pressure drop can be established. This allows for the calibration of the roughness height. Without experimental determination of the roughness height, the wall temperature cannot be accurately predicted.
6. The new method in OpenFOAM is steady-state, resulting in a shorter computation time than the transient solver of La Sapienza University. The successful use of wall functions reduced the required computation time substantially. Combined, these two advantages make the new method two orders of magnitude faster than the reference solver.

Next to the multi-dimensional CFD tool, a simple, first order method based on one-dimensional heat transfer was developed from scratch in Python. This tool, called OMECA (One-dimensional Methane Engine Cooling Analysis), has been made available to Delft University of Technology and to the student rocketry group DARE. It is also available online [62].

7. A one-dimensional simulation tool was constructed to analyse rocket engine cooling channels. Although this tool cannot accurately predict the wall temperature at a specific location, it is useful to gain insight in the relevant variables and to obtain first order estimates of the pressure drop and channel dimensions.

For further research, the following recommendations can be made:

- It was proven that aluminium is not advantageous with respect to copper for a 10 kN, pressure fed engine. It would be interesting to extend the scope and verify if this conclusion also holds for larger and/or pump fed engines.
- It would be useful to perform an optimisation of the cooling channel geometry so as to minimise the pressure drop over the channel. This is a compelling optimisation problem because there are several independent variables (number of channels, channel height, rib thickness, turning angle in case of spiral channels) and changing the dimensions at one location has an influence on the result elsewhere.
- The wall function approach provided accurate estimates for the wall temperature in the experimental validation with a roughness height of 14.5  $\mu\text{m}$ . In section 5.2, it was shown that a fine mesh is required to predict heat transfer deterioration. It would be interesting to investigate whether heat transfer deterioration can also be simulated using the wall function approach with a relatively coarse mesh.
- The focus in this thesis has been on modelling of the cooling channels. The convective heat transfer from the hot combustion gases towards the wall has been calculated with simple equations. It is well known that these equations are inaccurate. To further improve the prediction of the wall temperature inside a rocket engine, it is recommended to use more advanced models (e.g. combustion CFD methods) to model the heat transfer from the hot gases inside the combustion chamber.
- The experimental validation shown in section 5.3 is limited to two test conditions of a single experimental campaign. To further prove the accuracy, it would be recommended to perform a more thorough experimental validation, for example at different mass flows, using different geometries and closer to the critical pressure. Ideally, one would want to compare the results to an actual rocket engine test.
- When designing the combustion chamber of a regeneratively cooled rocket, it is necessary to perform a detailed structural analysis in addition to the cooling analysis. A small wall thickness at high heat flux locations improves the cooling performance, so during design the cooling and structural analysis should be performed in parallel.

# A

## OPENFOAM GUIDELINES

In this appendix, a set of guidelines for CFD and CHT modelling in OpenFOAM is given. Some of these are not substantiated with proof, but rather based on personal experience, conventional wisdom or "the internet" – the forums at [www.cfd-online.com](http://www.cfd-online.com) in particular are a fount of knowledge. These guidelines may or may not be applicable to different problems. Because of this, they are not presented in the main body of the thesis. They are given here in the hope that they will be useful to someone.

### A.1. CONVERGENCE

For supercritical fluids, it is relatively difficult to obtain convergence. This is a result of the strong property variations. There are high gradients in the properties that can cause oscillatory behaviour. Two methods are needed to tackle this.

Under-relaxation is a tool often used in steady-state CFD, see e.g. Ferziger and Perić [88]. It is suggested to use the following under-relaxation factors. The under-relaxation factors for  $p$ ,  $\mathbf{U}$  and  $h$  were taken from Peeters et al. [101]. They accelerate convergence for supercritical fluids substantially.

- 0.3 for  $p$
- 0.05 for  $\rho$
- 0.4 for  $\mathbf{U}$
- 0.5 for  $h$
- 0.5 for all other equations, e.g.  $\epsilon$ ,  $\omega$ ,  $k$  or  $\nu_{\text{Tilda}}$

The second method to avoid oscillations is to use a flux limiters. These are discussed in chapter 4. Linear interpolation of the fluxes at the finite volume boundaries is almost guaranteed to result in oscillating solutions for supercritical fluids. The van Leer limiter is of second order and works excellently for straight channels. For curved nozzle channels, resorting to first order upwind discretisation was necessary to obtain converged results.

### A.2. SOLVERS

The `chtMultiRegionSimpleFoam` solver was adapted in this work. The solid domain needed no changes, but for the fluid domain the relevant equations were taken from `rhoSimpleFoam`. This was done because the fluid property tabulation seemed to work better with a `psiThermo` model than with a `heThermo` model. In addition, buoyancy was not deemed relevant in this context, so the buoyancy terms could be deleted. The resulting solver can be found on Github [57].

In terms of the linear matrix equation solvers, the standard solvers found in the tutorial case for `chtMultiRegionSimpleFoam` perform well. However, when parallel computing is used, the `PBiCG`

linear solver may lead to problems. Especially for the turbulence parameters, it can lead to erroneous results (characterised by a very sharp drop in residuals, but a non-physical solution). This problem can be circumvented by using `smoothSolver` for the turbulence parameters.

### A.3. WALL FUNCTIONS

For the parameters related to turbulence, wall functions can be used to avoid complete integration of the boundary layer. The wall functions are defined in the boundary condition specification files. The wall functions listed in table A.1 performed well in this thesis.

Table A.1: Appropriate wall functions in OpenFOAM

<code>alphat</code>	<code>compressible::alphatWallFunction</code>
<code>mut</code>	<code>mutURoughWallFunction</code> (not <code>mutkRoughWallFunction</code> , it gave nonsense results)
<code>k</code>	<code>compressible::kqRWallFunction</code>
<code>omega</code>	<code>compressible::omegaWallFunction</code>
<code>epsilon</code>	<code>compressible::epsilonWallFunction</code>

# BIBLIOGRAPHY

- [1] L. Denies, *Cooling analysis of oxygen/methane liquid rocket engines*, Literature study (2015), Delft University of Technology.
- [2] *State of the Satellite Industry Report*, Satellite Industry Association, Online presentation (2014), available online at <http://www.sia.org/wp-content/uploads/2014/09/SSIR-September-2014-Update.pdf>. Accessed March 18, 2015.
- [3] SpaceX, *The how and why of landing rockets*, (2015), available online at <http://www.spacex.com/news/2015/06/24/why-and-how-landing-rockets>. Accessed October 28, 2015.
- [4] Airbus Defence and Space, *Airbus Defence and Space's solution to reuse space launchers*, (2015), available online at <http://airbusdefenceandspace.com/reuse-launchers>. Accessed October 28, 2015.
- [5] P. B. de Selding, *ULA Touts Mid-air Recovery as More Cost-effective than SpaceX's Reusability Plan*, SpaceNews (2015), available online at <http://spacenews.com/ula-touts-mid-air-recovery-as-more-cost-effective-than-spacexs-reusability-plan/>. Accessed October 28, 2015.
- [6] T. McMahan, *NASA 3-D Prints First Full-Scale Copper Rocket Engine Part*, NASA (2015), available online at <http://www.nasa.gov/marshall/news/nasa-3-d-prints-first-full-scale-copper-rocket-engine-part.html>. Accessed October 28, 2015.
- [7] J. Foust, *Rocket Lab Unveils Battery-Powered, 3-D-Printed Rocket Engine*, SpaceNews (2015), available online at <http://spacenews.com/rocket-lab-unveils-battery-powered-3d-printed-rocket-engine/>. Accessed October 28, 2015.
- [8] G. P. Sutton and O. Biblarz, *Rocket Propulsion Elements*, (John Wiley & Sons, 2001) 7th ed.
- [9] R. Schuff, M. Maier, O. Sindiy, C. Ulrich, and S. Fugger, *Integrated Modeling and Analysis for a LOX/Methane Expander Cycle Engine: Focusing on Regenerative Cooling Jacket Design*, 42nd AIAA/ASME/SAE/ASEE Joint Propulsion Conference & Exhibit (Sacramento, 2006), AIAA 2006-4534, doi:10.2514/6.2006-4534.
- [10] D. Preclik, G. Hagemann, O. Knab, C. Mading, D. Haeseler, O. Haidn, A. Woschnak, and M. DeRosa, *LOX-Hydrocarbon Preparatory Thrust Chamber Technology Activities in Germany*, 41st AIAA/ASME/SAE/ASEE Joint Propulsion Conference & Exhibit (Tucson, 2005), AIAA-2005-4555, doi:10.2514/6.2005-4555.
- [11] J. B. Olansen, S. R. Munday, and J. L. Devolites, *Project Morpheus : Lessons Learned in Lander Technology Development*, AIAA SPACE 2013 Conference and Exposition (San Diego, 2013), AIAA 2013-5310, doi:10.2514/6.2013-5310.
- [12] R. Votta, F. Battista, M. Ferraiuolo, P. Roncioni, P. Vernillo, V. Salvatore, and P. de Matteis, *Design of an Experimental Campaign on Methane Regenerative Liquid Rocket Engine Cooling System*, 49th AIAA/ASME/SAE/ASEE Joint Propulsion Conference (San Jose, 2013), AIAA 2013-4146, doi:10.2514/6.2013-4146.
- [13] *BE-4 Rocket Engine*, United Launch Alliance, available online at [http://www.ulalaunch.com/uploads/docs/BE-4\\_Fact\\_Sheet\\_Web\\_Final\\_2.pdf](http://www.ulalaunch.com/uploads/docs/BE-4_Fact_Sheet_Web_Final_2.pdf). Accessed February 23, 2015.

- [14] D. Leone, *SpaceX Could Begin Testing Methane-fueled Engine at Stennis Next Year*, Space News (2013), available online at <http://spacenews.com/37859spacex-could-begin-testing-methane-fueled-engine-at-stennis-next-year/>. Accessed February 23, 2015.
- [15] D. K. Huzel and D. H. Huang, *Modern Engineering for Design of Liquid-Propellant Rocket Engines*, (American Institute of Aeronautics and Astronautics, 1992) Chap. Thrust Chambers and Other Combustion Devices, pp. 85–104.
- [16] M. Pizzarelli, *Modeling of Cooling Channel Flow in Liquid-Propellant Rocket Engines*, PhD thesis, Universita degli Studi di Roma "La Sapienza" (2007).
- [17] H. Burkhardt, M. Sippel, A. Herbertz, and J. Klevanski, *Kerosene vs. Methane: A Propellant Tradeoff for Reusable Liquid Booster Stages*, Journal of Spacecraft and Rockets **41**(5), pp. 762–769 (2004), doi:10.2514/1.2672.
- [18] T. Neill, D. Judd, E. Veith, and D. Rousar, *Practical uses of liquid methane in rocket engine applications*, Acta Astronautica **65**, pp. 696–705 (2009), doi:10.1016/j.actaastro.2009.01.052.
- [19] A. Chaikin, *Is SpaceX Changing the Rocket Equation?* National Air and Space Museum, Air & Space/Smithsonian article (2012), available online at <http://www.airspacemag.com/space/is-spacex-changing-the-rocket-equation-132285884/>. Accessed February 24, 2015.
- [20] K. Liang, B. Yang, and Z. Zhang, *Investigation of Heat Transfer and Coking Characteristics Introduction*, Journal of Propulsion and Power **14**(5), pp. 789–796 (1998), doi:10.2514/2.5342.
- [21] R. T. Cook and G. A. Coffey, *Space Shuttle Orbiter Engine Main Combustion Chamber Cooling and Life*, AIAA/SAE 9th Propulsion Conference (Las Vegas, 1973), AIAA-73-1310, doi:10.2514/6.1973-1310.
- [22] H. Ziebland and R. C. Parkinson, *Heat transfer in rocket engines* (Advisory Group for Aerospace Research & Development, 1971), AGARDograph 148.
- [23] M. Pizzarelli, F. Nasuti, and M. Onofri, *CFD analysis of transcritical methane in rocket engine cooling channels*, Journal of Supercritical Fluids **62**, pp. 79–87 (2012), doi:10.1016/j.supflu.2011.10.014.
- [24] J. M. Locke and D. B. Landrum, *Study of Heat Transfer Correlations for Supercritical Hydrogen in Regenerative Cooling Channels*, Journal of Propulsion and Power **24**(1), pp. 94–103 (2008), doi:10.2514/1.22496.
- [25] O. Kunz, R. Klimeck, W. Wagner, and M. Jaeschke, *The GERG-2004 Wide-Range Equation of State for Natural Gases and Other Mixtures*, GERG TM15 2007 (Groupe Européen de Recherches Gazières, Düsseldorf, 2007).
- [26] J. D. Jackson and W. B. Hall, *Forced convection heat transfer to fluids at supercritical pressure, Turbulent Forced Convection in Channels and Bundles*, edited by S. Kakac and D. B. Spalding (Hemisphere Publishing Corporation, 1979), pp. 563–611.
- [27] J. Licht, M. Anderson, and M. Corradini, *Heat transfer to water at supercritical pressures in a circular and square annular flow geometry*, International Journal of Heat and Fluid Flow **29**(1), pp. 156–166 (2008), doi:10.1016/j.ijheatfluidflow.2007.09.007.
- [28] A. Urbano, M. Pizzarelli, and F. Nasuti, *Numerical Analysis of Transcritical Fluids Heating in Liquid Rocket Engine Cooling Channels*, Aerotecnica Missili & Spazio, Journal of Aerospace Science, Technology and Systems **88**(1-2), pp. 20–30 (2009).
- [29] M. Pizzarelli, S. Carapellese, and F. Nasuti, *A Quasi-2-D Model for the Prediction of the Wall Temperature of Rocket Engine Cooling Channels*, Numerical Heat Transfer, Part A: Applications **60**(1), pp. 1–24 (2011), doi:10.1080/10407782.2011.578011.

- [30] M. Pizzarelli, A. Urbano, and F. Nasuti, *Numerical Analysis of Deterioration in Heat Transfer to Near-Critical Rocket Propellants*, Numerical Heat Transfer, Part A: Applications **57**(5), pp. 297–314 (2010), doi:10.1080/10407780903583016.
- [31] M. Pizzarelli, F. Nasuti, R. Votta, and F. Battista, *Assessment of a Conjugate Heat Transfer Model for Rocket Engine Cooling Channels Fed with Supercritical Methane*, 51st AIAA/SAE/ASEE Joint Propulsion Conference (2015), AIAA 2015-3852, doi:10.2514/6.2015-3852.
- [32] Y.-Z. Wang, Y.-X. Hua, and H. Meng, *Numerical Studies of Supercritical Turbulent Convective Heat Transfer of Cryogenic-Propellant Methane*, Journal of Thermophysics and Heat Transfer **24**(3), pp. 490–500 (2010), doi:10.2514/1.46769.
- [33] B. Ruan and H. Meng, *Supercritical Heat Transfer of Cryogenic-Propellant Methane in Rectangular Engine Cooling Channels*, Journal of Thermophysics and Heat Transfer **26**(2), pp. 313–321 (2012), doi:10.2514/1.T3670.
- [34] L. Wang, Z. Chen, and H. Meng, *Numerical study of conjugate heat transfer of cryogenic methane in rectangular engine cooling channels at supercritical pressures*, Applied Thermal Engineering **54**(1), pp. 237–246 (2013), doi:10.1016/j.applthermaleng.2013.02.007.
- [35] H. Negishi, Y. Daimon, H. Kawashima, and N. Yamanishi, *Flowfield and Heat Transfer Characteristics of Cooling Channel Flows in a Methane-Cooled Thrust Chamber*, 48th AIAA/ASME/SAE/ASEE Joint Propulsion Conference & Exhibit (Atlanta, 2012), AIAA 2012-4122, doi:10.2514/6.2012-4122.
- [36] E. Kirner, D. Thelemann, and D. Wolf, *Development Status of the Vulcain Thrust Chamber*, Acta Astronautica **29**(4), pp. 271–282 (1993), doi:10.1016/0094-5765(93)90140-R.
- [37] P. Caisso, J. Barton, M. Illig, and T. Margat, *Development Status of the Vulcain 2 Engine*, 36th AIAA/ASME/SAE/ASEE Joint Propulsion Conference & Exhibit (Huntsville, 2000), AIAA 2000-3781, doi:10.2514/6.2000-3781.
- [38] K. Katsuta, H. Miyajima, T. Ito, and K. Suzuki, *Development Status of LE-7 H-II Rocket Main Engine*, AIAA/ASME/SAE/ASEE 22nd Joint Propulsion Conference (Huntsville, 1986), AIAA-86-1409, doi:10.2514/6.1986-1409.
- [39] G. P. Sutton, *History of Liquid Propellant Rocket Engines in the United States*, Journal of Propulsion and Power **19**(6), pp. 978–1007 (2003), doi:10.2514/2.6942.
- [40] *Masten and Armadillo Claim Lunar Lander Prizes*, National Aeronautics and Space Administration (2009), available online at [http://www.nasa.gov/offices/oct/early\\_stage\\_innovation/centennial\\_challenges/cc\\_ll\\_feature\\_lv12.html](http://www.nasa.gov/offices/oct/early_stage_innovation/centennial_challenges/cc_ll_feature_lv12.html). Accessed March 10, 2015.
- [41] *XCOR and ULA Demonstrate Revolutionary Rocket Engine Nozzle Technology*, United Launch Alliance, Press release (2011), available online at <http://www.ulalaunch.com/also-sign-contract-for-liquid-hydrogen.aspx?title=XCOR+and+ULA+Demonstrate+Revolutionary+Rocket+Engine+Nozzle+Technology>. Accessed March 10, 2015.
- [42] *OpenFOAM User Guide*, CFD Direct (2014), available online at <http://foam.sourceforge.net/docs/Guides-a4/UserGuide.pdf>. Accessed April 8, 2015.
- [43] M. Pizzarelli, F. Nasuti, and M. Onofri, *Flow Analysis of Transcritical Methane in Rectangular Cooling Channels*, 44th AIAA/ASME/SAE/ASEE Joint Propulsion Conference & Exhibit (Hartford, 2008), AIAA 2008-4556, doi:10.2514/6.2008-4556.
- [44] B. Younglove and J. F. Ely, *Thermophysical Properties of Fluids. II. Methane, Ethane, Propane, Isobutane, and Normal Butane*, Journal of Physical and Chemical Reference Data **16**(4), pp. 577–798 (1987), doi:10.1115/1.2790020.

- [45] F. Q. Zhong, X. J. Fan, J. Wang, G. Yu, and J. G. Li, *Characteristics of compressible flow of supercritical kerosene*, *Acta Mechanica Sinica/Lixue Xuebao* **28**(1), pp. 8–13 (2012), doi:10.1007/s10409-012-0006-x.
- [46] H. Hoge and J. Lassiter, *Critical temperatures, pressures, and volumes of hydrogen, deuterium, and hydrogen deuteride*, *Journal of Research of the National Bureau of Standards* **47**(2), pp. 75 (1951), doi:10.6028/jres.047.010.
- [47] P. Brossel, S. Eury, P. Signol, H. Laporte-Weywada, and J. Micewicz, *Development Status of the Vulcain Engine*, *31st AIAA/ASME/SAE/ASEE Joint Propulsion Conference and Exhibit* (San Diego, 1995), AIAA 95-2539, doi:10.2514/6.1995-2539.
- [48] F. Kirby, *Space Shuttle Main Engine Program Status*, *AIAA/SAE 9th Propulsion Conference* (Las Vegas, 1973), AIAA-73-1177, doi:10.2514/6.1973-1177.
- [49] R. Sekita, M. Yasui, and S. Warashina, *The LE-5 Series Development, Approach to Higher Thrust, Higher Reliability and Greater Flexibility*, *36th AIAA/ASME/SAE/ASEE Joint Propulsion Conference and Exhibit* (Huntsville, 2000), AIAA 2000-3453, doi:10.2514/6.2000-3453.
- [50] *NIST Chemistry WebBook*, National Institute of Standards and Technology, available online at <http://webbook.nist.gov/chemistry/>. Accessed April 11, 2015.
- [51] U. Setzmann and W. Wagner, *A New Equation of State and Tables of Thermodynamic Properties for Methane Covering the Range from the Melting Line to 625 K at Pressures up to 1000 MPa*, *Journal of Physical and Chemical Reference Data* **20**(6), pp. 1061–1155 (1991), doi:10.1063/1.555898.
- [52] S. E. Quiñones-Cisneros and U. K. Deiters, *Generalization of the Friction Theory for Viscosity Modeling*, *Journal of Physical Chemistry B* **110**(25), pp. 12820–12834 (2006), doi:10.1021/jp0618577.
- [53] A. Urbano and F. Nasuti, *Parametric Analysis of Heat Transfer to Supercritical-Pressure Methane*, *Journal of Thermophysics and Heat Transfer* **26**(3), pp. 450–463 (2012), doi:10.2514/1.T3840.
- [54] E. P. Sakonidou, H. R. van den Berg, C. A. ten Seldam, and J. V. Sengers, *The thermal conductivity of methane in the critical region*, *The Journal of Chemical Physics* **105**(23), pp. 10535–10555 (1996), doi:10.1063/1.472943.
- [55] G. A. Olchowy and J. V. Sengers, *A Simplified Representation for the Thermal Conductivity of Fluids in the Critical Region*, *International Journal of Thermophysics* **10**(2), pp. 417–426 (1989), doi:10.1007/BF01133538.
- [56] D. G. Friend, J. F. Ely, and H. Ingham, *Thermophysical Properties of Methane*, *Journal of Physical and Chemical Reference Data* **18**(2), pp. 583–638 (1989).
- [57] L. Denies, *OpenFOAM module for tabulated fluid properties*, (2015), available online at <https://github.com/lldenies/tabulatedProperties>. Accessed November 26, 2015.
- [58] J. J. Esposito and R. F. Zabora, *Thrust Chamber Life Prediction Volume I - Mechanical and Physical Properties of High Performance Rocket Nozzle Materials*, NASA CR-134806 (National Aeronautics and Space Administration, 1975).
- [59] *Glidcop, copper dispersion strengthened with aluminum oxide*, SCM Metal Products, Inc., Materials fact sheet, available online at [http://www.aps.anl.gov/APS\\_Engineering\\_Support\\_Division/Mechanical\\_Operations\\_and\\_Maintenance/Miscellaneous/tech\\_info/Glidcop/SCM\\_Glidcop\\_product\\_info.pdf](http://www.aps.anl.gov/APS_Engineering_Support_Division/Mechanical_Operations_and_Maintenance/Miscellaneous/tech_info/Glidcop/SCM_Glidcop_product_info.pdf). Accessed November 4, 2015.
- [60] *Aluminum 7075-T6*, CRP MECCANICA, Online data sheet, available online at <http://www.crpmeccanica.eu/PDF/aluminium-7075-t6-7075-t651.pdf>. Accessed April 7, 2015.
- [61] J. G. Kaufman, ed., *Properties of aluminum alloys: tensile, creep, and fatigue data at high and low temperatures*, (The Aluminum Association, 1999) pp. 206–212.

- [62] L. Denies, *OMECA*, (2015), available online at <https://github.com/ldenies/OMECA>. Accessed November 26, 2015.
- [63] M. Pizzarelli, B. Betti, F. Nasuti, D. Ricci, P. Roncioni, F. Battista, and V. Salvatore, *Cooling Channel Analysis of a LOX/LCH4 Rocket Engine Demonstrator*, 50th AIAA/ASME/SAE/ASEE Joint Propulsion Conference (Cleveland, 2014), AIAA 2014-4004, doi:10.2514/6.2014-4004.
- [64] S. Gordon and B. J. McBride, *Computer Program for Calculation of Complex Chemical Equilibrium Compositions and Applications I. Analysis*, NASA RP-1311-P1 (National Aeronautics and Space Administration, 1994).
- [65] M. J. Bedard, T. W. Feldman, A. Rettenmaier, and W. Anderson, *Student Design / Build / Test of a Throttleable LOX-LCH 4 Thrust Chamber*, 48th AIAA/ASME/SAE/ASEE Joint Propulsion Conference & Exhibit (Atlanta, 2012), AIAA 2012-3883, doi:10.2514/6.2012-3883.
- [66] V. A. Kurganov, *Adiabatic wall temperature*, Begell House, Thermopedia article (2011), available online at <http://www.thermopedia.com/content/291/>. Accessed May 6, 2015.
- [67] D.R.Bartz, *A simple equation for rapid estimation of rocket nozzle convective heat transfer coefficient*, Jet Propulsion **27**(1), pp. 49–51 (1957).
- [68] H. Tamura, F. Ono, A. Kumakawa, and N. Yatsuyanagi, *LOX/Methane Staged Combustion Rocket Combustor Investigation*, AIAA/SAE/ASME/ASEE 23rd Joint Propulsion Conference (San Diego, 1987), AIAA-87-1856, doi:10.2514/6.1987-1856.
- [69] C. U. Kirchberger, *Investigation on Heat Transfer in Small Hydrocarbon Rocket Combustion Chambers*, PhD thesis, Technische Universität München (2014).
- [70] C. Kirchberger, R. Wagner, H.-P. Kau, S. Soller, P. Martin, M. Bouchez, and C. Bonzom, *Prediction and Analysis of Heat Transfer in Small Rocket Chambers*, 46th AIAA Aerospace Sciences Meeting and Exhibit (Reno, 2008), AIAA 2008-1260, doi:10.2514/6.2008-1260.
- [71] M. Niino, A. Kumakawa, N. Yatsuyanagi, and A. Suzuki, *Heat Transfer Characteristics of Liquid Hydrogen as a Coolant for the LO2/LH2 Rocket Thrust Chamber with the Channel Wall Construction*, AIAA/SAE/ASME 18th Joint Propulsion Conference (Cleveland, 1982), AIAA-82-1107, doi:10.2514/6.1982-1107.
- [72] M. L. Meyer, *The Effect of Cooling Passage Aspect Ratio on Curvature Heat Transfer Enhancement*, TM-107426 (National Aeronautics and Space Administration, 1997).
- [73] F. Neuner, D. Preclik, M. Popp, and M. K. Funke H., *Experimental and Analytical Investigation of Local Heat Transfer in High Aspect Ratio Cooling Channels*, 34th AIAA/ASME/SAE/ASEE Joint Propulsion Conference and Exhibit (Cleveland, 1998), AIAA 1998-3439, doi:10.2514/6.1998-3439.
- [74] M. Pizzarelli, F. Nasuti, and M. Onofri, *Analysis of Curved-Cooling-Channel Flow and Heat Transfer in Rocket Engines*, Journal of Propulsion and Power **27**(5), pp. 1045–1053 (2011), doi:10.2514/1.B34163.
- [75] M. Popp and G. Schmidt, *Rocket engine combustion chamber design concepts for enhanced life*, 32nd AIAA/ASME/SAE/ASEE Joint Propulsion Conference and Exhibit (Lake Buena Vista, 1996), AIAA 96-3303, doi:10.2514/6.1996-3303.
- [76] J. A. Carlile and R. Quentmeyer, *An Experimental Investigation of High-Aspect-Ratio Cooling Passages*, AIAA/SAE/ASME/ASEE 28th Joint Propulsion Conference and Exhibit (Nashville, 1992), AIAA-92-3154, doi:10.2514/6.1992-3154.
- [77] F. Lebail and M. Popp, *Numerical Analysis of High Aspect Ratio Cooling Passage Flow and Heat Transfer*, AIAA/SAE/ASME/ASEE 29th Joint Propulsion Conference (Monterey, 1993), AIAA 93-1829, doi:10.2514/6.1993-1829.

- [78] R. Votta, F. Battista, A. Gianvito, A. Smoraldi, V. Salvatore, M. Pizzarelli, G. Leccese, F. Nasuti, S. Shark, R. Feddema, and S. Meyer, *Experimental Investigation of Methane in Transcritical Conditions*, 50th AIAA/ASME/SAE/ASEE Joint Propulsion Conference (Cleveland, 2014), AIAA 2014-4005, doi:10.2514/6.2014-4005.
- [79] V. Salvatore, F. Battista, P. de Matteis, L. Arione, M. Rudnykh, and F. Ceccarelli, *Recent Progress on the Development of a LOX/LCH<sub>4</sub> Rocket Engine Demonstrator in the Framework of the Italian Hyprob Program*, 64th International Astronautical Congress (Beijing, 2013), IAC-13,C4,3,4,x19439.
- [80] D. Jones, *Reusable Rocket Propulsion for Space Tourism Vehicles*, 40th AIAA/ASME/SAE/ASEE Joint Propulsion Conference & Exhibit (Fort Lauderdale, 2004), AIAA 2004-3742, doi:10.2514/6.2004-3742.
- [81] V. Weingarten, P. Seide, and J. Peterson, *Buckling of Thin-walled Circular Cylinders*, SP-8007 (National Aeronautics and Space Administration, 1968).
- [82] X. Q. Cao, R. Vassen, and D. Stoeber, *Ceramic materials for thermal barrier coatings*, Journal of the European Ceramic Society **24**(1), pp. 1–10 (2004), doi:10.1016/S0955-2219(03)00129-8.
- [83] J. A. Nesbitt, *Thermal Response of Various Thermal Barrier Coatings in a High Heat Flux Rocket Engine*, Surface and Coatings Technology **43-44**(1), pp. 458–469 (1990), doi:10.1016/0257-8972(90)90097-V.
- [84] J. Nesbitt, *Thermal modeling of various thermal barrier coatings in a high heat flux rocket engine*, Surface and Coatings Technology **130**(2-3), pp. 141–151 (2000), doi:10.1016/S0257-8972(00)00723-4.
- [85] R. J. Quentmeyer, H. J. Kasper, and J. M. Kazaroff, *Investigation of the Effect of Ceramic Coatings on Rocket Thrust Chamber Life*, AIAA/SAE 14th Joint Propulsion Conference (Las Vegas, 1978), AIAA 1978-1034, doi:10.2514/6.1978-1034.
- [86] J. Lee, Y. Kim, U. Jung, and W. Chung, *Thermal conductivity of anodized aluminum oxide layer: The effect of electrolyte and temperature*, Materials Chemistry and Physics **141**(2-3), pp. 680–685 (2013), doi:10.1016/j.matchemphys.2013.05.058.
- [87] H. Jasak, *Error Analysis and Estimation for the Finite Volume Method with Applications to Fluid Flows*, PhD thesis, Imperial College of Science, Technology and Medicine (1996).
- [88] J. H. Ferziger and M. Perić, *Computational Methods for Fluid Dynamics*, (Springer, Berlin, 2002) 3rd ed.
- [89] F. M. White, *Viscous Fluid Flow*, (McGraw-Hill, 2006) Chap. Incompressible Turbulent Mean Flow, pp. 411 – 498, 3rd ed.
- [90] H. Jasak, *Numerical Solution Algorithms for Compressible Flows*, Lecture Notes, University of Zagreb (2006), available online at <http://www.scribd.com/doc/27927305/Numerical-Solution-Algorithms-for-Compressible-Flows>. Accessed June 22, 2015.
- [91] G. Ribert, D. Taieb, and V. Yang, *Large-eddy simulation of a supercritical channel flow using a shock capturing numerical scheme*, Computers & Fluids **117**, pp. 103–113 (2015), doi:10.1016/j.compfluid.2015.05.014.
- [92] J. B. Calvo and K. Hannemann, *Numerical Simulation of Liquid Rocket Engine Cooling Channels*, 45th AIAA/ASME/SAE/ASEE Joint Propulsion Conference & Exhibit (Denver, 2009), AIAA 2009-5302, doi:10.2514/6.2009-5302.
- [93] S. H. El Tahry, *k- $\epsilon$  equation for compressible reciprocating engine flows*, Journal of Energy **7**(4), pp. 345–353 (1983).
- [94] F. R. Menter, *Zonal Two Equation k- $\omega$  Turbulence Models for Aerodynamic Flow*, 24th Fluid Dynamics Conference (Orlando, 1993), AIAA 93-2906, doi:10.2514/6.1993-2906.

- [95] F. R. Menter, M. Kuntz, and R. Langtry, *Ten Years of Industrial Experience with the SST Turbulence Model*, *Turbulence Heat and Mass Transfer* 4 pp. 625–632 (2003).
- [96] P. R. Spalart and S. R. Allmaras, *A One-Equation Turbulence Model for Aerodynamic Flows*, *30th Aerospace Sciences Meeting & Exhibit* (Reno, 1992), AIAA-92-0439, doi:10.2514/6.1992-439.
- [97] B. Aupoix and P. R. Spalart, *Extensions of the Spalart - Allmaras turbulence model to account for wall roughness*, *International Journal of Heat and Fluid Flow* 24(4), pp. 454–462 (2003), doi:10.1016/S0142-727X(03)00043-2.
- [98] B. Aupoix, *Roughness Corrections for the  $k$ - $\omega$  Shear Stress Transport Model: Status and Proposals*, *Journal of Fluids Engineering* 137(2), pp. 021202 (2014), doi:10.1115/1.4028122.
- [99] B. Aupoix, *Improved heat transfer predictions on rough surfaces*, *International Journal of Heat and Fluid Flow* 56, pp. 160–171 (2015), doi:10.1016/j.ijheatfluidflow.2015.07.007.
- [100] D. Dipprey and R. Sabersky, *Heat and momentum transfer in smooth and rough tubes at various prandtl numbers*, *International Journal of Heat and Mass Transfer* 6(5), pp. 329–353 (1963), doi:10.1016/0017-9310(63)90097-8.
- [101] J. W. R. Peeters, C. T’Joel, and M. Rohde, *Investigation of the thermal development length in annular upward heated laminar supercritical fluid flows*, *International Journal of Heat and Mass Transfer* 61(1), pp. 667–674 (2013), doi:10.1016/j.ijheatmasstransfer.2013.02.039.
- [102] P. Sweby, *High Resolution Schemes Using Flux Limiters for Hyperbolic Conservation Laws*, *SIAM Journal on Numerical Analysis* 21(5), pp. 995–1011 (1984), doi:10.1137/0721062.
- [103] B. A. Kader, *Temperature and concentration profiles in fully turbulent boundary layers*, *International Journal of Heat and Mass Transfer* 24(9), pp. 1541–1544 (1981), doi:http://dx.doi.org/10.1016/0017-9310(81)90220-9.
- [104] M. Pizzarelli, F. Nasuti, M. Onofri, P. Roncioni, R. Votta, and F. Battista, *Heat transfer modeling for supercritical methane flowing in rocket engine cooling channels*, *Applied Thermal Engineering* 75, pp. 600–607 (2014), doi:10.1016/j.applthermaleng.2014.10.008.
- [105] X. Cheng, B. Kuang, and Y. H. Yang, *Numerical analysis of heat transfer in supercritical water cooled flow channels*, *Nuclear Engineering and Design* 237(3), pp. 240–252 (2007), doi:10.1016/j.nucengdes.2006.06.011.
- [106] M. Sharabi and W. Ambrosini, *Discussion of heat transfer phenomena in fluids at supercritical pressure with the aid of CFD models*, *Annals of Nuclear Energy* 36(1), pp. 60–71 (2009), doi:10.1016/j.anucene.2008.10.006.
- [107] J. Y. Yoo, *The Turbulent Flows of Supercritical Fluids with Heat Transfer*, *Annual Review of Fluid Mechanics* 45(1), pp. 495–525 (2013), doi:10.1146/annurev-fluid-120710-101234.
- [108] J. Xiong and X. Cheng, *Turbulence modelling for supercritical pressure heat transfer in upward tube flow*, *Nuclear Engineering and Design* 270, pp. 249–258 (2014), doi:10.1016/j.nucengdes.2014.01.014.
- [109] A. Fröhlich, H. Immich, F. LeBail, M. Popp, and G. Scheuerer, *Three-Dimensional Flow Analysis in a Rocket Engine Coolant Channel of High Depth/Width Ratio*, *AIAA/SAE/ASME 27th Joint Propulsion Conference* (Sacramento, 1991), AIAA 91-2183, doi:10.2514/6.1991-2183.
- [110] J. DiValentin and M. H. Naraghi, *Effects Cooling Channel Curvature on Coolant Secondary Flow and Heat Transfer*, *46th AIAA/ASME/SAE/ASEE Joint Propulsion Conference & Exhibit* (AIAA, Nashville, 2010), AIAA 2010-6973, doi:10.2514/6.2010-6973.
- [111] B. Zandbergen, *Thermal Rocket Propulsion Lecture Notes*, (Delft University of Technology, 2010) Chap. Heat Transfer and Cooling, pp. 141–181.